Late Quaternary Asian Monsoon variability as recorded in marine archives from the Northern Bay of Bengal and the Northern South China Sea

Dissertation Submitted by

Lorena Astrid Contreras Rosales

In partial fulfillment of the requirements for the degree of

Doctor in Natural Sciences (Dr. rer. nat.)

Faculty of Geosciences

University of Bremen

April 2016

Universität Bremen

Thesis Colloquium:

26 August 2016

Board of Examiners:

Reviewers:

PD Dr. Tim Jennerjahn

Leibniz Center for Tropical Marine Ecology (ZMT), Bremen

Prof. Dr. Gesine Mollenhauer

Faculty of Geosciences, University of Bremen, Bremen

Alfred Wegener Institute Helmholtz Center for Polar and Marine Research (AWI), Bremerhaven

Examiners:

Dr. Enno Schefuß

Center for Marine Environmental Sciences (MARUM), University of Bremen, Bremen

Prof. Dr. Dierk Hebbeln

Faculty of Geosciences, University of Bremen, Bremen

Center for Marine Environmental Sciences (MARUM), University of Bremen, Bremen

Members:

Dr. Daniela Pittauer

Center for Marine Environmental Sciences (MARUM), University of Bremen, Bremen

Andreas Eich

Master Student at the Faculty of Biology/Chemistry, University of Bremen, Bremen

To my husband,

for your infinite understanding, patience and support;

you have taught me an exceptional lesson about love.

To my mother, my sister, my aunt and my grandparents,

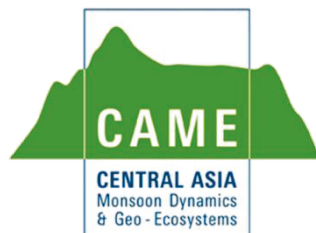*for your unfailing support, constant love and endless hope in me.*

To my parents,

for my education.

Abstract

Among the monsoon systems around the world, the largest one in extension and intensity takes place in the Asian continent. The Asian monsoon system is composed of two domains: the South Asian (or Indian) and the East Asian, divided at about 105°E. The different boundary conditions of these two domains are associated mainly to the differences in the land-ocean configuration and topography. The Asian continent is also the cradle of the world's most ancient civilizations. Nowadays, it is home to about 3 billion people whose lives are intrinsically linked to and dependent on summer monsoon rainfall. Therefore, it is of prime importance to understand the forcing and response mechanisms associated to summer monsoon variability from decennial to millennial time scales and use this knowledge to prepare society to mitigate or prevent natural and social disasters. The approached followed in this work is based on the use of marine sedimentary archives to reconstruct past summer monsoon variability in two of the most anciently populated regions of Asia: the Ganges-Brahmaputra-Meghna basin, at the northern rim of the Bay of Bengal, and the Pearl River basin-Taiwan region, at the northern rim of the South China Sea. Three marine sediment cores were retrieved to perform geochemical analyses: one from the Northern Bay of Bengal continental slope, and two from the Northern South China Sea continental slope. The quantity and composition of sedimentary bulk organic matter and terrestrial biomarkers (plant wax n-alkanes) are investigated to detect changes in paleo-precipitation patterns, terrestrial vegetation composition, and nature of terrestrial and marine organic matter exported to the deep ocean.

In the Northern Bay of Bengal (NBoB) region, summer monsoon evolution is reconstructed over the last 18 ka (Late Pleistocene and Holocene). Continuous high resolution paleo-precipitation and paleo-vegetation records, based on compound-specific carbon and hydrogen stable isotopic composition of terrestrial n-alkanes ($\delta^{13}C_{alkanes}$ and $\delta D_{alkanes}$), allowed the reconstruction of on-land moisture availability in relation to summer monsoon evolution. Results are compared to those from an isotope-enabled general atmospheric circulation model (IsoCAM) used to reconstruct spatial moisture transport and precipitation distribution over the Bengal region for selected time slices. In addition, continuous high resolution records of diverse bulk parameters (TN, TOC, TIC, TOC/TN, $\delta^{13}C_{TOC}$, $\delta^{15}N_{TN}$) and of total hydrolysable amino acid composition (THAA) are used to reconstruct changes of organic matter sources and preservation state in relation

to summer monsoon evolution. In the Northern South China Sea (NSCS) region, summer monsoon evolution is reconstructed over the last 11 ka (Holocene). Here, paleo-precipitation and paleo-vegetation records for the reconstruction of on-land moisture history in relation to summer monsoon are also produced based on the $\delta^{13}C_{alkanes}$ and $\delta D_{alkanes}$ composition of terrestrial n-alkanes. These records are a composite constructed with the two retrieved cores from this region which complement each other age-wise and display similar organic matter characteristics. Both in the NBoB and the NSCS, the role of eustatic sea level as regulator of the relative contribution of different organic matter sources is discussed in addition to summer monsoon. In the NSCS, the role of the Indo-Pacific Warm Pool (IPWP) as regulator of summer monsoon strength and tropical cyclone activity in the Western North Pacific (WNP) is assessed.

The summer monsoon was found to be the most important driver of paleo-hydrologic records in both study regions, with larger imprint in the NBoB than in the NSCS due to additional important sources of precipitation year-round in the second case. In both regions summer monsoon circulation reached maximum strength during the Early Holocene, though the peak of maximum precipitation was not uniform across South and Southeast Asia due to the intervention of additional regional atmospheric, oceanographic and geographic factors. Terrestrial vegetation composition over millennial time scales in both regions was primarily driven by changes of summer monsoon precipitation intensity. This dependence was stronger in the NBoB than in the NSCS due to the larger fraction of annual precipitation delivered by the summer monsoon in the first case as compared to the second case. The export of terrigenous organic matter to the ocean was higher in periods of stronger summer monsoon precipitation due to enhanced fluvial discharge. In addition, a considerably large export of terrestrial organic matter to the ocean was observed during periods of lower eustatic sea level, even under minimum summer monsoon strength conditions, due to a significantly shorter distance between the river mouth and the continental shelf break. Altogether, the export of organic matter to the deep ocean, its preservation through the water column and sediments, and its accumulation and burial were largely promoted by the increased availability of fluvial lithogenic ballasting particles both during periods of lower eustatic sea level and strong summer monsoon. A warming IPWP background state was related to stronger Asian summer monsoon circulation and enhanced tropical cyclone activity in South China, whereas a cooling IPWP background state was related to weaker Asian summer monsoon circulation and enhanced tropical cyclone activity in Taiwan. Due to the strong connection in atmospheric circulation and

moisture transport pathways during the summer monsoon throughout the Indian and Pacific Oceans, it is concluded that the evolution of summer monsoon circulation should be studied as a single phenomenon across South and Southeast Asia.

Keywords

Zusammenfassung

Das weltweit intensivste und größte aller Monsunsysteme erstreckt sich über den asiatischen Kontinent. Das asiatische Monsunsystem besteht aus zwei Domänen, dem südasiatischen (oder auch indischen) und dem ostasiatischen, welche sich bei etwa 105 °E aufteilen. Die unterschiedlichen Randbedingungen dieser beiden Domänen ergeben sich hauptsächlich aus der Land-Ozean Konfiguration und der Topographie. Der asiatische Kontinent ist zudem die älteste Wiege der Zivilisation. Dort leben derzeit über 3 Milliarden Menschen, deren Überleben untrennbar mit den Regenfällen des Sommermonsuns verbunden ist. Daher ist es von höchster Relevanz, die Antriebs- und Reaktionsmechanismen zu verstehen, die mit der Variabilität des Sommermonsuns über Zeitskalen von zehn bis tausenden von Jahren assoziiert sind, und dieses Wissen für die Gesellschaft zu nutzen.

In der vorliegenden Arbeit wurden marine Sedimentarchive verwendet, um die Paläo-Variabilität des Sommermonsuns in zwei der seit frühester Zeit besiedelten Regionen Asiens zu rekonstruieren: dem Ganges-Brahmaputra-Meghna Einzugsgebiet an der Nordseite des Golf von Bengalen und dem Pearl River Einzugsgebiet–Taiwan Region an der Nordseite des Südchinesischen Meeres. Für die Durchführung geochemischer Analysen wurden drei marine Sedimentkerne gezogen, einer vom Kontinentalrand des nördlichen Golf von Bengalen, und zwei vom Kontinentalrand des nördlichen Südchinesischen Meeres. Die Menge und Zusammensetzung der organischen Substanz und terrestrischer Biomarker (Pflanzenwachs n-Alkane) im Gesamtsediment wurde bestimmt, um Veränderungen in den Paläo-Niederschlagsmustern, der Zusammensetzung der terrestrischen Vegetation, und der Beschaffenheit des in die Tiefsee exportierten marinen und terrestrischen organischen Materials festzustellen.

Im nördlichen Golf von Bengalen (NBoB) wurde die Entwicklung des Sommermonsuns über die letzten 18 ka (spätes Pleistozän und Holozän) rekonstruiert. Kontinuierliche, hoch-aufgelöste Paläo-Niederschlags- und Paläo-Vegetationsmuster, basierend auf der stoffspezifischen isotopischen Zusammensetzung des Kohlen- und Wasserstoffs in terrestrischen n-Alkanen ($\delta^{13}C_{alkane}$ und δD_{alkane}), ermöglichte die Rekonstruktion des Feuchtigkeitsangebotes an Land in Relation zur Entwicklung des Sommermonsuns. Die Ergebnisse ausgewählter Zeitintervalle

wurden verglichen mit Resultaten eines Isotopen-basierten Zirkulationsmodells „Isotope-enabled general atmospheric circulation model" (IsoCAM), das verwendet wird, um den räumlichen Feuchtigkeitstransport und die Niederschlagsverteilung in der Bengalen Region zu rekonstruieren. Zusätzlich wurden kontinuierliche, hoch-aufgelöste Aufzeichnungen von diversen Sedimentparametern (TN, TOC, TIC, TOC/TN, $\delta^{13}C_{TOC}$, $\delta^{15}N_{TN}$) und der Aminosäurezusammensetzung (THAA) im Sediment verwendet, um Veränderungen der Quellen und des Preservationsstadiums des organischen Materials in Bezug zur Entwicklung des Sommermonsuns zu rekonstruieren.

In der Region des nördlichen Südchinesischen Meeres (NSCS) wurde die Sommermonsunentwicklung über die letzten 11 ka (Holozän) rekonstruiert. Auch hier wurden die Paläo-Niederschlags- und Paläo-Vegetationsmuster an Hand der isotopischen Zusammensetzung des Kohlen- und Wasserstoffs in terrestrischen *n*-Alkanen ($\delta^{13}C_{alkane}$ und δD_{alkane}) genutzt, um die Feuchtigkeitsgeschichte an Land in Relation zum Sommermonsun zu rekonstruieren. Dieser Datensatz basiert auf der Zusammenstellung beider Sedimentkerne aus der Region, die sich altersmäßig ergänzen und sich bezüglich der Eigenschaften des organischen Materials ähneln. Sowohl in der NBoB, als auch in der NSCS Region wird zusätzlich zum Sommermonsun die Rolle des eustatischen Meeresspiegels als Regulator für den relativen Beitrag von unterschiedlichen Quellen des organischen Materials diskutiert. In der NSCS Region wurde des Weiteren die Rolle des Indo-Pacific Warm Pool (IPWP) als Regler der Ausprägung des Sommermonsuns und der Aktivität tropischer Wirbelstürme im westlichen Nordpazifik (WNP) bewertet.

Der Sommermonsun wurde als der wichtigste Einflussfaktor paläo-hydrologischer Aufzeichnungen in beiden Arbeitsgebieten identifiziert, wobei der Einfluss in der NBoB Region auf Grund zusätzlicher, ganzjähriger Niederschlagsquellen stärker ausgeprägt war, als in der NSCS Region. In beiden Regionen erreichte die Sommermonsun-Zirkulation maximale Stärke während des frühen Holozäns. Allerdings ereignete sich auf Grund regionaler atmosphärischer, ozeanographischer und geographischer Faktoren der Höhepunkt der Maximalniederschläge nicht einheitlich innerhalb Süd- und Südostasiens. Die Zusammensetzung der terrestrischen Vegetation über tausendjährige Zeitskalen wurde primär durch Veränderungen der Niederschlagsintensität während des Sommermonsuns bestimmt. Diese Abhängigkeit war ausgeprägter in der NBoB als in der NSCS Region, weil der durch den Sommermonsun hervorgebrachte Anteil der jährlichen

Niederschläge in ersterer größer war als in letzterer. Der Austrag von terrigenem, organischem Material in den Ozean war stärker in Phasen stärkerer Sommermonsun-Niederschläge auf Grund eines verstärkten Flusswasserablaufs. Zusätzlich wurde in Phasen mit niedrigerem eustatischen Meeresspiegel ein wesentlich stärkerer Austrag an terrestrischer, organischer Substanz in den Ozean beobachtet. Dies war auch während minimaler Sommermonsunausprägung der Fall, und resultiert aus einer erheblich verkürzten Strecke zwischen der Flussmündung und der Abbruchkante des Festlandsockels. Alles in allem wurde der Austrag organischen Materials in die Tiefsee, dessen Konservierung innerhalb der Wassersäule und des Sediments sowie dessen Anreicherung im Sediment stark durch das verstärkte Vorhandensein fluvialer, lithogener Ballastpartikel begünstigt, sowohl in Zeiten eines niedrigeren eustatischen Meeresspiegels als auch während eines starken Sommermonsuns. Ein wärmender IPWP Hintergrundstatus steht in Zusammenhang mit einer verstärkten asiatischen Sommermonsun-Zirkulation und einer verstärkten Aktivität tropischer Wirbelstürme in Südchina. Dagegen steht ein kühlender IPWP Hintergrundstatus in Bezug zu einer schwächeren asiatischen Sommermonsun-Zirkulation und einer verstärkten Aktivität tropischer Wirbelstürme in Taiwan. Aufgrund des engen Zusammenhangs der atmosphärischen Zirkulation mit den Feuchtigkeitstransportwegen während des Sommermonsuns im Indischen und im Pazifischen Ozean wird geschlussfolgert, dass die Entwicklung der Sommermonsun-Zirkulation künftig als ein zusammenhängendes Phänomen innerhalb Süd- und Südostasiens behandelt werden sollte.

Table of contents

List of Figures

List of Tables

List of Abbreviations

6K	Six thousand years before the present (Mid-Holocene)
ACL	Average chain length
ALA	Alanine
AMOC	Atlantic meridional overturning circulation
ARG	Arginine
ASE	Accelerated solvent extractor
ASP	Aspartic acid
B/A	Bölling/Alleröd
BALA	β-alanine
BoB	Bay of Bengal
BP	Before the present (with respect to the year 1950 of the Common Era)
C_3	Photosynthetic pathway based on the Calvin Cycle
C_4	Photosynthetic pathway based on the Hatch-Slack Cycle
CAM	Crassulacean acid metabolism
CAM3.0	Community Atmospheric Model 3.0
CCSM3.0	Community Climate System Model 3.0
CH_4	Methane
CMZ	Core monsoon zone
CO_2	Carbon dioxide
CPI	Carbon preference index

DCM	Dichloromethane
EA	Element Analysis
EASM	East Asian summer monsoon
EHCO	Early Holocene climatic optimum
ENSO	El Niño-Southern Oscillation
GABA	γ-aminobutyric acid
G-B-M	Ganges-Brahmaputra-Meghna river system
GC/IR-MS	Gas chromatography/isotope ratio-mass spectrometry
GLU	Glutamic acid
GLY	Glycine
HIS	Histidine
HOM	High organic matter accumulation
HS1	Heinrich Stadial 1
I-B	Indo-Burman ranges
ILE	Isoleucine
IPWP	Indo-Pacific warm pool
ISM	Indian summer monsoon
IsoCAM	Isotope-enabled Community Atmospheric Model 3.0
ITCZ	Inter-Tropical Convergence Zone
ka	kilo annum i.e. thousands of years
LEU	Leucine
LG	Late Glacial
LGM	Last glacial maximum

LH	Late Holocene
LSR	Linear sedimentation rate
LYS	Lysine
MAP	Mean annual precipitation
MAR	Mass accumulation rate
MAT	Mean annual temperature
MeOH	Methanol
MET	Methionine
MLH	Mid-to-Late Holocene
MOM	Marine organic matter
MT	Monsoon trough
MWP	Melt water pulse
NBoB	Northern Bay of Bengal
NE	Northeast
NP-AA	Non-protein amino acids
NSCS	Northern South China Sea
NW	Northwest
OLC	Odd-long-chain (*n*-alkanes)
OM	Organic matter
ORN	Ornithine
P-AA	Protein amino acids
*p*CO$_2$	Partial pressure of carbon dioxide in the atmosphere
PCA	Principal component analysis

PHE	Phenylalanine
PI	Pre-industrial (with respect to the year 1750 of the Common Era)
PMIP2	Paleoclimate Modelling Intercomparison Project Phase II
RV	Research Vessel
SCS	South China Sea
SD	Standard deviation
SE	Southeast
SER	Serine
SSS	Sea surface salinity
SST	Sea surface temperature
SW	Southwest
TAU	Taurine
TC	Tropical cyclones
THAA	Total hydrolysable amino acids
THR	Threonine
TIC	Total inorganic carbon
TN	Total organic nitrogen
TOC	Total organic carbon
TOC/TN	Total organic carbon to total nitrogen ratio
TOM	Terrestrial organic matter
TYR	Tyrosine
VAL	Valine
VPDB	Vienna Pee Dee Belemnite

VSMOW   Vienna standard mean ocean water

WNP   Western North Pacific

WNPH   Western North Pacific High

YD   Younger Dryas

$\delta^{13}C_{alkanes}$ Stable carbon isotopic composition of n-alkane biomarkers

$\delta^{13}C_{TOC}$ Stable carbon isotopic composition of total organic carbon

$\delta^{15}N_{TN}$ Stable nitrogen isotopic composition of total nitrogen

$\delta D_{alkanes}$ Stable hydrogen isotopic composition of n-alkane biomarkers

Chapter 1

General introduction

1.1. The Asian Monsoon System: An overview

1.1.1. What is the Asian monsoon?

Monsoon, in its most simple form, is defined as the seasonal reversion of the atmospheric circulation in a given location (Duplessy, 1982; Wang et al., 2003). The reversion is caused by the switch of the atmospheric pressure gradient between the land and the ocean; since land has lower thermal capacity than water, land warms-up (or cools-down) faster than the ocean. In a typical monsoonal system, during the warm (cold) season winds blow from (to) the cooler (warmer) ocean to (from) the warmer (cooler) land (Fig. 1.1). Monsoon seasonality is therefore experienced as drastic changes in air temperature and precipitation patters over land, with cool-dry winters and warm-wet summers, whereas variations in the ocean include strong seasonality in sea surface temperature and salinity, surface current strength and direction and eventual upwelling along continental margins (P. Wang et al., 2005).

There are several monsoon systems around the world; however, the largest one in extension and intensity takes place in the Asian continent as it is the largest land mass of the planet. The Asian monsoon is composed of two mayor domains: the Indian (or South Asian) monsoon domain and the East Asian monsoon domain, divided at circa 105°E (P. Wang et al., 2005). The different thermal boundary conditions of the two subsystems are associated mainly to the differences in the land-ocean configuration and topography. The Indian monsoon is driven by the north-south thermal contrast between the Indian subcontinent and the Indian Ocean; this contrast is additionally strengthened by the location of the Tibetan Plateau to the north of the Indian land-mass. The Indian monsoon is composed of a single tropical component associated to the seasonal migration of the intertropical convergence zone (ITCZ) (Fleitmann et al., 2007; Wang et al., 2003). The East Asian monsoon is driven by the north-south thermal contrast between the Australian land mass and the Western North Pacific (WNP), and the west-east thermal contrast between the East Asian land mass (with the Tibetan Plateau to the west) and the Pacific Ocean. The East Asian monsoon has

two components, a tropical and a subtropical one; the first is associated to the seasonal displacement of the ITCZ, whereas the second is associated to the seasonal displacement of the subtropical Meiyu Front (Wang et al., 2003). Modern meteorological observations and moisture transport budgets indicate that the southern hemisphere Indian Ocean is the dominant source of moisture (latent heat) to the Indian and East Asian summer monsoons (Ding et al., 2004). This is a good indication that both systems are closely linked and therefore Asian monsoon behavior should be interpreted with southern hemisphere Indian Ocean dynamics in consideration (Clemens et al., 2010).
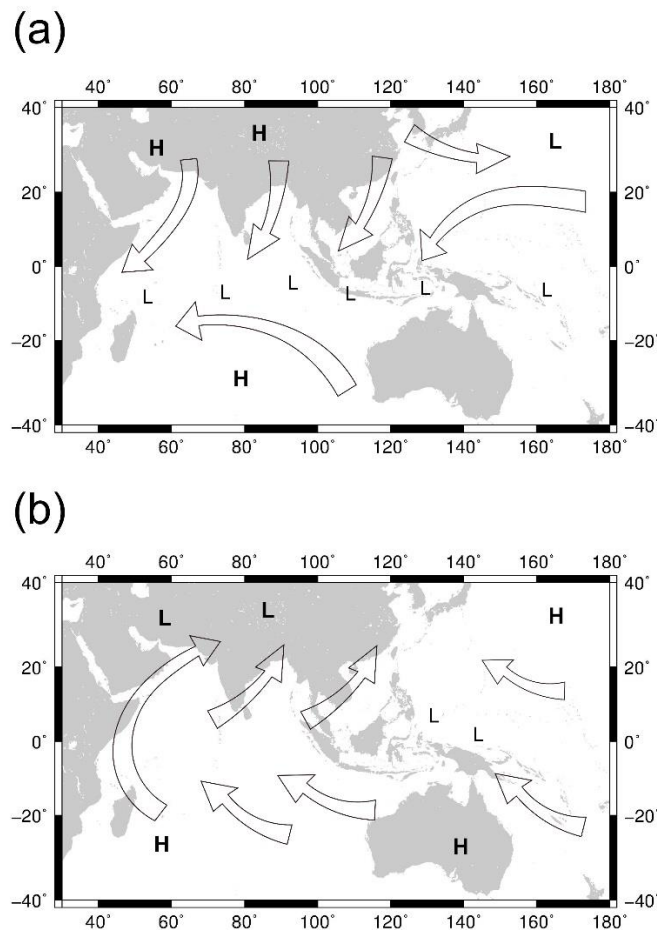
Fig. 1.1. Surface pressure and wind patterns over land and sea during winter and summer monsoon. **(a)** winter monsoon; **(b)** summer monsoon. Based on P. Wang et al. (2005).

1.1.2. Factors controlling Asian monsoonal intensity

The changes in monsoon intensity derive from the continuous interaction of several forcing mechanisms operating at different time scales. These mechanisms can be divided in two groups: (1) external, i.e. independent to the land-ocean-atmospheric system, they usually act at intermediate time scales (centennial, millennial) and derive from insolation changes controlled by variations in orbital configuration and solar activity; (2) internal, i.e. dependent to the land-ocean-atmospheric system, they usually act at short to intermediate time scales (inter-annual, decadal, centennial, millennial) and derive from the climate system and its associated feedbacks, oscillations and teleconnections. Additionally, at geological time scales (millions of years), tectonic forcing also plays an important role in the development and evolution of monsoonal systems since they modify the land-ocean distribution and topography (P. Wang et al., 2005).

El Niño Southern Oscillation (ENSO) would be an important internal forcing mechanism of monsoon intensity at interannual to decadal time scales with a non-stationary periodicity in the range of 3 to 8 years (P. Wang et al., 2005). ENSO regulates monsoon intensity through the sea surface temperature (SST) anomalies originated in the Pacific Ocean. Also on decadal to centennial time scales, external forcing by solar activity cycles cause weak variations in the incident solar radiation, modifying the planetary heat budget and thus monsoonal circulation and intensity, with periodicities centered around 11, 20-24, 60, 80-102, 145, 210, 510-560, 700 and 900 years (P. Wang et al., 2005; Y. Wang et al., 2005).

At millennial time scales, climate records from monsoonal regions have strong similarities with ice core records form Greenland, indicating a climatic coupling between high and low latitude regions (Y. Wang et al., 2005). Among the shortest millennial oscillations are the Dansgaard-Oeschger cycles, with a periodicity of ca. 1500 years, which are related to changes in the rate of the Atlantic meridional overturning circulation (AMOC) (P. Wang et al., 2005; Y. Wang et al., 2005). For the Asian monsoon, a correlation with North Atlantic ice-rafted debris layers in marine sediments —Heinrich events— has also been identified (Leuschner and Sirocko, 2000). Altogether, previous studies in the Arabian Sea, the Bay of Bengal, the South China Sea and the Sea of Japan have revealed intensified winter monsoons during stadials (cold spells) and intensified summer monsoons during interstadials (warm spells) (P. Wang et al., 2005).

Longer millennial cycles are associated with changes in the Earth's orbital configuration derived from precession of the equinoxes (19-23 Ka cycle) and obliquity of the Earth's rotation axis with respect to the orbital plane (41 Ka cycle). Modulation of precession by the eccentricity introduces an additional cycle with period of ca. 100 Ka (Ruddiman, 2006). Changes in orbital parameters are related to the changes in the planet's insolation budget, later expressed in the waxing and waning of polar ice sheets (main component of the cryosphere), their associated sea level changes, and the sequestration or release of greenhouse gases (mainly CO_2 and CH_4). These processes are paced by orbital cycles and further modulated by internal feedback mechanisms while their impacts in climate derive from the modification of the latent heat redistribution around the planet. Through the modification of atmospheric and oceanic circulation, all these processes have important impacts in monsoonal intensity and evolution. A recent study from the South China Sea (SCS) over the monsoonal response to orbital forcing in the last 5 Ma, found that Asian monsoon varies dominantly and directly in response to changes in low-latitude insolation, mostly regulated by precession forcing, whereas its response to obliquity and eccentricity forcing is rather weak because their impacts are stronger at middle and high latitudes (Ao et al., 2011).

On geological time scales of millions of years, monsoon circulation is bound to exist every time that the tropics are occupied by land and sea, however its intensity varies greatly with induced geographic and topographic changes such as tectonic uplift, sea-land distribution and the opening or closing of oceanic gateways. For the modern Asian monsoon, the fundamental factors determining monsoonal development and evolution are the rise the Tibetan Plateau —intensified after 8 Ma ago (Wan et al., 2006)—, the retreat of the Paratethys Sea (30-10 Ma ago) which lead to the continentalization of the Asian interior, and the closure of the Indonesian seaway (3-4 Ma ago) which restrained water exchange between the Pacific and the Indian Oceans (P. Wang et al., 2005).

1.1.3. Asian monsoon evolution

Long term monsoon records from the Indian Ocean as well as sequences from the Chinese Loess Plateau, indicate that the initiation on the modern Asian monsoon took place about 10-8 Ma ago (Kroon et al., 1991; Prell et al., 1992; Zhisheng et al., 2001), when the uplift of the Himalayas and the Tibetan plateau crossed the threshold in which monsoonal circulation could be developed by

the enhanced aridity of the Asian interior (Boos and Kuang, 2010; Liang and Wang, 1998; Zhisheng et al., 2001). Monsoonal circulation intensified around 8 Ma ago with two maximum summer monsoon strength periods between 8.5-7.6 Ma and 7.1-6.2 Ma (Wan et al., 2006). Accelerated tectonic uplift of the Tibetan Plateau occurred around 3.5 Ma ago along its northern and eastern margin, while East Asian monsoon proxy records indicate summer and winter monsoon strengthening at ca. 3.6-2.5 Ma (Wan et al., 2006; Zhisheng et al., 2001); this could indicate a link to the plateau rise however further direct evidence is still necessary. A long term decreasing trend of the low-latitude Asian summer monsoon intensity, with increased oscillation amplitude, has been observed for the last 2.8 Ma and is probably associated to the onset and further development of sustained major ice sheets in the Northern Hemisphere (Ao et al., 2011). Strengthening of East Asian winter monsoon was hypothesized between 2.5-1.0 Ma ago (Zhisheng et al., 2001).

Some classic studies on the Asian monsoon behavior suggest that stronger summer monsoon activity is observed during interglacial periods and is linked to weaker winter monsoon; on the other hand, stronger winter monsoon activity is thought to occur mostly during glacials in combination to weaker summer monsoon (Duplessy, 1982). However, this concept is being challenged with new evidence of parallel behavior between summer and winter monsoon intensity found at shorter time scales during the Holocene (Steinke et al., 2011). Furthermore, the traditional vision appears to be an over-simplification, since high resolution records put in evidence millennial oscillations that depart from the glacial/interglacial general background trend (Ao et al., 2011).

High resolution speleothem $\delta^{18}O$ records from four caves in continental China —Hulu cave (Wang et al., 2001), Dongge cave (Yuan et al., 2004), Sanbao cave (Wang et al., 2008) and Linzhu cave (Cheng et al., 2009)— document Late Pleistocene and Holocene history of the East Asian monsoon for the last 224 ka. However, debate has arisen from the question of precisely what signal/signals are recorded in these records. Recent studies based on improved crossed spectral analysis indicate that cave $\delta^{18}O$ is actually a mixed record composed from both summer and winter monsoon precipitation signals, but not as a ratio —i.e. stronger summer precipitation signal always implying weaker winter precipitation signal and vice versa— but as a mix of independent signals (Clemens et al., 2010). Among the most important observations made on these cave $\delta^{18}O$ records is that they resemble quite closely the millennial stadial/interstadial stages recorded in the $\delta^{18}O$

records from Greenland ice cores (Wang et al., 2008), as well as Greenland ice CH_4 and CO_2 concentrations (Cheng et al., 2009). Besides, observed correlation with the proportion of ice rafted debris in North Atlantic sediments also suggests a connection with Heinrich events (Cheng et al., 2006; Wang et al., 2001), which are particularly obvious around times of glacial termination (T-I, T-II, T-III, T-IV) during weak monsoon intervals associated to major reduction of the Atlantic Meridional Overturning Circulation (AMOC) after abrupt ice-sheet collapse (Cheng et al., 2009).

During the Early Holocene, also known as the Holocene optimum period or the Holocene thermal maximum, several marine and cave proxy records of moisture and temperature reveal enhanced summer monsoon precipitation worldwide, including the South Asian and East Asian monsoon systems, though not all the areas within modern monsoon boundaries recorded increased moisture in this period (Wang et al., 2010). Primary productivity and wind dust transport proxies recorded in lake sediments from the Qinghai-Tibetan Plateau indicate that, during the Late Holocene (last 3770 years), periods of intensified summer (winter) monsoon in this region are well correlated with increased (reduced) solar output (Liu et al., 2009). In particular, five distinct periods of stronger Asian winter monsoon were correlated with different sunspot minima (Wolf, Spörer, Maunder, Dalton and Oort), and three of them could be further associated with Holocene ice-rafting events in the North Atlantic (Bond events 0 to 2). The weakening in the monsoon during the most recent part of the Holocene is in contradiction to the trend suggested by some Chinese speleothem $\delta^{18}O$ records which would point to an increase in precipitation up to ca. 100 years ago, when reversion on this trend is observed (Y. Wang et al., 2005); but is in agreement to some proxy records from the Qinghai Plateau (Z. Liu et al., 2008) and from lake sediments from Southern China (Wang et al., 2010 and references therein).

In any case, an important conclusion to be extracted is that Asian monsoon is a complex system and that, due to its large geographic range, can be affected by a great diversity of factors. Furthermore, the monsoon is a dynamic phenomenon that moves both in time and space and whose effects can reach different areas at different times. All this has to be kept into account when interpreting monsoonal paleo-records.

1.2. Overview of proxies used for reconstructing monsoon evolution from marine archives

1.2.1. Proxies for organic matter sources and preservation state

Bulk composition of terrestrial organic matter has particular chemical and isotopic properties that distinguish it from marine organic matter (e.g. Jennerjahn et al., 2008). For instance, plant tissues are richer in macromolecules free of nitrogen (such as lignin, tannin, hemicellulose, cellulose, cutin and suberin) in proportion to proteins, which makes plant tissues particularly rich in carbon versus nitrogen (C/N = 20-500) in comparison to phytoplankton (C/N $\approx$ 7), bacteria (C/N $\approx$ 4) and fungi (C/N $\approx$ 10), which have a carbon/nitrogen ratio closer to that of proteins (C/N $\approx$ 3-4) (Hedges and Oades, 1997). However, vegetal tissues tend to preferentially gain nitrogen during microbial decay, whereas marine phytoplankton tends to preferentially loose nitrogen. In turn, the high aromaticity of lignin and tannins are good indication of terrestrial derived material against aromatic amino acids such as phenylalanine, histidine and tryptophan, and simple phenols in other organisms (Hedges et al., 1997).

Characterization of sedimentary organic matter isotopic composition ($\delta^{13}C$ and $\delta^{15}N$) can also be used to determine its terrestrial or aquatic origin and preservation state (e.g. Dupont et al., 2010; Jennerjahn et al., 2004), as well as the composition of terrestrial vegetal organic matter sources to soils and sediments (e.g. Galy et al., 2008a; Li et al., 2009). For instance, terrestrial C_4 plants have a distinctively $\delta^{13}C$ signature in their tissues of ca. -12‰, whereas C_3 plants are within the range of -28‰ and -25‰; finally, marine phytoplankton values are between -22‰ and -19‰ (Hedges et al., 1997). Likewise, $\delta^{13}C$ isotopic values can also be used as indicators of the organic matter degradation state, determined by the time and distance of transport and reworking before final deposition, which is partly related to runoff activity (e.g. Galy et al., 2008a). On the other hand, $\delta^{15}N$ of organic matter can be altered by several processes such as the degree of nutrient utilization, nitrification or denitrification, organic matter diagenesis, and organic matter inputs from different sources (Dupont et al., 2010). Nitrogen fixation by bacteria occurs with minimal isotopic fractionation ($\delta^{15}N$ = 0‰). Because of the prevalence of nitrogen fixation on land, low $\delta^{15}N$ values in sedimentary organic matter are therefore good indication of terrestrial organic matter contribution (Peters et al., 1978; Robinson, 2001). However, there are considerable variations in the $\delta^{15}N$ of marine organic materials depending on their source and state of

degradation, which complicates up to a certain point the applicability of this proxy as indicator of organic matter origin (Hedges and Oades, 1997).

Other specific compounds such as amino acids and hexosamines are also an alternative to determine the origin and degradation state of sedimentary organic matter (Chen et al., 2004; Dauwe et al., 1999; Suthhof et al., 2000). For example, the non-protein amino acids (γ-aminobutiric acid and β-alanine) are produced by bacteria from protein precursors and high concentrations are indication of intermediate to highly degraded organic matter (Dauwe et al., 1999; Jennerjahn and Ittekkot, 1999). On the other hand, hexosamines (glucosamine and galactosamine) are incorporated into structural biopolymer matrices like bacterial cell walls and chitin, for this reason they tend to be found in high concentrations in refractory material indicating high degree of organic matter degradation (Dauwe and Middelburg, 1998). In a similar way, high ratio values between amino acids/hexosamines have been used as indicators of degraded organic matter (Chen et al., 2004). Finally, the concentrations of the aromatic amino acid tyrosine (Tyr) has also been proposed as a degradation indicator since it is particularly labile in the presence of oxygen, for which low concentrations of Tyr could indicate longer exposure of organic matter to oxygen and thus enhanced degradation (Jennerjahn and Ittekkot, 1999; Suthhof et al., 2000).

1.2.2. Proxies for precipitation over land and vegetation cover

One of the most recent and accurate approaches to estimate precipitation patterns over land from short to intermediate time scales is the analysis of $\delta^{18}O$ in cave speleothems calcite (Hendy, 1971). This is possible due to the fractionation of oxygen isotopes during the evaporation and precipitation of rain water following the principles of the Rayleigh fractionation process (Craig and Gordon, 1965). Due to mass dependence effects, light isotopes evaporate easier than heavy isotopes but heavy isotopes precipitate easier than light isotopes. In this way, rain nearby the ocean and at low latitudes is usually enriched with heavy isotopes whereas rain far from the ocean and at high latitudes is enriched with light isotopes, allowing tracing the origin of rain water (Araguás-Araguás et al., 1998) . On top of this, the isotopic composition of rain at mid and high latitudes is linearly related to the mean annual atmospheric temperature at the site of precipitation (Jouzel et al., 2000). Calcite in cave speleothems derives from carbonate dissolved in infiltrated rain water, and carries thus a precipitation signal that can be further used to reconstruct rain patterns over a

given area (Lachniet, 2009). Cave speleothems have been widely used to reconstruct monsoon intensity (e.g. Cheng et al., 2009; Wang et al., 2001), mainly because of their high temporal resolution and the possibility to make accurate age models with absolute radiometric methods based on the Th/U series (e.g. Fleitmann et al., 2007). The same principle has been applied to the analysis of $\delta^{18}O$ in carbonate deposits from lake sediments (Z. Liu et al., 2008).

In marine archives, reconstruction of precipitation and runoff patterns over land can be done with the study of mineral assemblage composition, usually focused on the proportion of specific terrestrial elements and minerals, but also with the analysis of grain size distribution, as all these proxies allow to elucidate the different origins of the transported material (e.g. Ao et al., 2011; Durum and Haffty, 1963; J. Huang et al., 2011; Wan et al., 2006). Continental pollen records are also stored in marine archives and can be used as reliable indicators of monsoon precipitation because they provide an overview of the composition of continental vegetation, which is in great part determined by the precipitation patterns (e.g. Dupont et al., 2010; Jiang and Ding, 2008).

Terrestrial biomarkers can also be used to infer moisture, vegetation and runoff patterns over land. Among the most studied compounds for this purpose are *n*-alkanes, which constitute the building blocks of plant waxes. Using these compounds, several indexes can be calculated to obtain different kinds of information. For example, the average chain length (ACL) and the carbon preference index (CPI) can be used as proxies to trace terrestrial high plant material transported by river discharge or dust (He et al., 2008). This is because *n*-alkanes produced by higher plants usually have long chain carbon numbers —ranging from C_{21} to C_{35}, with C_{29}, C_{31} or C_{33} as the most abundant— and display odd-to-even carbon number predominance (Eglinton and Hamilton, 1967; Meyers and Ishiwatari, 1993). In contrast, *n*-alkanes produced by aquatic organisms have usually shorter chain carbon numbers —C_{11} to C_{25}, with C_{17} and C_{19} as the most abundant— and do not show odd-to-even carbon predominance (Meyers and Ishiwatari, 1993). Besides, the carbon preference index (CPI) can also be used to estimate the degree of maturation and distinguish fresh from fossil material. This is because fresh plant material will present strong odd-to-even carbon-chain predominance and this difference decreases as material is degraded (Killops and Killops, 2005). On the other hand, the average chain length (ACL) can also be used as a proxy for vegetation type, where higher values are related to grass vegetation and lower values are related to tree vegetation (He et al., 2008). Accumulation rates and concentrations of these terrestrial

biomarkers in marine sediments can be used to estimate runoff intensity (Hu et al., 2009) or even sea level changes, as low stands are usually associated to higher terrestrial input due to the expansion of the continental margins (e.g. Pelejero, 2003). Furthermore, the discovery in soil organic matter of branched isoprenoid glycerol dialkyl glycerol tetraethers (GDGTs), derived from anaerobic soil bacteria, and Crenarchaeol, derived from soil archaea, has made possible the construction of the BIT index, used to determine the relative contribution of terrestrial organic matter into marine sediments (Hopmans et al., 2004; Weijers et al., 2007).

Another application of terrestrial biomarkers is the analysis of their compound-specific stable isotopes (e.g. Duan and Wu, 2008; Rao et al., 2009; Schefuß et al., 2005). For example, carbon stable isotopes ($\delta^{13}C$) of terrestrial plant lipid biomarkers can be used as a proxy of continental aridity since different photosynthetic pathways (C_3 and C_4) produce different isotopic signatures (Bender, 1971; Smith and Epstein, 1971). Typical $\delta^{13}C$ values in plant lipid biomarkers are in the range of -32 to -39‰ for C_3 plants and -18 to -25‰ for C_4 plants (Collister et al., 1994). On the basis of the observation that C_4 plants can withstand arid conditions better than C_3 plants (e.g. Osborne and Freckleton, 2009), it is possible to infer the moisture history in a region based on the proportion of C_4-lipids versus C_3-lipids in marine sediments as inferred form their $\delta^{13}C$ signature (e.g. Hu et al., 2002; Rao et al., 2009; Schefuß et al., 2003). Alternatively, the analysis of the hydrogen stable isotopic composition (δ^2H or δD) in plant lipids can be used as a proxy for continental precipitation on the basis of the same fractionation principles for oxygen isotopes. The δD signal of precipitation depends on the equilibrium isotopic fractionation, which is affected by four main aspects, known as the latitude, altitude, continental and amount, effects (Dansgaard, 1964). These refer to the progressive depletion of deuterium (^2H or D) versus hydrogen (^1H) with higher latitude, higher altitude, longer distance from the ocean, and increased amount of rainfall, respectively. The first three are strongly driven by condensation temperature and Rayleigh fractionation conditions. Deuterium in precipitation is also affected by kinetic fractionation during water evaporation/condensation (Dansgaard, 1964). The depletion or enrichment value of deuterium in terrestrial biomarkers depends ultimately on the moisture source (Chikaraishi and Naraoka, 2005); however isotopic fractionation can also depend on the photosynthetic pathway of the plant (C_3, C_4 or CAM; Chikaraishi et al., 2004). Furthermore, δD values of terrestrial plant lipids also reflect the balance between precipitation and evaporation in a given area (Sauer et al.,

2001). This is because moisture loss by evapotranspiration in plants leads to deuterium enrichment, while soil waters also become deuterium enriched by evaporation under arid conditions. The overall fractionation is thus represented as $^2\varepsilon_w$ and can be calibrated comparing the δD of plant wax lipids to that of meteoric precipitation (Hou et al., 2008).

1.3. Study areas

1.3.1. The Northern Bay of Bengal and the Ganges-Brahmaputra-Meghna River catchment

The Northern Bay of Bengal (NBoB) is located within the area of influence of the Indian (South Asian) monsoon system. The surface circulation of the NBoB (Fig. 1.2) is characterized by multiple open ocean meso-scale gyres (eddies) and coastal boundary currents that reverse throughout the year (Sarma et al., 1999; Shetye et al., 1993; Varkey et al., 1996). Between May and September, SW summer monsoon winds induce coastal upwelling in a narrow strip (~40 km) along the northeastern Indian margin (Shetye et al., 1991); the eastward Ekman transport that fuels the upwelling pushes the G-B-M river plume offshore (Rao et al., 1988; Shetye et al., 1991). Further from the coast, the SW winds induce a cyclonic (anticlockwise) eddy in the northwestern bay which spreads the river plume in southward direction parallel to the coast (Shetye, 1993; Shetye et al., 1991; Varkey et al., 1996). Heavy monsoon precipitation fuels large fresh water discharge from the Ganges-Brahmaputra-Meghna (G-B-M) River, inducing an important reduction of sea surface salinity (26 to 34 psu) in the northern part of the bay associated with strong water column stratification (Levitus and Boyer, 1994). The large amounts of freshwater introduced during summer form a thin layer (~10 m or less) across the NBoB, reaching as far south as 16.5 °N (Vinayachandran and Kurian, 2007). This summer freshwater layer continues to spread and mix with the underlying waters throughout the rest of the year (Shetye, 1993). Between October and January, the reversal of the winds cause the collapse of the upwelling, and the G-B-M river plume is then channeled in a narrow strip (~50 km) along the eastern Indian coast as an equatorward coastal current (Chauhan et al., 2005; Shetye, 1993). Further offshore, the NE winter monsoon winds induce the formation of an anticyclonic (clockwise) eddy in the northwestern bay which further spreads the remains of the summer freshwater layer across the NBoB (Shetye, 1993; Varkey et al., 1996). Between February and April (spring intermonsoon), a basin-wide anticyclonic gyre is formed which reaches the eastern Indian margin and establishes a typical

western boundary current with poleward flow (Shetye et al., 1993). This pushes the G-B-M river plume in southeastward direction perpendicular to the coast and spreads it, together with the remains of the summer freshwater layer, all across the central Bay of Bengal as far as 10° N (Shetye, 1993).

The Ganges-Brahmaputra-Meghna (G-B-M) drainage area is approximately 1650×10^3 km^2 and provides an average fresh water and sediment supply of respectively 1120 km^3 yr^{-1} and 1060 Mt yr^{-1} to the Bay of Bengal (Milliman and Farnsworth, 2011), with more than 95% of the delivered sediments being transported during the summer monsoon season. The Bengal Fan is the largest active submarine fan of the world with a sediment volume of ca. 12.5×10^6 km^3 (Curray et al., 2003). Today, the river floodplain is covered by seasonal forests and tropical savanna, whereas the Himalayan reaches are covered by subtropical forests at lower altitude, and with cool temperate and mixed forests, and boreal montane forests at higher altitude (Blasco et al., 1996). Modern crops within the catchment area include wheat, barley, millet, maize, rice and sugar-cane (Ganguli, 1938). Historically, the Ganges Valley has registered civilized human activities (urbanization, agriculture) since the first millennium before Christ with the establishment of Aryan groups in the region (Erdosy, 1985).

1.3.2. The Northern South China Sea, the Pearl River catchment and Southern Taiwan
The South China Sea (SCS) is the largest marginal sea in the world. It is a semi-enclosed basin delimited by continental China, the Indochinese Peninsula, the Malay Peninsula, the island of Taiwan, and the archipelagos of the Philippines and Indonesia. Marine surface circulation in the South China Sea (Fig. 1.2) is seasonally reversed in response to the shift of monsoon winds (Liu et al., 2016 and references therein). The northern rim of the basin is characterized by the year-round presence of the Longshore Current traveling south along the Chinese margin (Li et al., 2016; J. Liu et al., 2011; Wang et al., 1986). Main circulation in the central basin is cyclonic during winter due to the predominant NE-SW wind direction and anticyclonic during summer due to the predominant SW-NE wind direction (Liu et al., 2016 and references therein). The year-round inflow of the Kuroshio Current into the NSCS through the Luzon Strait is characterized by the formation of a series of surface mesoscale anticyclonic (clockwise) eddies that propagate westwards (J. Liu et al., 2011; Z. Liu et al., 2010). The southern rim of this series of gyres conforms

what is known as the "Kuroshio Branch Current" that flows in NE-SW direction along the slope. In turn, the northern rim of this series of gyres forms a "Warm Current" flowing in SW-NE direction along the shelf break (J. Liu et al., 2011), permanently during summer and at intervals during winter, in periods of NE-wind relaxation (Chiang et al., 2008).

The northern South China Sea (NSCS) is significantly affected by fresh water input from the Pear River (Zhu Jiang) which modifies oceanographic conditions inducing estuarine circulation and seasonal stratification, especially during the rainy season (Dong et al., 2004). The Pearl River catchment area is about 442×10^3 km^2 in size, with a modern delta area of ca. 17,200 km^2 (Weng, 2007). The total water discharge has been estimated on 330 km^3 yr^{-1} and the annual suspended sediment load on around 80 Mt (Zhao, 1990). Modern land-use activities within the river basin include paddy rice cultivation, sugarcane and fruit horticulture, and dike pond-agriculture aquaculture in the delta area (Weng, 2007). Land reclamation has historically occurred around the river delta, where shoreline modification for agricultural purposes derived into extensive dike construction. This practice, in combination to the natural progradation of the delta, has yield a significant amount of new agricultural land since the Late Neolithic Age (ca. 5200 years B.P.) (Li et al., 1991). Natural vegetation in the basin includes evergreen broad-leaved forests (*Castanopsis*, Theaceae, Lauraceae), while above 1200 m upper montane rain forests appear (*Podocarpus, Cyclobalanopsis, Betula*), with the furthest NW reaches of the river basin dominated by conifer forests (*Tsuga*) (Wu, 1980).

The NSCS is also affected by the discharge from Taiwanese rivers (Liu et al., 2016). The total annual water discharge of the rivers located in the SW of Taiwan (Tsengwen, Erhjen, Kaoping, Tungkang, and Linpien) ranges between 0.8 to 6 km^3, while the total annual sediment discharge is estimated in 60 Mt (Milliman and Kao, 2005). From these, the Kaoping River is the largest with a basin area over 2000 km^2 and accounts for about 80 % of the water and sediment efflux in this region. River discharge in Taiwan is highly seasonal due to summer monsoon rains and the pass of typhoons, with the runoff from June to October being about a hundred times higher as compared to the rest of the year (Milliman and Kao, 2005). Natural vegetation in Taiwan is strongly determined by altitude and is composed, from low to high elevations, of tropical (*Ficus, Machilus*) and subtropical (*Machilus, Castanopsis*) evergreen forest, warm temperate evergreen (*Cyclobalanopsis*) and mixed (*Quercus, Alnus, Chamecyparis, Pinus*) forests, cool/cold temperate

conifer (*Tsuga, Picea, Abies*) forests, and alpine (*Yushania, Miscanthus*) vegetation (Yu et al., 2003). Earliest evidence of rice cultivation in Taiwan dates back to ca. 4800 BP (Zhang and Hung, 2010). Modern land uses include intensive agriculture in the low altitude areas with production of rice, sugar cane and horticultural fruits; other land uses include livestock husbandry of poultry and hog (www.taiwan-agriculture.org).
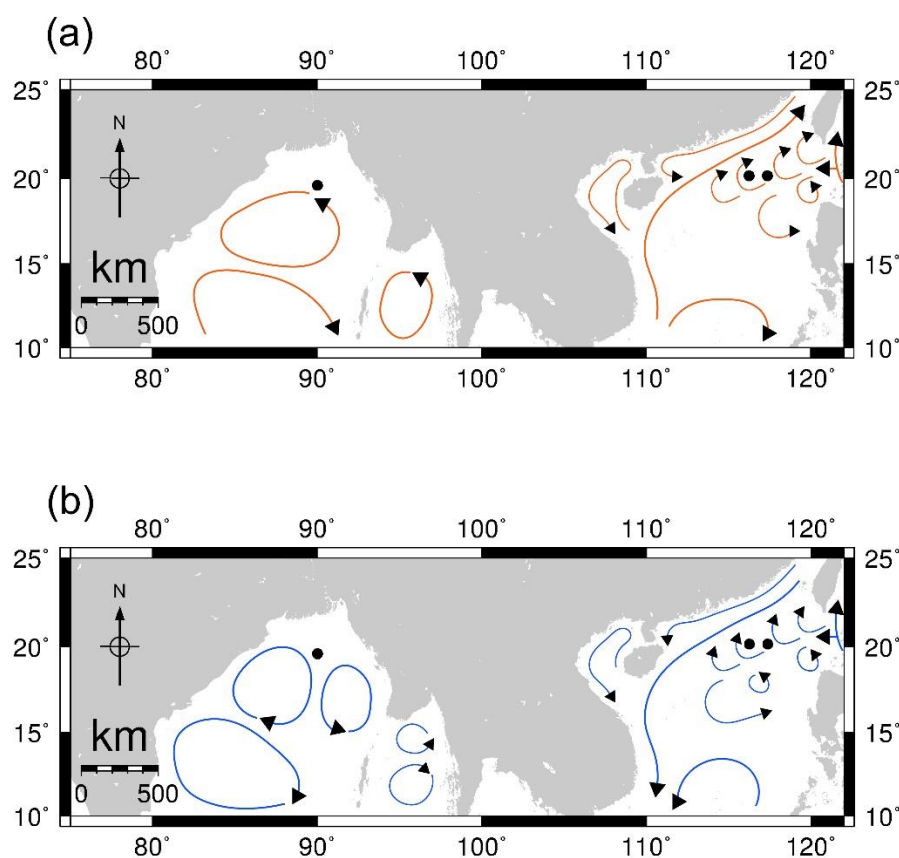
Fig. 1.2. Simplified sea surface circulation in the Bay of Bengal and the South China Sea. The panels illustrate major circulation features during **(a)** summer monsoon and **(b)** winter monsoon. The black dots indicate the location of cores used in this study: SO188-342KL in the Northern Bay of Bengal, and GeoB16601-5 and MD05-2905 in the Northern South China Sea. Circulation features are based on the studies of Varkey et al. (1996) and Liu et al. (2016).

Chapter 2

Motivation, objectives, hypotheses, materials, methods and thesis outline

2.1. Motivation

Asia is the cradle of the world's most ancient civilizations, and for over 5000 years has supported ever larger human populations and continuous human-induced land transformations. Nowadays, it is home for about 3 billion people whose lives are intrinsically linked to and dependent on monsoonal rainfall. The monsoon effects over human society are extent and diverse, the most fundamental one is related to summer monsoon precipitation that makes agriculture possible. Weakening of the summer monsoon for long periods of time in the past has led to severe droughts, the collapse of agriculture and, eventually, the collapse of entire civilizations (Weiss and Bradley, 2001; Wu and Liu, 2004; Zhang et al., 2008). Therefore, it is of prime importance to understand the forcing and response mechanisms associated to summer monsoon variability over decennial, centennial and millennial time scales and use them to prepare society for future monsoon variability in order to mitigate or prevent natural and/or social disasters.

This PhD project is developed within the framework of a large cooperation project funded by the BMBF entitled "Natural versus anthropogenic controls of past monsoon variability in Central Asia recorded in marine archives (CARIMA)". The CARIMA project has as general aim to improve our understanding of the Asian monsoon dynamics during the Holocene at timescales of societal relevance.

The approached followed in this work is based on the use of marine sedimentary archives to study the history of both marine and terrestrial paleo-environmental processes, with large focus on terrestrial aspects. The reason to use marine archives is due to the advantages they offer, such as: (1) recording long and continuous periods of time; (2) recording several environmental processes in just one archive; (3) having high time resolution; (4) integrating processes at a regional level.

2.2. General objectives

I. To reconstruct the natural variability of the Asian Summer Monsoon and its effects during the Late Quaternary through the analysis of changes in terrestrial vegetation composition, on-land precipitation patterns and the quality and quantity of organic matter exported to the deep ocean.

II. To identify common and specific patterns of summer monsoon variability between the Indian (South Asian) and East Asian monsoon domains during the Late Quaternary.

2.3. Research hypotheses

1. Summer monsoon precipitation is the main driver of the variability in paleo-hydrologic records from the Northern Bay of Bengal and the Northern South China Sea.

2. Summer monsoon reached maximum strength during the Early Holocene both in the Northern Bay of Bengal and the Northern South China Sea.

3. Terrestrial vegetation composition over millennial time scales is primarily driven by changes of summer monsoon strength both study regions.

4. Export of terrigenous organic matter to the ocean is higher in periods of stronger summer monsoon due to enhanced fluvial discharge associated to higher precipitation amount.

5. Sedimentary organic matter accumulation and preservation is higher in periods of stronger summer monsoon.

2.4. Materials

Three marine sediment cores (Table 2.1; Fig. 2.1) were retrieved to perform geochemical analyses: (1) core SO188-342KL from the Northern Bay of Bengal continental slope, (2) core MD05-2905 from the Northern South China Sea continental slope, and (3) core GeoB16601-5 also from the Northern South China Sea continental slope. The three cores are located in the neighborhood of important river systems such as the Ganges-Brahmaputra-Meghna system in the northern rim of the Bay of Bengal, as well as the Pearl River system and the Taiwanese montane rivers in the

northern rim of the South China Sea, which guarantee the input of terrestrial organic matter to the core sites.

Table 2.1. Sediment cores analyzed in this thesis.

Core	Length	Time Span	Latitude	Longitude	Water depth	Research Vessel	Cruise	Date
SO188-342KL	12.58 m	0-18.1 ka	19°58.40'N	90°02.03'E	1256 m	RV *Sonne*	SO-188	July 2006
MD05-2905	11.98 m	2.4-11.2 ka	20°08.17'N	117°21.61'E	1647 m	RV *Marion Dufresne*	MD147	May/June 2005
GeoB16601-5	0.38 m	0-2.1 ka	20°09.04'N	116°14.41'E	1013 m	RV *Sonne*	SO-221	May/June 2012
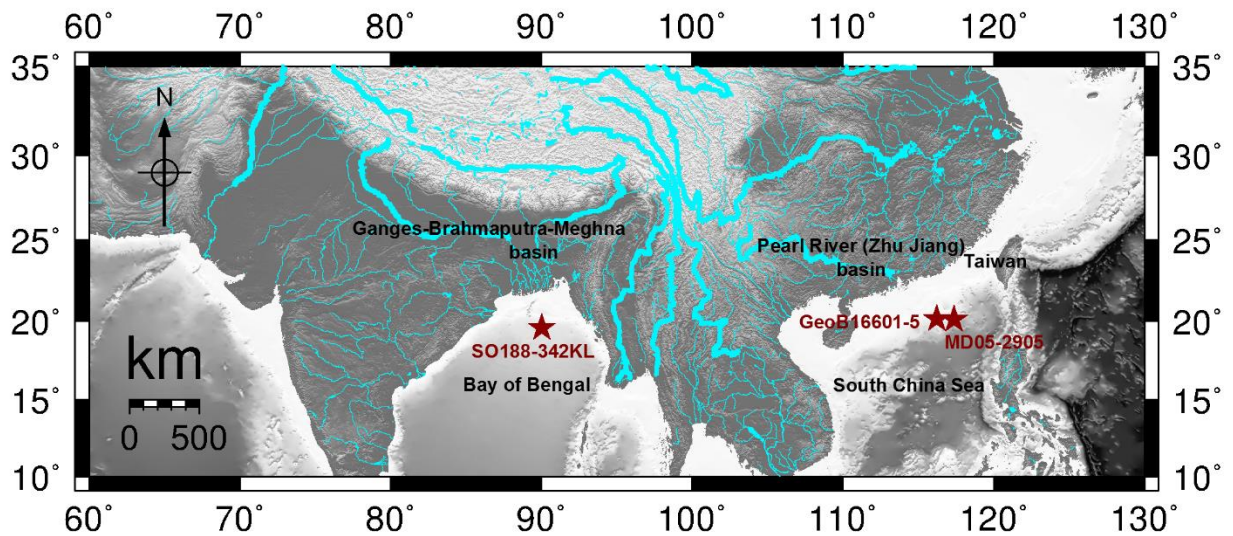
Fig. 2.1. Map of South Asia showing the location of the three sediment cores analyzed in this thesis, as well as the location of terrigenous sediment source regions to the core sites.

2.5. Methods

The quantity and composition of bulk organic matter and terrestrial biomarkers (plant wax *n*-alkanes) recovered from the three marine sediment cores were investigated to detect terrestrial

vegetation changes, changes in paleo-precipitation patterns and changes in the nature of terrestrial and marine organic matter exported to the deep ocean. A summary of the methods used in this thesis is presented as a flow chart in Fig. 2.2.

Briefly, after collection sediment cores were sliced and maintained at 4°C for transport and storage. Previous to analysis, sediment samples were dried and homogenized. Radiocarbon age models were constructed for cores SO188-342KL and GeoB16601-5 using planktic foraminifera. The age model of core MD05-2905 had previously been published by Yang et al. (2008). Sediment samples of the three cores were analyzed in high depth resolution for content of bulk total organic carbon (TOC), total inorganic carbon (TIC) and total nitrogen (TN), total organic carbon and total nitrogen stable isotopic composition ($\delta^{13}C_{TOC}$, $\delta^{15}N_{TN}$), content and composition of total hydrolysable amino acids (THAA), content and composition of plant wax n-alkanes, and compound-specific carbon and hydrogen stable isotopic composition of plant wax n-alkanes ($\delta^{13}C_{alkanes}$, $\delta D_{alkanes}$). TOC and TN contents, mass ratio (TOC/TN) and isotopic composition ($\delta^{13}C_{TOC}$, $\delta^{15}N_{TN}$) were used for the reconstruction of organic matter input and origin (Dupont et al., 2010; Jennerjahn et al., 2008, 2004). THAA content and composition were used to obtain complementary information about organic matter origin and degradation state (Dauwe et al., 1999; Dauwe and Middelburg, 1998; Jennerjahn and Ittekkot, 1999). The carbon and hydrogen isotopic composition of plant wax n-alkanes ($\delta^{13}C_{alkanes}$, $\delta D_{alkanes}$) were used to reconstruct changes in terrestrial vegetation composition and on-land precipitation patterns, respectively (Hu et al., 2002; Rao et al., 2009; Schefuß et al., 2011, 2005, 2003). All the analytical methods used in this thesis have been previously applied with success in marine and terrestrial sediment records.

Preparation

Sediment core → Sampling → Drying → Grinding → Weighing

Bulk sediment

Bulk sediment — Decarbonation (1N HCl) — Evaporation (40 °C, 48 h)

Bulk sediment — Decarbonation (1N HCl) — Evaporation (40 °C, 48 h)

Bulk sediment

Bulk sediment — Hydrolysation (6N HCl + N₂, 110 °C, 22 h) — Evaporation (60 °C, 40 mbar) — Resuspension (Na-citrate)

Bulk sediment + Squalene (10 ng mL⁻¹) — Total lipid extraction (ACE, DCM/MeOH 9:1 v/v, 1000 psi, 100 °C) — Evaporation (37 °C)

- Asphaltene precipitation (lipid extract + Na₂SO₄ column + hexane)
- Saponification (lipid extract + 6% KOH, 85 °C, 2 h + hexane)
- Neutral compounds elution (lipid extract-KOH solution + hexane)
- Apolar hydrocarbons elution (neutral extract + Silica-gel column + hexane)
- Unsaturated hydrocarbons removal (apolar extract + AgNO₃-Si column + hexane)

Method

- Element Analysis
- Element Analysis + Isotope Ratio-Mass Spectrometry
- Cation Exchange Chromatography + Fluorometry
- Gas Chromatography/Flame Ionization Detection
- Gas Chromatography/Isotope Ratio Mass Spectrometry

Instrument (place)

- Euro EA 3000 (ZMT)
- Flash 1112 EA + Thermo Finnigan Delta Plus IR-MS (ZMT)
- Biochrom 30 amino acid analyzer (ZMT)
- Thermo Trace GC Ultra (MARUM)
- Thermo Trace GC Ultra + GC/C III combustion interface (1000 °C) + Finnigan MAT 252 IR-MS (MARUM)
- Thermo Trace GC Ultra + GC Isolink pyrolysis interface (1420 °C) + Finnigan MAT 253 IR-MS (MARUM)

Measurement

- TN, TC content
- TOC content
- δ¹³C_TOC composition
- δ¹⁵N_TN composition
- THAA content and composition
- OLC n-alkanes (n-C₂₅ to n-C₃₃) content and composition
- δ¹³C n-alkanes composition
- δD n-alkanes composition

Proxies

TN, TOC/TN, TOC, TIC, δ¹³C_TOC, δ¹⁵N_TN, P-AA, NP-AA, THAA, CPI, ACL, n-C₂₉, n-C₃₁, δ¹³C_n-C29, δ¹³C_n-C31, δD_n-C29, δD_n-C31

Information

OM content, OM source, OM preservation, Terrestrial OM input, Paleo-vegetation, Paleo-precipitation

Fig. 2.2. Summary of the analytical methods used in this thesis. Details are given on sample preparation, methods for analysis, instruments used, the location of the laboratory where the measurement was performed, the parameters measured, the proxies obtained and the information provided by these proxies. Abbreviations are as follows: ZMT: Leibniz Center for Tropical Marine Ecology; MARUM: Center for Marine Environmental Sciences; TN: total nitrogen, TC: total carbon, TOC: total organic carbon, TIC: total inorganic carbon, TOC/TN: total organic carbon to total nitrogen ratio, THAA: total hydrolysable amino acids; P-AA: protein amino acids; NP-AA: non-protein amino acids; CPI: carbon preference index, ACL: average chain length; OLC n-alkanes: odd-long-chain n-alkanes; OM: organic matter.

2.6. Thesis outline

To address the objectives of this thesis, data analysis and interpretation are organized in three manuscripts presented in chapters 3 to 5.

Chapter 3 focuses on the evolution of the Indian Summer Monsoon (ISM) in the lower Ganges-Brahmaputra-Meghna catchment and the Indo-Burman ranges over the last 18 ka (i.e. since the end of the Last Glacial period). The proxy records presented in this chapter derive from the marine sediment core SO188-342KL from the northern Bay of Bengal (NBoB). A continuous record of precipitation intensity, based on the hydrogen stable isotopic signature of plant wax n-alkanes (δD_{alk}), is used to reconstruct the ISM variability. A continuous record of terrestrial vegetation composition, based on the carbon stable isotopic signature of plant wax n-alkanes ($\delta^{13}C_{alk}$), is used to determine the response of terrestrial vegetation to changes in summer monsoon intensity. Furthermore, the δD_{alk} record is compared to results from an isotope-enabled general atmospheric circulation model (IsoCAM) that reconstructed spatial moisture transport and precipitation distribution over the Bengal region for three selected time slices (pre-industrial, mid-Holocene and Heinrich Stadial 1) to get an insight of the regional atmospheric processes behind summer monsoon in different climatic periods. This chapter has been published in *Quaternary Science Reviews* 102 (2014): 133-148.

Chapter 4 deals with the origin and fate of sedimentary organic matter in the Northern Bay of Bengal during the last 18 ka. This chapter presents a comprehensive history of OM origin and fate as well as a quantification of carbon sediment storage in the NBoB since the end of the Last Glacial period. Continuous proxy records in this chapter include TN, TOC, TIC, TOC/TN, $\delta^{13}C_{TOC}$, $\delta^{15}N_{TN}$ to investigate changes in sedimentary OM input and sources. Content of terrestrial

OLC *n*-alkanes is used to determine variability of terrigenous OM export to the ocean. Content and composition of THAA are used to establish the degradation state of sedimentary OM and to refine details about OM sources. The determinant role played by eustatic sea level change as driver of terrestrial organic matter input to the ocean is analyzed. The role of summer monsoon evolution on the export of terrestrial organic matter to the ocean through fluvial discharge is discussed in combination to its role as driver and regulator of marine productivity. This chapter has been submitted for publication to *Global and Planetary Change*.

Chapter 5 targets the precipitation and vegetation history in Southeast China and Taiwan throughout the Holocene and their links to sea level change, summer monsoon strength and tropical cyclone activity. In this chapter, composite proxy records are constructed from sediment cores MD05-2905 and GeoB16601-5 from the Northern South China Sea (NSCS) to document the history of precipitation and vegetation variability through the last 11 ka. The compatibility between the two sediment cores to construct composite records was established based on the match of bulk and biomarker proxies. The roles of South China and Taiwan as terrigenous sediment sources to the NSCS continental slope are discussed. Precipitation patterns are reconstructed based on the hydrogen stable isotopic signature of plant wax *n*-alkanes ($\delta D_{alkanes}$), whereas terrestrial vegetation composition is reconstructed based on the carbon stable isotopic signature of plant wax *n*-alkanes ($\delta^{13}C_{alkanes}$). The role of eustatic sea level-change as regulator of terrestrial OM input from different sources is analyzed. The variability of different moisture sources in the study region throughout the Holocene, including South Asian summer monsoon and Western North Pacific (WNP) tropical cyclones, is discussed. Finally, the role of the Indo-Pacific Warm Pool as regulator of both Asian summer monsoon strength and tropical cyclone activity in the WNP is assessed. This chapter is in preparation for submission.

Chapter 6 presents a synoptic discussion and general conclusions of this thesis in function of the established research hypotheses and general objectives, and an outlook is given for future research work.

Chapter 3

Evolution of the Indian Summer Monsoon and terrestrial vegetation in the Bengal region during the past 18 ka

Contreras-Rosales, L.A. [1,2,], Jennerjahn, T.[1], Tharammal, T. [2], Meyer, V.[2,4], Lückge, A.[3], Paul, A. [2], Schefuß, E.[2]

[1] ZMT - Leibniz Center for Tropical Marine Ecology, Bremen, Germany.

[2] MARUM - Center for Marine Environmental Sciences, University of Bremen, Bremen, Germany.

[3] BGR - Federal Institute for Geosciences and Natural Resources, Hannover, Germany.

[4]AWI - Alfred Wegener Institute, Helmholtz Center for Polar and Marine Research, Bremerhaven, Germany

Abstract

The Indian Summer Monsoon (ISM) is a major global climatic phenomenon. Long-term precipitation proxy records of the ISM, however, are often fragmented and discontinuous, impeding an estimation of the magnitude of precipitation variability from the last glacial to the present. To improve our understanding of past ISM variability, we provide a continuous reconstructed record of precipitation and continental vegetation changes from the lower Ganges-Brahmaputra-Meghna catchment and the Indo-Burman ranges over the last 18,000 years (18 ka). The records derive from a marine sediment core from the northern Bay of Bengal (NBoB), and are

complemented by numerical model results of spatial moisture transport and precipitation distribution over the Bengal region. The isotopic composition of terrestrial plant waxes (δD and δ^{13}C of *n*-alkanes) are compared to results from an isotope-enabled general atmospheric circulation model (IsoCAM) for selected time slices (pre-industrial, mid-Holocene and Heinrich Stadial 1). Comparison of proxy and model results indicate that past changes in the δD of precipitation and plant waxes were mainly driven by the amount effect, and strongly influenced by ISM rainfall. Maximum precipitation is detected for the Early Holocene Climatic Optimum (EHCO; 10.5–6 ka BP), whereas minimum precipitation occurred during the Heinrich Stadial 1 (HS1; 16.9–15.4 ka BP). The IsoCAM model results support the hypothesis of a constant moisture source (i.e. the NBoB) throughout the study period. Relative to the pre-industrial period the model reconstructions show 20% more rain during the mid-Holocene (6 ka BP) and 20% less rain during the Heinrich Stadial 1 (HS1), respectively. A shift from C_4-plant dominated ecosystems during the glacial to subsequent C_3/C_4-mixed ones during the interglacial took place. Vegetation changes were predominantly driven by precipitation variability, as evidenced by the significant correlation between the δD and δ^{13}C alkane records. When compared to other records across the ISM domain, precipitation and vegetation changes inferred from our records and the numerical model results provide evidence for a coherent regional variability of the ISM from the Last Glacial to the present.

Keywords

Indian Summer Monsoon; paleo-precipitation; paleo-vegetation; *n*-alkanes; numerical model, Bengal; glacial/interglacial

3.1. Introduction

Variations in the strength of the Indian Summer Monsoon (ISM) precipitation have been associated to the rise and demise of civilizations across Southern Asia over the last ten thousand years (e.g. Sandweiss et al., 1999; Staubwasser and Weiss, 2006; Weiss and Bradley, 2001). Long-term monsoon weakening has been linked to soil aridification, forest retreat, expansion of scrublands and grasslands, and crop failure, whereas opposite developments have been associated to monsoon strengthening. Thus, understanding natural variations in monsoon strength and their consequences

for ecosystems is critical to predict future environmental changes and distinguish them from human-induced changes. Most of ISM precipitation falls in the surroundings of the northern Bay of Bengal (NBoB) and ultimately drains into it (Naqvi, 2010; Rashid et al., 2011; Willmott and Feddema, 1992). For this reason, paleoclimatic records from the NBoB are a central piece for understanding the ISM evolution; however, only few records are currently available (e.g. Berkelhammer et al., 2012; Cai et al., 2012; Sinha et al., 2007, 2005) and none are continuous since the Last Glacial to the present. Fluvial discharge from the Ganges-Brahmaputra-Meghna (G-B-M) system, transports large amounts of terrigenous material into the ocean, providing the possibility to reconstruct monsoon variability and its consequences for natural ecosystems based on terrestrial biomarkers in sedimentary archives.

Rainfall isotopic composition is a well-suited indicator of regional atmospheric circulation dynamics (Risi et al., 2013, 2012, 2008), since progressive depletion of heavy isotopes in precipitation is associated with increasing latitude, altitude, continentality, and rainfall amount (Dansgaard, 1964). Many studies have demonstrated that qualitative changes in the hydrogen isotopic signature (δD) of precipitation are effectively preserved by plant leaf waxes and can be used for continental rainfall reconstructions (Sachse et al., 2012 and references therein). In addition, the stable carbon isotopic composition (δ^{13}C) of leaf waxes can provide information about vegetation composition in relation to environmental moisture/aridity (Rommerskirchen et al., 2006; Vogts et al., 2012). The reason is that plants have distinct stable carbon isotopic composition (δ^{13}C) depending on their photosynthetic carbon fixation pathway (C_3, C_4 or Crasulacean Acid Methabolism; CAM) and life form (Collister et al., 1994; Rieley et al., 1993). Long-chain *n*-alkanes are leaf-wax compounds widely used for isotope-based precipitation and vegetation reconstructions (e.g. Collins et al., 2011; Duan and Wu, 2008; Hoffmann et al., 2013; Hou et al., 2008; Krull et al., 2006; Niedermeyer et al., 2010; Rao et al., 2009; Schefuß et al., 2011), since the compounds and their isotopic signatures are resistant to degradation over millennial time scales (Schimmelmann et al., 2006). Numerical models, on the other hand, enable the analysis of the dynamic relations between different climatic components under specific boundary conditions and provide insights on the temporal and spatial dimensions of climatic changes. Since most long-term ISM records are discontinuous in time, an estimation of the magnitude of precipitation variability and associated vegetation response from the last glacial to the present has remained elusive. In this study, we reconstruct the history of the ISM strength

through continuous records of continental precipitation variability and vegetation composition for the last 18 ka by analyzing leaf-wax-derived lipid biomarkers of a marine sediment core from the NBoB. In addition, we reconstruct temporal and spatial variations of moisture transport, precipitation amount and precipitation isotopic composition for three climatic periods (pre-industrial, mid-Holocene and Heinrich Stadial 1) using the Community Atmospheric Model 3.0 (CAM3.0) equipped with a water stable isotopes tracer module (IsoCAM). Finally, we compare our precipitation and vegetation records with other available proxy records from the ISM domain to evaluate summer monsoon variability on a regional scale.

3.2. Study Area

3.2.1. Core location

Gravity core SO188-342KL was retrieved during RV *Sonne* cruise SO188 in 2006. The core location (19.9733° N, 90.0338° E) lies ~222 km southwest of the main G-B-M outlet on the continental slope off Bangladesh (1265 m water depth, Fig. 3.1). Sedimentation at the core location is mostly hemi-pelagic as most of the bottom sediment drift upon the NBoB shelf is deflected towards the canyon head and funneled to the Bengal Fan, largely preventing lateral advection of sediments across the continental slope (Weber et al., 2003).

3.2.2. The Ganges-Brahmaputra-Meghna basin and the Indo-Burman ranges

Studies on sediment sources and transport in the NBoB have pointed out mixed sediment contributions from the G-B-M basin and the Indo-Burman (I-B) ranges (Colin et al., 1999; Pierson-Wickmann et al., 2001). Although the actual sediment contribution from the I-B ranges is currently impossible to quantify, dominant circulation patterns in the bay point to material derived from the G-B-M basin as the dominant sediment source to the core location (Shetye, 1993; Varkey et al., 1996; Vinayachandran et al., 2002). Therefore, we regard the G-B-M basin as the main source of continental organic material to the core location, while contributions from the I-B ranges are considered of relative minor importance during the Holocene; though they were likely higher during the Late Glacial period (see section 3.5.1).

The outflow of the G-B-M system constitutes about half of the total Indian Ocean runoff (Naqvi, 2010). The drainage area is approximately 1650×10^3 km^2, providing an average fresh water and sediment supply of respectively 1120 km^3 yr^{-1} and 1060 Mt yr^{-1} to the NBoB (Milliman and Farnsworth, 2011), respectively, with more than 95% of the delivered sediments transported during the summer monsoon season (Goodbred Jr., 2003). Vegetation is composed of seasonal forests and tropical savanna in the floodplains and subtropical, temperate and mixed forests, in the Himalayan reaches (Blasco et al., 1996). The I-B ranges are located in northeast India and northwest Burma, constituting a physiographic and climatic border between the Bengal delta plains and the central Burman lowlands. Their natural vegetation is composed of lowland evergreen, semi-evergreen, mixed-deciduous and montane cloud forests; at the higher altitudes, scrubland and savanna cover the ridge summits and rain shadowed areas (Basumatary et al., 2014).

The surroundings of the NBoB receive most of their annual precipitation during the summer monsoon season (June to September), fueled by intense atmospheric moisture convection over the NBoB. The modern average annual precipitation amount in northeast India is 2155 ± 176 mm (in the interval 1829-2006), of which 70 % corresponded to summer precipitation (data archive of the Indian Institute of Tropical Meteorology, IITM; http://www.tropmet.res.in). Precipitation during the pre-monsoon months (March to May; 435 ± 82 mm) originates from local moisture convection, while that of post-monsoon months (October to December; 41 ± 22 mm) derives from occasional atmospheric disturbances over the NBoB (Breitenbach et al., 2010).
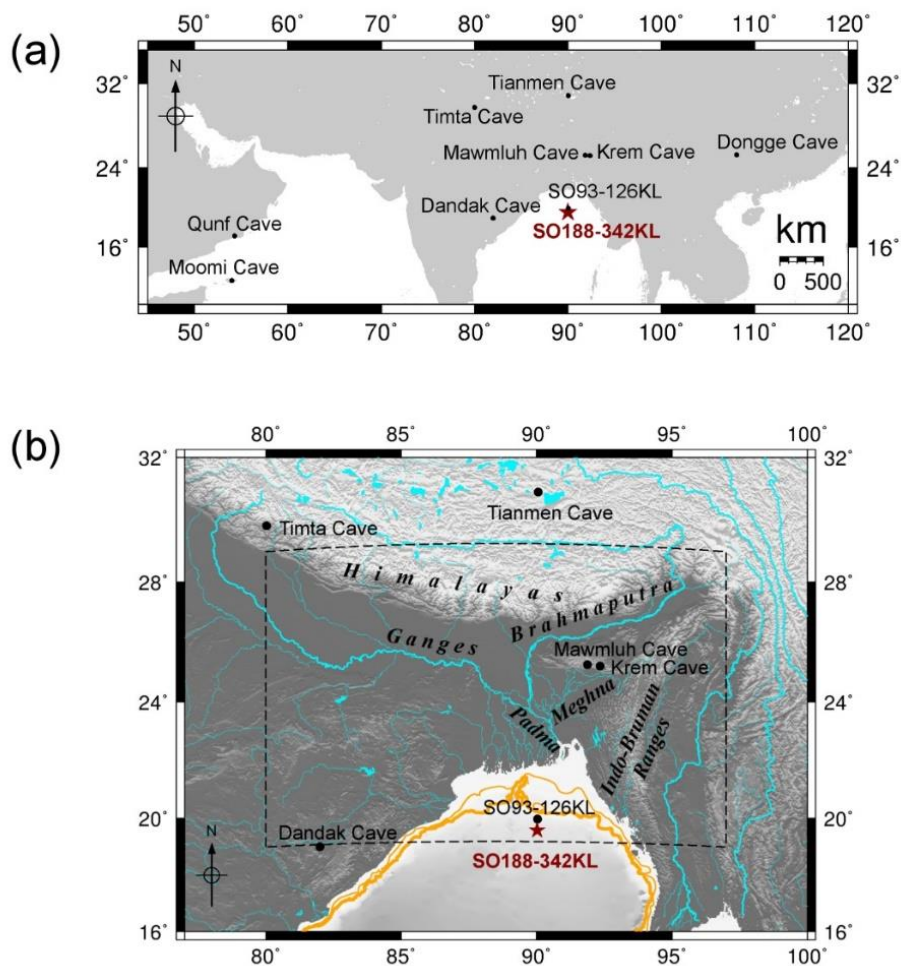
Fig 3.1. Maps of South Asia and the Northern Bay of Bengal showing core location and location of other records mentioned in the text. **(a)** Map of South Asia showing the location of all the records discussed in the text. Red star: sediment core SO188-342KL (this study). Black dots: sediment core SO93-126KL (Kudrass et al., 2001), Qunf Cave (Fleitmann et al., 2007), Moomi Cave (Shakun et al., 2007), Dandak Cave (Sinha et al., 2007), Mawmluh Cave (Berkelhammer et al., 2012), Krem Umsynrang Cave (Breitenbach, 2010), Timta Cave (Sinha et al., 2005) and Tianmen Cave (Cai et al., 2012), Dongge Cave (Dykoski et al., 2005); **(b)** Map of the Northern Bay of Bengal surroundings with the location of core SO188-342KL and neighboring ISM records. The dashed box indicates the model region (19°N-29°N, 80°E-97°E) for which area-weighted averages were calculated from the IsoCAM results. Major rivers are shown in blue. The -120 m isobath (thick orange line) is shown as reference for the approximate coastline around 18 ka BP, while the -80 m isobath (thin orange line) represents the approximate coastline around 14 ka BP.

3.3. Materials and Methods

3.3.1. Sampling and age model

After collection, the core was stored at 4 °C at the German Federal Institute for Geosciences and Natural Resources (BGR, Hannover, Germany). A total of 100 samples were taken for analysis. The age model (Fig. 3.2a) was constructed based on 9 AMS-radiocarbon ages on mixed planktic foraminiferal species (Table 3.1). The radiocarbon ages were corrected for a local reservoir age of 322 years (R = 400 years, ΔR = -78 years) (Southon et al., 2002). Conversion to calendar ages was based on the INTCAL04 curve (Reimer et al., 2004) using the on-line program CALIB 5.0.2 (Stuiver et al., 2005). Down-core ages were calculated by linear interpolation between dated sediment layers and linear extrapolation at the bottom of the section. The ages are reported in thousands of years before present (ka BP). The age at the bottom of the section is 18.1 ka BP, the average time resolution between samples is 186 ± 141 years, and sedimentation rates range between 4 – 55 cm ka^{-1} (Fig. 3.2a).

Table 3.1. Radiocarbon and calibrated ages based on planktic foraminifera from the core SO188-342KL. The calibrated ages were used to construct the age model shown in Fig. 3.2a.

Sample Name	Lab.Number (Poznan)	Depth (cm)	^{14}C-Age (BP)	± SD (year)	min.	max.	mean
			Radiocarbon Age		**CALIB 5.0.2 CalAge p(95%) [calBP(0=AD1950)]**		
SO188-342KL 11-12	Poz-47830	**11.5**	2065	30	1565	1875	**1720**
SO188-342KL 31-32	Poz-47833	**31.5**	5025	35	5309	5579	**5444**
SO188-342KL 48-49	Poz-47834	**48.5**	6240	40	6624	6950	**6787**
SO188-342KL 71-72	Poz-47835	**71.5**	8360	60	8789	9282	**9036**
SO188-342KL 101-102	Poz-47828	**101.5**	9660	50	10440	10827	**10634**
SO188-342KL 111-112	Poz-47829	**111.5**	11470	60	12762	13228	**12995**
SO188-342KL 157-158	Poz-47880	**157.5**	13060	100	14501	15697	**15099**
SO188-342KL 185-186	Poz-47831	**185.5**	14240	70	16756	17237	**16997**
SO188-342KL 198-199	Poz-47832	**198.5**	14470	70	16905	17561	**17233**

1
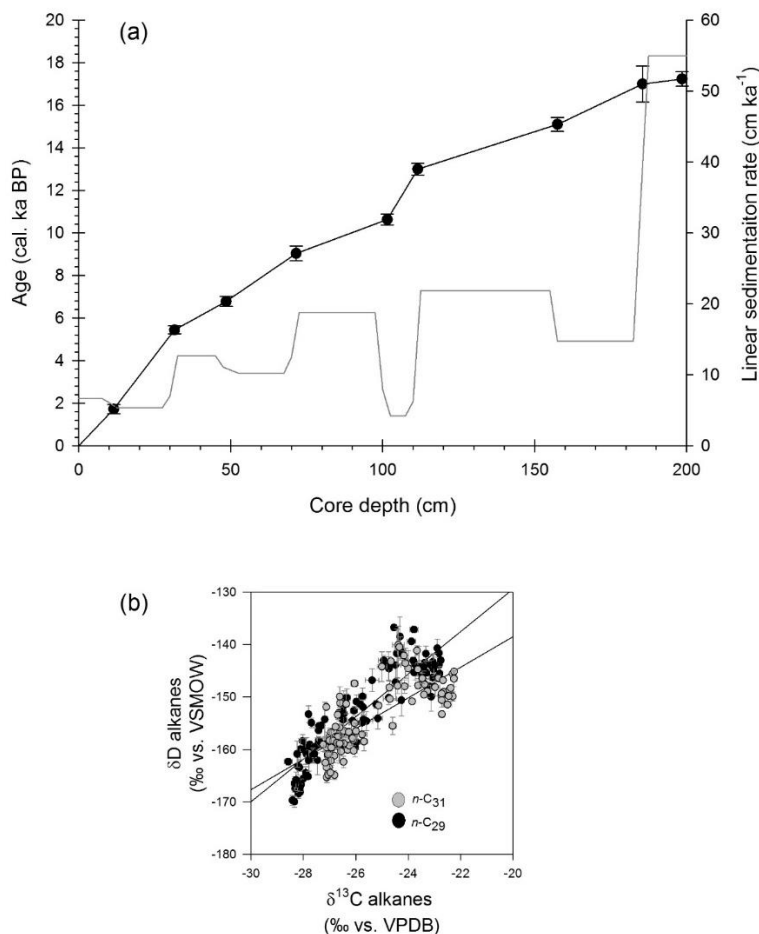
Fig 3.2. Age model and *n*-alkane stable isotopic composition of core SO188-342K. (a) Age model showing the calibrated-^{14}C age control points (black dots), and linear sedimentation rates between the age control points (gray line). (b) Cross-plot between the carbon and hydrogen stable isotopic compositions of the alkanes *n*-C_{29} (in back) and *n*-C_{31} (in grey), respectively.

3.3.2. Extraction and separation of n-alkanes

Lipids were extracted from dried and finely ground sediments with a DIONEX accelerated solvent extractor (ASE) using dichloromethane/methanol (DCM/MeOH; 9:1 v/v). Squalene was added as internal standard prior to the extraction. Total lipid extracts were dried by rotary evaporation. Extracts were saponified by the addition of a 6% KOH solution in MeOH for the hydrolysis of ester bonds. Hexane was added to the saponified extracts for extraction of neutral compounds such as hydrocarbons, ketones and alcohols. Apolar hydrocarbons from the neutral fraction were separated from this fraction by column chromatography by elution with hexane through a silica-gel column and a subsequent $AgNO_3$-Si column, to remove unsaturated compounds. Identification

of individual *n*-alkanes was done with a gas chromatography/flame ionization detector (GC/FID) by comparing their retention times to that of an external standard. Concentration of *n*-alkanes in the samples was determined by the integration of the chromatogram peak areas calibrated against the external standard, composed of a mix of several *n*-alkanes with known concentrations. Repeated measurements of the external standard yielded a quantification uncertainty of < 5 %.

3.3.3. Compound-specific isotope analyses

The stable carbon isotopic composition ($\delta^{13}C$) of *n*-alkanes was analyzed using a Thermo Trace GC Ultra, coupled via a modified GC/C III combustion interface operated at 1000 °C to a Finnigan MAT 252 isotope ratio mass spectrometer (GC/IR-MS). Isotopes were measured against calibrated CO_2 reference gas. The alkane-$\delta^{13}C$ values are reported in ‰ notation against the Vienna Pee Dee Belemnite (VPDB). Measurements of the squalane internal standard ($\delta^{13}C$ = -19.8 ‰) yielded a precision (i.e. reproducibility of the measurement, reported as 1σ standard deviation) of ± 0.1 ‰ and an average accuracy (i.e. systematic offset with respect to the actual isotopic composition of the standard) of -0.3 ‰ (n = 171). Long term repeated analysis of an external standard mixture of 16 *n*-alkane compounds rendered a precision (1σ) of ± 0.3 ‰ and an average accuracy of +0.1 ‰. The stable hydrogen isotopic composition (δD) of *n*-alkanes was analyzed using a Thermo Trace GC Ultra coupled via a GC Isolink pyrolysis interface operated at 1420°C to a Finnigan MAT 253 isotope ratio mass spectrometer. Isotopes were measured against calibrated H_2 reference gas. The alkane-δD values are reported in ‰ notation against the Vienna Standard Mean Ocean Water (VSMOW). The measurements of the internal standard squalane (δD = -180 ‰) rendered a precision (1σ) of ± 4 ‰ and an average accuracy of +1 ‰ (n = 167). Long term repeated analysis of the external standard mixture with 16 *n*-alkanes rendered a precision (1σ) of ± 3 ‰ and an average accuracy of -1 ‰. The H_3^+ factor varied around 5.96 ± 0.02 ppm nA^{-1} throughout the measurement period.

3.3.4. IsoCAM model setup

CAM3.0 is the atmospheric component of the Community Climate System Model (CCSM3.0) (Collins et al., 2006a) and successfully reproduces the present-day annual cycle of precipitation variability and the seasonality of rainfall over Southeast Asia (Hack et al., 2006; Kripalani et al.,

2007; Meehl et al., 2006). The isotope scheme in the IsoCAM version is detailed in Sturm et al. (2010), and it captures well the present-day global distribution of isotopes in precipitation. Time-slice simulations were carried out for three past climatic scenarios, constrained in the model according to the PMIP2 protocol (Braconnot et al., 2007a). The scenarios were: preindustrial (PI), Mid-Holocene (6 ka BP, hereafter 6K), and the Heinrich Stadial 1 (HS1). Sea surface temperature (SST) data and sea ice extensions for the pre-industrial (PI) and Heinrich Stadial 1 (HS1) simulations were adapted from the coupled simulations for these two scenarios (Merkel et al., 2010). The coupled HS1 simulation was conducted under the LGM boundary conditions (21 ka BP orbital parameters; LGM greenhouse gas concentration, ICE-5G ice-sheets and topography) (Peltier, 2004) with a permanent freshwater anomaly of 0.2 Sv distributed over the whole Greenland-Iceland-Norwegian Seas (north of about 65° N) that was not compensated for elsewhere. To correct for the ice volume changes during the glacial period, the sea surface enrichment of water isotopes was set to 0.83 ‰ for $\delta^{18}O$ and 7.3 ‰ for δD in the HS1 simulation. The 6K simulation was initialized and forced with the SST and sea ice concentration derived from a fully coupled CCSM3.0 run for the mid-Holocene period (Rima Rachmayani, personal communication), and the orbital parameters were set to 6 ka BP.

The horizontal resolution of the model in all simulations was ~3.75 degrees (~400 km) in both longitude and latitude. The IsoCAM simulations were carried out for a total of 35 model years and the last 10 years of the simulations were used for the analysis. To get a better representation of the precipitation in the proximity of the orographic features and to minimize the model bias in precipitation in the leeward side of the Himalayas, that is due to the rather coarse horizontal resolution, we chose to calculate area-weighted means over the region within 19° N–29° N and 80° E–97° E. This area comprises the major portion of the G-B-M basin and the full extension of the I-B ranges, but also a large part of the Himalayas and the Eastern Ghats and the south of the Tibetan Plateau (Fig. 3.1b).

3.4. Results

3.4.1. Sedimentary n-alkanes content and composition

Dry-sediment concentrations of odd long-chain n-alkanes (n-C_{25} to n-C_{33}) ranged between 0.12 and 1.50 μg g^{-1}, with an average of 0.76 μg g^{-1}. The alkanes n-C_{29} and n-C_{31} were the most abundant

in all the samples (23–33 wt. % of total odd long-chain n-alkanes), with average dry-sediment concentrations of 0.23 ± 0.08 µg g^{-1} and 0.24 ± 0.09 µg g^{-1}, respectively. The carbon preference index (CPI; see Appendix section A3.1) of total long-chain n-alkanes (n-C$_{24}$ to n-C$_{34}$) ranged between 4.0 and 5.5, with an average of 4.8, confirming the predominant contribution of plant-derived material (Killops and Killops, 2005).

3.4.2. Compound-specific stable isotopes in sedimentary n-alkanes

The stable isotopic compositions of carbon and hydrogen will be further discussed only for the compounds n-C$_{29}$, and n-C$_{31}$ which yielded the most precise signals due to their high abundance. The $\delta^{13}C_{n\text{-C29}}$ values varied between -28.6 ‰ and -22.8 ‰, with an average standard deviation (SD; 1σ) of ±0.1 ‰, while the $\delta^{13}C_{n\text{-C31}}$ values varied between -27.2 ‰ and -22.2 ‰, with an average SD of ± 0.1 ‰ (Fig. 3.2b). The $\delta D_{n\text{-C29}}$ values varied between -169 ‰ and -129 ‰, with an average SD of ±1 ‰, while $\delta D_{n\text{-C31}}$ values varied between -164 ‰ and -133 ‰, with an average SD of ± 1 ‰ (Fig. 3.2b). Overall, a highly significant positive correlation was observed between the $\delta^{13}C$ and the δD values of the same compounds (Fig. 3.2b; for n-C$_{29}$ Spearman's ρ = 0.908, p > 0.001, n = 98, d.f. = 22; for n-C$_{31}$ Spearman's ρ = 0.823, p > 0.002, n = 96, d.f. = 11).

3.4.2.1. The alkane $\delta^{13}C$ record

Maximum alkane $\delta^{13}C$ values were observed before 17 ka BP (mean $\delta^{13}C_{n\text{-C29}}$ = -23.2 ± 0.3 ‰; mean $\delta^{13}C_{n\text{-C31}}$ = -22.8 ± 0.5 ‰), displaying a steady decrease between 17–9.2 ka BP (Fig. 3.3a). Minimum values occurred between 9.3–6.6 ka BP (mean $\delta^{13}C_{n\text{-C29}}$ = -28.1 ± 0.3 ‰; mean $\delta^{13}C_{n\text{-C31}}$ = -27.0 ± 0.2 ‰), with the absolute minimum, more pronounced in the $\delta^{13}C_{n\text{-C29}}$ record, around 9.2 ka BP. During the last 6 ka values increased subtly until 0.7 ka BP and decreased again from this time until the present. Both records showed similar values between 18.1–10.2 ka BP, but displayed a systematic offset during the last 10 ka. A weighted-average of the $\delta^{13}C_{n\text{-C29}}$ and $\delta^{13}C_{n\text{-C31}}$ records was constructed ($\delta^{13}C_{alk}$) and is used for further discussion (Fig. 3.3b).
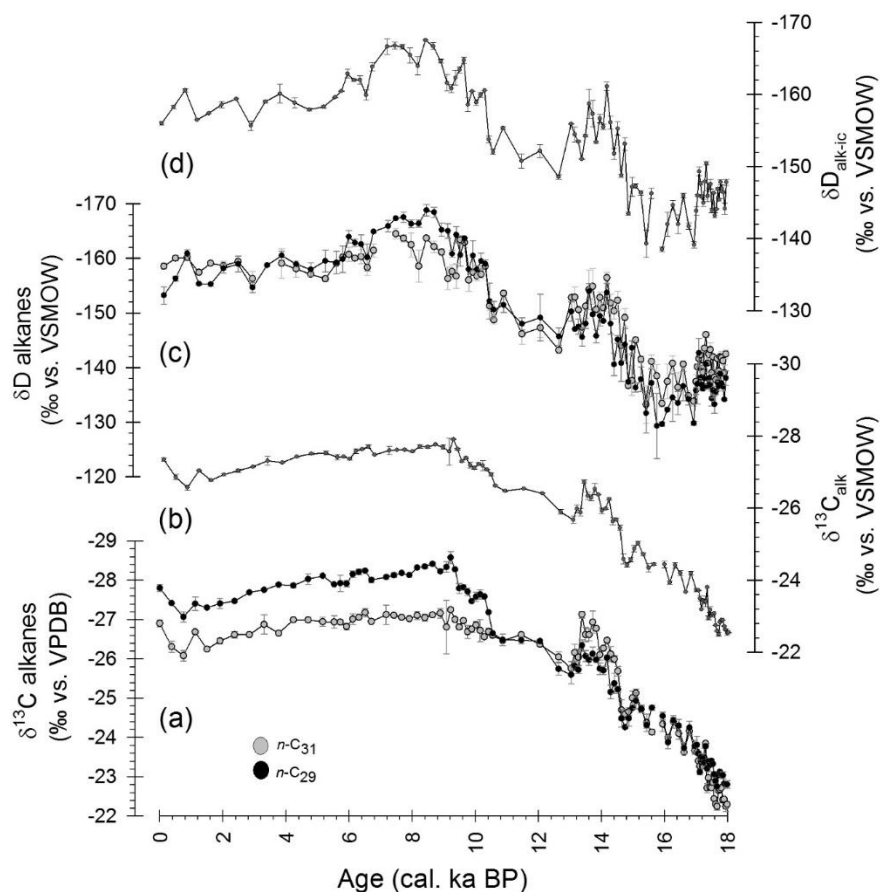
Fig. 3.3. Compound-specific stable isotopic alkane records from core SO188-342KL. **(a)** Measured *n*-alkane carbon stable isotopic records ($\delta^{13}C$) of *n*-C_{29} and *n*-C_{31}; **(b)** Weighted-average of the *n*-C_{29} and *n*-C_{31} carbon isotopic records ($\delta^{13}C_{alk}$); **(c)** Measured *n*-alkane hydrogen stable isotopic record (δD) of *n*-C_{29} and *n*-C_{31}; **(d)** Weighted-average of the *n*-C_{29} and *n*-C_{31} ice-volume-corrected hydrogen isotopic records (δD_{alk-ic}). Axes are reversed in all plots to show precipitation intensification and increase of C_3 vegetation towards the top of the graph. In black, *n*-C_{29}; in grey, *n*-C_{31}.

3.4.2.2. The alkane δD record

Maximum alkane δD values were observed between 17–15.3 ka BP (mean $\delta D_{n\text{-}C29}$ = -135 ± 4 ‰; $\delta D_{n\text{-}C31}$ = -138 ± 3 ‰), with the absolute maximum at 15.8 ka BP (Fig. 3.3c). Two steep decreases were observed between 15.3–14.6 ka BP and 10.6–9.6 ka BP, with a period of relative stability between 13–10.8 ka BP. Lowest values were observed between 9.6–6.6 ka BP (mean $\delta D_{n\text{-}C29}$ = -163 ± 3 ‰; mean $\delta D_{n\text{-}C31}$ = -160 ± 3 ‰), with the absolute minimum at 8.4 ka BP. Thereafter, values increased slightly until the present, showing less variability through the last 6 ka compared to the period before. Measured alkane-δD values were corrected to account for the global ice-

volume effect (see Appendix section A3.2). The corrected values showed a maximum difference with respect to the original values of -7 ‰ before 15 ka BP which decreased until the present. Similar correction differences apply to both records. A weighted-average of the ice-corrected $\delta D_{n\text{-}C29}$ and $\delta D_{n\text{-}C31}$ records ($\delta D_{alk\text{-}ic}$) is used for further discussion (Fig. 3.3d).

3.4.3. IsoCAM model simulations

The model results show that the moisture advection pathways to the study area remained similar during the HS1, 6K and PI periods (Fig. 3.4), despite considerable changes in the intensity of the moisture transport (Fig. 3.5a). Major differences in precipitation amounts and precipitation isotopic composition (δD_p) between the three studied time periods were recorded in the summer months (June to September; Fig. 3.5b, c; Fig. 3.6), while during the rest of the year values were similar (Fig. 3.6).

Owing to the lower sea surface temperature (SST), annual precipitation over Southeast Asia was generally lower during HS1. Higher sea-level pressure anomalies over southern Asia led to a reduction in the southwest moisture advection during the summer (JJAS; Fig. 3.5a). Summer monsoon average precipitation over the region considered in the model (4.8 mm day^{-1}) was 21% lower during the HS1 than during the PI (6.1 mm day^{-1}), while the peak of precipitation was in August, instead of June-July in the PI simulation (Fig. 3.6a). In the summer months, higher δD_p values were observed during the HS1 in comparison to the 6K and PI (Fig. 3.6b), resulting in summer δD_p anomalies up to +19 ‰ compared to PI values. For the 6K time-slice, the model simulated increased summer monsoon precipitation over southwest Asia and over eastern India when compared to the PI time slice (Fig. 3.5b). A negative surface pressure anomaly to the west of the NBoB caused increased wind speeds over the region, consequently enhancing the lower level moisture convergence near the coast (Fig. 3.5a), and increasing the amount of precipitable water. The summer precipitation in the region considered in the model (7.3 mm day^{-1}) was ~21% higher during 6K than during PI, and the monsoon retreat was extended to the month of October (Fig. 3.6a). For the same area, the model yielded lower summer δD_p values than in the HS1 and PI simulations, with anomalies up to -8 ‰ with respect to the PI (Fig. 3.6b).
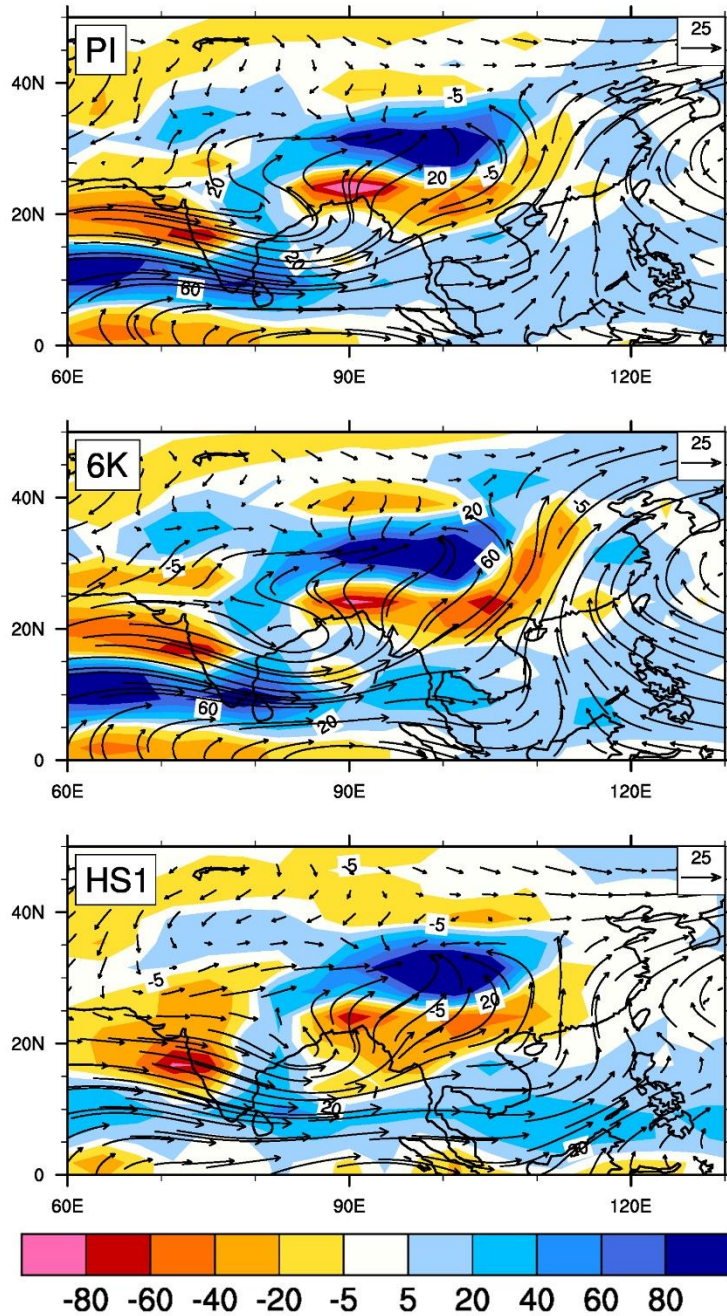
Fig. 3.4. IsoCAM results of absolute moisture convergence and moisture transport. Absolute moisture convergence (contour intervals, in 10^{-6} g kg^{-1} s^{-1}) and moisture transport (vectors, in g kg^{-1} m s^{-1}; reference vectors are given in the right top of the panels) at 850 hPa for the summer season (June to September) for the Pre-Industrial (PI), Mid-Holocene (6K) and Heinrich Stadial 1 (HS1).
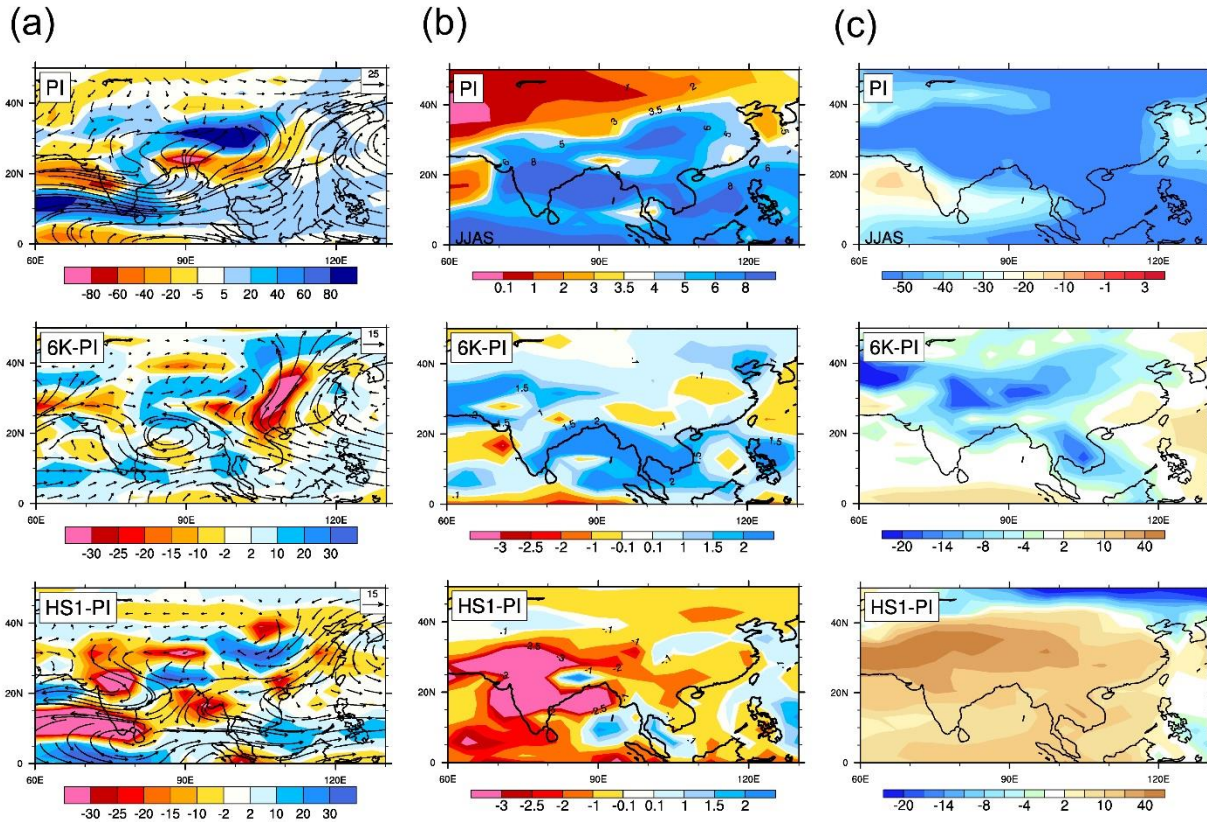
Fig. 3.5. IsoCAM results of moisture convergence and transport, precipitation intensity and precipitation isotopic composition. **(a)** Moisture convergence (contour intervals, in 10^{-6} g kg^{-1} s^{-1}) and moisture transport (vectors, in g kg^{-1} m s^{-1}, reference vectors are given in the right top of the panels) at 850 hPa for the summer season (June to September); absolute values for the pre-industrial (PI), and anomalies for the Mid-Holocene (6K) and Heinrich Stadial 1 (HS1) versus PI. **(b)** Summer (June to September) precipitation intensity (mm/day); absolute values for the pre-industrial (PI), and anomalies for the Mid-Holocene (6K) and Heinrich Stadial 1 (HS1) versus PI. **(c)** Summer (June to September) precipitation δD (‰); absolute values for the pre-industrial (PI), and anomalies for the Mid-Holocene (6K) and Heinrich Stadial 1 (HS1) versus PI.

(a) Precipitation amount (19°N-29°N, 80°E-97°E)

(b) Precipitation δD (19°N-29°N, 80°E-97°E)
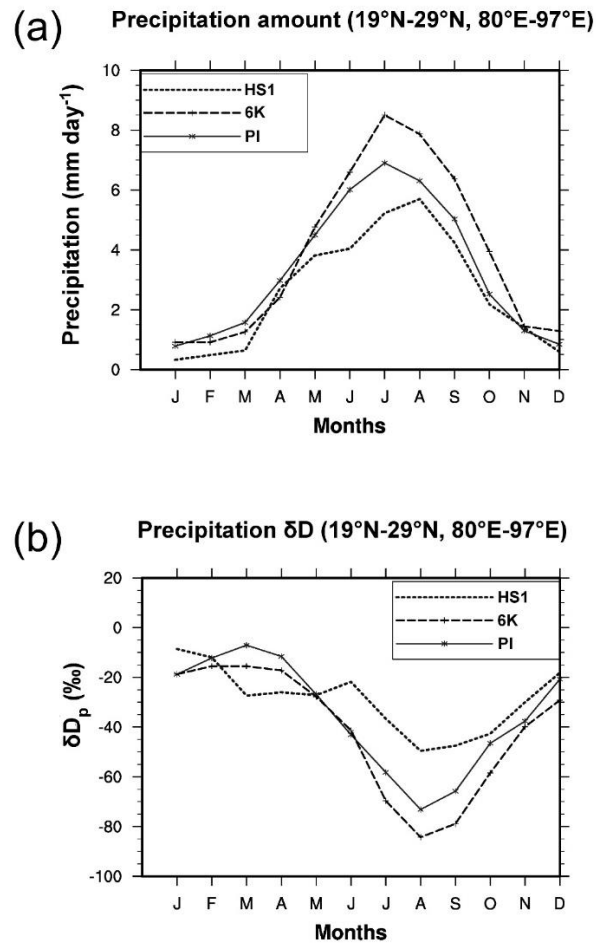
Fig. 3.6. IsoCAM results of monthly average precipitation intensity and monthly average precipitation isotopic composition. **(a)** Monthly averages of precipitation intensity (mm/day) for the three different time-slices: Pre-Industrial (PI), Mid-Holocene (6K) and Heinrich Stadial 1 (HS1); **(b)** Monthly averages of precipitation δD (‰) for the three time-slices.

3.5. Discussion

3.5.1. Spatio-temporal variation of n-alkane sources

Within the large extension of the G-B-M basin, Galy et al. (2008a) proposed that the organic carbon from Himalayan rivers was largely replaced during its transit across the floodplain by locally produced organic carbon, helping to constrain the source area of the leaf-waxes at Site 342KL to the lower G-B-M course. The isotopic signature of the core-top alkanes was comparable with that of modern leaf-waxes from the Padma river (Galy et al., 2011), which is the final stretch of the G-B-M fluvial system and the last integration step of organic matter over the basin before

export to the ocean. Mean $\delta^{13}C$ values of the n-C_{29} and n-C_{31} alkanes in the Padma (-31.5 ± 0.5 ‰) were on average 4.2 ‰ lower compared to those from the 342KL core-top ($\delta^{13}C_{alk}$ of -27.3 ‰). Mean δD values of the n-C_{30} and n-C_{32} alkanoic acids (-172 ± 0 ‰), which are isotopically comparable to the n-C_{29} and n-C_{31} alkanes in their quality of biosynthetic precursors (Chikaraishi et al., 2004; Diefendorf et al., 2011; Kolattukudy et al., 1976), were approximately 16 ‰ lower than those from the core-top (δD_{alk-ic} of -156 ± 1 ‰). The discrepancies between the Padma river waxes and those from the Site 342KL core-top may be explained by the difference of time spans recorded by the two types of samples: sub-annual in the case of the river samples, and centennial in the case of the core-top (~374 years). Speleothem records from the Dandak and Gupteswar caves (Yadava and Ramesh, 2005), in the Indian Core Monsoon Zone, reveal two periods of drier-than-present conditions around 400 a BP and between 250–125 a BP, corresponding to the Little Ice Age (LIA). Such drier conditions would account for the higher $\delta^{13}C$ and δD values of the core-top n-alkanes, with respect to the modern riverine waxes, by implying higher abundance of C_4 vegetation (see section 3.5.5) and reduced precipitation in the lower G-B-M basin for the last few hundred years compared to the present.

The export of n-alkanes from the G-B-M basin into the ocean is considered to be fast, as suggested by the good synchronicity between our n-alkane δD record and high resolution speleothem $\delta^{18}O$ records from the Himalayas and Tibet (Berkelhammer et al., 2012, 2010; Cai et al., 2012; Sinha et al., 2005) (see section 3.5.4). Galy and Eglinton (2011), found that the average radiocarbon age of long-chain n-alkanoic fatty acids (also leaf waxes) in the G-B-M basin ranged between 0.5 and 1.3 ka. This coincides with the observations of Lupker et al. (2012a, 2012b), who estimated transfer times across the floodplain in the scale of 1 ka for the finer (<100 μm) sediments, although the good match of our alkane records with other high-resolution ISM records suggests transfer times on the order of centuries. Changes in sediment erosion and transfer over glacial/interglacial time scales, analyzed based on Sr and Nd isotopes (Lupker et al., 2013), were estimated to be stable for the last 20 ka with a roughly constant balance between the Brahmaputra and Ganges sediment input to the Bengal fan. We thus expect similar contributions of these sources throughout our record.

It is worth noting that the shape and size of the G-B-M basin underwent important changes since the glacial period, when sea level was approximately 120 m lower than present (Lambeck et

al., 2002). This resulted in an increase of distance (100–150 km) between the core site and the shore from the glacial to the present. Despite lower weathering intensity over the basin during the glacial due to reduced summer monsoon precipitation (Lupker et al., 2013), the higher proximity of the core site to the shore allowed for a high sediment accumulation as reflected in the elevated sedimentation rates observed before 17 ka BP (Fig. 3.2a). The sediment contribution of rivers in the I-B ranges to the NBoB is considered small for the present. However, sedimentary isotopic evidence suggests higher contribution during the late glacial (Colin et al., 1999; Pierson-Wickmann et al., 2001). Indeed, paleo-drainage reconstructions for the Bengal Shelf (Palamenghi, 2012) suggest that the I-B ranges were incorporated into the G-B-M drainage basin until about 14 ka BP (Fig. 3.1b), implying a higher efficiency of sediment transport from this area to the ocean before this time. Overall, enhanced sediment remobilization due to the rapid shelf flooding during sea level rise could have led to reworking of previously deposited plant waxes, with a biasing effect on the *n*-alkane isotopic signals. However, this is not observed in our records, in which the magnitude and timing of changes during deglaciation is comparable to records not affected by sea level changes (Shakun et al., 2007; Sinha et al., 2005) (Fig. 3.7c, e). Thus, we consider the contribution of reworked plant waxes to our records negligible.

3.5.2. Influence of the moisture source on the hydrogen isotopic composition of precipitation

In the present, surface water of the NBoB is the main moisture source for precipitation in the Bengal region (Breitenbach et al., 2010). The IsoCAM model results suggest that the moisture source remained constant since the late glacial period (Fig. 3.4); although the net moisture advection was enhanced (reduced) during the 6K (HS1) period compared to the present (Fig. 3.5a).

Since the oceanic moisture source to the region is uniform in all the simulations, the isotopic enrichment of precipitation during the HS1 period, and the depletion during the 6K period, depend particularly on the changes of the monsoon intensity, on the decrease/increase in the convective activity in the source region, and on the rain-out experienced by the air mass. During the HS1, reduced convection over the ocean than during the PI led to water vapor enrichment in heavier isotopes, as convection generally depletes the water vapor of the total air column from heavy isotopes (Risi et al., 2008). Additionally, a weakened monsoon circulation was responsible for a lower number of rainfall events during the summer further enriching the heavier isotopes in

precipitation. At 6K, an increase in the deep convection activity, increased rainfall amount, and higher number of rainfall events led to lower isotope ratios in precipitation over the NBoB. Only a slight increase in the evaporation over the catchment was observed in the 6K simulation when compared to the PI. Thus the effect of changes in post-condensation moisture recycling, which further lowers the precipitation isotopic signature (Field et al., 2010; Lee and Fung, 2007; Risi et al., 2008), was likely weaker compared to that of moisture advection and convective activity. The increase of ISM precipitation and enhanced advection of moisture to the land in the 6K simulation are also seen in other PMIP simulations and have been associated to stronger Northern Hemisphere summer insolation (Braconnot et al., 2007b, 2002; Joussaume et al., 1999).

Therefore, we conclude that δD variability of precipitation in the Bengal region derives from changes in the precipitation amount and not from changes in the regional moisture source over glacial/interglacial scales. This conclusion is supported by the model-based study of LeGrande and Schmidt (2009) who also observed a sustained correlation between the amount and isotopic composition of precipitation in the ISM domain throughout the Holocene. Yet Breitenbach et al. (2010) found that the isotopic composition of the NBoB surface water displays seasonal variability, and is only governed by the amount effect (Dansgaard, 1964) during the pre-monsoon and early summer monsoon seasons. During the late summer monsoon, when precipitation amounts decline, the most negative δD values of precipitation are observed. This is because large part of the meteoric water raining over the G-B-M basin originates from G-B-M river plume (Breitenbach et al., 2010), which forms a large and stable freshwater layer across the NBoB.

Under equilibrium conditions, meteoric water becomes depleted in deuterium relative to the ocean water due to isotopic fractionation during evaporation, transport, condensation and precipitation (Dansgaard, 1964). In the NBoB there is a depletion loop formed when the river water, derived from early monsoon precipitation, becomes the source of new meteoric water as it returns to the ocean surface. Here, the water is depleted for second and successive times with a new loop of evaporation, transport, condensation and precipitation. As the loop repeats itself many times during the season, the river plume and the meteoric water derived from it become abnormally depleted in deuterium towards the late monsoon, as compared to meteoric water formed during the early monsoon or outside the river plume. This depletion loop is called the "plume effect" (Breitenbach et al., 2010) and can be misleading regarding the reconstruction of precipitation

amounts at the annual time scale. However, over longer time spans records are still expected to reflect precipitation amounts, because the magnitude of the plume effect is directly related to the amount of summer precipitation, as seen in the two-year dataset from Breitenbach et al. (2010) (see Appendix section A3.3). We thus conclude that the δD_{alk} record is governed by the amount effect over time spans longer than a year, with enhanced deuterium depletion in periods of increased precipitation.

3.5.3. ISM paleo-precipitation reconstruction in the Bengal region: a combined proxy-model approach

The magnitude of paleo-precipitation changes in the NBoB was evaluated following a combined approach based on the comparison of δD anomalies between proxy and model data. To this end, approximately five representative $\delta D_{alk\text{-}ic}$ values were averaged from the Late Holocene (1.4–0 ka BP), the Mid-Holocene (5.9–6.7 ka BP) and the Heinrich Stadial 1 (16.9–15.4 ka BP). From the model side, average δD_p values in the model box were taken for the PI, 6K and HS1 simulations. The Late Holocene proxy-record interval was compared to the model PI simulation, the Heinrich Stadial 1 proxy-record interval was compared to the model HS1 simulation, and the Mid-Holocene proxy-record interval was compared with the model 6K simulation. Anomalies were calculated with respect to the Late Holocene mean for the proxy data and with respect to the PI simulation for the model. A summary is provided in Table 3.2.

For the Mid-Holocene period, the comparison shows that proxy-δD anomalies are 4 ‰ higher than model-δD anomalies of the 6K scenario. Part of the difference may be explained by the natural variability observed in the averaged proxy data points from the two periods compared, which could contribute to reduce the difference between the Late and Mid-Holocene average $\delta D_{alk\text{-}ic}$ values. However this cannot account for all the offset observed between proxy and model anomalies. An additional explanation may be the model's overestimation of the net surface freshwater flux (i.e. precipitation minus evaporation) during the Mid-Holocene, which may derive from a wet bias that has been previously observed in the atmospheric stand-alone version of the CAM3.0 model (Collins et al., 2006b; Hack et al., 2006). Finally, the mismatch could also derive from the model's incapability of reproducing reduced precipitation in two of the model grid cells within the catchment basin at the leeward side of the Tibetan Plateau, as previously observed in

other studies in rain shadow regions (Gent et al., 2010). For the HS1 period, the proxy anomaly value lies between the model's annual and summer anomaly values. This could be partially explained by the model's overestimation of the total annual precipitation amount due to the reasons discussed above. However, it could also suggest that the time for wax production by vegetation in the G-B-M basin was less restricted to the summer season during the HS1 than it is in the present, resulting in higher δD_{alk-ic} values. Finally, the differences can also derive from changes in deuterium fractionation by vegetation, caused by major vegetation composition shifts between the glacial period and the Holocene, which would affect the δD_{alk-ic} values.

Table 3.2. Proxy-versus-model comparison of δD signatures and anomalies for different climatic periods. Proxy-based estimations are based on ice-corrected *n*-alkane δD values (δD_{alk-ic}; see section 3.4.2.2). The values are averages from five data points within the indicated time frames; the 1σ standard deviation (SD) values are propagated errors. The climatic periods from the proxy record are: Late Holocene (0 – 1.4 ka BP), Mid-Holocene (5.9 – 6.7 ka BP) and Heinrich Stadial 1 (16.9 – 15.4 ka BP). The time slices from the IsoCAM model are: Pre-Industrial (PI), Mid-Holocene (6K) and Heinrich Stadial 1 (HS1). Anomalies are given with respect to the Late Holocene (LH) mean for the proxy data, and to the PI for the model data. IsoCAM model results are averaged over the region inside 19°N-29°N and 80°E-97°E (see Fig. 3.1b).

| | | NBoB Site 342KL | | | IsoCAM (19°N-29°N, 80°E-97°E) | | | |
| | | δD of sedimentary *n*-alkanes | | | δD in precipitation | | | |
Proxy time frame	Model time slice	Average δD_{alk-ic} for the period (‰)	SD (‰)	Anomalies relative to LH mean (‰)	Annual δD_p (‰)	Anomalies relative to PI (‰)	Summer δD_p (‰)	Anomalies relative to PI (‰)
0 - 1.4 ka BP	PI	-158	0.4		-47		-60	
5.9 - 6.7 ka BP	6K	-162	0.3	**-4**	-56	**-9**	-68	**-8**
16.9 - 15.4 ka BP	HS1	-143	0.4	**15**	-37	**11**	-42	**19**

An attempt to evaluate the effects of vegetation isotopic fractionation on the δD signature of the sedimentary *n*-alkanes was carried out after Collins et al. (2011). The details of the method are explained in the Supplementary Discussion at the end of this chapter (sections S3.1 and S3.2). The outcome indicates minor differences (max. 3 ‰) between the δD anomalies estimated without considering vegetation composition changes and those accounting for them in the period of 0– 16.9. ka BP. The differences however become larger (5–6 ‰) towards the Late Glacial section of the core (16.9–18.1 ka BP) when vegetation was strongly dominated by C_4 vegetation. Though the

method has several shortcomings and the values should be taken with caution, the importance of considering vegetation fractionation changes in settings where large vegetation modifications took place is clear and further research efforts should be addressed to this end.

Overall, the good agreement between model and proxy data for the investigated time periods encourages future work on combined reconstructions. Given the large amount of proxy evidence suggesting maximum ISM strength between 8–10 ka BP (Berkelhammer et al., 2012; Breitenbach, 2010; Cai et al., 2012; Dykoski et al., 2005; Fleitmann et al., 2007; Sinha et al., 2005; this study), the implementation of a standard Early Holocene scenario is highly recommended for future model reconstructions in the Indian monsoon domain.

3.5.4. Precipitation variability in the context of Asian summer monsoon evolution

Based on the variations observed in the δD_{alk-ic} record, we distinguished six climatic periods (Fig. 3.7a): the late glacial (LG; 18.1-17 ka BP); the Heinrich Stadial 1 (HS1; 17–15.4 ka BP); the Bølling/Allerød (B/A; 14.7–13 ka BP); the Younger Dryas (YD; 12.6–11.6 ka BP); the Early Holocene Climatic Optimum (EHCO; 10.5–6 ka BP); and the Mid-to-Late Holocene (MLH; 6–0 ka BP). The time boundaries of these periods are in agreement with previous observations in records from North Atlantic sediment cores (Bond et al., 1999; Hemming, 2004), Greenland ice cores (Dansgaard et al., 1993; Stuiver and Grootes, 2000), and speleothem records from the Asian continent (Sinha et al., 2005; Wang et al., 2001; Yuan et al., 2004). The link between the G-B-M fluvial discharge and precipitation intensity over land is shown by the co-variation of the δD_{alk-ic} record with the sea surface salinity reconstruction of Kudrass et al. (2001) (Fig. 3.7b) for the NBoB (core SO93-126KL; Fig. 3.1), based on planktic foraminiferal $\delta^{18}O$. Close co-variability of the records is observed between 18–10 ka BP, while the discrepancies observed during the last 10 ka are possibly derived from an underestimation of the sea surface temperatures (Sonzogni et al., 1998) used for correcting the foraminiferal $\delta^{18}O$, as compared to the observations from Rashid et al. (2011).

A coherent maximum in summer monsoon strength during the Early Holocene (EHCO) across the ISM domain is evidenced by the general agreement between the NBoB precipitation record and the high-resolution speleothem $\delta^{18}O$ records from the Arabian Sea, central India, the Himalayas and the Tibetan Plateau (Fig. 3.7c, d, e). The first substantial rise of precipitation

intensity during the B/A in our record is synchronous with that observed in the Moomi Cave in Yemen (Shakun et al., 2007) and the Timta Cave in the central Himalayas (Sinha et al., 2005), with maximum precipitation observed around 14.2 ka BP. During the EHCO, maximum monsoon precipitation in the NBoB matches that observed in the stalagmite records of the Qunf Cave in southern Oman (Fleitmann et al., 2007) and the Tianmen Cave in southern Tibet (Cai et al., 2012), but differs with the observations from the Mawmluh Cave in Meghalaya, northeast India (Berkelhammer et al., 2012). There, the period between 10–8.5 ka BP is characterized by low precipitation and the onset of strong monsoon rainfall takes place only after 8.4 ka BP. However, a $\delta^{18}O$ record from the Krem Umsynrang Cave (Breitenbach, 2010; not shown), also in Meghalaya (Fig. 3.1), does present a strong monsoon period from 11–6 ka BP, with maximum precipitation centered around 9 ka BP, suggesting a local bias of the Mawmluh Cave record. Furthermore, maximum precipitation has also been documented between 11–8 ka BP in records from southwestern China, at the eastern borders of the ISM domain (An et al., 2000).

Further, comparison of the Bengal and Arabian ISM records with the stalagmite record of Dongge Cave in southern China (Dykoski et al., 2005) (Fig. 3.7f), would suggest a shorter duration of maximum monsoon strength in the Bengal region compared to the down-stream region of South China (LeGrande and Schmidt, 2009; Lewis et al., 2010; Pausata et al., 2011) (Fig. 3.4), at the border with the East Asian Summer Monsoon (EASM). Pollen-based reconstructions of effective moisture across monsoonal Asia indicate that maximum monsoon strength was attained by the ISM between 11–7 ka BP and followed by the EASM between 8–4 ka BP (Herzschuh, 2006; Wang et al., 2010). Maximum summer insolation in the northern hemisphere around 11 ka BP (Berger and Loutre, 1991) (Fig. 3.8d) forced the ISM maximum henceforth, driven by strong convection over the Tibetan Plateau during the Early Holocene in response to maximum insolation. Only when this circulation weakened around 7a ka BP, in response to decreasing insolation, could the EASM domain experience its maximum in precipitation (Wang et al., 2010). This was largely due to a better development of the Meiyu Front (see Chapter 5). Given the location of the Dongge Cave, the $\delta^{18}O$ record was likely affected by both the monsoon and the frontal systems recording thus both summer monsoon and Meiyu maximum precipitation. The influence of ISM on speleothem records in southeast China has been previously tested and confirmed by Clemens et al. (2010).
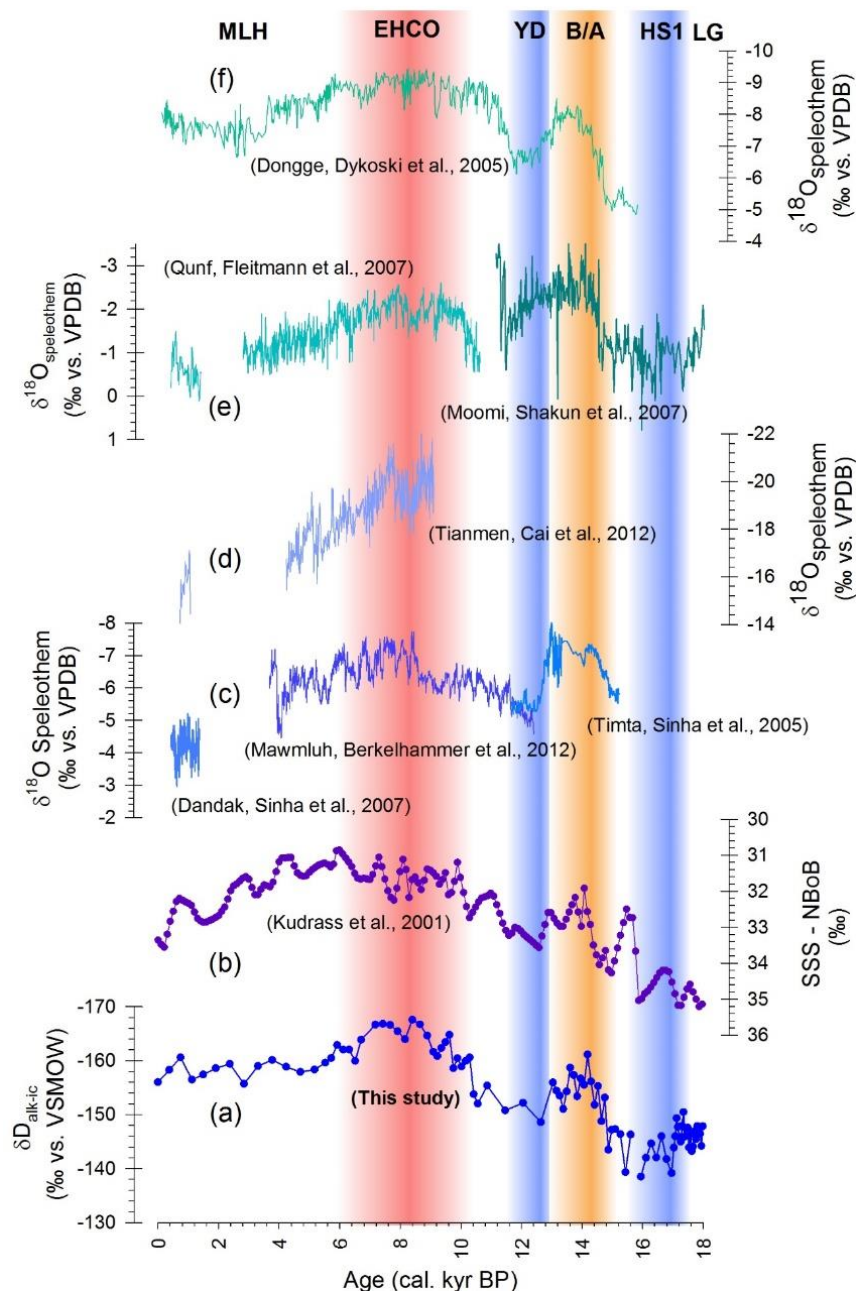
Fig. 3.7. Comparison of Asian summer monsoon records. **(a)** Weighted-average of the *n*-C_{29} and *n*-C_{31} hydrogen isotopic records ($\delta D_{alk\text{-}ic}$; this study) **(b)** Sea surface salinity of the Northern Bay of Bengal (SSS–NBoB) based on planktic foraminifera $\delta^{18}O$ (Kudrass et al., 2001), lower salinity values result from increased fresh water discharge from the Ganges-Brahmaputra-Meghna river system; **(c)** Himalayan speleothem $\delta^{18}O$ records: Dandak Cave, East-Central India (Sinha et al., 2007); Mawmluh Cave, Northeast India (Berkelhammer et al., 2012); and Timta Cave, North India (Sinha et al., 2005); **(d)** Tibetan speleothem $\delta^{18}O$ record: Tianmen Cave, Southern Tibetan Plateau (Cai et al., 2012); **(e)** Arabian speleothem $\delta^{18}O$ records: Qunf Cave, Oman (Fleitmann et al., 2007); and Moomi Cave, Yemen (Shakun et al., 2007); **(f)** Chinese speleothem $\delta^{18}O$ record: Dongge Cave, South China (Dykoski et al., 2005).

Axes are reversed in all plots to show precipitation intensification and higher fluvial discharge towards the top of the graph. Color bars and abbreviations at the top represent distinctive climatic periods discussed in section 3.5.4 as follows: LG, Late Glacial; HS1, Heinrich Stadial 1; B/A, Bølling/Allerød; YD, Youger Dryas; EHCO, Early Holocene Climatic Optimum; MLH, Mid-to Late Holocene.

3.5.5. Main drivers of vegetation composition

Two major $\delta^{13}C$ end members can be distinguished in relation to plant ecophysiology (Collister et al., 1994; Kohn, 2010; Rommerskirchen et al., 2006; Vogts et al., 2012); these are (1) C_3 woody plants, dominant in (semi-) moist environments with a $\delta^{13}C$ from -39 to -32 ‰; and (2) C_4 non-woody plants, dominant in (semi-) arid environments with a $\delta^{13}C$ from -25 to -18 ‰. The isotopic signature of all other C_3 and C_4 plant groups, as well as that of CAM plants, ranges between these two end-members (Bender, 1971; O'Leary, 1988). Except in extremely dry environments, CAM plants have low biomass productivity compared to C_3 and C_4 plants, because their life strategy is focused on stress survival and not on high productivity and dominance (Lüttge, 2004). Therefore, we consider their contribution to the sedimentary alkane pool as negligible. Based on this, vegetation changes deduced from the alkane $\delta^{13}C$ record indicate a shift from C_4-plant dominated ecosystems during the Late Glacial to mixed C_3/C_4-plant vegetation during the Holocene (Fig. 3.8a). Due to the large moisture availability in the region even during the Late Glacial period (see Appendix section A3.4), we rule out significant enrichment of ^{13}C in C_3 plants during the study period as a consequence of water stress (e.g. Diefendorf et al., 2010; Douglas et al., 2012; Kohn, 2010; Prentice et al., 2011). In addition to moisture stress, differential wax production between plants groups (e.g. Bush and McInerney, 2013), or the large range of $\delta^{13}C$ values of C_3 species alone (Ehleringer and Cerling, 2002) potentially reduce the accuracy of the two-end member mixing model approach. Unfortunately, these factors are very difficult to quantify even in modern settings, and the lack of long-term pollen record studies in the G-B-M basin and NBoB surroundings make it impossible to evaluate their imprints on the $\delta^{13}C_{alk}$ signature. Nevertheless, we are confident that alkane $\delta^{13}C$ changes do represent a shift from C_3 to C_4 vegetation in the region because of the better adaptation of C_4 vegetation to glacial environmental conditions (Ehleringer et al., 1997).

Our results agree with those from Galy et al. (2008b), who reconstructed higher abundance of C_4 vegetation in the lower G-B-M basin during the Late Glacial and predominance of C_3

vegetation in the Holocene with the dynamic vegetation model CARAIB. In the Indian Core Monsoon Zone (CMZ), substantial aridification was inferred between 4–1.7 ka BP from $\delta^{13}C$ values of n-alkanoic acids in a marine sediment core off the Godavari River (Ponton et al., 2012). Comparison with results from Site 342KL indicate stronger reduction in the C_3 vegetation relative abundance from the Early to Late Holocene in the CMZ ($\delta^{13}C$ increase of ~4 ‰) related to that of the G-B-M basin ($\delta^{13}C$ increase of ~1 ‰). Higher abundance of C_4 vegetation in the CMZ (e.g. Galy et al., 2008b) would be justified by a more pronounced dry season lengthening respect to the G-B-M basin from the Early to Late Holocene. Supporting this hypothesis is the evidence of a steeper annual moisture gradient currently observed in the CMZ compared to the G-B-M basin (IITM data archive).

Long-term pollen records from northeast India reaching the last glacial period are scarce, but there are some available from the Assam region in the Upper Brahmaputra floodplain (Mehrotra et al., 2014 and references therein). Though Assam is not part of the sediment source region for the 342KL core, we assume that climatic shifts were similar, allowing a qualitative comparison. The pollen records from Assam suggest dry-cold conditions between 18–12 ka BP, with vegetation being composed of grasslands, savanna forests, temperate forests and subtropical forests (Bera, 2003; Bhattacharya and Chanda, 1988; Sharma and Chauhan, 1994). These observations match the higher abundance of C_4 vegetation derived from our record. Increased fluvial activity in Assam (pollen-barren zone) around 14.1 ka BP (Dixit and Bera, 2012) is coherent with monsoon intensification during the B/A, and captured in the $\delta^{13}C_{alk}$ record by a sharp increase in C_3 vegetation (Fig. 3.8a). A subsequent expansion of tropical savanna around 12.7–10.8 ka BP is associated with the cool-dry climate of the YD, and observed as a decrease in C_3 vegetation between 13.2–12 ka BP in our record. Expansion of tropical mixed deciduous forest under warm and semi-humid climate, observed in multiple northeast Indian pollen records between 10–1.5 ka BP (Mehrotra et al., 2014; and references therein), coincides with sustained high proportions of C_3 vegetation in our record.

Based on the strong overall correlation of the δD and $\delta^{13}C$ isotopic signals of the plant waxes in our records (see section 3.4.2 and Fig. 3.2b), we propose a predominant control of moisture availability on vegetation composition. Galy et al. (2008b), in contrast, concluded that a lower pCO_2, together with moisture limitation, likely contributed to the dominance of C_4 in the G-

B-M basin in the last glacial period. A detailed comparison of the $\delta^{13}C_{alk}$ and δD_{alk-ic} records indeed reveals that both signals diverge before 15 ka BP (Fig. 3.8a, b). We therefore suggest that precipitation control of vegetation composition became dominant only after a certain pCO_2 threshold was crossed. The crossing of the critical atmospheric pCO_2 threshold in our record seems to have occurred at the early stages of the deglaciation when pCO_2 values were around 220 ppmV (Fischer et al., 1999; Monnin et al., 2004, 2001) (Fig. 3.8c). The covariation observed between the $\delta^{13}C_{alk}$ and δD_{alk-ic} records for the last 15 ka, in contrast to the lack of covariation observed prior to this time (Fig. 3.8a, b), indicates that pCO_2 was likely the major determinant of vegetation composition until the end of the last glacial period, while precipitation became the major driver of vegetation composition ever since the deglaciation.
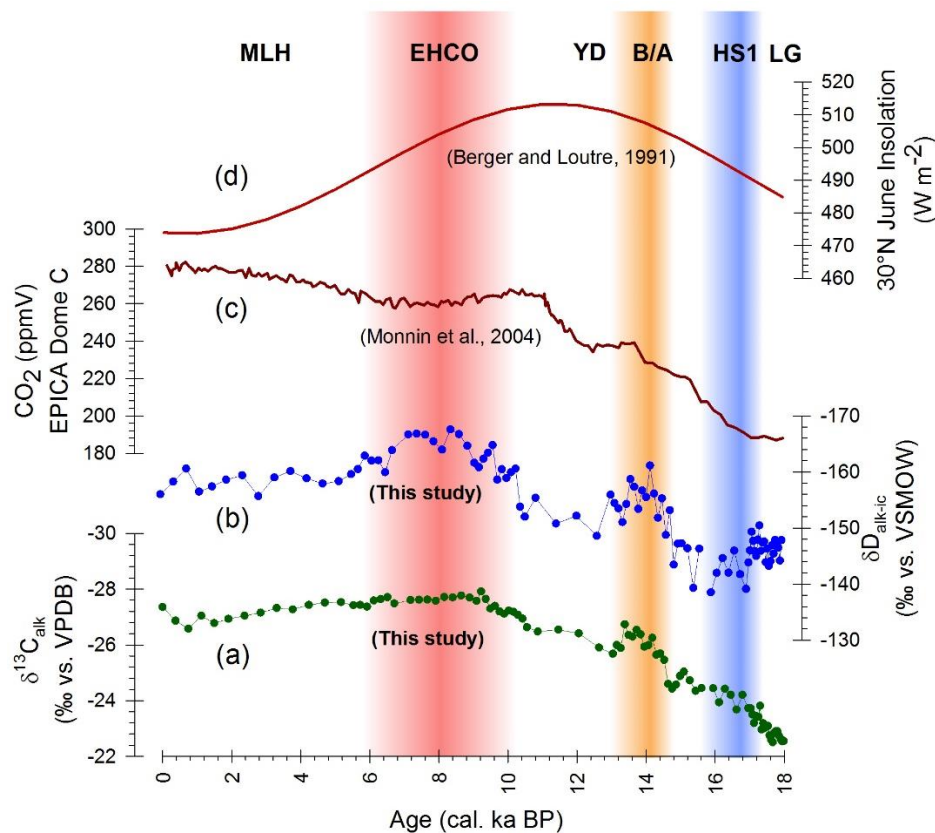
Fig. 3.8. Response of vegetation composition to precipitation variability in the Bengal region. **(a)** Weighted-average of the n-C_{29} and n-C_{31} carbon isotopic records ($\delta^{13}C_{alk}$); **(b)** Weighted-average of the n-C_{29} and n-C_{31} hydrogen isotopic records (δD_{alk-ic}); **(c)** EPICA Dome C ice-core Holocene and transition CO_2 record (Monnin et al., 2004); **(d)** 30°N June insolation curve (Berger and Loutre, 1991), showing the insolation maximum around 11 ka BP. Axes are reversed in (a) and (b) to show increase of C_3 vegetation and precipitation intensification towards the top of the graph. For the meaning of color bars and abbreviations at the top of the figure see Fig. 3.7.

3.6. Summary and conclusions

The changes in the δD of precipitation and plant waxes around the NBoB were mainly driven by the amount effect and strongly influenced by summer monsoon precipitation originating from a constant moisture source (i.e. the NBoB) throughout the study period, as supported by model results. Summer precipitation amount as simulated by the IsoCAM model indicates enhanced convective activity over the NBoB and 20% more rain during the 6K scenario, as well as reduced convective activity and 20% less rain during the HS1 scenario, relative to the pre-industrial period. Qualitative precipitation changes inferred from the alkane δD record suggest that, overall, the Holocene (last 10 ka) was moister than the Late Glacial period (18–10 ka BP), with a two-step intensification of the monsoon during the B/A and the Early Holocene. Precipitation was strongest during the EHCO (10.5–6 ka BP), whereas the most arid conditions were recorded during the HS1 (16.9–15.4 ka BP). Regional coherent variability of the ISM is supported by the highly similar proxy-derived and model-derived precipitation anomalies. Maximum monsoon strength during the Early Holocene is coherent with other records from the ISM domain, from Arabia to southwest China. Vegetation changes deduced from the alkane $\delta^{13}C$ record indicate a shift from C_4-plant dominated ecosystems during the Late Glacial to mixed C_3/C_4-plant vegetation during the Holocene. The highly significant correlation of δD and $\delta^{13}C$ in our record evidences that vegetation composition is strongly linked to precipitation variability, and became independent from atmospheric CO_2 concentration after about 15 ka BP. Precipitation and vegetation changes inferred from our records in comparison to other records across the ISM domain point to synchronous variability of the western (Arabian) and eastern (Bengal) summer monsoon branches. Our records provide for the first time an integrated continuous history of ISM evolution and associated vegetation changes in the Bengal region during the past 18 ka.

Acknowledgements

geomorphology of the Bengal basin. This work was supported by the DFG Research Center/Cluster of Excellence `MARUM - The Ocean in the Earth System' and `GLOMAR - Bremen International Graduate School for Marine Sciences'. We gratefully acknowledge the financial support of the German Federal Ministry of Education and Research (BMBF) in the framework of the project CARIMA (Grant no. 03G0806D). Finally, we would like to acknowledge the comments and recommendations of two reviewers which helped us to improve the quality of this work.

Appendixes

A3.1. n-Alkane homologues distribution

The *n*-Alkanes are synthesized by higher plants as part of their leaf waxes (Eglinton and Hamilton, 1967) and are typically odd-numbered homologues containing between 25 and 33 carbon atoms. This predominance of odd-over-even homologues is recorded in the carbon preference index (CPI) (Bray and Evans, 1961). Leaf waxes have typical CPI values of 4 or higher, whereas petrogenic *n*-alkanes have CPI values around 1 (Killops and Killops, 2005). The CPI of total long-chain *n*-alkanes (*n*-C_{24} to *n*-C_{34}) was calculated according to the following equation:

$$CPI = 0.5 * \left(\frac{\sum_{n=25}^{33}[C_n]}{\sum_{n=24}^{32}[C_n]} + \frac{\sum_{n=25}^{33}[C_n]}{\sum_{n=26}^{34}[C_n]} \right) \qquad \text{Eq. A3.1}$$

where C_n refers to the alkane concentration and *n* refers to the number of carbon atoms in each homologue.

A3.2. Correction of alkane δD values for the global ice volume effect

The measured alkane-δD values were corrected to account for changes in global ice volume during the studied time-span (Collins et al., 2013; Niedermeyer et al., 2010; Schefuß et al., 2005). We used the benthic foraminiferal oxygen isotope curve from Waelbroeck et al. (2002) to estimate the mean ocean water $\delta^{18}O$ through the last 18.1 ka by interpolating the curve to each sample age from

our record, then we calculated the corrected δD values using the following equation (after Jouzel et al., 2003; Wang et al., 2013):

$$\delta D_{alk-ic} = \delta D_{measured} - 8\Delta\delta^{18}O_{MOW} * \left(1 + \frac{\delta D_{alk}}{1000}\right) / \left(1 + 8\frac{\Delta\delta^{18}O_{MOW}}{1000}\right) \quad \text{Eq. A3.2}$$

where δD_{alk-ic} is the ice-volume corrected alkane isotopic composition, the δD_{alk} is the original alkane isotopic composition, and the $\Delta\delta^{18}O_{MOW}$ is the change in the mean ocean water $\delta^{18}O$ with respect to the present.

A3.3. The plume effect versus the amount effect in the northern Bay of Bengal

To test the hypothesis that the magnitude of the plume effect is directly related to the amount of summer precipitation, we compared the precipitation hydrogen isotopic composition (δD_p) measured by Breitenbach et al. (2010) for the summer (June to September) of 2007 and 2008. Their measurements were carried out in Cherrapunji (northeast India) with monthly rainfall data for the same periods recorded by the IITM at the Shillong meteorological station (WMO station # 42516). The comparison indicates lower δD_p in the rainier summer of 2007 (weighted summer mean = -46 ± 27 ‰; total summer precipitation = 14 733 mm) than in 2008 (weighted summer mean = -31 ± 10 ‰; total summer precipitation = 14 094 mm), supporting the idea that the amount effect dominates the isotopic composition of rain in time spans longer than a year.

A3.4. Effects of precipitation variability on the carbon isotopic composition of C₃ plants

Recent evidence indicates a positive and nearly linear correlation between the mean annual precipitation and the $\delta^{13}C$ composition of C_3 plants (Diefendorf et al., 2010; Kohn, 2010; Prentice et al., 2011), due to the interplay between water use efficiency and leaf-CO_2 concentration during photosynthesis (Cowan and Farquhar, 1977; Diefendorf et al., 2010; Farquhar et al., 1982; Prentice et al., 2011). Such an observation would imply that the C_3 end-member may vary according to moisture availability, becoming more positive under more arid conditions due to a reduced fractionation of water isotopes by plants (Douglas et al., 2012). However, we believe that this observation would not have major implications for our data set. This is because the study area is presently among the most humid regions in the planet, with mean annual precipitation (MAP)

amounts between 1000-3000 mm yr^{-1} (most part of the alkanes source area is actually above 1500 mm yr^{-1}). According to observations, the linear relationship between MAP and the $\delta^{13}C_{leaf}$ values begins when local MAP falls below ~2000 mm yr^{-1} (Diefendorf et al., 2010; Kohn, 2010), but the $\delta^{13}C_{leaf}$ values significantly depart from the $\delta^{13}C$ global C$_3$ averages (upon which the C$_3$ end-member is based) only when MAP falls below ~1000 mm yr^{-1}. During the HS1, when precipitation in the record was at its minimum, the estimations of the IsoCAM model suggest that MAP was on average >900 mm yr^{-1} for the region considered in the model, and the effect on the vegetation $\delta^{13}C$ composition would be minor.

Supplementary Discussion

S3.1. Vegetation fractionation effects on the isotopic signature of n-alkanes

We attempted to reconstruct the paleo-source water isotopic composition for the *n*-alkanes (δD_w) and at the same time evaluate the effects of glacial/interglacial vegetation composition changes on the isotopic signature of sedimentary alkanes. To this end, a binary mixing model between C$_3$ and C$_4$ plants was used in order to account for changes in vegetation composition throughout the record. Subsequently, the hydrogen isotopic composition of the alkane's paleo-source water (δD_w) was approximated based on the estimation of apparent fractionation factors ($\varepsilon_{alk/w}$) between the sedimentary alkanes and the plants' source water (Collins et al., 2013; Sessions et al., 1999), which varied according to the C$_3$/C$_4$ vegetation changes.

S3.1.1. Calculation of apparent fractionation factors by vegetation and calculation of paleo source water δD

Plants with different photosynthetic pathways have different apparent fractionation factors ($\varepsilon_{alk/w}$; see review by Sachse et al., 2012 and references therein), and sedimentary alkanes are composed by material from large vegetal communities. Thus, changing the proportions of plants with different photosynthetic pathways within a vegetal community will have an impact on the $\varepsilon_{alk/w}$ inferred from sedimentary alkanes (e.g. Douglas et al., 2012). In order to account for the effects of vegetation changes in the signal derived from sedimentary alkanes we applied a two-components mixing model as follows:

$$\varepsilon_{alk/w} = f_{C3} * \varepsilon_{C3a/w} + f_{C4} * \varepsilon_{C4a/w} \quad \text{Eq. S3.1}$$

Where, for each sample, $\varepsilon_{alk/w}$ is the fractionation factor reconstructed from the sedimentary alkanes of a given sample level; $\varepsilon_{C3a/w}$ and $\varepsilon_{C4a/w}$ are inferred fractionation factors for C_3 and C_4 angiosperms respectively; and f_{C3} and f_{C4} are the fractional contributions of C_3 and C_4 plants, respectively, estimated from the alkanes $\delta^{13}C$ signature assuming that:

$$\delta^{13}C_{alk} = f_{C3} * \delta^{13}C_{C3d} + f_{C4} * \delta^{13}C_{C4m} \quad \text{Eq. S3.2}$$

The mean fractionation factor used for C_3 angiosperms ($\varepsilon_{C3a/w}$) was -130 ± 21 ‰, while that used for C_4 angiosperms ($\varepsilon_{C4a/w}$) was -111 ± 27 ‰, both calculated from the data compiled by Sachse et al. (2012; supplementary material). We included all angiosperms in the calculation of the $\varepsilon_{alk/sw}$ coefficients because vegetation diversity in the study area is rather large and vegetation in the different sub-basins can be highly contrasting (e.g. the Ganga sub-basin is largely dominated by grasslands, while the Brahmaputra sub-basin and the Indo-Burman ranges are largely dominated by forests), increasing the likeliness of having contributions from many different plant types. The average n-alkane $\delta^{13}C$ of C_3 dicotyledons ($\delta^{13}C_{C3d}$) was taken as the negative-most end member (-35.4 ± 2.3 ‰ for n-C_{29} and -35.6 ± 2.3 ‰ for n-C_{31}, average of -35.5 ± 1.6 ‰) and that of C_4 monocotyledons ($\delta^{13}C_{C4m}$) was taken as the positive-most end member (-20.7 ± 2.8 ‰ for n-C_{29} and -21.1 ± 2.8 ‰ for n-C_{31}, average of -20.9 ± 2.0 ‰), based on the dataset complied by Sachse et al. (2012).

Estimated down-core $\varepsilon_{alk/w}$ values ranged between -113 ± 32 ‰ during the HS1 ‰ and -119 ± 29 ‰ during the Late Holocene. These values should be taken with caution, since some important factors could not be taken into account. For instance, the estimations of C_3/C_4 vegetation proportions can be biased by differential wax production between plants groups, or by the large range of $\delta^{13}C$ values of C_3 species alone, both of which can lead to over/under estimations of C_3 plant species abundance. These factors are however very difficult to quantify and the lack of long-term pollen record studies in the G-B-M basin and NBoB surroundings make it impossible to evaluate their imprints on the $\delta^{13}C_{alk}$ signature. Likewise, the estimated $\varepsilon_{alk/w}$ values used for the correction were largely based on data from mid-latitude plant species, which may differ from those of tropical species.

S3.2. The isotopic composition of paleo-source water from sedimentary alkanes of the NBoB

The isotopic composition of the paleo source water (δD_w) was calculated after Sessions et al. (1999) by using the down-core δD_{alk-ic} data and the down-core $\varepsilon_{alk/w}$ calculated values as follows:

$$\delta D_w = 1000 * \left[\frac{\delta D_{alk-ic} + 1000}{\varepsilon_{alk/sw} + 1000} - 1 \right] \quad \text{Eq. S3.3}$$

Estimated down-core δD_w values ranged between -26 ± 7 ‰ during the HS1 ‰ and -54 ± 13 ‰ during the Late Holocene (Fig. S3.1). In order to elucidate if the isotopic signature of Site 342KL sedimentary alkanes reflects either seasonal or annual precipitation, we used as reference the δD_p dataset of Breitenbach et al. (2010) together with the precipitation amount records from the Indian Institute of Tropical Meteorology (IITM) to calculate weighted average δD_p values for the pre-monsoon (April-May), monsoon (June to September) and post-monsoon (October-November) seasons. The range of values reported by Breitenbach et al. (2010) oscillated from +18.5 ‰ to -144.4 ‰, and we calculated an annual δD_p amount-weighted average of -33 ± 35 ‰. The seasonal amount-weighted averages were +2 ± 16 ‰ for the pre-monsoon, -38 ± 20 ‰ for the summer monsoon, and -86 ± 24 ‰ for the post-monsoon, respectively. The estimated core-top δD_w value (-42 ± 10 ‰; Fig. S1a) is close to the amount-weighted average δD_p of modern summer monsoon precipitation in the basin (-38 ± 20 ‰, see previous section). This points to the summer monsoon season as being the period of major leaf wax production within the study area, and suggests a strong bias of the alkane δD signature in our record towards that of summer precipitation. Down-core reconstructed values are also comparable with those reconstructed by the IsoCAM model for the relevant time periods (see Table 3.2 in the main text).

Though an overall good match was observed between modern δD_p observations in the NBoB and the δD_w estimated values, this approach has shortcomings that need to be addressed in future research. We thus recommend taking the vegetation-corrected values with caution and at the same time suggest future research focused on: (a) plant ecophysiological responses to specific environmental gradients that could affect plant wax production and/or isotopic composition, and (b) the generation of more comprehensive datasets for tropical regions.
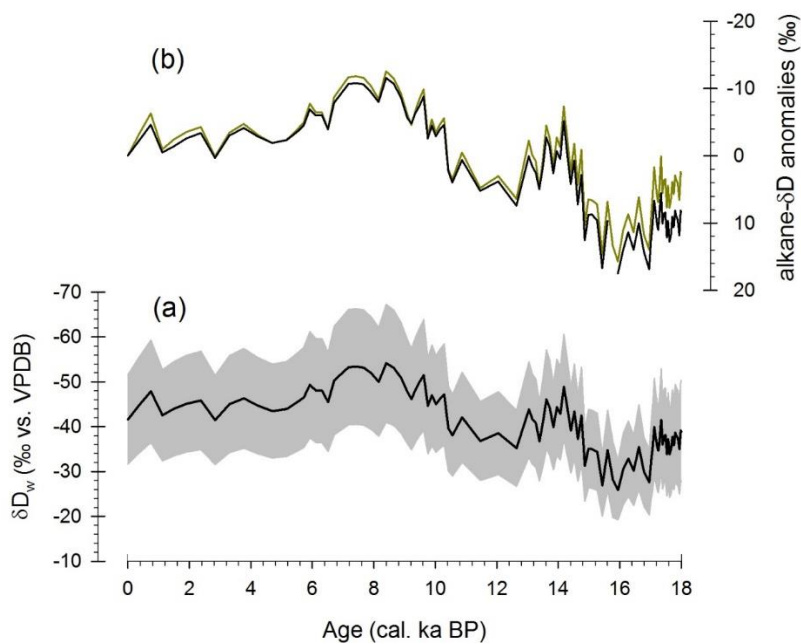
Fig. S3.1. Reconstructed hydrogen isotopic composition of paleo source water around the NBoB and comparison with sedimentary *n*-alkanes hydrogen isotopic composition. **(a)** Reconstructed hydrogen isotopic composition of paleo source water (δD_w). The gray coating is the propagated error associated to the estimated vegetation apparent fractionation factors ($\varepsilon_{alk/w}$). **(b)** Comparison between anomalies (respect to the core top) between δD_{alk-ic} data (black line; not accounting for changes in vegetation fractionation) and δD_w data (green line; accounting for changes in vegetation fractionation). Note departure of values at the oldest part of the section due to major differences in vegetation composition with respect to the present. Axes are reversed in both plots to show precipitation intensification towards the top of the graph.

Chapter 4

Origin and fate of sedimentary organic matter in the northern Bay of Bengal during the last 18 ka

Contreras-Rosales, L.A. [1,2], Schefuß, E.[2], Meyer, V. [3,4], Palamenghi, L. [3], Lückge, A.[5], Jennerjahn, T.[1]

[1] ZMT- Leibniz Center for Tropical Marine Ecology, 28359 Bremen, Germany.

[2] MARUM- Center for Marine Environmental Sciences, University of Bremen, D-28359 Bremen, Germany.

[3] Faculty of Geosciences, University of Bremen, D-28359 Bremen, Germany.

[4] AWI - Alfred Wegener Institute, Helmholtz Center for Polar and Marine Research, Bremerhaven, Germany

[5] BGR- German Federal Institute for Geosciences and Natural Resources, D-30655 Hannover, Germany.

Abstract

The Northern Bay of Bengal (NBoB) is considered a globally important region for deep-sea organic matter (OM) export due to the massive fluvial discharge from the Ganges-Brahmaputra-Meghna (G-B-M) system and the moderate to high surface productivity. Surprisingly, little is known on the long-term storage of carbon in the sediments of this region. Therefore, this study presents a comprehensive history of OM origin and fate as well as a quantification of carbon

sediment storage in the NBoB during the last 18 ka. Bulk organic proxies (TOC, TIC, TN, $\delta^{13}C_{TOC}$, $\delta^{15}N_{TN}$), content of terrestrial biomarkers (long-chain *n*-alkanes), and content and composition of total hydrolysable amino acids (THAA) in a sediment core from the Eastern Bengal Slope (SO188-342KL) were analyzed. Three periods of high OM accumulation were identified: the Late Glacial (LG), the Bölling/Alleröd (B/A), and the Early Holocene Climatic Optimum (EHCO). Lower eustatic sea level before 15 ka BP allowed a closer connection between the Eastern Bengal Slope and the G-B-M fluvial debouch, favoring high terrestrial OM input to the core site. This connection was progressively lost between 15−7 ka BP as sea level rose to its present position and terrestrial OM input decreased considerably. Marine primary production was stimulated during periods of summer monsoon intensification (B/A and EHCO) by enhanced cyclonic-eddy nutrient pumping and fluvial nutrient delivery into the photic zone. Marine productivity was partially hindered under maximum monsoon strength by the extreme freshening of the ocean surface. Changes in the THAA composition indicate that the marine plankton community structure shifted from calcareous-dominated before 13 ka BP to siliceous-dominated afterwards. They also indicate that the relative proportion of marine versus terrestrial OM deposited at site 342KL was primarily driven by relative sea level and was larger during the Holocene. The export and preservation of OM was largely promoted by the ballasting effect of lithogenic particles during periods of high coastal proximity and/or enhanced fluvial discharge. The high organic carbon accumulation rates in the LG (18−17 ka BP) were 5-fold higher than at present and comparable to those of upwelling areas, characterizing the NBoB as a key region for carbon sequestration during sea level low stands.

Keywords

Organic matter; Indian Summer Monsoon; Northern Bay of Bengal; Ganges-Brahmaputra-Meghna; relative sea level; carbon sequestration.

4.1. Introduction

Within the Indian Monsoon Domain, the Northern Bay of Bengal (NBoB) is intensely affected by the discharge of one of the largest fluvial systems on Earth: the Ganges-Brahmaputra-Meghna (G-B-M) system. In comparison to other tropical continental margins at similar latitude, e.g. the

Arabian Sea (Muraleedharan et al., 2007), the NBoB shows lower rates of primary productivity which is caused by the intense cloud cover and the strong stratification of surface waters as result of fluvial discharge (Madhu et al., 2006; Prasanna Kumar et al., 2004). Modern sedimentation in the central and eastern part of the NBoB is hemipelagic (Weber et al., 2003). However, this situation differed in the Last Glacial Maximum, when mean global sea level was more than 120 m lower and lateral advection of terrestrial sediments increased due to coastline progression about 100 km seawards (Colin et al., 1999). With different coastal configuration in the past, the sources, transport mechanisms, and preservation/degradation processes of terrestrial and marine OM in the NBoB were most likely modified. Additionally, changes in monsoon intensity from glacial to interglacial periods have also affected the amount of sediment discharged from the continent (Goodbred Jr. and Kuehl, 2000a), the degree of OM degradation (Pattan et al., 2013), and the weathering of lithogenic particles (Colin et al., 1998).

Organic matter in the oceans contains a large fraction of the carbon sequestered from the atmosphere; therefore, its origin and fate over millennial time spans are important for the long-term global carbon budget. The Northern Bay of Bengal (NBoB) is considered a globally important region in terms of organic matter (OM) export to the deep-ocean but little is known on the long-term storage of carbon in sediments of this region. In this study, we present for the first time a comprehensive history of organic matter (OM) input and preservation in the Northern Bay of Bengal (NBoB) since the end of the last glacial period. The general aim of this study is to determine the sources of OM and the mechanisms controlling its deposition and degradation as well as their variability throughout the last 18 ka. The specific objectives are to evaluate (a) the impact of sea level rise and Indian Summer Monsoon evolution on the regulation of terrestrial versus marine OM input to the core site, (b) the effects of the Ganges-Brahmaputra-Megnha fluvial discharge on the supply of terrestrial OM, and (c) the fate of OM driven by degradation/preservation processes.

4.2. Study Area

The NBoB is located within the Indian Monsoon Domain in which low-level southwest (SW) winds blow from the Indian Ocean into South Asia during summer monsoon. During winter monsoon instead, low-level northeast (NE) winds blow from South Asia onto the Indian Ocean. From June to September the NBoB experiences torrential monsoonal rains which account for 70

% of the total annual precipitation in the region (data archive of the Indian Institute of Tropical Meteorology, IITM; http://www.tropmet.res.in). Monsoonal rains induce a massive discharge of freshwater and sediments from the G-B-M river system of respectively 1120 km^3 yr^{-1} and 1060 Mt yr^{-1} (Milliman and Farnsworth, 2011). This represents 80 % of the G-B-M yearly water outflow and 95 % of its yearly sediment discharge (Goodbred Jr., 2003). Altogether, it accounts for about half of the total Indian Ocean runoff (Naqvi, 2010). The large excess of precipitation over evaporation together with the extensive fluvial discharge to the NBoB lead to water column stratification and formation of a strong barrier layer of 15–20 m thick, which persists through and beyond the summer monsoon period (Madhu et al., 2006; Vinayachandran et al., 2002).

Biological productivity in the NBoB is primarily driven year-round by cyclonic eddies which pump nutrients from the subsurface back into the photic zone, increasing biological productivity 2- to 8-fold compared to regions outside the eddies (Muraleedharan et al., 2007; Prasanna Kumar et al., 2007, 2004). Most of eddy-driven productivity takes place in the subsurface (below 15 m depth) due to the strong stratification of the surface waters (Prasanna Kumar et al., 2004). Eddy nutrient pumping is complemented with riverine nutrient input but primary productivity does not reach its full potential due to nitrate and light limitation, the later due to high river plume turbidity and thick cloud cover over the NBoB during the summer monsoon (Madhu et al., 2006; Prasanna Kumar et al., 2004). Even though, integrated primary productivity in the upper 120 m of the water column reaches up to 200–400 mg C m^{-2} d^{-1} within eddies in the central NBoB (18–20 °N), and up to 300–450 mg C m^{-2} d^{-1} within eddies near the northeastern Indian margin (17–19 °N) (Prasanna Kumar et al., 2007). In addition to eddy-driven productivity, summer upwelling along the eastern Indian margin also injects nutrients into the photic zone (Rao, 2002; Shetye et al., 1991), promoting an integrated productivity up to 300−500 mg C m^{-2} d^{-1} in the upper 120 m of the water column (Madhu et al., 2006; Muraleedharan et al., 2007). New production, based on freshly injected nutrients into the photic zone, constitutes approximately half of the total production across the bay (Kumar et al., 2004b; Kumar and Ramesh, 2005).

According to sediment trap data from the NBoB, peak fluxes of lithogenics, organic carbon and biogenic opal are observed in May, during the early summer monsoon season, as a result of increased fluvial nutrient discharge (including silica) which fuels primary production driven by diatoms (Stoll et al., 2007). The peak flux of organic carbon during this period is associated to a

true increase of marine primary production and not only to the ballasting effect of lithogenic particles (Stoll et al., 2007). Peak fluxes of carbonate and maximum abundance of upwelling indicator species are recorded from July to September, during the late summer monsoon season, due to intense cyclonic eddy formation and the take-over of primary production by coccolithophorids in response to progressive silica depletion by diatoms (Stoll et al., 2007).

An oxygen minimum zone (OMZ) has been observed in the Bay of Bengal (Singh et al., 2011), characterized by dissolved oxygen concentrations < 5−10 μM with an upper (lower) boundary around 70−120 m (250−500 m), deepening towards the north of the bay and presenting maximum expansion (ca. 450 m) during the summer monsoon (Kumar et al., 2004a; Rao et al., 1994; Sarma et al., 2013). The occurrence of the OMZ has been attributed to the combination of export of low oxygen intermediate waters from the Arabian Sea into the Bay of Bengal, strong stratification due to the fluvial freshwater plume, and increase of productivity due to nutrient injection into the photic zone (Rao et al., 1994; Sarma et al., 2013; Wyrtki, 1971). Nevertheless, respiration (i.e. aerobic degradation) rates within the Bay of Bengal water column are lower than expected, which has been attributed to the rapid sinking of OM particles driven by the ballasting effect of terrestrial lithogenic particles (Naqvi et al., 1996; Rao et al., 1994).

4.3. Materials and Methods

4.3.1. Sediment core

Gravity core SO188-342KL was retrieved on the continental slope off Bangladesh (1265 m water depth; Fig 4.1) during RV *Sonne* cruise SO188 in 2006. The core location (19.9733 °N, 90.0338 °E) is ~220 km southwest of the main G-B-M outlet. Modern sedimentation at the core location is mostly hemi-pelagic as most of the suspended sediment load on the NBoB shelf is deflected towards the Swatch of No Ground (SoNG) canyon head (Palamenghi et al., 2011), and funneled into the Bengal Fan, preventing lateral advection of sediments across the continental slope (Weber et al., 2003).
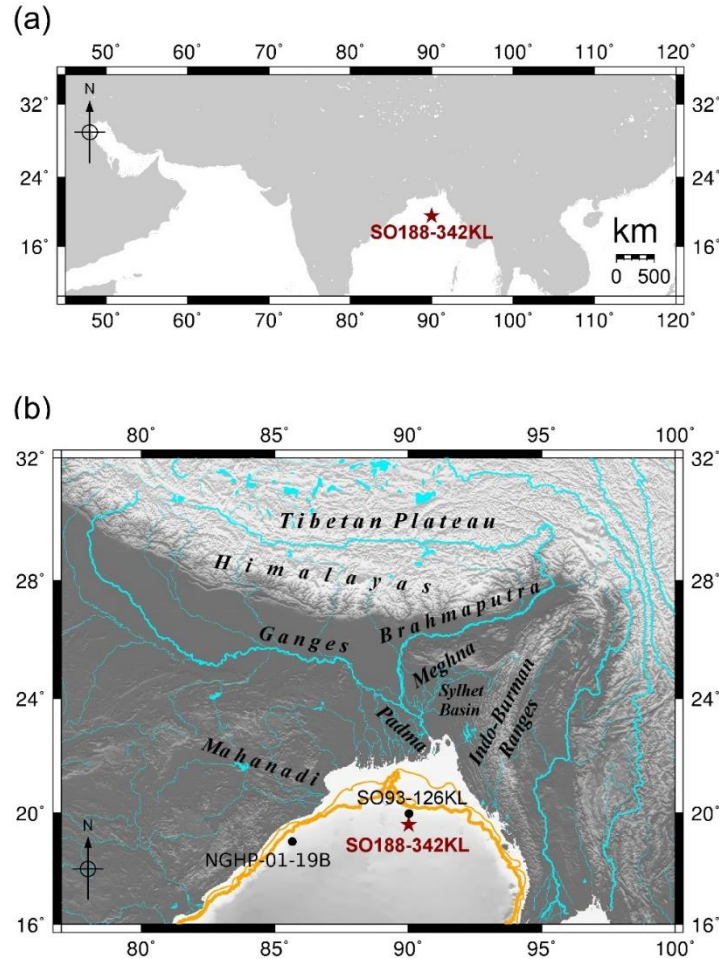
Fig 4.1. Maps of South Asia and the Northern Bay of Bengal showing core location and location of other records mentioned in the text. **(a)** Map of South Asia showing the location of sediment core SO188-342KL. **(b)** Map of the Northern Bay of Bengal area with the location of core SO188-342KL (red star; this study) and neighboring cores SO93-126KL (Kudrass et al., 2001; Pierson-Wickmann et al., 2001) and NGHP-01-19B (Phillips et al., 2014). Major rivers are shown in blue. The -120 m isobath (thick orange line) is shown as reference for the approximate coastline around 18 ka BP, while the -80 m isobath (thin orange line) represents the approximate coastline around 14 ka BP.

4.3.2. Sampling and age model

After collection, the core was stored at 4 °C at the German Federal Institute for Geosciences and Natural Resources (BGR, Hannover, Germany). A total of 100 samples were taken for analysis of bulk parameters and alkane biomarkers, while 63 samples were taken for analyses of total hydrolysable amino acids. The age model details have been previously published (Contreras-

Rosales et al., 2014). The age at the bottom of the section is 18.3 ka BP, the average time resolution between samples is 186 ± 141 years, and linear sedimentation rate (LSR) values ranged between 4–55 cm ka^{-1}. Mass accumulation rate (MAR) values were calculated based on extrapolated dry bulk density (DBD) values from the neighboring sediment core SO93-126KL (Fig. 4.1b) (Pierson-Wickmann et al., 2001), by using a grain density of 2.75 g cm^{-3} (Brusova, 2011) and assuming identical dry bulk densities for both cores at similar sediment depths.

4.3.3. Bulk analyses

Sediment samples were dried at 40 °C and homogenized by grinding in a planetary mill. Total carbon (TC) and total nitrogen (TN) content were analyzed by high temperature oxidation in a Euro EA 3000 elemental analyzer. Based on repeated measurements of selected samples, TC and TN measurements had a precision of ± 0.03 % and ± 0.01 % respectively. Total organic carbon (TOC) was measured after removal of carbonate from the samples by the addition of a 1N HCl solution and subsequent drying at 40 °C. Total inorganic carbon (TIC) was determined my subtracting the TOC content from the TC content of the sample. TOC, TN and TIC are reported as % of bulk dry weight. For these parameters, MAR values were calculated by multiplying the bulk MAR by the sediment content of each parameter, expressed in mg g^{-1} of sediment.

Total nitrogen isotopic composition ($\delta^{15}N_{TN}$) was determined with a Thermo Finningan Delta Plus gas isotope ratio mass spectrometer after high temperature combustion in a Flash 1112 EA elemental analyzer. The $\delta^{15}N_{TN}$ is reported as the per mil (‰) deviation from the nitrogen isotopic composition of atmospheric air. Repeated measurements of selected samples yielded an analytical precision of ± 0.13 ‰. The total organic carbon isotopic composition ($\delta^{13}C_{TOC}$) was determined following the same procedure as for nitrogen isotopes after the addition of 1N HCl solution and subsequent drying at 40 °C. The $\delta^{13}C_{TOC}$ is reported as per mil (‰) deviation from the carbon isotope composition of the Vienna Pee Dee Belemnite (VPDB). Repeated measurements of selected samples yielded an analytical precision of ± 0.05 ‰.

4.3.4. Extraction and separation of n-alkanes

Lipids were extracted from dried and finely ground sediments with a DIONEX accelerated solvent extractor (ASE) using dichloromethane/methanol (DCM/MeOH; 9:1 v/v; 1000 psi, 100 °C, 3 cycles). Squalene was added as internal standard prior to the extraction. Total lipid extracts were dried by rotary evaporation and saponified by addition of a 6% KOH solution in MeOH for the hydrolysis of ester bonds. Hexane was added to the saponified extracts for extraction of neutral compounds such as hydrocarbons, ketones and alcohols. Apolar hydrocarbons from the neutral fraction were separated by elution with hexane through a silica-gel column and a subsequent $AgNO_3$-Si column to remove unsaturated compounds. Identification of individual *n*-alkanes was conducted with a gas chromatography/flame ionization detector (GC/FID) by comparing their retention times to that of an external standard. Concentration of *n*-alkanes in the samples was determined by the integration of the chromatogram peak areas calibrated against the external standard composed of a mix of several *n*-alkanes with known concentrations. Repeated measurements of the external standard yielded a quantification uncertainty of < 5 %. Only the abundances of odd-number-long-chain *n*-alkanes (odd *n*-C25 to *n*-C33; hereafter *n*-alkanes) were considered for further discussion as these derive from terrestrial plant material (Killops and Killops, 2005). The alkane content is reported as carbon percentage of total organic carbon (C% of TOC).

4.3.5. Total hydrolysable amino acids

Total hydrolysable amino acids (THAA) were analyzed with a Biochrom 30 amino acid analyzer after hydrolysis with 6 N HCl for 22 h at 110 °C. Hydrolysis was performed under nitrogen. An aliquot of the hydrolysate was evaporated to dryness at 60 °C and 40 mbar to remove the remaining HCl. The residue was taken up in sodium citrate buffer solution and an aliquot was injected into the analyzer for chromatographic separation on a cation exchange column. Monomer detection was done fluorometrically after derivatization with o-phytaldialdehyd and mercaptoethanol. The following amino acids were detected: (1) acidic (negatively charged): aspartic acid (ASP), glutamic acid (GLU); (2) neutral (uncharged): threonine (THR), serine (SER) , glycine (GLY), alanine (ALA), valine (VAL), isoleucine (ILE), leucine (LEU); (3) basic (positively charged): histidine (HIS), ornithine (ORN), lysine (LYS), arginine (ARG); (4) aromatic: tyrosine (TYR),

phenylalanine (PHE); (5) sulfur-containing: methionine (MET), taurine (TAU); (6) non-protein: β-alanine (BALA), γ-aminobutyric acid (GABA). The THAA content is reported as carbon percentage of total organic carbon (C% of TOC); the relative concentration of individual amino acids is expressed as mol % of THAA. Repeated measurements of a standard solution showed a relative standard deviation between 0.1 and 3.9 % for the concentrations of individual monomers.

4.3.6. Statistical methods

Principal component analysis (PCA) was carried out with the software STATISTICA 8.0 to evaluate the variability in the amino acids composition. The PCA was performed using the mol % of protein amino acids (ASP, THR, SER, GLU, GLY, ALA, VAL, MET, ILE, LEU, TYR, PHE, HIS, ARG and LYS) and the mol % of non-protein amino acids (BALA and GABA) per sediment depth level. Only the factors with eigenvalues > 1 and accounting for > 10 % of the total variance in the dataset were considered for discussion.

4.4. Results

4.4.1. Bulk mass accumulation rates

The bulk-MAR values from site 342KL range between 2–43 g cm^{-2} ka^{-1} (Fig. 4.2a) and display large variability throughout the record with trends strongly associated to relative sea level and sea level change rate (Fig. 4.2c and Fig. 4.2d) (Stanford et al., 2011), as well as to summer monsoon intensity (Fig. 4.2e) (Contreras-Rosales et al., 2014). The mass accumulation rates of TOC (Fig. 4.2b), TN, TIC, alkanes and THAA follow the general trends described by the bulk-MAR. Mass accumulation was highest before 17 ka BP (bulk-MAR > 40 g cm^{-2} ka^{-1}), and relative maxima were observed between 15–13 ka BP, 10.4–9 ka BP and 6.5–5.5 ka BP. Minimum mass accumulation was observed between 12.5–10.5 ka BP (bulk-MAR ~ 3 g cm^{-2} ka^{-1}), and relative minima were observed between 16.8–15.1 ka BP and the last 6.8 ka.
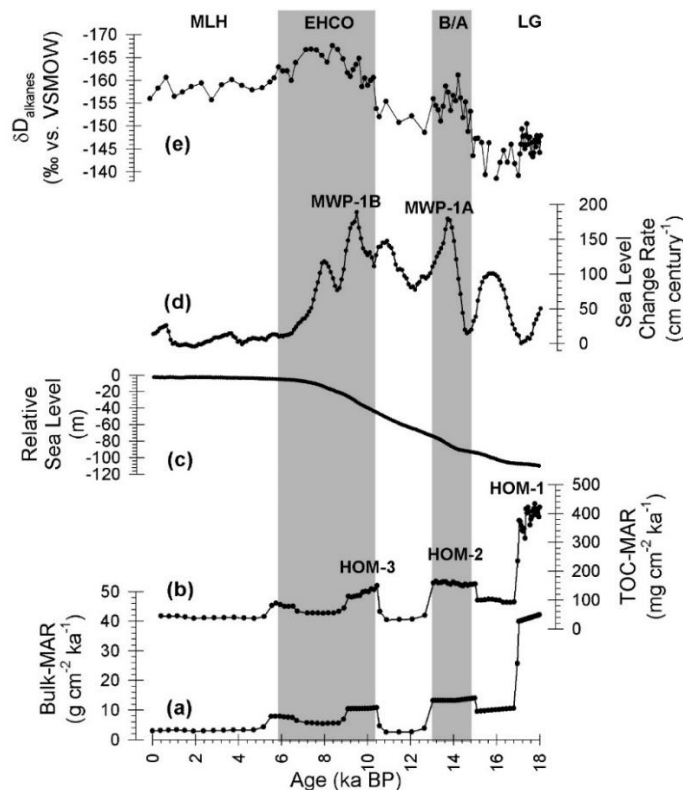
Fig. 4.2. Mass accumulation rates of bulk sediment and total organic carbon from core SO188-342KL and comparison to other paleo-environmental parameters. **(a)** Bulk mass accumulation rate (bulk-MAR), **(b)** total organic carbon mass accumulation rate (TOC-MAR). Periods of high organic matter accumulation (HOM-1 to 3) are indicated in the TOC-MAR curve. For comparison: **(c)** relative eustatic sea level with respect to the present (Stanford et al., 2011), **(d)** relative sea level change rate (Stanford et al., 2011), showing the Melt Water Pulses 1A and 1B (MWP-1A and -1B), and **(e)** weighted-average of the n-C_{29} and n-C_{31} ice-volume-corrected hydrogen isotopic records from core SO188-342KL ($\delta D_{alkanes}$), as indicator of precipitation intensity over the lower G-B-M basin (Contreras-Rosales et al., 2014). Axis is reversed in (e) to show precipitation intensification towards the top of the graph. Abbreviations at the top represent distinctive climatic periods discussed throughout the paper as follows: LG, Late Glacial; B/A, Bölling/Alleröd; EHCO, Early Holocene Climatic Optimum; MLH, Mid-to-Late Holocene. Gray bars highlight periods of summer monsoon intensification.

4.4.2. Bulk composition

The TOC content ranges between 0.7 and 1.5 % with TOC-MAR values between 31 and 468 mg cm^{-2} ka^{-1} (Fig. 4.2b). High TOC content (> 1.2 %) occurs during the periods 14–10 ka BP and 4–0 ka BP, whereas low TOC content (< 1.1 %) occurs during 18–16 ka BP and 9–5 ka BP. The TN content ranges between 0.08 and 0.18 % with TN-MAR values between 3 and 52 mg cm^{-2} ka^{-1}. The down core correlation between the TOC and TN contents is highly significant (r = 0.97, n =

100, p < 0.001), indicating that both parameters have predominantly the same origin (i.e. biological; regression-line intercept at -0.01). The weight ratio between TOC and TN (TOC/TN) is used as an indicator for terrestrial versus marine OM input (Hedges et al., 1997; Hedges and Oades, 1997). The TOC/TN ratios range between 8.0 and 9.6 with highest values observed between 18–13 ka BP and 11–3 ka BP and lowest values between 13–12 ka BP and the last 1 ka (Fig. 4.3a). Relative minima occur between 16.7–15.6 ka BP, 9.2–8.1 ka BP and 7.1–5.9 ka BP. The TIC content ranges between 0.4 and 1.3 % with TIC-MAR values between 12 and 549 mg cm^{-2} ka^{-1}. High TIC content (> 1 %) occurs before 15 ka BP whereas low concentrations (< 0.6 %) were measured around 14 ka BP and between 12–10 ka BP. The weight ratio between TIC and TOC is used as an indicator of high abundance of calcareous producers in the marine biological carbon pump (De La Rocha and Passow, 2007). The TIC/TOC ratios range between 0.4 and 1.3 with highest values before 15.4 ka BP and lowest values between 4.6–10.9 ka BP (Fig. 4.3b). The $\delta^{13}C_{TOC}$ values vary between -22.3 ‰ to -18.5 ‰ with high values before 14 ka BP followed by a sustained decrease between 14–12 ka BP and low values henceforth (Fig. 4.3c). The $\delta^{15}N_{TN}$ values range between 4.1 ‰ and 5.1 ‰ with highest values between 13–6 ka BP and lowest values between 16–15 ka BP and 5–0.5 ka BP (Fig. 4.3d).

4.4.3. n-alkanes content

The sedimentary concentration of *n*-alkanes varies between 0.2 and 1.5 µg g^{-1}, accounting for 9.9 x 10^{-4} and 1.3 x 10^{-2} C% of TOC (Fig. 4.3e). The *n*-alkanes-MAR ranges between 2 and 55 µg cm^{-2} ka^{-1}.

4.4.4. THAA content and composition

Sediment concentration of THAA ranges between 0.8 and 3.0 mg g^{-1} with THAA-MAR values between 2.9 and 49.1 mg cm^{-2} ka^{-1}. THAA constitute 3.5–12.3 C% of the TOC (Fig. 4.3f) and 10.5–37.2 N% of the TN. The most abundant amino acids (> 9 mol % of THAA) are GLY, ASP, GLU and ALA. The mol % of THAA is presented in the appendix at the end of this chapter (Table A4.1). The ratio between glycine and aspartic acid (GLY/ASP) is used as indicator of the predominance of siliceous over calcareous phytoplankton (Ingalls et al., 2003; King, 1977). The GLY/ASP ratio ranges between 1.0 and 1.3, with lowest values before 13.2 ka BP (Fig. 4.3g).
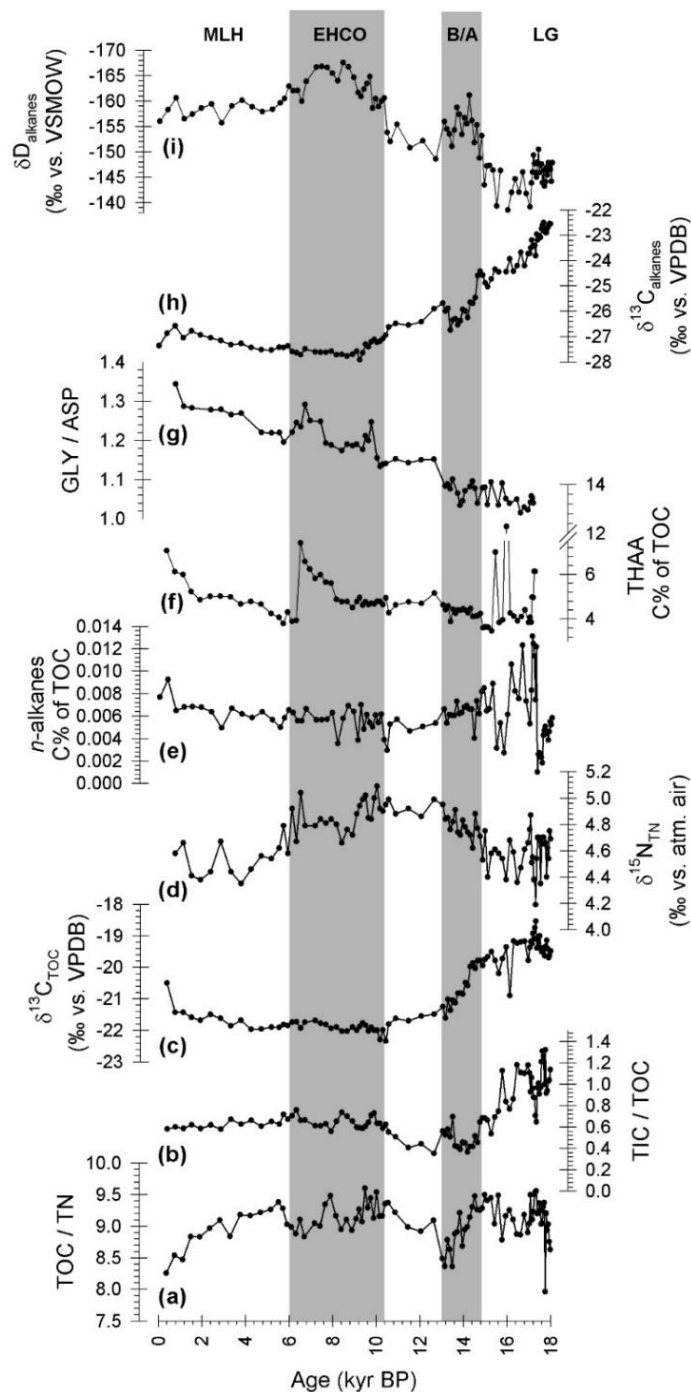
Fig. 4.3. Selected bulk and biomarker parameters from core SO188-342KL. **(a)** bulk total organic carbon to total nitrogen weight ratio (TOC/TN); **(b)** bulk total inorganic carbon to total organic carbon weight ratio (TIC/TOC); **(c)** stable isotopic composition of bulk total organic carbon ($\delta^{13}C_{TOC}$); **(d)** stable isotopic composition of bulk total nitrogen ($\delta^{15}N_{TN}$); **(e)** content of odd-long-chain-*n*-alkanes (C_{25} to C_{33}) expressed as carbon percentage of total organic carbon (*n*-alkanes C% of TOC); **(f)** bulk content of total hydrolysable amino acids expressed as carbon percentage of total organic carbon (THAA C% of TOC); **(g)** glycine to aspartic acid mol % ratio (GLY/ASP), as indicator of plankton

community composition, higher values represent higher proportion of siliceous over calcareous plankton; **(h)** weighted-average of the n-C_{29} and n-C_{31} carbon isotopic records from core SO188-342KL ($\delta^{13}C_{alkanes}$), as indicator of vegetation composition in the lower G-B-M basin (Contreras-Rosales et al., 2014), higher values indicate higher proportion of C_4 over C_3 vegetation; **(i)** weighted-average of the n-C_{29} and n-C_{31} ice-volume-corrected hydrogen isotopic records from core SO188-342KL ($\delta D_{alkanes}$), as indicator of precipitation intensity over the lower G-B-M basin (Contreras-Rosales et al., 2014). Axis is reversed in (i) to show precipitation intensification towards the top of the graph. Gray bars highlight periods of summer monsoon intensification. For the meaning of abbreviations see Fig. 4.2 caption.

Table 4.1. Principal Component Analysis (PCA) results of THAA composition. Factor score coefficients (Coeff.) and factor coordinates of variables (Coord.; equivalent to factor loadings) are presented for Factor 1 (eigenvalue = 8.3; 49 % of total variance) and Factor 2 (eigenvalue = 3.3; 19 % of total variance).

PCA of THAA Factor Score Coefficients and Factor Coordinates of Variables

Factor 1			Factor 2		
Variable	Coeff.	Coord.	Variable	Coeff.	Coord.
GLY	0.874	0.105	GABA	0.551	0.168
SER	0.872	0.105	BALA	0.466	0.142
THR	0.691	0.083	MET	0.466	0.142
HIS	0.549	0.066	TYR	0.393	0.120
MET	0.133	0.016	HIS	0.065	0.020
ALA	-0.021	-0.003	VAL	-0.043	-0.013
TYR	-0.040	-0.005	LYS	-0.044	-0.013
ARG	-0.402	-0.048	ILE	-0.060	-0.018
ASP	-0.485	-0.058	SER	-0.226	-0.069
GABA	-0.772	-0.093	GLY	-0.277	-0.084
LEU	-0.775	-0.093	ARG	-0.357	-0.109
GLU	-0.778	-0.093	GLU	-0.371	-0.113
BALA	-0.779	-0.093	PHE	-0.404	-0.123
PHE	-0.786	-0.094	LEU	-0.483	-0.147
VAL	-0.884	-0.106	ASP	-0.623	-0.190
ILE	-0.940	-0.113	THR	-0.631	-0.192
LYS	-0.962	-0.115	ALA	-0.896	-0.273

4.4.4.1. PCA results

The PCA produced two factors with eigenvalues > 1 and each one representing > 10 % of the total variance in the dataset; together these two factors explain 68 % of the total variance (Table 4.1). Factor 1 (F1; Fig. 4.4a): with an eigenvalue of 8.3 this factor represents 49 % of the total variance. F1 is characterized by strong positive loadings (i.e. factor coordinate coefficients) for GLY, SER, THR and HIS, and strong negative loadings for LYS, ILE, VAL, PHE, BALA, GLU, LEU and GABA. Factor 2 (F2; Fig. 4.4b): with an eigenvalue of 3.3 this factor represents 19 % of the total variance. F2 is characterized by strong positive loadings for GABA and BALA, and strong negative loadings for ALA, THR and ASP.
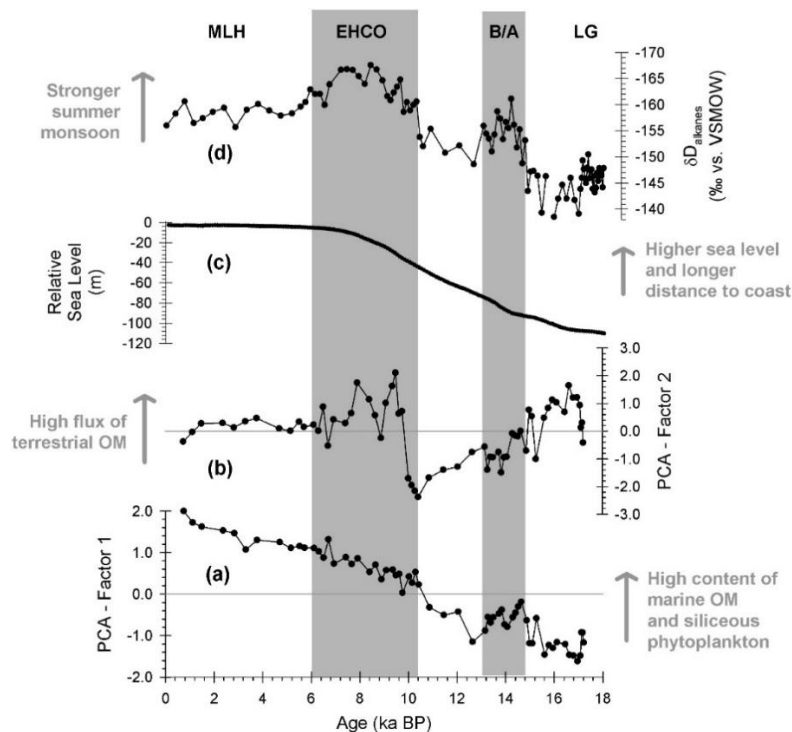
Fig. 4.4. Principal Component Analysis (PCA) results of the total hydrolysable amino acids composition from core SO188-342KL. **(a)** PCA-Factor 1 (49 % of the total variance) is interpreted as indicator for OM origin and degradation driven by sea level change; higher values indicate higher marine-versus-terrestrial OM contribution and higher proportion of siliceous-over-calcareous plankton; **(b)** PCA-Factor 2 (19% of the total variance) is interpreted as indicator for high flux of degraded terrestrial OM to the Eastern Bengal Slope. For comparison: **(c)** relative sea level with respect to the present (Stanford et al., 2011); **(d)** weighted-average of the n-C$_{29}$ and n-C$_{31}$ ice-volume-corrected hydrogen isotopic records from core SO188-342KL (δD$_{alkanes}$), as indicator of precipitation intensity over the lower G-B-M basin (Contreras-Rosales et al., 2014). Axis is reversed in (d) to show precipitation intensification towards the

top of the graph. Gray bars highlight periods of summer monsoon intensification. For the meaning of abbreviations see Fig. 4.2 caption.

4.5. Discussion

4.5.1. OM sources to the NBoB slope sediments

The $\delta^{13}C_{TOC}$ values and TOC/TN ratios of sedimentary OM from Site 342KL are found within the range of marine particulate organic matter (POM; Fig. 4.5) (after Lamb et al., 2006). However, the core top $\delta^{13}C_{TOC}$ value (-20.5 ‰) is also similar to those reported in suspended modern sediments of the G-B-M delta in Bangladesh (-24.3 to -20.7) (Galy et al., 2008a) and the down core $\delta^{13}C_{TOC}$ values (-22.3 to -18.5) and TOC/TN ratios (9.3 to 11.2) are within the range of those reported for Late Glacial and Holocene paleo-soils from the western G-B-M delta plain (Sarkar et al., 2009) (Fig. 4.5). Consequently, though a large contribution of marine OM to Site 342KL is indisputable, terrestrial OM contribution through the last 18 ka cannot be discarded. Therefore, we propose that sedimentary OM at site 342KL is a mixture of terrestrial and marine OM, with changing proportions over time in response to sea-level and climatic changes as discussed in the following sections.
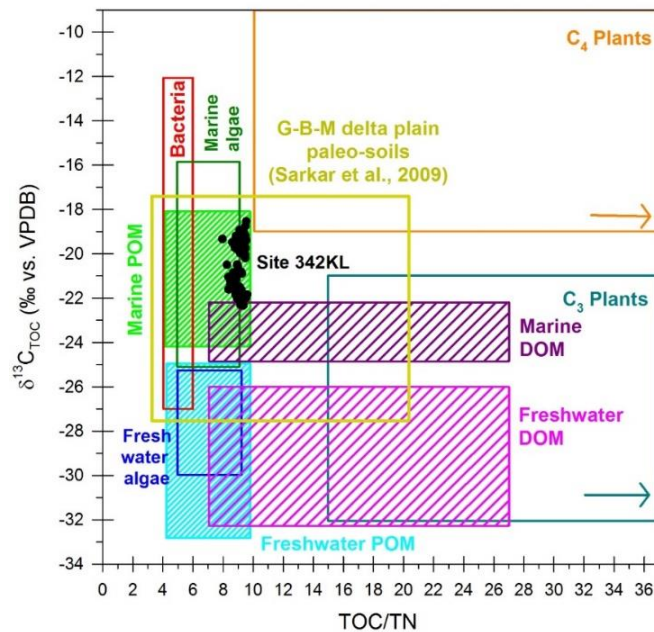
Fig. 4.5. Cross-plot between the down core bulk total organic carbon to total nitrogen weight ratio (TOC/TN) and the down core stable isotopic composition of bulk total organic carbon ($\delta^{13}C_{TOC}$) from core SO188-342KL. The $\delta^{13}C$

and C/N value ranges of different potential organic matter sources are shown in color boxes. Abbreviations POM and DOM stand for particulate and dissolved organic matter respectively. Value ranges of $\delta^{13}C_{TOC}$ and TOC/TN from the Ganges-Brahmaputra-Meghna (G-B-M) delta plain paleo-soils were taken from Sarkar et al. (2009). Cross-plot modified from Lamb et al. (2006).

4.5.2. Evolution of organic matter accumulation at the NBoB slope

4.5.2.1. The Late Glacial (LG: 18–17 ka BP)

Very high TOC-MAR during the LG (387 ± 47 mg OC cm^{-2} ka^{-1}) gives testimony of a first period of High Organic Matter accumulation (HOM-1; Fig. 4.2b). These values are even comparable to that of the Arabian Sea (555 ± 441 mg OC cm^{-2} ka^{-1}) (Sirocko and Ittekkot, 1992) and other upwelling areas in the same period (between 150 and 543 mg OC cm^{-2} ka^{-1} in the coasts off Chile, Southern California, Benguela and Northern California) (Dean, 2007; Mollenhauer et al., 2002; Mortyn and Thunell, 1997; Romero et al., 2006). At the end of the glacial period sea level was approximately 120 m lower than at present (Fig. 4.2c) (Lambeck et al., 2002; Stanford et al., 2011); and site 342KL was approximately 100 to 150 km closer to the shoreline. Paleo-drainage reconstructions of the G-B-M delta area indicate the presence of a river course debouching very close to the Eastern Bengal Slope (Palamenghi, 2012). Such river-mouth proximity resulted in more effective delivery of sediments to the core site, allowing high accumulation rates despite reduced fluvial discharge due to weak summer monsoon (Contreras-Rosales et al., 2014). High availability of terrestrial lithogenic particles serving as ballast likely promoted the rapid sinking of both terrestrial and marine OM (Armstrong et al., 2002).

A high proportion of terrestrial OM contribution during the LG is inferred from the higher $\delta^{13}C_{TOC}$ values (-20 to -19 ‰; Fig. 4.3c) which overlap with the lower limit for C$_4$-plants. Furthermore, the $\delta^{13}C_{TOC}$ is significantly correlated with the $\delta^{13}C_{alkanes}$ measured on the same samples (Fig. 4.3h) (Contreras-Rosales et al., 2014). This feature indicates significant terrestrial contribution because during the late glacial and early deglaciation the G-B-M delta plain had a high proportion of C$_4$ vegetation (Contreras-Rosales et al., 2014; Sarkar et al., 2009). TOC/TN ratios > 8.7 (Fig. 4.3a) also indicate higher terrestrial OM contribution to site 342KL, as relatively low C/N ratios (~ 10-15) have been reported for some C$_4$ plants such as Chenopodiaceae and Amaranthaceae (Pañuelas and Estiarte, 1997). In the water column, high abundance of calcareous

marine producers is inferred from high TIC/TOC values (> 0.8; Fig. 4.3b) and low GLY/ASP ratios (~ 1; Fig. 4.3g).

4.5.2.2. The Bölling/Alleröd (B/A: 14.7−13.0 ka BP)

During the B/A interstadial an increase in TOC-MAR indicates a second period of high organic matter accumulation (HOM-2; Fig. 4.2b) caused by the first summer monsoon intensification at the beginning of the deglaciation (Fig. 4.2e) (Contreras-Rosales et al., 2014). Paleo-drainage reconstructions (Palamenghi, 2012) indicate the persistence of the river channel north of the Eastern Bengal Shelf and the initial formation of a subaqueous delta (Fig. 4.6), which trapped some of the sediments transported by the river outlet. The formation of the subaqueous delta was stimulated by the rapid sea level rise during the Melt Water Pulse 1A (MWP-1A; Fig. 4.2d) (Stanford et al., 2011), which drowned the distal Bengal shelf (Palamenghi, 2012) and elevated sea level between 90 to 70 m lower than present (Fig. 4.2c) (Lambeck et al., 2002; Stanford et al., 2011). Enhanced river discharge driven by monsoon intensification and coastal proximity secured high sediment input to the core site, though lessened as compared to the glacial. During this period of summer monsoon intensification (Contreras-Rosales et al., 2014) marine primary production likely increased due to higher supply of nutrients to the photic zone by fluvial discharge and cyclonic eddies, ultimately resulting in higher OM export to the sediments.

During the B/A, the $\delta^{13}C_{TOC}$ presents a sharp decrease (Fig. 4.3c) reflecting both a substantial increase of C_3 vegetation over land (Contreras-Rosales et al., 2014) and an increase of marine OM accumulation at the core site (see section 4.5.1). However, TOC/TN ratios > 9 (Fig. 4.3a) indicate that terrestrial OM contribution is still important between 15.5 and 13.6 ka BP in direct response to monsoon intensification. The decrease in TOC/TN ratios after 13.6 ka BP reflect the reduction of terrestrial OM input to the core site after the MWP-1A. A drop of TIC/TOC values (~0.4; Fig. 4.3b) between 14.6 and 13.6 ka BP indicates a decrease of marine calcareous productivity, likely as the result of decreased salinity of the NBoB surface waters (Kudrass et al., 2001). Modern observations in the NBoB indicate that decrease in the abundance of foraminifera is caused by the excessive freshening of the ocean surface (Stoll et al., 2007). Around 12.6 ka BP, a steady increase in the GLY/ASP ratio (Fig. 4.3g) indicates a gradual and sustained displacement of calcareous organisms by siliceous ones. This is in agreement with previous observations from

the northwestern BoB (Site NGHP-01-19B; Fig. 4.1b), where maximum accumulation of biogenic CaCO₃ has been reported between 25 ka BP and 12 ka BP but a sharp decline was observed after 13 ka BP combined with a substantial increase of the biogenic silica accumulation (Phillips et al., 2014). In present day conditions, coccolithophorids and foraminifera only predominate over diatoms in the NBoB after dissolved silica has been depleted and diatoms can no longer thrive (Stoll et al., 2007). Altogether, this indicates that enhanced fluvial discharge of dissolved silica, derived from monsoon intensification, gave diatoms a competitive advantage over coccolithophorids and foraminifera, changing the structure of the plankton community from calcareous-dominated during the late glacial period to siliceous-dominated during the deglaciation and the Holocene.
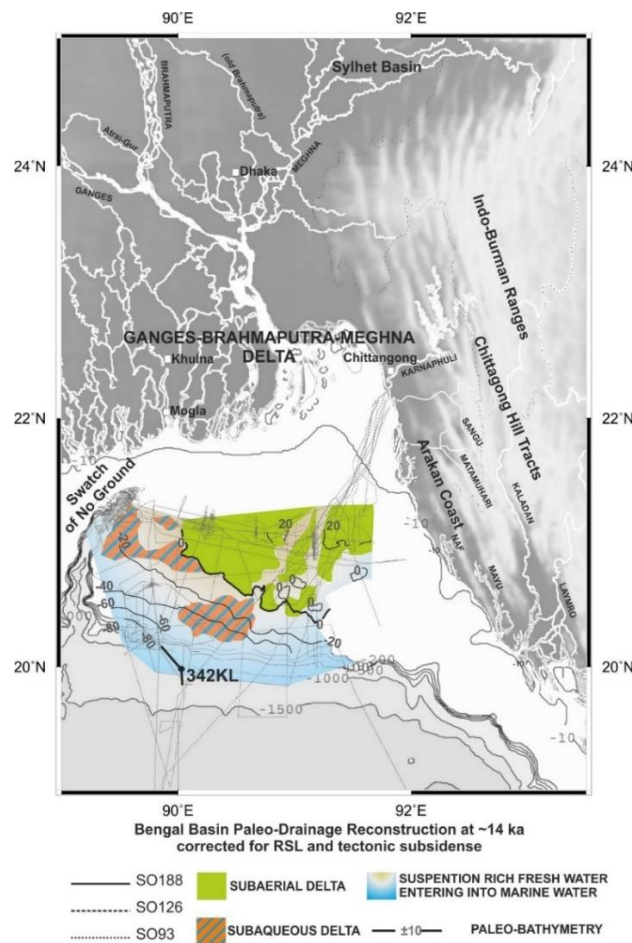
Fig. 4.6. Paleo-drainage reconstruction for the Bengal Basin around 14 ka BP (Bölling/Alleröd), when a retrogradational delta developed at the outer shelf. Due to the coastal proximity, high sediment supply to site 342KL was favored (taken from Meyer, 2012; adapted from Palamenghi, 2012).

4.5.2.3. The Early Holocene Climatic Optimum (EHCO: 10.5–6 ka BP)

The EHCO was characterized by the maximum monsoon intensity in the last 18 ka (Fig. 4.2e) (Contreras-Rosales et al., 2014); and by a third period of high organic matter accumulation between 10.5−9 ka BP (HOM-3; Fig. 4.2b). The EHCO also witnessed the Melt Water Pulse 1B (MWP-1B; Fig 4.2d) (Stanford et al., 2011), an event which spanned for several millennia and translated in a substantial coastline retreat which finally drowned the entire Bengal Shelf (Goodbred Jr. and Kuehl, 2000b; Palamenghi, 2012). Though this increased considerably the distance between site 342KL and the river mouth, the estimated fluvial sediment discharge during the EHCO was double of the present amount in response to maximum summer monsoon intensity (Goodbred Jr., 2003; Goodbred Jr. and Kuehl, 2000a, 2000b). Besides, marine primary production was likely enhanced by higher fluvial nutrient supply and cyclonic-eddy pumping (Muraleedharan et al., 2007). However, the establishment of the Sylhet Basin (Fig. 4.1b; Fig. 4.6) as a major floodplain and sediment depo-center for the Brahmaputra River between 11 and 9 ka BP (Goodbred Jr. and Kuehl, 2000a) may have prevented large amounts of sediments from reaching the coast. Consequently, the bulk-MAR during the Early Holocene at Site 342KL is lower compared to that reported, for instance, offshore the Mahanadi Basin in the northwestern BoB (Phillips et al., 2014). A reduction in bulk-MAR and TOC-MAR is observed between 9 and 7 ka BP when summer monsoon activity was strongest (Fig. 4.2a, b) (Contreras-Rosales et al., 2014). Migration of the Brahmaputra main course westward of the Sylhet Basin after 9 ka BP allowed the majority of sediments to reach the coast, but a substantial amount was trapped by the rapidly aggrading subaerial delta (Goodbred Jr. and Kuehl, 2000a, 2000b). Indeed, the shoreline position was relatively stable during the EHCO because the delta aggradation matched sea level rise due to the enormous fluvial sediment discharge from the G-B-M system (Goodbred Jr. and Kuehl, 2000b). Furthermore, the Early Holocene also records very active turbidite deposition in the upper Bengal Fan (Weber et al., 1997), indicating an effective funneling of the sediments through the Swatch of No-Ground canyon.

An increase of terrestrial OM input between 10.5 and 9.5 ka BP is confirmed by TOC/TN ratios > 8.7 (Fig. 4.3a), whereas enhancement of marine productivity is suggested by higher TIC/TOC ratios (> 0.5; Fig. 4.3b). The steep increase in the GLY/ASP ratio indicates that the community of marine producers is dominated by siliceous organisms, as a result of the enhanced input of dissolved silica. The period between 8.0 and 7.0 ka BP shows a steady increase in the

THAA-C% of TOC. As THAA represent the fresher portion of sedimentary OM, higher abundance after 8.4 ka BP may indicate that maximum marine productivity could only occur when the adverse effects caused by the extreme freshening of the ocean surface, the enhanced river plume turbidity and the intense cloud cover were mitigated during the early phase of monsoonal decline (Contreras-Rosales et al., 2014; Madhu et al., 2006; Prasanna Kumar et al., 2004).

4.5.2.4. The Mid-Late Holocene (MLH: last 6 ka)

At the beginning of the MLH, summer monsoon weakened (Fig. 4.2e) (Contreras-Rosales et al., 2014). Sea level rise showed a major deceleration between 8 and 7 ka BP and stabilized henceforth (Fig. 4.2d) (Stanford et al., 2011). The delta system changed from aggradational to progradational (Goodbred Jr. and Kuehl, 2000a), and the modern subaqueous delta in the Bengal Shelf began to form (Goodbred Jr. and Kuehl, 2000a; Palamenghi, 2012). The further decline of summer monsoon strength during the MLH, the reduction of fluvial discharge, the maximum distance to the shoreline, and the reduction of terrestrial lithogenic ballasting particles resulted in minimum accumulation rates at Site 342KL (Fig. 4.2a, b).

The gradual decline of TOC/TN ratios during this period indicates an increasing proportion of marine OM (Fig. 4.3a). High marine productivity is supported by high TIC/TOC ratios comparable to those of the EHCO (~ 0.6; Fig. 4.3b), and siliceous organisms remain the dominant marine primary producers as indicated by the highest GLY/ASP ratios (> 1.2; Fig. 4.3g).

4.5.3. Sources and fate of nitrogen

4.5.3.1. The roles of OM degradation, denitrification and nutrient sources as discerned from the $\delta^{15}N_{TN}$ record

The $\delta^{15}N_{TN}$ values at the core top of site 342KL (4.6 ‰) are higher than those observed for the suspended sediments in the G-B-M delta in Bangladesh (-3.5 ‰ to 2.7 ‰) (Sarkar et al., 2009) and match those in the upper range of modern sediment traps from the Bay of Bengal (3.6 − 4.5 ‰) (Gaye-Haake et al., 2005; Unger et al., 2006). Compared to the Arabian Sea, where extensive water column degradation and denitrification take place and lead to high $\delta^{15}N$ (> 6 ‰), low $\delta^{15}N_{TN}$ (< 5 ‰) in the NBoB are due to the input of terrestrial OM typically depleted in ^{15}N (Gaye-Haake

et al., 2005; Möbius et al., 2011). The down core $\delta^{15}N_{TN}$ record (Fig. 4.3d) shows higher values (4.7–5.1 ‰) from the beginning of the B/A until the end of the EHCO (14.5−6 ka BP) as compared to the periods before and after. Since terrestrial discharge was higher in the B/A and EHCO due to summer monsoon strengthening, higher $\delta^{15}N_{TN}$ points to enhanced OM degradation, water column denitrification and/or a change in the nitrate source to the photic zone.

Preservation of OM is strongly associated to its reduced exposure to oxygen (Hartnett et al., 1998; Hartnett and Devol, 2003). In the NBoB, the largest impact of degradation on the $\delta^{15}N$ of OM occurs in the upper 300 m of the water column (Kumar et al., 2004a). Through the deeper water column, degradation hardly affects the $\delta^{15}N$ signature because of fast sinking and burial of OM driven by the high availability of fluvial-derived lithogenic ballasting particles (Gaye-Haake et al., 2005). As the supply of lithogenic ballast was large between 14.5 and 6 ka BP it is unlikely that higher $\delta^{15}N_{TN}$ at this time is a product of enhanced OM degradation. Besides, we observed no correlation between the $\delta^{15}N_{TN}$ values with either PCA factors extracted from the THAA composition (section 4.5.3.2), thus we conclude that the $\delta^{15}N_{TN}$ record is not considerably influenced by OM degradation.

Intense oxygen depletion in the water column of highly productive oceanic regions has also been linked to the occurrence of denitrification in intermediate waters and marine sediments, leading to an increase of sedimentary $\delta^{15}N$ (e.g. Altabet et al., 1999; Lückge et al., 2012; Robinson et al., 2012; Suthhof et al., 2001, 2000). However, despite the existence of an Oxygen Minimum Zone (OMZ) in the Bay of Bengal, the occurrence of denitrification has not been proven (Naqvi et al., 1996; Rao et al., 1994; Sarma et al., 2013). Denitrification could potentially exert a predominant influence on the $\delta^{15}N_{TN}$ record of site 342KL during high productivity periods with associated oxygen depletion in the water column. In this light, we would expect to observe a correlation between the $\delta^{15}N_{TN}$ values and the mol % of the aromatic amino acid TYR, which is considered redox-sensitive and better preserved under low oxygen conditions (Jennerjahn and Ittekkot, 1999; Möbius et al., 2011; Suthhof et al., 2000). However, no significant correlation was observed, suggesting that even at periods of high productivity (e.g. EHCO and B/A), the oxygen depletion in the water column was not strong enough for denitrification to take place. Besides, it is likely that enhanced lithogenic ballasting would remove organic particles from the water column

and burry them in the sediments much faster than at present, reducing the transit time of suspended OM through the NBoB-OMZ.

Nitrate is considered a limiting nutrient in the NBoB region and it has been suggested that its utilization is complete (Dowling et al., 2003; Kumar et al., 2004b; Madhupratap et al., 2003). Therefore particulate matter $\delta^{15}N$ reflects the annual average isotopic composition of all the nitrate supplied to the photic zone (Altabet, 1988; Kumar et al., 2004a, 2004b; Kumar and Ramesh, 2005). Previous estimations of the nutrient pool availability and requirements suggest that 80 % of the nitrate utilized in the BoB must be supplied by the pumping of intermediate waters into the photic zone by cyclonic eddies (Kumar and Ramesh, 2005; Madhupratap et al., 2003). As the period between 14.5 and 5 ka BP was marked by intensification of summer monsoon activity, stronger wind-stress could have promoted more intense eddy formation, which increased the injection of nutrients from larger depths (and thus higher $\delta^{15}N$) into the photic zone (Muraleedharan et al., 2007). Therefore, we consider the higher $\delta^{15}N_{TN}$ being the product of a shift in nutrient sources and not a result of degradation or denitrification in the water column.

4.5.3.2. History of organic matter sources and degradation inferred from total hydrolysable amino acids

The final composition of sedimentary amino acids can be attributed to three main diagenetic processes (Keil et al., 2000; Vandewiele et al., 2009): (1) selective preservation of specific amino acids, (2) bacterial transformation of the original amino acids into degradation products, (3) amino acids produced as structural components of bacterial biomass. The interplay of the abovementioned processes is the basis for the interpretation of PCA results.

4.5.3.2.1. PCA factor 1: OM origin and degradation driven by sea level change

Amino acids with positive loadings in F1 (GLY, THR and SER) indicate degradation of marine OM through the water column. Previous studies indicate that GLY, THR and SER are strongly associated to diatom silica walls and become enriched with OM degradation as a result of selective preservation (Hecky et al., 1973; Ingalls et al., 2003; Lee and Cronin, 1984; Siezen and Mague, 1978). In our data set, they likely also represent high input of OM by siliceous phytoplankton due

to the take-over of diatoms as dominant primary producers in the NBoB since 13 ka BP. Thus, positive scores of F1 are interpreted as predominance of marine degraded OM and high abundance of siliceous phytoplankton.

Amino acids with negative loadings in F1 (LYS, ILE, VAL, PHE, LEU, ASP, GLU) have been linked to fresher OM (Dauwe et al., 1999; Unger et al., 2013; Vandewiele et al., 2009) and likely represent well preserved marine OM. Some of these amino acids could have also been delivered to the NBoB by fluvial discharge though their binding to clay minerals (Hedges and Hare, 1987). For instance, VAL and ILE have been observed to be enriched in the OM transported by the G-B-M system (Unger et al., 2005). Negative loadings of F1 also include the non-protein amino acids BALA and GABA, which are usually associated to an advanced OM degradation state (Ingalls et al., 2003; Jennerjahn and Ittekot, 1997; Lee and Cronin, 1984; Möbius et al., 2011; Terashima, 1991; Unger et al., 2005). The grouping of BALA and GABA in the negative loadings of F1 together with the most labile amino acids seems a contradiction. These amino acids can accumulate in sediment cores over the course of long-term organic matter degradation as they are degradation products of the amino acids ASP and GLU, respectively (e.g. Ingalls et al., 2003; Möbius et al., 2011). However, we did not observe an inverse correlation between the concentrations of BALA vs. ASP or GABA vs. GLU, which suggest that the non-protein amino acids must have an additional external source. A possibility is that BALA and GABA are indicators of high terrestrial degraded OM input to the core site (e.g. Unger et al., 2013), as terrestrial OM is often highly degraded and refractory before its discharge into the ocean (Hedges et al., 1997; Hedges and Keil, 1995). Therefore, negative scores of F1 are interpreted as a mix of well-preserved marine OM with degraded terrestrial OM.

As the overall trend displayed by F1 is a linear increase throughout the record (Fig. 4.4a), we infer that OM source and degradation is primarily driven by relative sea level change, which is mainly responsible for increasing the transit time of OM through the water column and decreasing the input of terrestrial OM and lithogenic ballast to the core site. Secondarily, F1 reflects the take-over of siliceous versus calcareous phytoplankton since the end of the LG period.

4.5.3.2.2. PCA factor 2: High flux of (degraded) terrestrial OM

This factor is characterized by positive loadings of GABA and BALA which likely derive from enhanced flux of degraded terrestrial OM, as discussed in the previous section.

Negative loadings of F2 are composed by the amino acids ALA, THR and ASP. The amino acid ALA is among the major components of living plankton (Ingalls et al., 2003) and is an abundant amino acid in bacterial peptidoglycan cell walls (Schleifer and Kandler, 1972; Vollmer, 2015). The enrichment of ALA with particle diagenesis has been previously observed in the water column of the Equatorial Pacific (Lee et al., 2000), likely as the result of microbial biomass formation. THR and ASP are also found in living plankton as part of the protein templates of silica (THR) and carbonate (ASP) matrices (King, 1977). Therefore they become progressively enriched with depth as OM is remineralized and not-bound amino acids are preferentially degraded (Ingalls et al., 2003). Thus, negative scores of F2 are interpreted to reflect a predominance of degraded marine OM deposited under periods of low terrestrial flux.

The trend displayed by F2 (Fig. 4.4b) supports the conclusions based on bulk proxies that high flux of degraded terrestrial OM mainly occurred during periods of closest proximity to the shoreline (before 15 ka BP) and under maximum summer monsoon strength (EHCO).

4.6. Summary and Conclusions

The organic carbon accumulation rate in the NBoB was considerably high towards the LG period (387 ± 47 mg OC cm^{-2} ka^{-1}; $17-18$ ka BP) and comparable to that of the Arabian Sea and other upwelling areas in glacial times. The situation changed drastically during the deglaciation and the Holocene, when organic carbon accumulation rates dropped dramatically (about 300 mg OC cm^{-2} ka^{-1} less than during the LG period) mainly due to the disconnection of the Eastern Bengal Slope from the river mouth. Thus, the role played by the NBoB, and likely other river connected margins, on global carbon sequestration during low relative sea level is more important than previously thought and requires further investigation.

Over the last 18 ka, the sources and preservation of OM at site 342KL were driven by the following factors: (a) relative sea level, which determined the spatial connection between the Eastern Bengal Shelf and the river mouth, (b) summer monsoon strength, which determined runoff

intensity, the extension of the freshwater plume, cloud cover over the NBoB, and the delivery of nutrients to the photic zone, and (c) the availability of fluvial-discharged lithogenic particles to serve as ballast for rapid deposition of OM in the ocean. Throughout the record we observed two main gradients: (1) a shift from high to low terrestrial OM contribution from the LG to the Holocene, and (2) a shift from a calcareous-dominated to a siliceous-dominated marine plankton community. Marine primary production was stimulated during periods of enhanced summer monsoon activity due to high delivery of nutrients to the photic zone, both by cyclonic-eddy pumping of subsurface waters and fluvial discharge. The export from the photic zone and preservation of OM through the water column was largely promoted by the ballasting effect of lithogenic particles during periods of high coastal proximity and/or enhanced fluvial discharge. The characteristics and boundary conditions of the high organic matter accumulation periods LG, B/A and EHCO are summarized in the following paragraphs and Fig. 4.7. For comparison, the MLH, which represents the modern setting, characterized by low OM accumulation, is included.
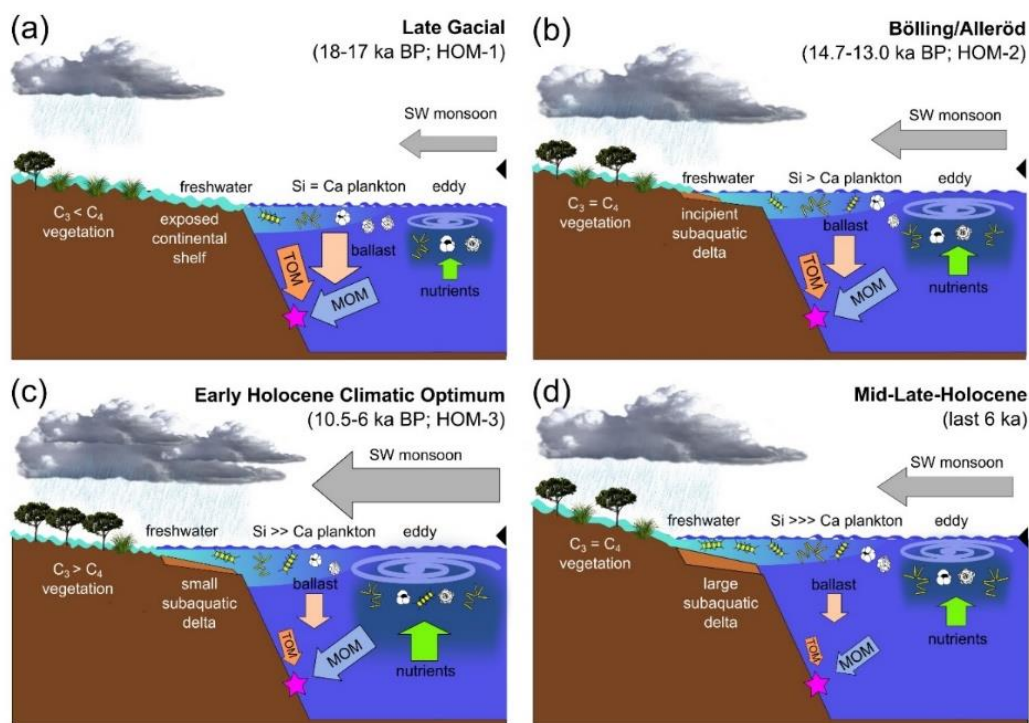
Fig. 4.7. Synoptic sketch illustrating processes affecting organic matter accumulation in the NBoB during relevant periods of the last 18 ka. The location of core SO188-342KL in the Eastern Bengal Slope is marked with a pink star.

Calcareous plankton is presented in white color; siliceous plankton is presented in yellow color. The black arrowhead at the right of each panel represents modern sea level. Magnitudes are not to scale. For detailed explanation of the different scenarios see section 4.6 of the main text. Abbreviations stand for: ka BP, thousands of years before the present; HOM, period of high organic matter accumulation; SW, southwest; TOM, Terrestrial Organic Matter; MOM, Marine Organic Matter.

Late Glacial (HOM-1; Fig. 4.7a): The summer monsoon showed minimum intensity. Eustatic sea level was approximately 120 m lower than at present and there was a direct connection between the Eastern Bengal Slope and the river mouth. Sediment and OM accumulation at site 342 KL was maximum. Large amounts of highly degraded terrestrial OM and lithogenic particles were delivered to the NBoB. Preservation of marine OM was very good due to the ballasting effect of lithogenic particles. Eddy-driven marine productivity was relatively low. Calcareous marine producers were as abundant as siliceous producers or maybe even dominant.

Bölling/Alleröd (HOM-2; Fig. 4.7b): The summer monsoon intensified and eustatic sea level rose rapidly during MWP1-A. The connection between the Eastern Bengal Slope and the paleo-river mouth was progressively weakened and marked the start of a subaqueous delta formation and sediment trapping on the Bay of Bengal Shelf. Terrestrial OM and lithogenic particle input began to decrease although it was still considerably large. Eddy-driven productivity strengthened. Marine OM preservation was good during the B/A due to the high availability of lithogenic particles and enhanced surface marine productivity. Siliceous producers started replacing calcareous producers across the NBoB due to larger supply of dissolved silica by fluvial discharge.

Early Holocene Climatic Optimum (HOM-3; Fig. 4.7c): The summer monsoon experienced maximum intensity and eustatic sea level approached its maximum and stabilized around 7 ka BP. Rapid aggradation of the subaerial delta trapped massive amounts of sediment. Terrestrial OM and lithogenic particle input to the core site was very high due to massive fluvial discharge. Marine productivity increased considerably due to enhanced eddy nutrient pumping and fluvial nutrient delivery, but was also partially hindered under maximum monsoon strength due to extreme freshening of the NBoB surface, high turbidity of the river plume and enhanced cloud cover. Preservation of marine OM was very good due to the ballasting effect of lithogenic particles. Siliceous producers became dominant.

Middle to Late Holocene (Fig. 4.7d): The summer monsoon intensity decreased and eustatic sea level reached its maximum. This marked the start of the subaerial delta progradation and formation of the modern subaqueous delta. Sedimentation at the core site became hemipelagic and terrestrial OM and lithogenic particle input became minimal. Eddy-driven marine productivity became weaker. Preservation of marine OM was reduced along with the availability of lithogenic ballasting particles. Siliceous producers remained dominant.

Acknowledgements

Appendix

Table A4.1. Relative molar composition (mol %) of total hydrolysable amino acids (THAA) from sediment core SO188-342KL.

Age (ka BP)	Depth (cm)	ASP	THR	SER	GLU	GLY	ALA	VAL	MET	ILE	LEU	TYR	PHE	HIS	ARG	LYS	BALA	GABA	RI	DI
0.748	5.0	12.7	5.9	6.6	8.5	17.0	8.9	4.4	0.0	2.9	4.1	0.9	2.8	1.7	3.7	5.0	1.6	1.0	1.0	-0.7
1.122	7.5	12.8	5.9	6.2	8.7	16.5	9.0	4.5	0.0	2.8	4.1	1.3	2.9	1.7	3.7	4.9	1.8	1.0	1.1	-0.4
1.496	10.0	12.7	5.8	5.9	8.7	16.2	9.0	4.4	0.0	2.9	4.2	1.6	2.9	1.8	3.7	4.9	2.0	1.1	1.1	0.0
2.372	15.0	12.5	5.8	5.9	8.6	15.9	8.9	4.3	0.0	2.9	4.3	1.3	3.0	1.8	3.7	4.9	2.2	1.0	0.9	0.2
2.837	17.5	12.4	5.8	5.8	8.6	15.9	8.9	4.4	0.0	3.0	4.3	0.9	3.0	1.8	3.7	5.0	2.2	1.0	0.9	-0.3
3.303	20.0	12.3	5.8	5.6	8.6	15.6	8.9	4.6	0.0	3.2	4.4	1.2	3.1	1.9	3.8	5.2	2.4	1.0	0.9	0.0
3.768	22.5	12.3	5.7	5.6	8.5	15.6	8.9	4.5	0.0	3.0	4.4	0.9	3.0	1.9	3.8	5.2	2.3	0.9	1.0	-0.1
4.699	27.5	12.8	5.7	5.4	8.6	15.6	9.2	4.5	0.0	2.9	4.3	1.0	3.0	1.7	3.8	5.1	2.5	0.9	0.9	-0.4
5.165	30.0	12.7	5.7	5.3	8.6	15.5	9.2	4.5	0.0	3.0	4.3	0.7	3.0	1.7	3.8	5.1	2.5	0.9	1.0	-0.6
5.523	32.5	12.6	5.7	5.3	8.7	15.4	9.0	4.4	0.0	2.9	4.3	0.9	2.9	1.7	3.9	5.1	2.6	0.9	1.1	-0.5
5.721	35.0	13.0	5.7	5.3	8.7	15.5	9.2	4.5	0.0	3.0	4.3	1.0	2.9	1.7	3.8	5.0	2.6	1.0	0.8	-0.4
6.116	40.0	12.7	5.7	5.3	8.7	15.6	8.9	4.6	0.0	3.0	4.4	1.0	2.9	1.9	3.8	5.2	2.5	1.1	0.8	-0.5
6.313	42.5	13.0	5.7	5.3	8.8	16.2	9.0	4.5	0.0	3.0	4.3	0.8	2.9	2.1	3.8	5.5	2.3	0.9	0.8	-0.4
6.511	45.0	12.5	5.6	5.0	8.6	15.4	8.9	4.8	0.0	3.0	4.2	1.4	2.9	1.7	4.0	5.2	2.7	0.8	0.8	-0.2
6.708	47.5	12.7	5.8	5.6	8.7	16.4	9.3	4.4	0.0	3.0	4.4	0.6	2.9	1.8	3.9	5.2	2.4	0.8	1.0	-1.0
6.934	50.0	12.4	5.6	5.2	8.6	15.5	9.0	4.7	0.0	3.1	4.4	1.1	3.0	1.7	3.9	5.3	2.6	0.8	1.0	-0.3
7.422	55.0	12.4	5.6	5.3	8.9	15.5	9.1	4.5	0.0	3.0	4.4	1.1	3.0	1.7	3.9	5.2	2.6	0.8	0.8	-0.3
7.667	57.5	12.6	5.6	5.1	8.8	15.0	9.0	4.6	0.0	3.0	4.3	0.8	2.9	1.7	3.9	5.3	2.7	0.7	0.7	-0.4
7.911	60.0	12.5	5.6	5.0	8.6	14.9	9.0	4.8	0.8	3.0	4.3	1.6	2.9	1.6	3.8	5.1	2.7	2.6	0.8	0.7
8.400	65.0	12.9	5.5	5.1	9.0	15.1	9.2	5.0	0.7	3.0	4.4	1.5	2.9	1.8	3.9	5.2	2.7	2.6	0.8	0.5
8.644	67.5	12.6	5.5	5.1	8.8	15.0	9.0	4.5	0.0	3.1	4.5	1.1	3.0	1.8	3.9	5.1	2.3	2.3	0.8	-0.1
8.889	70.0	12.8	5.6	5.2	9.1	15.2	9.3	5.0	0.0	3.3	4.7	1.0	3.1	1.8	3.9	5.3	2.5	2.3	0.9	-0.1
9.089	72.5	12.3	5.4	5.0	8.8	14.6	9.1	4.6	0.0	3.2	4.5	1.3	3.1	1.8	3.9	5.3	2.6	2.4	0.9	0.4
9.355	77.5	12.4	5.4	5.0	8.8	14.6	9.0	5.0	0.7	3.1	4.5	1.6	3.1	1.7	3.9	5.1	2.5	2.5	0.9	1.0
9.488	80.0	12.3	5.3	4.8	8.6	14.9	8.9	5.1	0.7	3.2	4.3	1.6	3.0	1.7	3.8	5.4	2.6	2.8	0.9	1.1
9.621	82.5	12.4	5.4	5.1	8.8	14.9	9.1	4.8	0.0	3.2	4.6	1.2	3.1	1.7	3.9	5.3	2.5	2.4	0.9	0.2
9.755	85.0	11.9	5.3	4.8	8.5	14.8	9.0	5.3	0.0	3.7	4.8	0.7	3.2	1.8	4.0	6.0	2.4	2.5	0.8	0.2
10.021	90.0	13.8	5.9	5.5	9.1	16.0	9.7	5.0	0.0	3.3	4.9	1.2	3.1	1.7	3.9	5.3	2.4	2.1	1.0	-0.6
10.154	92.5	13.9	5.9	5.5	9.3	15.7	9.8	5.0	0.0	3.3	5.0	1.3	3.2	1.7	3.9	5.5	2.3	1.8	1.1	-0.5
10.287	95.0	14.0	5.9	5.5	9.2	15.9	9.8	4.8	0.0	3.2	4.9	0.8	3.2	1.7	3.9	5.4	2.3	1.7	1.0	-0.8
10.420	97.5	13.8	5.9	5.5	9.2	15.8	9.8	4.9	0.0	3.3	5.0	1.3	3.3	1.8	4.0	5.8	2.3	1.7	1.0	-0.8
10.870	102.5	13.2	5.7	5.3	9.2	15.2	9.5	5.4	0.0	3.6	5.3	1.1	3.5	1.8	4.0	5.8	2.3	1.7	1.1	-0.1
11.460	105.0	12.8	5.7	5.2	9.2	14.6	9.5	5.5	0.0	3.7	5.4	1.0	3.6	1.7	4.0	5.8	2.3	1.9	1.1	0.1
12.050	107.5	12.9	5.6	5.2	9.0	14.8	9.5	5.5	0.0	3.6	5.3	0.9	3.6	1.7	4.0	5.9	2.5	1.9	1.1	0.1
12.641	110.0	12.8	5.5	5.5	9.0	14.7	9.3	6.1	0.0	4.1	5.4	0.9	3.6	1.7	4.1	6.2	2.4	2.5	0.9	0.2
13.155	115.0	13.5	5.5	4.8	9.4	14.6	9.3	5.4	0.0	3.6	5.2	1.6	3.4	1.6	4.1	6.0	2.6	2.6	1.0	0.3
13.269	117.5	13.6	5.7	5.0	9.4	14.8	9.4	5.2	0.0	3.4	5.1	0.9	3.4	1.7	4.1	5.9	2.2	2.6	0.9	-0.4
13.384	120.0	13.7	5.7	5.0	9.7	14.4	9.2	5.2	0.0	3.5	5.0	1.0	3.4	1.6	4.0	5.9	2.2	2.4	1.0	0.2
13.498	122.5	13.4	5.6	5.1	9.6	14.5	9.4	5.3	0.0	3.5	5.2	1.2	3.4	1.6	4.0	5.9	2.4	2.0	1.0	0.2
13.727	127.5	13.2	5.5	5.1	9.8	14.4	9.4	5.3	0.0	3.3	5.2	1.3	3.4	1.6	3.9	5.8	2.5	2.0	1.0	0.3
13.841	130.0	13.7	5.8	4.8	9.9	14.4	9.6	6.1	0.0	3.3	5.0	0.7	3.4	1.6	3.9	5.7	1.9	2.6	1.1	-0.1
13.956	132.5	13.7	5.8	4.9	9.6	14.3	9.3	5.2	0.0	3.5	5.0	1.1	3.4	1.7	4.1	6.1	2.7	2.4	0.9	-0.2
14.070	135.0	13.7	5.5	4.9	9.7	14.6	9.4	5.2	0.0	3.5	5.0	1.0	3.4	1.7	4.1	6.0	2.6	2.4	0.9	-0.2
14.299	140.0	13.6	5.6	4.9	9.7	14.0	9.2	4.7	0.0	3.4	4.1	1.7	3.2	1.6	3.8	5.9	2.6	2.9	0.9	-0.2
14.413	142.5	13.0	5.6	5.2	9.7	14.2	9.3	4.9	0.0	3.4	5.0	1.3	3.3	1.6	3.8	5.7	2.8	2.2	0.9	0.4
14.527	145.0	13.2	5.6	4.9	9.7	14.2	9.2	4.7	0.0	3.3	4.9	1.4	3.4	1.6	3.8	5.6	2.7	2.1	1.0	0.4
14.642	147.5	13.4	5.6	5.0	9.6	13.9	9.2	4.3	0.0	3.2	4.9	1.5	3.4	1.5	3.8	5.6	2.7	2.0	1.0	0.5
14.870	152.5	14.1	5.5	3.9	9.9	15.2	9.4	5.1	0.0	3.4	4.7	0.9	3.2	1.4	3.9	5.6	2.7	2.0	0.8	-0.6
14.985	155.0	12.8	5.4	4.6	9.5	13.8	9.0	5.6	0.0	3.4	4.7	1.4	3.3	1.6	3.9	6.2	2.7	2.9	0.8	0.8
15.099	157.5	13.1	5.4	4.7	9.4	13.6	8.9	5.6	0.0	3.9	5.1	0.9	3.4	0.9	3.9	6.2	2.9	3.0	0.7	0.5
15.268	160.0	14.0	5.6	5.1	9.9	15.3	9.3	5.2	0.0	3.5	4.7	0.4	3.2	0.3	3.9	6.0	2.7	2.8	0.6	-1.5
15.607	165.0	13.4	5.5	4.6	9.4	13.9	9.0	5.6	0.0	3.5	5.1	1.4	3.4	1.5	3.9	6.6	3.0	3.3	0.8	0.6
15.777	167.5	12.8	5.3	4.5	9.3	14.0	9.0	5.5	0.0	3.9	5.0	1.4	3.4	1.6	3.9	6.3	2.9	3.3	0.8	0.7
15.946	170.0	12.9	5.3	4.5	9.3	13.6	8.9	5.5	0.0	3.9	5.0	1.0	3.3	1.6	3.9	6.3	2.9	3.3	0.8	-0.1
16.116	172.5	13.1	5.3	4.6	9.5	13.7	8.8	5.3	0.0	3.7	4.8	1.0	3.3	1.5	3.9	6.4	3.1	3.4	0.7	0.7
16.454	177.5	13.0	5.3	4.7	9.5	13.7	8.9	5.4	0.0	3.7	4.8	1.0	3.2	1.5	3.9	6.4	3.1	3.4	0.7	0.3
16.624	180.0	13.1	5.2	4.5	9.3	13.3	8.8	5.6	0.0	3.8	4.9	1.4	3.2	1.5	4.0	6.4	3.0	3.3	0.8	0.6
16.793	182.5	13.2	5.3	4.6	9.4	13.5	8.8	5.5	0.0	3.9	5.0	1.4	3.3	1.4	3.9	6.3	3.2	3.6	0.7	0.6
16.963	185.0	13.2	5.3	4.3	9.6	13.5	8.9	5.8	0.0	3.9	5.0	1.4	3.4	1.4	3.8	6.6	3.1	3.5	0.7	0.8
17.078	190.0	13.0	5.3	4.3	9.4	13.6	8.9	5.7	0.0	3.9	4.9	1.2	3.1	1.5	3.9	6.7	3.1	3.4	0.7	0.4
17.124	192.5	13.7	5.4	4.7	9.7	14.5	9.3	5.4	0.0	3.5	4.6	0.9	3.2	1.3	3.8	6.3	3.1	3.2	0.6	-0.2
17.169	195.0	13.7	5.4	4.6	9.6	14.4	9.2	5.4	0.0	3.6	4.6	0.7	3.1	1.3	3.7	6.4	3.1	3.2	0.6	-0.2
17.215	197.5	14.2	5.5	3.9	10.0	14.8	9.3	5.5	0.0	3.7	4.8	0.6	3.2	1.2	3.8	6.4	3.0	3.2	0.6	-0.6

Chapter 5

Precipitation and vegetation history in Southeast China and Taiwan throughout the Holocene: links between Asian Summer Monsoon strength and tropical cyclone activity

Contreras-Rosales, L.A. [1,2], Jennerjahn, T.[1], Schefuß, E.[2]

[1] ZMT- Leibniz Center for Tropical Marine Ecology, 28359 Bremen, Germany.

[2] MARUM- Center for Marine Environmental Sciences, University of Bremen, D-28359 Bremen, Germany.

Abstract

Two marine sediment cores (MD05-2905 and GeoB16601-5) from the Northern South China Sea (NSCS) were retrieved to create composite records of paleo-vegetation composition and paleo-precipitation variability over Southeast China (Pearl River basin) and Taiwan for last 11.2 thousand years (11.2 ka) based on the carbon and hydrogen stable isotopic composition of higher-plant-wax n-alkane biomarkers ($\delta^{13}C_{alkanes}$ and $\delta D_{alkanes}$). The compatibility between the two sediment cores to construct composite records was established based on the match of bulk and biomarker proxies. The $\delta^{13}C_{alkanes}$ record indicates a an overall predominance of C_3 vegetation under (semi-) moist conditions throughout the last 11.2 ka, with higher representation of herbs and grass vegetation during the Early Holocene related to larger expansion of the coastal plains over the exposed continental shelf before 8 ka BP due to lower eustatic sea level, and higher representation of arboreal vegetation following the drowning of the shelf after 8 ka BP. The variability in the isotopic composition of the $\delta D_{alkanes}$ record is regarded in function of changes in

the relative contribution of different moisture sources and sea level change. Lower eustatic sea level before 8 ka BP likely contributed to an enhanced continental effect on precipitation isotopic composition resulting in minimum $\delta D_{alkanes}$ values. South Asian summer monsoon moisture contribution to Southeast China and Taiwan was associated to more positive $\delta D_{alkanes}$ values between 9 and 2 ka BP, whereas moisture contribution from the Pacific Ocean in the shape of tropical cyclones was associated to more negative $\delta D_{alkanes}$ values before 9 ka BP and after 2 ka BP. We proposed enhanced tropical cyclone activity over South China due to a warming background warming state of the Indo Pacific Warm Pool (IPWP) during the Early Holocene and an enhanced tropical cyclone activity over Taiwan derived from a cooling background state of the IPWP during the Late Holocene. In general, a warming IPWP was related to summer monsoon circulation strengthening whereas a cooling IPWP was related to summer monsoon circulation weakening. This study highlights the high sensitivity of paleo-climatic records from the region around the Northern South China Sea regarding the variability of background boundary conditions.

Keywords

Northern South China Sea; paleo-precipitation; paleo-vegetation; *n*-alkanes; South China; Taiwan; Pearl River; Asian Summer Monsoon; tropical cyclones; Indo Pacific Warm Pool.

5.1. Introduction

Located to the south of China in the East Asian Monsoon domain, the South China Sea (SCS) is the largest marginal sea in Asia (Liu et al., 2016) and its morphology has been largely affected by sea level rise since the end of the Last Glacial Period until the Middle Holocene (Liu et al., 2016). Besides, the SCS is located in the neighbourhood of the Indo-Pacific Warm Pool (IPWP), an area of high sea surface temperature (SST $\geq$ 28.5 °C) which is key regulator of ocean-atmosphere interactions that influence Asian Monsoon circulation, tropical cyclone activity and El Niño Southern Oscillation (ENSO) events in the Western North Pacific Ocean (Conroy et al., 2008; Linsley et al., 2010; Moy et al., 2002).

Atmospheric circulation patterns of the summer and winter monsoons over Asia dominate seasonal wind, precipitation and run-off intensity, all of which largely determine the character of

land vegetation cover (Lau and Yang, 1997; Webster et al., 1998). The organic matter transported by rivers to the ocean contains information about biological and ecological processes linked to organisms living over land and thus, with the aid of biomarker compounds, we can retrieve specific information from specific organisms to study these processes. Such is the case of long-chain n-alkanes, which are hydrocarbon compounds produced by higher plants as part of their protective leaf waxes. The analysis of the stable isotopic composition of hydrogen (δD) and carbon ($\delta^{13}C$) in long-chain n-alkanes has previously rendered valuable information about changes in precipitation and vegetation patterns on land in other monsoonal regions over millennial time-scales (e.g. (Collins et al., 2011; Contreras-Rosales et al., 2014; Schefuß et al., 2005; Thomas et al., 2014). The region of South China is drained by the Pearl River (Zhu Jiang) which is the third largest river in China (Dong et al., 2004) whereas southern Taiwan is drained by numerous small mountainous rivers (Milliman and Kao, 2005), and all of these rivers debouch into the Norther South China Sea (NSCS) transporting to the ocean large amounts of terrigenous organic matter. Thus, it is to be expected that variations in natural on-land precipitation and vegetation patterns captured in the terrigenous organic matter exported by rivers around the NSCS would capture background changes in monsoon atmospheric circulation and typhoon activity at a regional scale, and that these would be in turn directly or indirectly recorded in marine sediment archives.

In this line, the general objectives of this study are: (1) to analyze the effects of eustatic sea level change throughout the Holocene on the variability in terrigenous sediment sources to the NSCS based on the bulk organic matter composition (TOC %, TN %, $\delta^{13}C_{TOC}$, $\delta^{15}N_{TN}$) and terrestrial n-alkane biomarkers composition (ACL, CPI, $\delta^{13}C$, δD) of two marine sediment cores (MD05-2905 and GeoB16601-5)from the NSCS continental slope; (2) to reconstruct a continuous history of on-land paleo-vegetation and paleo-precipitation around the NSCS throughout the Holocene (last 11.2 ka) based on composite records of compound-specific $\delta^{13}C$ and δD composition of long-chain n-alkanes (n-C_{29} and n-C_{31}) from cores MD05-2905 and GeoB16601-5; (3) to elucidate the interactions between Asian Monsoon circulation and tropical cyclone activity in the East Asian climate throughout the Holocene.

5.2. Study area

The NSCS is located in the area of oceanic and climatic interaction between the Pacific and the Indian oceans (He et al., 1992), and oceanic surface circulation in the region is dominated by seasonal monsoon winds (Q. Liu et al., 2008). From November to February, winter monsoon winds blow from the Asian landmass bearing cold-dry air into the SCS. Winter monsoon winds induce basin-wide cyclonic surface circulation with southwestward water flow powered by northeast wind stress. From June to August, wind reversion originates summer monsoon winds blowing from the SCS into the Asian landmass bringing warm-moist air from the Western Equatorial Pacific and Eastern Indian Ocean. The basin-wide surface circulation becomes anticyclonic with northeastward water flow powered by south and southeast wind stress. During summer months, the SW-to-NE winds may induce upwelling along the Chinese margin, enhancing surface water primary productivity (H. Liu et al., 2011). In addition to monsoon-driven surface circulation, a permanent surface water intrusion from the Western North Pacific Ocean into the NSCS through the Luzon Strait occurs as a detachment of the northward flowing Kuroshio Current. The main path of this detached current flows from northeast Luzon towards southwest Taiwan and deflects westward flowing along the NSCS shelf break (J. Liu et al., 2011, 2010b; Liu et al., 2016; Zhifei Liu et al., 2008).

The NSCS is significantly affected by fresh water input from the Pear River (Zhu Jiang) which modifies the oceanographic conditions inducing estuarine circulation and seasonal stratification, especially during the rainy season (Dong et al., 2004). Total annual precipitation in Southeast China ranges between 900 and 3300 mm, depending on the region, with highest amounts from May to September (Global Network for Isotopes in Precipitation; GNIP; IAEA/WMO, 2015). The Pearl River catchment area is about 442 x 10^3 km^2 in size (Fig. 5.1b), with a modern delta area of ca. 17,200 km2 (Weng, 2007). The total water discharge has been estimated on 330 km^3 yr^{-1} and the annual suspended sediment load on around 80 Mt (Zhao, 1990). Natural vegetation in the basin includes evergreen broad-leaf forests (*Castanopsis*, Theaceae, Lauraceae), while above 1200 m upper montane rain forests (*Podocarpus, Cyclobalanopsis, Betula*) appear, with the furthest NW reaches of the river basin dominated by conifer forests (*Tsuga*) (Wu, 1980). Earliest evidence of rice cultivation in Fujian and Guangdong provinces dates back to ca. 5000 BP (Zhang and Hung, 2010). Modern land-use activities within the river basin include paddy rice cultivation, sugarcane cultivation, fruit horticulture, and dike pond-agriculture aquaculture in the delta area (Weng,

2007). Deep-sea pollen records from the NSCS indicate that throughout the Holocene, the wild vegetation in South China has been similar to that observed in the present (Sun and Li, 1999).

In addition to the Pearl River efflux, the NSCS also receives large fluvial discharge from small mountainous rivers in Taiwan, an island that combines high elevations, soft rocks, frequent earthquakes, typhoons and heavy monsoon rainfalls which produce very high denudation rates and fluvial sediment loads (Li, 1976; Milliman and Kao, 2005; Milliman and Syvitski, 1992).

5.3. Materials and Methods

5.3.1. Core collection and age model

The CASQ core MD05-2905 (20° 08.17' N, 117° 21.61' E; 1647 m water depth; 11.94 m core length; Fig. 5.1) was collected on board of the RV *Marion Dufresne* during the Marco Polo IMAGES XII campaign in May-June 2005. After collection, the core was stored at 4 °C and transported to the State Key Laboratory of Marine Geology at Tongji University, China, for sampling. The core was sliced at 1 cm resolution and a total of 266 samples (taken every other centimeter) from the upper 5 m of the core were transported to the Leibniz Center for Tropical Marine Ecology (ZMT, Bremen, Germany) and the Center for Marine Environmental Sciences (MARUM, University of Bremen, Germany) for analysis. The calibrated age model of core MD05-2905 (hereafter 2905) was constructed and published by Yang et al. (2008) on the basis of 14 AMS-radiocarbon ages obtained from the planktic foraminiferal species *Globigerinoides ruber* (white) and *Globigerinoides sacculifer* and calibrated with the program CALIB 5.0 (Stuiver and Reimer, CALIB Radiocarbon Calibration package, http://calib.qub.ac.uk/calib/). The ages are reported in thousands of years before the present (ka BP), where the present is set to AD 1950.

The short marine sediment core GeoB16601-5 (20° 09.04' N, 116° 14.41' E; 1013 m water depth; 38 cm core length) was retrieved with a multi-corer during the RV *Sonne* cruise SO-221 in May-June 2012, in order to expand the time-span of the MD05-2905 records towards the present. Its location is approximately 100 km to the west of core 2905. The GeoB16601-5 core (hereafter 16601-5) was split on board the ship into 38 samples of 1 cm resolution and stored in Petri dishes at 4 °C during its transport to the ZMT and the MARUM for analysis. Three AMS-radiocarbon dates were obtained for the top, middle and bottom of core 16601-5 from specimens of the planktic

foraminifera *Globigerinoides ruber* and calibrated with the program CALIB 7.0 (online version; access date 04-December-2014; Stuiver and Reimer, CALIB Radiocarbon Calibration package, http://calib.qub.ac.uk/calib/) following the same method as with core 2905. A reservoir age of 375 years was considered for the calibration, based on the reported local reservoir age of -25 years for the central South China Sea and the global marine reservoir age of 400 years (Southon et al., 2002). The ages are reported in thousands of years before the present (ka BP) and the present is set to AD 1950 (Table 5.1).

Table 5.1. Radiocarbon and calibrated ages obtained from *Globigerinoides ruber* planktic foraminifera from sediment core GeoB16601-5. Mean calibrated ages were used to construct the age model of this core. The online version of the program CALIB 7.0 was used, with access date of 04-December-2014.

| Sample Name | Lab Code | Radiocarbon Age | | | CALIB 7.0 Calibrated Age (95.4 % area, 2 sigma) [calBP(0=AD1950)] | | | |
		Depth (cm)	^{14}C-age (years BP)	± SD (years)	Max. Age (years BP)	Min. Age (years BP)	Mean Age (years BP)	± SD (years)
GeoB16601-5 0-1cm	UCIAMS-133831	0.5	0	20				
GeoB16601-5 17-18cm	UCIAMS-133832	17.5	1345	20	824	989	906.5	116.7
GeoB16601-5 35-36cm	UCIAMS-133833	35.5	2360	20	1922	2109	2015.5	132.2
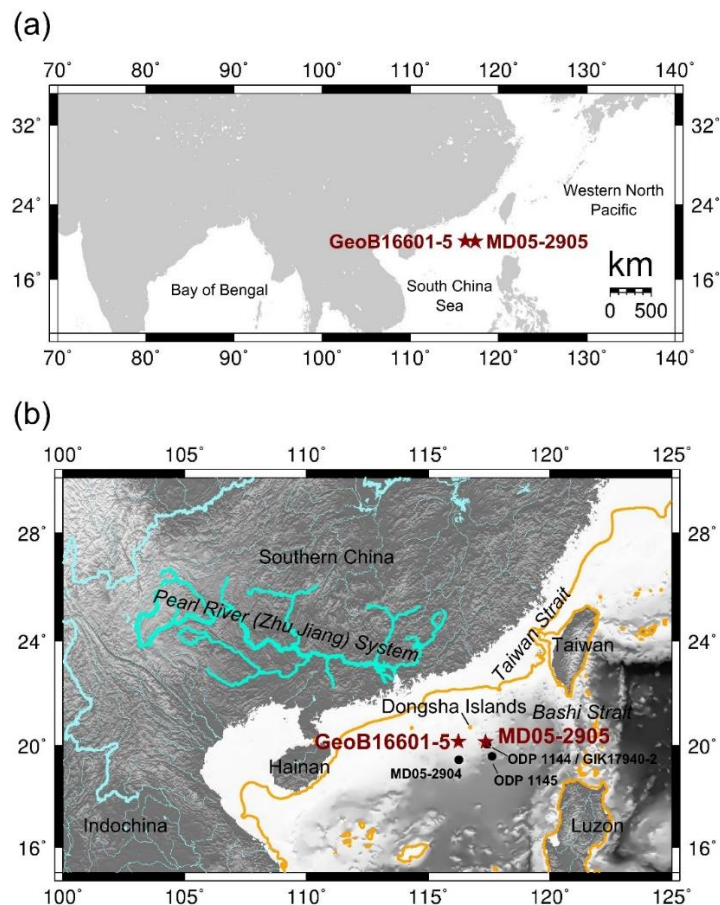
Fig. 5.1. Maps of South Asia and the Northern South China Sea showing core locations and location of other records mentioned in the text. **(a)** Map of South Asia showing the location of sediment cores MD05-2905 and GeoB16601-5. **(b)** Map of the Northern South China Sea area with the location of cores MD05-2905 and GeoB16601-5 (red stars; this study) and neighboring cores ODP1145, ODP1144, GIK17940-2 and Dongge Cave. Major rivers are shown in blue; the Pearl River (Zhu Jiang) system is shown in darker blue. The -58 m isobath (orange line) is shown as reference for the approximate coastline around 11.2 ka BP.

5.3.2. Biogeochemical analyses

5.3.2.1. Bulk analyses

Analysis of bulk parameters was performed to understand the sediment sources of both cores throughout the study period and to evaluate their compatibility for the construction of composite records. To this end, total organic carbon (TOC) and total nitrogen (TN) contents, as well as the stable isotopic composition of total organic carbon ($\delta^{13}C_{TOC}$) were measured.

Sediment samples were transferred to pre-combusted glass vials and dried at 40 °C in a continuous circulation oven. Dried samples were homogenized by grinding in a planetary mill. For determination of total carbon and total nitrogen content, homogenized sediment samples were analyzed with a Euro EA 3000 elemental analyzer. TOC content was measured after removal of carbonate from the samples, by the addition of a 1N HCl solution and subsequent drying at 40 °C. TOC and TN are reported as % of bulk dry weight. Repeated measurements of selected samples yielded an average precision of ± 0.004 % for TOC and ± 0.001 % for TN. The $\delta^{15}N_{TN}$ was determined from homogenized samples with the aid of a Thermo Finningan Delta Plus gas isotope ratio mass spectrometer by high-temperature combustion in a Flash 1112 EA elemental analyzer. $\delta^{15}N_{TN}$ values are reported as a per mil (‰) deviation from the nitrogen isotopic composition of atmospheric air. Repeated measurements of selected samples yielded an analytical average precision of ± 0.08 ‰ for $\delta^{15}N_{TN}$. The $\delta^{13}C_{TOC}$ was determined following the same procedure as for $\delta^{15}N_{TN}$ after the removal of carbonates from the sample by the addition of 1N HCl solution and subsequent drying at 40 °C. $\delta^{13}C_{TOC}$ values are reported as a ‰ deviation from the carbon isotope composition of the Vienna Pee Dee Belemnite (VPDB) standard. Repeated measurements of selected samples yielded an analytical average precision of ± 0.13 ‰.

5.3.2.3. n-alkanes biomarker analyses

For the recovery of *n*-alkanes from the bulk samples, sediments were extracted with a DIONEX accelerated solvent extractor (ASE) using dichloromethane:methanol (DCM:MeOH; 9:1 v/v). Squalene was added before the extraction as an internal standard. After rotary evaporation, samples were dried on a small column of Na_2SO_4 with hexane and DCM as eluents. Extracts were later saponified by the addition of a 6% KOH solution in MeOH for the hydrolysis of ester bonds. The resulting extracts were further separated into apolar, keto and polar fractions in a chromatographic column of pre-combusted silica (Si) with the successive addition of pure hexane, pure DCM and DCM:MeOH (1:1 v/v) as eluents. Unsaturated components from the apolar fraction were separated by gas chromatography (GC), the compounds were eluted with hexane through an $AgNO_3$-Si column. Concentration of *n*-alkanes in the samples was determined by the integration of the areas under the chromatogram peak areas calibrated against the external standard composed of a mix of several *n*-alkanes with known concentrations. Repeated measurements of the external standard

yielded a quantification uncertainty of < 5 %. The carbon preference index (CPI; Bray and Evans, 1961) of the long-chain (C_{23}-C_{35}) *n*-alkanes, was used as a source indicator, since terrestrial higher plants are characterized by values >4 and petroleum ~1 (Collister et al., 1994; Killops and Killops, 2005), whereas the average chain length (ACL; Gagosian and Peltzer, 1986) was used as indicator for the most abundant compounds of the alkane mix. Samples with CPI values < 2 and the presence of an unresolved complex mixture hump in the chromatogram baseline were discarded due to the suspicion of contamination with petroleum-derived hydrocarbons. Oil contamination of surface sediments in the NSCS has been previously reported (Gao et al., 2007), likely derived from anthropogenic activities.

Hydrogen isotopic composition of *n*-alkanes ($\delta D_{alkanes}$) was analyzed on a Thermo Trace GC Ultra coupled via pyrolisis reactor to a Finnigan MAT 253 mass spectrometer. Isotope values were measured against calibrated H_2 reference gas. $\delta D_{alkanes}$ values are reported in ‰ notation against the Vienna Standard Mean Ocean Water (VSMOW). Repeated measurements of selected samples yielded an analytical average precision of ± 0.08 ‰. Measured δD values were corrected for changes in global ice volume as described in (Contreras-Rosales et al., 2014; Chapter 3). Carbon isotopic composition of *n*-alkanes ($\delta^{13}C_{alkanes}$) was determined with the aid of a Thermo Trace GC Ultra coupled via combustion reactor to a Finnigan MAT 252 mass spectrometer. Isotope values were measured against calibrated CO_2 reference gas. $\delta^{13}C_{alkanes}$ are reported in ‰ notation against the VPDB standard. Repeated measurements of selected samples yielded an analytical average precision of ± 0.14 ‰.

5.4. Results

5.4.1. Linear sedimentation rates

Linear sedimentation rate (LSR) values for cores 2905 and 16601-5 are shown in Fig. 5.2a. For core 2905, the calibrated age at the bottom of the section is 11.213 ka BP whereas that at the top is 2.356 ka BP, with average time resolution between samples of 36 ± 10 years and LSR between 43–97 cm ka^{-1}. For core 16601-5, the calibrated age at the bottom of the sequence is 2.139 ka BP and that at the top is 0 ka BP. The average time resolution between samples is 58 ± 4 years and the LSR between 16–19 cm ka^{-1}.
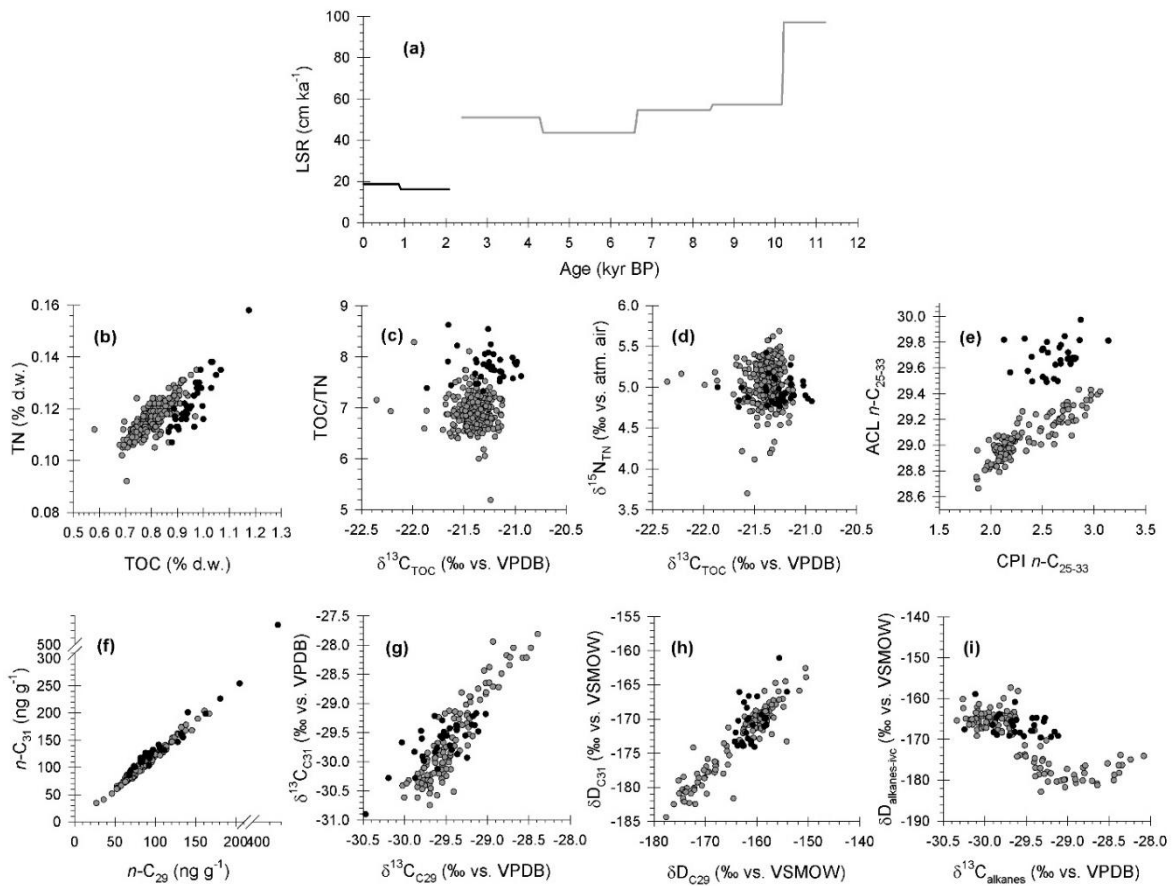
Fig. 5.2. Comparison of bulk and biomarker parameters between cores MD05-2905 and GeoB16601-5. **(a)** Bulk linear sedimentation rate (LSR) of cores MD05-2905 (gray line) and GeoB16601-5 (black line). **(b-i)** Cross plots of bulk and *n*-alkane biomarker parameters from cores MD05-2905 (gray dots) and GeoB16601-5 (black dots): **(b)** Total organic carbon dry-weight percentage (TOC % d.w.) versus total nitrogen dry-weight percentage (TN % d.w.); **(c)** stable carbon isotopic composition of bulk total organic carbon ($\delta^{13}C_{TOC}$) versus bulk total organic carbon to bulk total nitrogen ratio (TOC/TN); **(d)** stable carbon isotopic composition of bulk total organic carbon ($\delta^{13}C_{TOC}$) versus stable nitrogen isotopic composition of bulk total nitrogen ($\delta^{15}N_{TN}$); **(e)** Carbon Preference Index of odd-long-chain *n*-alkanes between 25 and 33 carbon atoms (CPI *n*-C$_{25-33}$) versus Average Chain Length of odd *n*-C$_{25}$ to *n*-C$_{33}$ alkanes (ACL *n*-C$_{25-33}$); **(f)** dry sediment concentration of the *n*-C$_{29}$ and *n*-C$_{33}$ alkanes; **(g)** stable carbon isotopic composition of the *n*-C$_{29}$ versus that of the *n*-C$_{33}$ alkanes ($\delta^{13}C_{C29}$ and $\delta^{13}C_{C33}$); **(h)** stable hydrogen isotopic composition of the *n*-C$_{29}$ versus that of the *n*-C$_{33}$ alkanes (δD_{C29} and δD_{C33}); **(i)** weighted-average of measured stable carbon isotopic composition of the *n*-C$_{29}$ and *n*-C$_{33}$ alkanes ($\delta^{13}C_{alkanes}$) versus weighted average of ice-volume-corrected hydrogen isotopic composition of the *n*-C$_{29}$ and *n*-C$_{33}$ alkanes ($\delta D_{alkanes-ivc}$).

5.4.2. Core 2905: bulk parameters and n-alkane biomarkers

The TOC content fluctuated between 0.09 % and 0.97 %, while TN ranged between 0.09 % and 0.14 %. Both TOC and TN displayed a highly significant positive correlation ($r = 0.81$, $p < 0.001$, $n = 247$; Fig. 5.2b) and the TOC/TN ratio ranged between 5.2 and 8.3 (Fig. 5.2c). $\delta^{13}C_{TOC}$ values ranged between -22.4 ‰ and -21.1 ‰ and $\delta^{15}N_{TN}$ values ranged between 3.7 ‰ and 5.7 ‰ (Fig. 5.2d). Total odd long-chain alkane (odd n-C_{25} to n-C_{33}) sediment concentrations ranged between 87 and 485 ng g^{-1} (average 204 ± 56 ng g^{-1}). The CPI values ranged between 1.9 and 3.1 (Fig. 5.2e), and down-core ACL varied between 28.7 and 29.4 carbon atoms (Fig. 5.2e). Due to the suspicion of contamination with petroleum-derived hydrocarbons four samples at the top of this core were discarded. The C_{29} and C_{31} n-alkanes, had the highest abundances of all long chain n-alkanes, with individual sedimentary concentrations between 27 to 166 ng g^{-1} for n-C_{29} and 34 to 219 ng g^{-1} for n-C_{31} (Fig. 5.2f), and total combined concentration between 42 and 241 ng g^{-1}. Measured compound-specific $\delta^{13}C$ of the n-C_{29} ranged between -30.0 ‰ and -28.4 ‰, and that of n-C_{31} ranged between -30.7 ‰ and -27.8 ‰ (Fig. 5.2g). Average-weighted stable carbon isotopic composition of the n-C29 and n-C31 alkanes ($\delta^{13}C_{alkanes}$) ranged between -30.4 ‰ and -28.0 ‰ (Fig. 5.2i). Measured compound-specific δD of the n-C_{29} ranged between -178 ‰ and -143 ‰, while that of n-C_{31} ranged between -184 ‰ and -143 ‰ (Fig. 5.2h). Average-weighted ice-volume-corrected stable carbon isotopic composition of the n-C29 and n-C31 alkanes ($\delta D_{alkanes-ivc}$; Fig. 5.2i) ranged between -183 ‰ and -143 ‰.

5.4.3. Core 16601-5: bulk parameters and n-alkane biomarkers

The TOC content ranged between 0.87 % and 1.18 % while TN ranged between 0.11 % and 0.16 %. TOC and TN contents also displayed a highly significant positive correlation ($r = 0.89$, $p < 0.001$, $n = 38$; Fig. 5.2b) and the TOC/TN ratio ranged between 7.3 and 8.6 (Fig. 5.2c). The $\delta^{13}C_{TOC}$ values were between -21.8 ‰ and -20.9 ‰ and the $\delta^{15}N_{TN}$ values were between 3.7 ‰ and 5.7 ‰ (Fig. 5.2d). Total odd long-chain alkane (odd n-C_{25} to n-C_{33}) sediment concentrations were higher than in core 2905, and ranged between 270 and 1702 ng g^{-1} (average 204 ± 56 ng g^{-1}). The CPI values also ranged between 1.4 and 3.1 (Fig. 5.2e; average 2.5 ± 0.4), while the ACL ranged between 29.2 and 30.0 carbon atoms (Fig. 5.2e; average 29.7 ± 0.1 carbon atoms). Because of the suspicion of contamination with petroleum-derived hydrocarbons, four samples at the top of the

core were discarded. The C_{29} and C_{31} n-alkanes, had again the highest abundances of all long chain n-alkanes, with sedimentary concentrations between 68 to 434 ng g^{-1} and 81 to 554 ng g^{-1}, respectively (Fig. 5.2f), and total added concentration between 150 and 989 ng g^{-1}. Measured compound-specific δ^{13}C of the n-C$_{29}$ ranged between -30.5 ‰ and -28.7 ‰, and that of n-C$_{31}$ ranged between -30.9 ‰ and -28.5 ‰ (Fig. 5.2g). Average-weighted stable carbon isotopic composition of the n-C$_{29}$ and n-C$_{31}$ alkanes (δ^{13}C$_{alkanes}$) ranged between -30.8 ‰ and -28.6 ‰ (Fig. 5.2i). Measured compound-specific δD of the n-C$_{29}$ ranged between -164 ‰ and -148 ‰, while that of n-C$_{31}$ ranged between -174 ‰ and -155 ‰ (Fig. 5.2h). Average-weighted ice-volume-corrected stable carbon isotopic composition of the n-C$_{29}$ and n-C$_{31}$ alkanes (δD$_{alkanes-ivc}$) ranged between -170 ‰ and -152 ‰ (Fig. 5.2i).

5.5. Discussion

5.5.1. Terrigenous sediment sources to the northern South China Sea continental slope

Terrigenous sediment input to the NSCS is considered predominantly of fluvial origin with marginal importance of eolian supply, estimated in max. 5 % to the northeastern slope (Boulay et al., 2007). River-born sediment dispersal in surface waters of the NSCS varies seasonally due to the reversion of marine circulation by monsoon winds. Sediments from South China are primarily delivered to the northeastern shelf and slope during summer due to the general SW-NE direction of surface currents (Liu et al., 2016 and references therein). However, the year-round presence of the Longshore Current traveling south along the Chinese margin pushes most of the Pearl River sediments in a southwestward direction along the coast both in summer and in winter, depositing most of them between the Pearl River Mouth and Hainan, and allowing just a small fraction to be exported beyond the shelf break to the slope (Li et al., 2016; J. Liu et al., 2011; Wang et al., 1986). Sediments from Southwest Taiwan are delivered to the NSCS shelf and slope primarily in winter due to the predominant NE-SW surface current direction (Liu et al., 2016 and references therein). The year-round inflow of the Kuroshio Current into the NSCS is characterized by the formation of a series of surface mesoscale anticyclonic (clockwise) eddies that propagate westwards (J. Liu et al., 2011; Z. Liu et al., 2010). The southern rim of this series of gyres conforms what is known as the "Kuroshio Branch Current" that flows in NE-SW direction along the slope and facilitates the westward dispersion sediments from Southwest Taiwan. In turn, the northern rim of this series

of gyres forms a "Warm Current" flowing in SW-NE direction along the shelf break (J. Liu et al., 2011), permanently during summer and at intervals during winter, in periods of NE-wind relaxation (Chiang et al., 2008), which contributes to the eastward dispersion of sediments from South China (J. Liu et al., 2011). Finally, sediments from Northern Luzon are introduced to the NSCS by the Kuroshio Branch Current, but most of them are confined to the NW off Luzon by the formation of a surface cyclonic (anti-clockwise) eddy in this area (J. Liu et al., 2011). Sediment dispersal by bottom currents is stable throughout the year and follows a west-southwest direction along the northeastern NSCS continental slope, driven by the intrusion of North Pacific Deep Water (NPDW) through the Bashi Channel at a depth of ca. 2400 m in the Luzon Strait (J. Liu et al., 2011; Liu et al., 2016; Z. Liu et al., 2010; Lüdmann et al., 2005; Shao et al., 2007). This bottom current re-suspends slope sediments off Southern Taiwan, exported via submarine canyons, and injects them into the NSCS following the seafloor topography, the sediments are then pushed up-slope near the Dongsha Islands and redeposited between 2800 and 1200 m (Lüdmann et al., 2005; Shao et al., 2007).

The mineralogical and isotopic composition of the NSCS slope sediments (see Supplementary Discussion section S5.1 at the end of this Chapter for further discussion) suggests that the main modern sources of terrigenous material to the NSCS slope are primarily Southern Taiwan, followed by Southern China and with only a minor contribution from Northern Luzon (Boulay et al., 2005; Hu et al., 2012; E. Huang et al., 2011; Li et al., 2003; Liu et al., 2016; Z. Liu et al., 2010; Zhifei Liu et al., 2008; Wei et al., 2012). However, a different coastal configuration during the Early Holocene, due to a lower eustatic sea level of about 50 m (Fig. 5.1b; Stanford et al., 2011), may have modified the relative contribution of these three sources by changing coastal configuration and marine circulation patterns. The most striking change in the NSCS configuration during the Early Holocene would be the near closure of the Taiwan Strait and the considerable narrowing of the continental shelf, however monsoon-driven seasonal surface circulation reversal would still occur (Liu et al., 2016). Reconstructions suggest that sediment contribution from Southern China was ca. 15 % higher before 9 ka as compared to the present (Liu et al., 2016; Z. F. Liu et al., 2010). The position of the 50 m isobath (Fig. 5.1b) suggests that the Pearl River paleo-estuary would be located seaward and closer to the shelf break, facilitating the export of terrigenous material from Southern China to the NSCS slope (Liu et al., 2016), and thus the contribution of sediment from Southern China would be higher before maximum eustatic sea level stabilization

around 7 ka BP (Stanford et al., 2011). Terrigenous contribution from Southern Taiwan would remain important even at lower eustatic sea level because the transport exerted by the along-slope bottom current from the Bashi Channel is largely unaffected by sea level changes (Liu et al., 2016; Z. F. Liu et al., 2010), and because the coastal current which now flows through the Taiwan Strait would be displaced and flow along the eastern and southern rim of Taiwan (Liu et al., 2016). Based on this this evidence, we henceforth assume that proxy records from Sites 16601-5 and 2905 integrate a regional climatic signal derived primarily from Southern Taiwan and secondarily from Southeast China for the last 11.2 ka, with higher contribution from Southern China before the stabilization of maximum eustatic sea level around 7 ka BP.

5.5.2. Compatibility of records from cores 2905 and 16601-5

Due to the considerable distance (ca. 100 km) between the locations of both cores, it is necessary to evaluate if the processes affecting the history of their proxy records is similar enough as to allow the reconstruction of a continuous history of events in the NSCS during the last 11.2 ka. Sedimentation rates are significantly higher at site 2905 than at site 16601-5. Overall, but specifically around 2 ka BP when the timelines of both cores intersect, sedimentation rate is 2.5 times higher or more at site 2905 and suggests higher sediment input. Site 16601-5 is located to the southwest of the Dongsha Islands whereas site 2905 is located to the southeast. As discussed in the previous section, the influence of a sediment drift characterized by high sedimentation rates occurs within the area between the Dongsha Islands, Taiwan and Luzon (Lüdmann et al., 2005; Shao et al., 2007). Due to the deeper position on the slope of site 2905 and its up-stream location in the path of the along-slope bottom current, this site is likely to experience higher sediment deposition as compared to site 16601-5, located in a shallower and down-stream position. However, organic matter content (i.e. TOC and TN contents) is very similar between both cores, which would indicate that site 16601-5 is also affected by this sediment drift, though in a much lesser degree; otherwise the organic matter content would be diluted at site 2905 by high content of siliciclastic particles, characteristic from Taiwan and Luzon terrigenous contribution (J. Liu et al., 2010a; Liu et al., 2016), which does not seem to be the case.

Regarding the bulk parameters, TOC and TN contents in both cores are comparable to those observed in sediments across the NSCS continental shelf (Gao et al., 2007; Xu et al., 2014;

Yu et al., 2012). Slightly higher TOC content is observed in core 16601-5 (Fig. 5.2b) which is also reflected as higher TOC/TN ratios as compared to core 2905 (Fig. 5.2c), whereas the nitrogen content between the two sites is very similar. Due to the position of both sites on the continental slope, the input of marine organic matter, characterized by TOC/TN ratios < 10 (Hedges et al., 1997), is predominant in both cases. Surface chlorophyll-*a* concentration and phytoplankton-derived sedimentary lipid distributions indicate that productivity regimes are similar between the two sites (Dong et al., 2015), and thus the input of fresh marine organic matter is also comparable. Hence, the difference in TOC content between the two sites likely results of a slightly higher proportion of terrestrial organic matter reaching core 16601-5 due to its shallower position on the slope (ca. 500 m shallower as compared to site 2905) and its closer proximity to the Pearl River mouth. The stable isotopic composition of organic matter ($\delta^{13}C_{TOC}$ and $\delta^{15}N_{TN}$; Fig. 5.2d) of both cores also presents high similarity. The $\delta^{13}C_{TOC}$ value ranges from both sites (-22.4 ‰ to -20.9 ‰) are higher than those reported in sediments from the Pearl River estuary in southern China (-22 to -28 ‰; Hu et al., 2006; S. Yang et al., 2011; Yu et al., 2012) and sediments from the Kaoping submarine canyon offshore southwestern Taiwan (-22.5 to -24 ‰; Liu et al., 2006), but are highly similar to those reported in Holocene sediments from the NSCS continental slope in the neighboring core GIK-17940-2 (Fig. 5.1b; Kienast et al., 2001) and are well within the range of marine phytoplankton (-22 to -19 ‰; Hedges et al., 1997), suggesting altogether a predominant organic matter origin. Likewise, the $\delta^{15}N_{TN}$ values of both sites (3.7 ‰ to 5.7 ‰) are within the range of those in Holocene sediments from neighbor deep-sea sites ODP-1144 (Fig. 5.1; Higginson et al., 2003) and GIK-17940-2 (Fig. 5.1; Kienast, 2000), but higher than those observed in terrestrial organic matter (close to 0 ‰; Robinson, 2001) which is typically more depleted than marine organic matter due to the predominance of nitrogen fixation over land. Observations indicate that $\delta^{15}N_{TN}$ values are highly homogeneous across the NSCS continental slope during the Holocene (Higginson et al., 2003; Kienast, 2000). In fact, the $\delta^{15}N_{TN}$ in the NSCS are thought to be driven by the input of intermediate water from the Western Pacific ($\delta^{15}N > 6$ ‰), via the Bashi strait, with a strong overprint signal from local nitrogen fixation in the NSCS surface waters (Higginson et al., 2003).

Additional evidence of the similarities between both cores is provided by the *n*-alkane content as well as their isotopic composition. CPI values in samples from both sites are alike, though relatively low (1.8 – 3) as compared to material with predominant vascular plant origin (>

4) (Killops and Killops, 2005). Indeed, sediments across the NSCS have been reported to have generally low long-chain-n-alkane CPI values (Xu et al., 2014), particularly during the Holocene as compared to the Last Glacial Maximum, which has been attributed to a reduction in the contribution of higher-plant material due to sea level rise through the last 16 ka (He et al., 2008; Zhou et al., 2011). The ACL values are, in contrast, higher in core 16605-5 than in core 2905, which may result from the preferential settling of heavier alkanes in shallower locations of the slope, particularly those derived from the Pearl River system. Though the concentration of n-C_{29} and n-C_{31} is slightly higher at 16601-5, which could be explained by its closer proximity to the Pearl River estuary (e.g. Xu et al., 2014), the stable carbon and hydrogen isotopic compositions are very similar. The $\delta^{13}C$ values of the n-C_{29} and n-C_{31} alkanes from both cores are comparable to those measured in long-chain n-alkanes from surface sediments across the NSCS shelf and slope, which are characterized by very uniform values regardless their proximity to the coast of southern China or to the coast of southwestern Taiwan (Xu et al., 2014). A survey of δD values in surface sediments from the NSCS has not yet been conducted.

Altogether, the available evidence from bulk organic matter and biomarker composition suggests that the terrestrial sediment sources and the sediment distribution pathways are common to both cores, though possibly with slightly different relative contributions to each site. Furthermore, the regional environmental signals seem highly consistent across the whole NSCS surroundings. Previous evidence from multiple studies, also confirm the homogeneity of marine sediments from the NSCS continental shelf and slope around the Dongsha Islands (e.g. Higginson et al., 2003; Kienast, 2000; Kienast et al., 2001; Xu et al., 2014) and, thus, it seems safe to assume that organic matter data derived from 2905 and 16601-5 cores can be composed to render continuous regional paleo-environmental records for the last 11.2 ka.

5.5.3. Evolution of Holocene paleo-vegetation in the surroundings of the NSCS based on the $\delta^{13}C$ signature of sedimentary n-alkanes

The $\delta^{13}C_{alkanes}$ values from Site 16601-5 (i.e. the most recent part of the composite record; -30.8 ‰ to -28.6 ‰; Fig. 5.3a: black curve) are within the range of those measured in n-C_{29} (-36 to -27 ‰) and n-C_{31} (-36 to -26‰) alkanes extracted from soils of Southeast China under vegetation dominated by C_3 plants (Rao et al., 2008), and characterized by natural tropical and subtropical

conifer/broadleaf mixed forest ecosystems (Sun et al., 1999). Though similar data are lacking from Taiwan, the strong resemblance of vegetation distribution (Sun et al., 1999) leads us to assume that $\delta^{13}C$ values of n-C_{29} and n-C_{31} in soils should be comparable to those of Southeast China. The $\delta^{13}C_{alkanes}$ values of core 2905 (Fig. 5.3a: green curve) are in agreement to those previously reported by Zhou et al. (2012) from the same core, though our record has considerably higher resolution.

The region of Southeast China and Taiwan is characterized by a humid climate with mean annual precipitation (MAP) > 1200 mm yr^{-1} and up to 3000 mm yr^{-1} (GWSP Digital Water Atlas, 2008, Map 36: Mean Annual Precipitation 1950 - 2000 (V1.0), http://atlas.gwsp.org; China Meteorological Administration, http://www.cma.gov.cn; Hong Kong Observatory, http://www.hko.gov.hk; Taiwan Water Resources Agency, http://eng.wra.gov.tw) and has a positive annual water balance, which means that mean annual precipitation is larger than annual potential evapotranspiration (Prentice et al., 2011; Willmott and Feddema, 1992); GWSP Digital Water Atlas, 2008, Map 40: Climate Moisture Index (V1.0), http://atlas.gwsp.org). Model paleo-precipitation reconstructions suggest a maximum precipitation reduction of about 330 mm yr^{-1} in the study area during the Last Glacial Maximum (Tharammal et al., 2013), for which we regard as highly unlikely that mean annual precipitation ever fell under 1000 mm yr^{-1} during the Holocene. Thus, we discard moisture stress as an important source of positive bias to the stable carbon isotopic composition of C_3 plants ($\delta^{13}C_{C3}$) during the entire study period (Diefendorf et al., 2010; Kohn, 2010; Prentice et al., 2011), and we regard the changes in the $\delta^{13}C_{alkanes}$ record to be more closely linked to shifts of relative abundances between different plant functional types (PFTs) and C_3/C_4 plant species relative proportion (see Supplementary Discussion section S5.2 for further discussion of the physiological and ecological drivers of plant $\delta^{13}C$ composition). Global atmospheric pCO_2 in combination with local air temperature have also been documented to exert an important influence on plant photosynthetic rates and thus the final isotopic composition of plant tissues (e.g. Ehleringer and Cerling, 2002; Farquhar et al., 1989). However, the lack of any significant correlation between the $\delta^{13}C_{alkanes}$ signal and Holocene pCO_2 variability (260−280 ppmV until pre-industrial times) (Monnin et al., 2004), leads us to believe that pCO_2 played a marginal role as driver of vegetation composition during the study period.

The marine pollen record from Site 17940 in the vicinity of Site 2905 (Fig. 5.1b) gives evidence of the predominance of montane conifer forests, temperate montane rainforest and

Artemisia grasslands between 11.3 and 10.0 ka BP, and of tropical and subtropical broadleaf forests between 10.0 and 0.0 ka BP in the surroundings of the NSCS (Sun et al., 2000; Sun and Li, 1999), with all these vegetation types dominated by C_3 species. Accordingly, the $\delta^{13}C_{alkanes}$ record (-28 to -31 ‰; Fig. 5.3a) indicates an overall predominance of C_3 vegetation under (semi-) moist conditions for the last 11.2 ka. The highest $\delta^{13}C_{alkanes}$ between 11.2 and 8 ka BP are in agreement with higher relative abundances of herbs and grasses versus trees inferred from the pollen records of marine cores GIK17940 an MD05-2904 (Fig. 5.1b), whereas higher $\delta^{13}C_{alkanes}$ values after 8 ka BP can be related to an increase in the abundance of trees versus herbs and grasses (Dai et al., 2015; Sun et al., 2000; Sun and Li, 1999). Lacustrine pollen records from Southeast China and Central-Southern Taiwan show high moisture conditions during the Early Holocene between 11 and 8 ka BP (Lee and Liew, 2010; Li et al., 2013; P. M. Liew et al., 2006; Ping Mei Liew et al., 2006; Wang et al., 2007; T. N. Yang et al., 2011), for which a better development of forest ecosystems over grasslands at this time would be expected. The high abundance of herbs and grasses evident in marine pollen records between 11 and 8 ka BP is likely linked to the larger expansion of the coastal plains over the exposed NSCS continental shelf due to lower eustatic sea level (Fig. 5.3b; Stanford et al., 2011). During the LGM the exposed shelf area was largely dominated by grasslands, with high abundances of *Artemisia* (a C_3 grass) and Cyperaceae (sedges; both C_3 and C_4 representatives), and though their relative abundance declined throughout the Deglaciation and the Early Holocene, it remained an important component of the marine pollen record until about 8 ka BP (Dai et al., 2015; Sun et al., 2000). Thus, it was only until the full drowning of the shelf, and subsequent migration of the shoreline closer to the foothills of mountain ranges that the extension of grasslands was drastically reduced and tree vegetation became better represented in marine sedimentary archives. For this reason, we conclude that the $\delta^{13}C_{alkanes}$ record during the Early Holocene does not reflect vegetation changes as a function of moisture/precipitation variability in the NSCS region, but rather reflects the type of vegetation represented in the sediment archives in function of eustatic sea level changes.
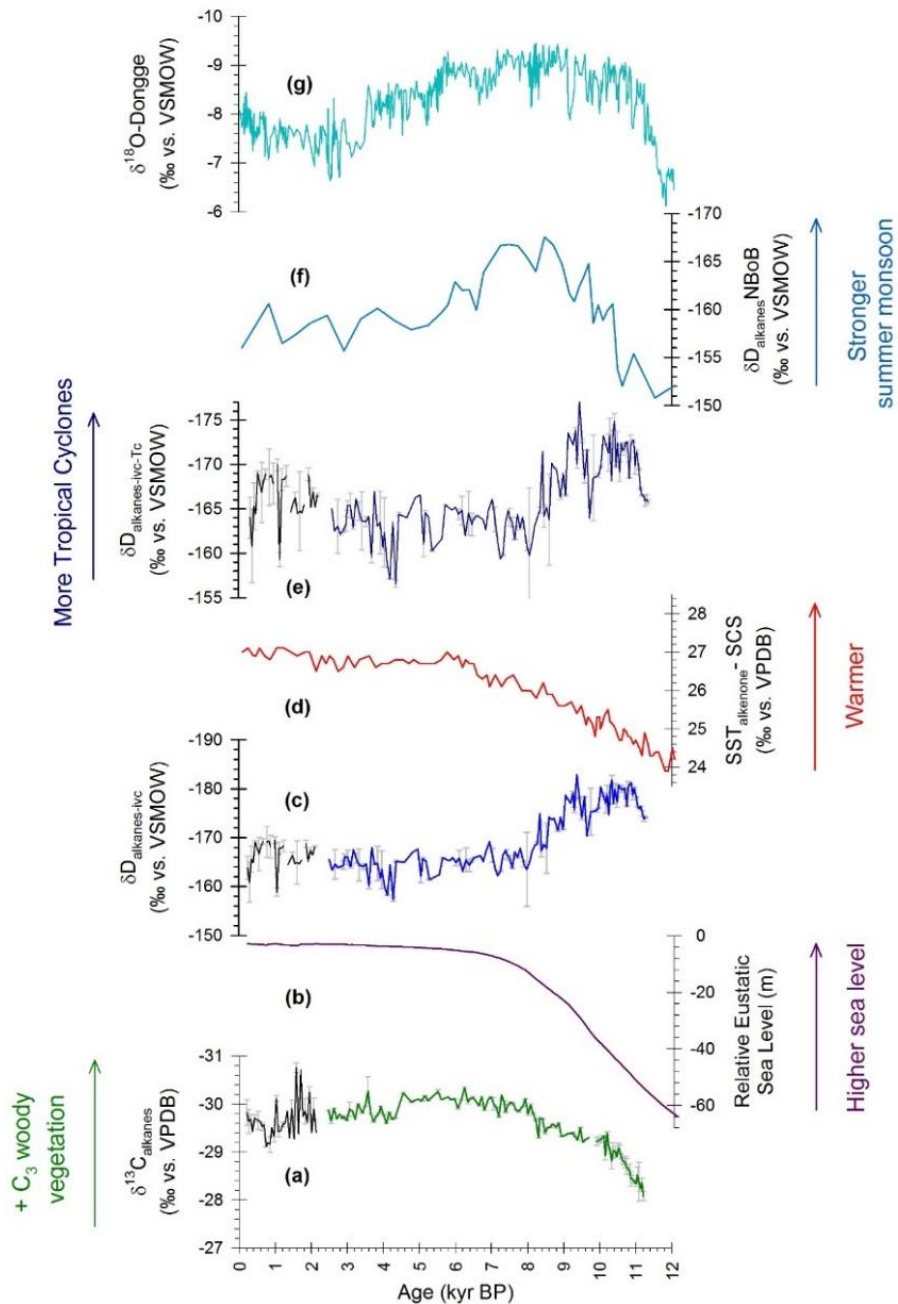
Fig. 5.3. Down-core records of biomarker parameters from cores MD05-2905 and GeoB16601-5 and comparison to other relevant paleo-environmental records. **(a)** weighted-average of measured stable carbon isotopic composition of the n-C$_{29}$ and n-C$_{33}$ alkanes (δ^{13}C$_{alkanes}$; this study); **(b)** relative sea level with respect to the present (Stanford et al., 2011); **(c)** weighted average of ice-volume-corrected hydrogen isotopic composition of the n-C$_{29}$ and n-C$_{33}$ alkanes (δD$_{alkanes-ivc}$; this study); **(d)** Alkenone-based Sea Surface Temperature record of the Northern South China Sea (SST$_{alkenone}$-NSCS) from core GIK17940 (Pelejero et al., 1999); **(e)** Temperature-corrected weighted average of ice-volume-corrected hydrogen isotopic composition of the n-C$_{29}$ and n-C$_{33}$ alkanes (δD$_{alkanes-ivc-Tc}$; this study); **(f)** weighted-average of the n-C$_{29}$ and n-C$_{31}$ ice-volume-corrected hydrogen isotopic records from core SO188-342KL

($\delta D_{alkanes}$), as indicator of summer monsoon intensity in the Northern Bay of Bengal region (Contreras-Rosales et al., 2014); **(g)** Speleothem $\delta^{18}O$ record of Dongge Cave from South China (Dykoski et al., 2005). Axes are reversed in (a), (c), (e), (f) and (g) to show higher proportion of C_3 vegetation, higher incidence of tropical cyclones, stronger summer monsoon and enhanced precipitation in South China towards the top of the graph. Color lines: core MD05-2905; black lines core GeoB16601-5.

During the Mid-Holocene, lowest $\delta^{13}C_{alkanes}$ values observed between 8-4 ka BP are possibly linked to the maximum expansion of tropical and subtropical evergreen forests in the region (Lee and Liew, 2010; P. M. Liew et al., 2006; Ping Mei Liew et al., 2006; Wang et al., 2007), as evergreen angiosperms perform the strongest carbon fractionation (Diefendorf et al., 2010). In turn, this expansion of tropical/subtropical tree taxa seemed more closely associated to temperature increase rather than to precipitation increase in Taiwan (Lee and Liew, 2010; P. M. Liew et al., 2006; Ping Mei Liew et al., 2006). The Late Holocene displays a tendency towards higher $\delta^{13}C_{alkanes}$ values in response to a reduced proportion of trees versus herbs observed in pollen records all around the NSCS (Dai and Weng, 2015; Lee and Liew, 2010; P. M. Liew et al., 2006; Ping Mei Liew et al., 2006; Wang et al., 2007). This is despite that moisture increase is documented as higher relative abundance of fern spores and/or Cyperaceae pollen, particularly in the last 3 ka (Dai and Weng, 2015; Lee and Liew, 2010; P. M. Liew et al., 2006; Ping Mei Liew et al., 2006; Sun et al., 1999; Wang et al., 2007). However, high abundance of Poaceae is also observed in most of these records, and may be possibly associated to the emergence of rice agriculture in Southeast China (ca. 5.0 ka BP) and in Taiwan (ca. 4.8 ka BP), and its expansion henceforth (Zhang and Hung, 2010). Evidence of enhanced agricultural activity during the last 2 ka has been proposed based on the analysis of terrestrial biomarker composition in sediments from the Pearl River estuary (Strong et al., 2013).

5.5.4. Factors affecting the δD signature of NSCS sedimentary n-alkanes and their implications for paleo-precipitation history around the NSCS

5.5.4.1. Vegetation apparent fractionation effect

Vegetation with different photosynthetic pathways and life styles perform differential isotopic fractionation of water molecules used in metabolic processes which result in an overall apparent isotopic fractionation (ε) between the water source to the plant and the final isotopic composition

of plant tissues (e.g. Chikaraishi et al., 2004; Sachse et al., 2012 and references therein). The apparent fractionation observed between the isotopic composition of plant waxes and that of the original source water ($\varepsilon_{alk/w}$) (Chikaraishi et al., 2004; Sessions et al., 1999) is stronger in C_3 angiosperms than in C_4 angiosperms (-130 ± 21 ‰ versus -111 ± 27 ‰ respectively) (Sachse et al., 2012, supplementary material); thus changing the proportions of these two plant groups within vegetal communities would result in different apparent fractionation and thus a source of bias when determining changes in precipitation intensity based on sedimentary n-alkanes δD signature (e.g. Douglas et al., 2012). As C_3 vegetation was predominant in the study region throughout the Holocene (see section 5.5.3) and changes in C_3/C_4 relative abundance was estimated to be ≤ 10 %, based on the $\delta^{13}C$-alkane record of core 2905 (Zhou et al., 2012), we expect little bias on the δD_{alk} record derived from relative changes in vegetation composition, and thus we assume it to be negligible. Furthermore, even when large alternations of C_3/C_4 species dominance in vegetal communities have taken place (e.g. > 40 %) as is the case of glacial/interglacial vegetation shifts (Collins et al., 2013), the effects of changes in C_3/C_4 apparent fractionation on the final δD composition of n-alkanes has been observed to be small as compared to those derived from changes in seasonality (i.e. wet season length and intensity) (Collins et al., 2013).

Evidence suggests that the length of the growing season of vegetation (i.e. the time of production of plant waxes) spans between 11-12 months in the study region (Thomas et al., 2014). There is evidence to suspect that seasonality was stronger during the Early-to-Mid Holocene due to simultaneous strengthening of summer and winter monsoon during this period (Steinke et al., 2011), however it is unlikely that the growing season in South China would have been shorter than 10 months (the estimated length of the current growing season in the temperate coastal regions of East China) due to its maritime climate that guarantees year-round moisture advection (Thomas et al., 2014). Therefore, the year-round production of leaf waxes in South China and Taiwan would integrate an annual record of δD in precipitation (Thomas et al., 2014) and we assume this relationship was maintained all throughout the Holocene.

5.5.4.2. Air temperature effect

Recent evidence from South China indicates that the isotopic signature of precipitation is more strongly correlated to mean annual temperature (MAT) than to mean annual precipitation (MAP),

though MAT and MAP are usually positively correlated between them (Dayem et al., 2010; Johnson and Ingram, 2004; Thomas et al., 2014). However, the correlation between MAT and δD (or δ^{18}O) is not derived from the temperature effect −which causes depletion of heavy isotopes in precipitation as temperature decreases (Dansgaard, 1964)− but rather is opposite to it, i.e. heavy isotopes depletion occurs with higher temperatures (Johnson and Ingram, 2004; Thomas et al., 2014). A possible explanation of this reversed temperature effect may be related to the type of precipitation (Dayem et al., 2010), e.g. precipitation formed under stronger convection will be more depleted in heavy isotopes than precipitation formed under weaker convection even if the amount of rainfall is the same (Johnson and Ingram, 2004; Risi et al., 2008), and strong convection is favored with higher air temperatures. Recently, a method has been proposed to attempt the removal of the regional temperature variability signature from an alkane isotopic record from South China using sea surface temperatures (SSTs) from the NSCS (Thomas et al., 2014). This method is based on the strong positive correlation (r = 0.96) between surface air temperature in South China and SST in the NSCS according to modelled data over 23 ka (Thomas et al., 2014, supplementary material). Though temperature changes over land are probably underestimated, this method seems a good approximation to remove long-term trends of temperature variability in the region. Therefore, we perform a temperature-effect correction to our $\delta D_{alkane-ivc}$ composite record using use the $U^{K'}_{37}$ alkenone-based SST record of core GIK17940 (Fig. 5.3; Pelejero et al., 1999) located very close to Site 2905 and the method proposed by Thomas et al. (2004; see Appendix A5.1 for details). The corrected record ($\delta D_{alkane-ivc-Tc}$) maintains the same general trends but shows a small shift towards positive values during the Early Holocene section of the record (from 11.2 to 8.6 ka BP; Fig. 5.3e).

5.5.4.3. Precipitation amount effect

Low latitude intense precipitation formed under strong convection (e.g. monsoon or typhoon precipitation), tends to be particularly depleted in heavy isotopes (Risi et al., 2008). This phenomenon, known as the amount effect (Dansgaard, 1964) results in a stronger depletion in heavy isotopes (D and ^{18}O) in rainfall as precipitation amount/intensity increases (Dansgaard, 1964; Risi et al., 2008; Rozanski et al., 1993). The amount effect is the main driver of isotopic composition of precipitation in monsoonal regions around the world, and can be observed as a

negative correlation between precipitation δD (or $\delta^{18}O$) and weighted precipitation amount (Araguás-Araguás et al., 1998; Rozanski et al., 1993). In the South China-Taiwan region, the amount effect is well observed at a given location on the intra-annual basis, as summer precipitation is considerably depleted in heavy isotopes as compared to winter precipitation (e.g. Dayem et al., 2010; Johnson and Ingram, 2004; Peng et al., 2010). However, on the inter-annual basis or between two given locations the amount effect is not observed (e.g. Aggarwal et al., 2004; Dayem et al., 2010; Thomas et al., 2014). Summer atmospheric circulation in the East Asian Monsoon Domain is considerably more complex than in the Indian Monsoon Domain due to the interaction of many large-scale atmospheric features including: the Western North Pacific Subtropical High (WNPH), the Monsoon Trough, the Meiyu Front, and the genesis location and tracks of tropical cyclones (Aggarwal et al., 2004; Chen and Huang, 2008; Ding and Chan, 2005; Wang and Qian, 2009). Thus the lack of a consistent amount effect across the East Asian Monsoon Domain is likely due to the variable location of large-scale circulation convergence over the South China region (i.e. the position of pressure cells and troughs), variability in frontal dynamics (e.g. Meiyu front), and variability in convection intensity (i.e. monsoon and typhoon convection) from one year to the next and in between locations (Aggarwal et al., 2004; Clemens et al., 2010; Dayem et al., 2010; Johnson and Ingram, 2004).

5.5.4.4. Moisture source changes

Moisture source explains about 26 % of the variability on the isotopic composition of speleothem $\delta^{18}O$ composition in the Dongge Cave as compared to 18 % explained by precipitation amount (Baker et al., 2015). Moisture sources for precipitation in the East Asian Monsoon Domain are considered stable throughout the Late Pleistocene and Holocene (Aggarwal et al., 2004) and variability in the isotopic composition of paleo-hydrologic records (e.g. cave speleothem or plant-wax *n*-alkanes) should be considered mostly in regard to the relative contribution of the different sources (Clemens et al., 2010; Dayem et al., 2010).

Moisture transport around the NSCS is highly governed by Asian monsoon circulation and thus displays strong seasonal variability. From June to September, large amounts of moisture are exported from the Northern Indian Ocean into the South China Sea under the summer monsoon circulation (Baker et al., 2015; Ding and Chan, 2005; He et al., 2007; Shi et al., 2008). The

Northern Indian Ocean is actually the primary moisture source for summer monsoon precipitation in South China and Taiwan (Ding and Chan, 2005), known as the equatorial maritime air mass (Araguás-Araguás et al., 1998). In fact, summer monsoon winds blowing from the Northern Indian Ocean can carry moisture between 500 and 1000 km away from the source region into the rainout location (Baker et al., 2015). Under the summer monsoon circulation, the Western North Pacific Ocean contributes with an overall minor portion of the moisture for rainfall, known as the tropical maritime air mass (Araguás-Araguás et al., 1998) and is largely delivered in the form of tropical cyclones. In turn, from October to March the winter monsoon circulation is established and the Western Pacific Ocean becomes a large source of moisture to Southeast China and Taiwan (largely derived from tropical cyclones in October-November), together with the moisture contribution from Continental China throughout the entire season (Baker et al., 2015; Clemens et al., 2010; Peng et al., 2010). Finally, during April-May the Western North Pacific Ocean becomes the dominant source of moisture during the formation of the Meiyu Front over South China, which occurs as an early sign for the establishment of summer monsoon circulation in the East Asian Monsoon Domain (Wang and Qian, 2009). Changes in the length and strength of seasonality may be partly responsible for the isotopic composition changes observed in paleo-precipitation records (Dayem et al., 2010) as large-scale atmospheric circulation in the Asian Monsoon Domain is fuelled by the seasonal land-ocean thermal contrast (e.g. Li and Yanai, 1996; Wang and Qian, 2009).

Altogether, moisture from the Indian Monsoon Domain between 80°E−100°E is relatively enriched in heavy isotopes (annual average weighted $\delta^{18}O \approx$ -2 to -4 ‰; annual average weighted $\delta D \approx$ -16 to -33 ‰) as compared to that from the East Asian Monsoon Domain between 100°E−120°E (annual average weighted $\delta^{18}O \approx$ -5 to -7 ‰; annual average weighted $\delta D \approx$ -40 to -70 ‰) because the later has largely been affected by continental moisture recycling/admixture of moisture above Indochina (Aggarwal et al., 2004). In general, maritime moisture sources tend to be enriched in heavy isotopes compared to continental sources because continental moisture suffers longer Rayleigh distillation of the water vapour in the air mass along its transport (continental effect; Dansgaard, 1964). Therefore, enhanced moisture export from the Indian Monsoon Domain into the East Asian Monsoon Domain can potentially increase the δD and $\delta^{18}O$ values of paleo-precipitation records from South China. In addition, the reduction of the continental surface in Indochina due to higher eustatic sea level could also explain an enrichment

in heavy isotopes (e.g. Aggarwal et al., 2004). Both of these processes can thus explain the excursion towards more positive values observed in the $\delta D_{alkanes-ivc-Tc}$ record between 9.5 and 8 ka BP (Fig. 5.3e) since this period coincides with (a) the maximum strength of the Indian Summer Monsoon (ISM) evidenced by lowest values in the alkane stable hydrogen isotopic record from the Northern Bay of Bengal ($\delta D_{alkanes}$–NBoB; Fig. 5.3f) (Contreras-Rosales et al., 2014; Chapter 3) and (b) with the early stages of gradual stabilization of the global eustatic sea level (Fig. 5.3b; Stanford et al., 2011). Enhanced continental effect due to lower eustatic sea level in the Early Holocene could also partially explain the early depleted values in Dongge Cave speleothem $\delta^{18}O$– record (Fig. 5.3g; Dykoski et al., 2005) during the first-phase of Asian Summer monsoon intensification (11-9 ka BP) before the attainment of its maximum strength (9-7 ka BP) as shown by Indian monsoon records (Fig. 5.3f; Contreras-Rosales et al., 2014 and references therein).

5.5.4.5. Interactions between the Indo-Pacific Warm Pool, tropical cyclone activity and the Asian summer monsoon strength

The region of South China and Taiwan is heavily impacted by the pass of tropical cyclones, which constitute an important source of heavy rains between July and October (Camargo and Sobel, 2005; Wang et al., 2012), partially overlapping with the summer monsoon rains. The incidence of tropical cyclones is tightly linked to the thermal state of the Indo-Pacific Warm Pool (IPWP) and the position of large-scale atmospheric features such as the Monsoon Trough and the Western North Pacific High (WNPH), which affect the cyclogenesis location as well as the course and shape of tropical cyclone tracks (Camargo and Sobel, 2005; Chen and Huang, 2008; Fig. 5.4). This is due to the fact that tropical cyclones are formed in the southwestern rim of the WNPH at its meeting point with the summer Monsoon Trough (Chen and Huang, 2008). Therefore, changes in the background thermal state of the IPWP, and the position and/or strength of the WNPH and the Monsoon Trough are all interconnected and have the potential to influence tropical cyclone activity and monsoon intensity throughout the Holocene.

Warm State of the IPWP (La Niña-like / Negative PDO-like; Fig. 5.4a): Studies suggest that when the IPWP is in a warming state the area of SST > 29 °C retreats westwards towards the Western Tropical North Pacific, causing the development of strong Walker circulation across the Tropical Pacific Ocean and the establishment of strong lower-level easterly winds (Chen and

Huang, 2008; Hung et al., 2006). The combined westward retreat of the > 29 °C area with strong easterly winds favours the establishment of enhanced vertical convection over the Philippines, the westward confinement of the summer Monsoon Trough and a more eastward position of the WNPH (Chen and Huang, 2008; Hung et al., 2006). The strong Walker circulation is also established in the Indian Ocean causing an early onset of summer monsoon circulation (late-April to early-May) and fuelling strong southwest summer monsoon winds that feed abundant precipitation to India, Indochina and Southern China (Hung et al., 2006; Krishnan and Sugi, 2003; Kumar and Krishnan, 2005). However, the relatively eastwards position of the WNPH hinders the development of the Meiyu Front in China during early spring (Wang and Qian, 2009). This is because the Meiyu Front is formed over land along the western rim of the WNPH by the blocking of warm moist monsoon winds by cool continental air masses (Jiang and Ni, 2004). Due to the eastward location of the WNPH, monsoon winds can penetrate further north into China but precipitation is reduced in areas under the influence of the Meiyu Front, such as the Yangtze River Valley (Wang and Qian, 2009). Under this scenario, the genesis location of tropical cyclones moves westwards, together with the Monsoon Trough (Camargo and Sobel, 2005; Chen and Huang, 2008). Strong lower-level and upper-level easterlies push tropical cyclones towards South China and Indochina resulting in straighter tracks (Chen and Huang, 2008; Kumar and Krishnan, 2005). Due to the reduced time over sea before landfall tropical cyclones are also shorter-lived and less intense; thus, fewer tropical cyclones evolve into typhoons and most of them remain as tropical storms (Camargo and Sobel, 2005).

Cool state of the IPWP (El Niño-like / Positive PDO-like; Fig. 5.4b): During a cooling state of the IPWP the area of SST > 29 °C displays an eastward extension towards the Central Equatorial Pacific, causing a weakening of the Walker circulation across the Tropical Pacific Ocean and a general weakening of the lower-level easterly winds (Chen and Huang, 2008; Hung et al., 2006). The area of strong vertical convection is located eastwards of the Philippines and the summer Monsoon Trough moves eastwards towards the dateline (Chen and Huang, 2008; Hung et al., 2006). Walker circulation is also weaker over the Indian Ocean which causes a later onset of summer monsoon circulation (late-May) and weaker summer monsoon westerly winds associated with reduced precipitation in India, Indochina and Southern China (Hung et al., 2006). The relative westward position of the WNPH, however, favours the development of a strong Meiyu Front, which confines summer monsoon winds to Southern China and results in abnormally high

precipitation in the areas located under the front, such as the Yangtze River Valley (Wang and Qian, 2009). This conditions also derive in an eastward displacement of the genesis location of tropical cyclones along with the Monsoon Trough (Camargo and Sobel, 2005; Chen and Huang, 2008). The weak lower-level easterly winds allow tropical cyclones to remain longer over the ocean, whereas the development of anomalous mid-latitude upper-level westerly winds over land push tropical cyclones north-eastwards forcing them to recurve offshore Taiwan and to make landfall more often in Japan (Chen and Huang, 2008; Kumar and Krishnan, 2005). Due to the longer time spent over sea, tropical cyclones are usually very intense, longer-lived, and a higher proportion of them evolves into typhoons (Camargo and Sobel, 2005).

5.5.4.6. Holocene evolution of the IPWP thermal state and precipitation history in the South China-Taiwan region

A recent study has proposed enhanced tropical cyclone activity in the NSCS region during the Early Holocene, between 11 and 8.5 ka BP, based on higher abundance of fine-grained detritus derived from enhanced fluvial discharge during this period of weaker summer monsoon as compared to later in the Holocene (Huang et al., 2015). At the same time, another study suggests a westward retraction of the IPWP during the Early Holocene (10−7 ka BP) based on SST anomalies of > 0.5 °C with respect to preindustrial values around the Indonesian region (Linsley et al., 2010). Finally, there is also evidence of strongly reduced El Niño events during the Early Holocene (Conroy et al., 2008; Moy et al., 2002) and a larger zonal SST gradient between the Western Tropical Pacific and the Eastern Tropical Pacific, i.e. warmer in the west and cooler in the east, with respect to the present (Conroy et al., 2008). The evidence also suggests a progressive reduction of this zonal SST gradient across the Pacific throughout the Holocene, which resulted on an enhanced occurrence of El Niño events during the last 4 ka, with maximum intensity in the last 2 ka (Conroy et al., 2008; Moy et al., 2002).

The previous evidence in combination with evidence from the $\delta D_{alkanes-ivc-Tc}$ composite record lead us to propose a predominant warming background state of the IPWP during Early Holocene, characterized by a high incidence of tropical cyclones making landfall in the region of South China that left a large imprint on the yearly amount and isotopic composition of precipitation in this region before 9 ka BP, which marks the start of the period of maximum summer monsoon

strength (Contreras-Rosales et al., 2014; Chapter 3). This could be a contributing factor behind the more negative values in the $\delta D_{alkanes-ivc-Tc}$ record before 8.5 ka BP as cyclonic rainfall is characterized by highly depleted δD and $\delta^{18}O$ values due to the intense deep convection (Ohsawa and Yusa, 2000) and due to a larger contribution of sediments from the Pearl River basin at the time. Enhanced cyclonic-precipitation contribution to Southern China during the Early Holocene may be an additional explanation for depleted speleothem $\delta^{18}O$ values observed in Dongge Cave before 9 ka BP (Fig. 5.3g). Strengthening of Asian Summer monsoon between 9 and 7 ka BP would have progressively masked the influence of cyclonic precipitation throughout this period. The gradual reduction of the SST gradient across the Pacific throughout the Holocene likely caused an overall decrease of tropical cyclone activity and its contribution to yearly precipitation in the study region, giving way to a strongly dominant contribution of summer monsoon precipitation. The remarkable increase of El Niño events during the last 2 ka BP could in turn be associated with a predominant cooling background state of the IPWP during the Late Holocene (Conroy et al., 2008; Moy et al., 2002). In this case, renewed tropical cyclone activity and higher typhoon incidence with stronger precipitation and even more depleted δD and $\delta^{18}O$ associated to stronger typhoons (Ohsawa and Yusa, 2000) in the Western Tropical Pacific would follow, though the effects would be mostly focused on Taiwan as a large part of the tropical cyclones would be redirected towards Japan. Asian Summer Monsoon weakening and higher incidence of tropical cyclones and typhoons hitting Taiwan during the Late Holocene may explain the slight excursion towards negative values observed in the $\delta D_{alkanes-ivc-Tc}$ record during the last 2 ka due to a larger sediment contribution from Taiwan under maximum sea-level conditions.
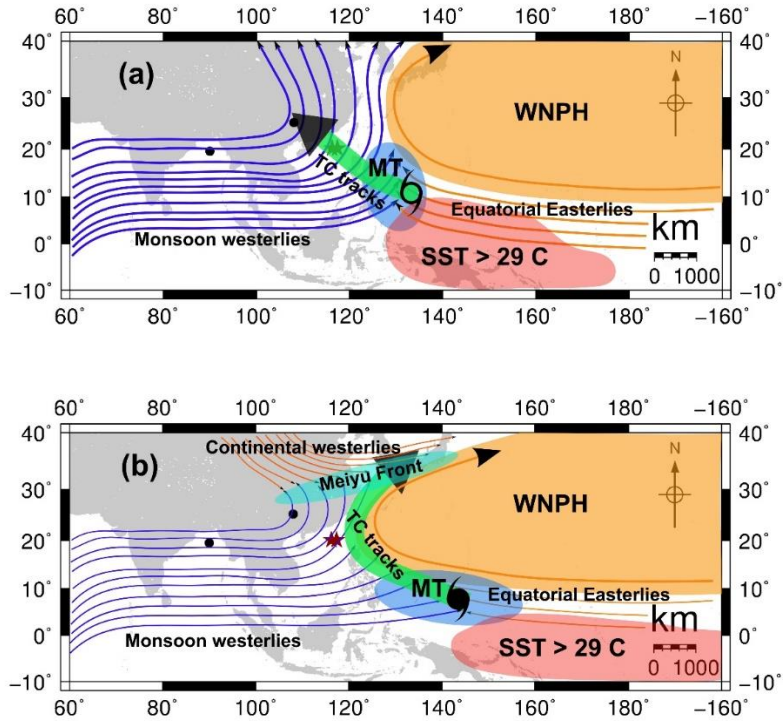
Fig. 5.4. Schematic representation of large-scale atmospheric features during the warming and cooling states of the Indo Pacific Warm Pool. **(a)** Warming state of the IPWP: the area of SST > 29 °C is focused in the Western North Pacific strengthening Walker (east-west) circulation; under this conditions the western rim of the Western North Pacific High (WNPH) shifts eastwards, the Monsoon Trough (MT) and the genesis location of tropical cyclones (open symbol) shift westwards, tropical cyclones (TC) show straighter tracks towards South China and Indochina more often and tend to be less intense (open symbol). **(b)** Cooling state of the IPWP: the area of SST > 29 °C is displaced towards the Equatorial Central Pacific weakening Walker (east-west) circulation; under this conditions the western rim of the Western North Pacific High (WNPH) shifts westwards, the Monsoon Trough (MT) and the genesis location of tropical cyclones (closed symbol) shift eastwards, tropical cyclones (TC) show recurved tracks towards Japan more often and tend to be more intense (closed symbol); due to monsoon weakening the Meiyu Front is strengthen in China. Red stars represent the location of Sites GeoB16601-5 and MD05-2905 discussed in this study. Black dots represent the location of Dongge Cave (South China) and the SO188-342KL sediment core (Northern Bay of Bengal) from where records are presented in Fig. 3. The position of major atmospheric features is based on the studies of Chen and Huang (2008) and Wang and Qian (2009).

5.6. Summary and conclusions

The mineralogical and isotopic composition of the NSCS slope sediments suggests that the main sources of terrigenous material to the NSCS slope are primarily Southern Taiwan, followed by

Southern China and with only a minor contribution from Northern Luzon. Different coastal configuration during the Early Holocene, due to a lower eustatic sea level of about 50 m, allowed higher contribution of sediments from the Pearl River basin until maximum sea level was attained around 7 ka BP, as the Pearl River paleo-estuary would be located seaward and closer to the shelf break. Available evidence from bulk organic matter and biomarker composition suggests that the terrestrial sediment sources and the sediment distribution pathways are common to both 16601-5 and 2905 cores, for which organic matter data derived from these cores can be composed to render continuous regional paleo-environmental records for the last 11.2 ka. The $\delta^{13}C_{alkanes}$ record indicates an overall predominance of C_3 vegetation under (semi) moist conditions throughout the last 11.2 ka. The $\delta^{13}C_{alkanes}$ record during the Early Holocene does not reflect vegetation changes as a function of moisture/precipitation variability in the NSCS region, but rather represents vegetation changes driven by the shift of eustatic sea level. Larger expansion of the coastal plains over the exposed NSCS continental shelf due to lower eustatic sea level favoured the expansion of herbs and grasses before 8 ka BP contributing to higher $\delta^{13}C_{alkanes}$ values. The drowning of the shelf after 8 ka BP caused a migration of the shoreline closer to the foothills of mountain ranges, drastically reducing the extension of grasslands and allowing a better representation of tree vegetation in marine sedimentary archives, contributing to lower $\delta^{13}C_{alkanes}$ values after 8 ka BP. The Late Holocene displays a tendency towards higher $\delta^{13}C_{alkanes}$ values possibly associated to the emergence of rice agriculture in Southeast China (ca. 5.0 ka BP) and in Taiwan (ca. 4.8 ka BP), and its expansion henceforth. The lack of a consistent amount effect across the East Asian Monsoon Domain is likely due to the variable location of large-scale circulation convergence over the South China region. Thus, the variability in the isotopic composition of paleo-hydrologic records in this area should be considered mostly in regard to the relative contribution of different moisture sources rather than solely on the amount effect. A stronger continental effect, derived from lower eustatic sea level, can partially explain the lowest $\delta D_{alkanes-ivc-Tc}$ values observed during the Early Holocene before 9 ka BP. Attainment of maximum sea level after 7 ka BP and the strengthening of monsoon circulation after 9 ka BP, resulting in maximum moisture export from the Indian Ocean, would in turn explain higher of $\delta D_{alkanes-ivc-Tc}$ values observed throughout the rest of the record. A predominant warming background state of the IPWP during Early Holocene was associated to a higher incidence of tropical cyclones making landfall in the region of South China contributed to more negative values in the $\delta D_{alkanes-ivc-Tc}$ record before 8.5 ka. The gradual

reduction of the SST gradient across the Pacific throughout the Holocene likely caused an overall decrease of tropical cyclone activity and its contribution to yearly precipitation in the study region between 8 and 4 ka BP, giving way to a strongly dominant relative contribution of summer monsoon precipitation to the annual moisture balance. A predominant cooling background state of the IPWP during the Late Holocene (last 4 ka) would be characterized by renewed tropical cyclone activity and higher typhoon incidence in the Western North Pacific, but with landfalls around Taiwan instead of South China, explaining the more negative values observed in the $\delta D_{alkanes-ivc-Tc}$ record during the last 2 ka. In general, a warming IPWP background state was related to stronger summer monsoon circulation whereas a cooling IPWP background state was related to weaker summer monsoon circulation. Altogether, this study highlights the complex interactions of climatic and geological processes at work around the Northern South China Sea area and the high sensitivity of paleo-climatic records from this region regarding the variability of background boundary conditions.

Appendix

A5.1. Removal of temperature effect from the composite n-alkane δD record from the NSCS

The procedure for removal of the temperature effect was done after Thomas et al. (2014) and briefly summarized in the following steps: (1) interpolation of the $U^{K'}_{37}$-SST values from the 17940-2 record (Pelejero et al., 1999) to obtain a $U^{K'}_{37}$-SST value for each age corresponding to a sample from the 16601-5/2905 composite record; (2) calculation of the temperature difference (ΔT) between each past interpolated $U^{K'}_{37}$-SST from the 16601-5/2905 record relative to the present (27 °C); (3) conversion of ΔT values into ΔδD values by using the $T-\delta D_p$ relationship of 3.5 ± 0.5 ‰ based on the multiplication times 8 of the $T-\delta^{18}O_p$ relationship of 0.46 ± 0.06‰ (Rozanski et al., 1993); (4) subtraction of the ΔδD values from the $\delta D_{alkanes-ivc}$ values to produce a temperature corrected record ($\delta D_{alkanes-ivc-Tc}$).

Supplementary Discussion

S5.1. Mineralogical and geochemical evidence of terrigenous sediment sources to the Northern South china Sea

There is evidence from several recent studies suggesting that the detrital fine-grained sediment input to the NSCS is a mix of Pearl River sediments and material discharged from rivers in southwestern Taiwan and the Luzon Arc as a result from the regional surface and deep current dynamics (Hu et al., 2012; E. Huang et al., 2011; Z. Liu et al., 2010; Zhifei Liu et al., 2008). The analysis of clay mineral composition of sediments along the NSCS continental shelf and slope, has identified the three potential end members to work as sediment sources for the SCS shelf and slope: (1) the Pearl River basin contributes with major kaolinite and moderate illite and chlorite input, (2) Taiwan contributes with predominant illite and chlorite input; (3) the Luzon Arc system has been identified as an additional sediment contributor to the area, via the Kuroshio current, with major amounts of smectite input (J. Huang et al., 2011; Z. Liu et al., 2010; Zhifei Liu et al., 2008). Diverse attempts to quantify the detrital contribution of different sources to the NSCS slope based on clay minerals has resulted in estimations between 15-31 % from South China, 23-55 % from Taiwan and 35-46 % from Luzon (Z. Liu et al., 2010; Zhifei Liu et al., 2008; Z. F. Liu et al., 2010). However, the clay mineral composition may not fully portrait the actual sediment contribution of different sources due to the differential settling among clay minerals. For instance kaolinite has

large particle size (0.5 to 8.0 μm) and is normally constrained to the marginal areas close to its sources due to fast flocculation in alkaline waters, whereas smectite has a small particle size (< 1 μm) and can travel longer distances across the basin (Liu et al., 2016 and references therein). Furthermore, smectite can also form through chemical weathering from volcanic tephra particles introduced to the SCS by wind transport after volcanic eruptions in the Philippine Arc (Liu et al., 2016).

An alternative analysis based on Nd and Sr isotopic composition has been used to shed more light onto the possible sediment sources to the NSCS. Regarding the Nd isotopic composition, it has been observed that the ε_{Nd} of sediments from South China and Taiwan are highly similar (Boulay et al., 2005; Li et al., 2003; Liu et al., 2016). Furthermore, the eastern tributaries of the Pearl River system and the Taiwanese rivers drain the Eastern South China Block (ε_{Nd} = -12.7 to -11.5), whereas the western tributaries of the Pearl River system drain the Western South China Block (ε_{Nd} = -13.5 to -10.2), and the sediments from both sub-provinces are mixed-up at the Pearl River estuary (Li et al., 2003; Wei et al., 2012 and references therein). In contrast, the ε_{Nd} composition of Luzon sediments is very different (+6.5 to +7.1) (Boulay et al., 2005; Liu et al., 2016; Wei et al., 2012). The Nd isotopic composition of sediments across the NSCS shelf and slope is highly homogeneous (ε_{Nd} = -12.4 to -11.3) and points to the Pearl River basin and Taiwan as dominant sediment sources (Li et al., 2003), whereas sediments from the northeastern deep basin (>3000 m) have higher values (ε_{Nd} = -9.7 to -7.1) and suggest a more important contribution from Luzon (Wei et al., 2012). This conclusion is also supported by the Sr isotopic composition, which has proven useful to distinguish between volcanic sediments from the Philippine Arc (e.g. Luzon; $^{87}Sr/^{86}Sr$ = 0.704 to 0.709) and those from continental sources (e.g. South China and Taiwan; $^{87}Sr/^{86}Sr$ = 0.710 to 0.740) (Boulay et al., 2005; Liu et al., 2016; Wei et al., 2012). The Sr isotopic composition across the NSCS continental shelf and slope ($^{87}Sr/^{86}Sr$ = 0.710 to 0.725) is closer to that of continental sources, whereas that of the northeastern deep basin ($^{87}Sr/^{86}Sr$ ca. 0.710) shows higher influence from the Philippine Arc (Boulay et al., 2005; Liu et al., 2016; Wei et al., 2012). Furthermore, the ε_{Nd} and $^{87}Sr/^{86}Sr$ composition of sediments from ODP site 1145 (3175 m) located deeper in the slope than site 2905 (1647 m; Fig. 1b) suggest a maximum sediment contribution of 3−15 % of sediments from Luzon for the past 450 ka (Boulay et al., 2005). Therefore, we shall hereupon consider that the terrestrial contribution to the northeastern SCS slope is dominated by sediments from Southwest Taiwan and South China.

S5.2. Physiological and ecological drivers of the carbon isotopic composition of plant tissues

The isotopic composition of plant waxes, and in general of plant tissues, is primarily determined by the plant's photosynthetic pathway and additionally influenced by the plant's ecophysiology (Collister et al., 1994; Diefendorf et al., 2010; Kohn, 2010; Pedentchouk et al., 2008; Rommerskirchen et al., 2006; Vogts et al., 2012). Within the wide range of $\delta^{13}C$ values in plants, two end-members can be recognized (Bender, 1971; Ehleringer and Cerling, 2002; O'Leary, 1988): C_3 woody angiosperms from highly-moist environments (minimum $\delta^{13}C$ of ca. -39 ‰), and C_4 non-woody angiosperms from highly-arid environments (maximum $\delta^{13}C$ of ca. -8 ‰), whereas the carbon isotopic composition of all other C_3, C_4 and CAM plants oscillates between these two end-members ($\delta^{13}C_{C3}$ = -20 to -39 ‰; $\delta^{13}C_{C4}$ = -20 to -8 ‰; $\delta^{13}C_{CAM}$ = -10 to -28 ‰). The $\delta^{13}C_{CAM}$ composition overlaps with both C_3 and C_4 signatures (Collister et al., 1994; O'Leary, 1981), however their biomass production, and thus their contribution to the sedimentary pool, is usually very low because their life strategy is mainly focused towards stress survival and not towards high productivity (Lüttge, 2004). In addition to the photosynthetic pathway, plant water use efficiency has a clear role modulating leaf-CO_2 concentration during photosynthesis and can thus influence the carbon isotopic composition in plant tissues, with moisture stress leading towards ^{13}C enrichment (Cowan and Farquhar, 1977; Diefendorf et al., 2010; Douglas et al., 2012; Kohn, 2010; Prentice et al., 2011). In this line, a significant positive correlation between mean annual precipitation (MAP) and $\delta^{13}C_{C3}$ has been observed over large regions worldwide (Diefendorf et al., 2010; Kohn, 2010; Prentice et al., 2011). This correlation between MAP and the $\delta^{13}C_{C3}$ becomes significant when local MAP falls below ~1000 mm yr^{-1} (Diefendorf et al., 2010; Kohn, 2010), whereas $\delta^{13}C_{C3}$ values above -25.5 ‰ are restricted to MAP regimes under 500 mm yr^{-1} (Kohn, 2010). In addition to MAP, the plant functional type (PFT; i.e. woody vs. non-woody, angiosperms vs. gymnosperms, deciduous vs. evergreen) can also affect the $\delta^{13}C_{C3}$ composition because it largely determines the plant's water use efficiency through leaf morphology, root depth, leaf temperature, mesophyll conductance, etc. (Diefendorf et al., 2010; Pedentchouk et al., 2008). Thus, changes in PFT abundance within ecosystems can induce small changes (up to $\pm$ 2.7 ‰) on the final $\delta^{13}C_{plant}$ composition of sedimentary organic matter under similar MAP regimes (Diefendorf et al., 2010; Prentice et al., 2011).

Chapter 6

Synopsis, conclusions and outlook

In the following sections the major findings in this thesis are discussed in function of the established research hypotheses and general objectives, while some important pointers are given at the end for future research efforts.

6.1 Synopsis

6.1.1. Summer monsoon precipitation as driver of the variability in paleo-hydrologic records from the Northern Bay of Bengal and the Northern South China Sea

Under the modern boundary conditions, seasonal precipitation patterns in South and Southeast Asia are strongly associated to Asian monsoon seasonality, and the largest amount of precipitation on the annual basis (50−80 %) is delivered around the summer monsoon season (Global Network for Isotopes in Precipitation; GNIP; IAEA/WMO, 2015). This lead to the hypothesis that summer monsoon precipitation is the main driver of the variability in paleo-hydrologic records from the Northern Bay of Bengal and the Northern South China Sea. The hypothesis was analyzed in *Chapter 3* and *Chapter 5*.

In the Northern Bay of Bengal (NBoB; *Chapter 3*), IsoCAM model results showed that changes in the δD of precipitation over millennial timescales were mainly driven by the amount effect, and strongly influenced by summer precipitation originating from a constant NBoB moisture source throughout the study period. The same conclusion was also reached after the removal of vegetation apparent fractionation effects from the hydrogen paleo-isotopic record of plant wax *n*-alkanes, while biasing impacts from the fluvial "plume effect" (Breitenbach et al., 2010) on the record were discarded. In the Northern South China Sea (NSCS; *Chapter 5*), in contrast, over millennial time scales the isotopic composition of precipitation was regarded as a product of the variability of large-scale circulation convergence over the South China region. Besides, the NSCS δD record of plant wax *n*-alkanes was regarded as capturing the annual

weighted average precipitation isotopic composition due to the lack of a clearly defined growing season (Thomas et al., 2014). Based on the evidence provided by previous studies (Aggarwal et al., 2004; Araguás-Araguás et al., 1998; Dayem et al., 2010; Ding and Chan, 2005; Peng et al., 2010), summer monsoon moisture was identified as moisture exported from the NBoB, characterized by higher isotopic values than moisture from the Western North Pacific (WNP). In turn, moisture exported from the WNP was mainly related to the activity of tropical cyclones originated in the WNP, active throughout the summer monsoon season and during the early onset of winter monsoon circulation. All in all, moisture derived from summer monsoon was considered to contribute the most to the annual precipitation balance in the NSCS and to the hydrogen isotopic signature of *n*-alkanes, partly because of the more random nature of tropical cyclones. However, the contribution of tropical cyclones to the annual precipitation balance in the NSCS was considered significant during the earliest and latest parts of the Holocene.

Therefore, the hypothesis that summer monsoon precipitation is the main driver of the variability in paleo-hydrologic records from the Northern Bay of Bengal and the Northern South China Sea is considered partially valid. Summer monsoon is an important driver of paleo-hydrologic records in both regions but its imprint is larger in the NBoB than in the NSCS. In both regions, however, the roles of precipitation sources besides the summer monsoon (mainly tropical cyclones) as drivers of the isotopic signature of hydrologic records should be properly assessed and quantified. The source of modern summer precipitation (i.e. monsoon or tropical cyclones) can be identified on the basis of precipitation δD, $\delta^{18}O$ and d-excess composition (e.g. Peng et al., 2010), however similar methods are difficult to apply for paleo-hydrologic records due to the need of simultaneous measurements for oxygen and hydrogen isotopes in the same archive. Thus, future studies addressed to quantify the relative contribution of different paleo-moisture sources could be focused on the analysis of paleo-water captured in glaciers or groundwater reservoirs (e.g. Aggarwal et al., 2004).

6.1.2. Indian and East Asian summer monsoons strength during the Late Pleistocene and the Holocene

A previous compilation of moisture records from across the Asian Monsoon domain which derived in the construction of an Asian effective moisture index (Fig. 6.1f; Herzschuh, 2006) suggested

that maximum moisture conditions in Asia occurred during the first half of the Holocene (11−5 ka BP). In previous studies, maximum summer monsoon strength in the Early Holocene has been attributed as a response to maximum summer insolation in the Northern Hemisphere (e.g. Y. Wang et al., 2005) which occurred around 11.5 ka BP (Fig. 6.1g). Thus, the hypothesis was proposed that summer monsoon reached maximum strength during the Early Holocene both in the Northern Bay of Bengal and the Northern South China Sea. This hypothesis was explored on *Chapter 3* and *Chapter 5*.

In the NBoB surroundings (*Chapter 3*), it was estimated based on the IsoCAM model results that summer precipitation amount was 20% higher during the Mid-Holocene (6K scenario), as well as 20% lower during the Heinrich Stadial 1 (HS1 scenario), relative to the pre-industrial period (PI scenario). In turn, precipitation changes inferred from the NBoB alkane δD record (Fig. 6.1d) indicated that the Holocene period (last 11 ka) was moister than the Late Pleistocene period of the record (18–11 ka BP), with a two-step intensification of the monsoon during the Bölling/Alleröd (B/A) and the Early Holocene. Precipitation was strongest during the Early Holocene Climatic Optimum (EHCO) with maximum monsoon strength reported between 10.5–6 ka BP, slightly after the peak of maximum summer insolation (Fig. 6.1d, g). In turn, the most arid conditions were recorded during the Heinrich Stadial 1 (HS1) between 16.9–15.4 ka BP due to severe North Atlantic cooling, giving evidence of teleconnections between the Asian summer monsoon system and the North Atlantic climate through changes in Hadley circulation (Leuschner and Sirocko, 2000; Mohtadi et al., 2014). Maximum monsoon strength recorded during the Early Holocene was coherent with other paleo-hydrologic records from the ISM domain (Berkelhammer et al., 2010; Breitenbach, 2010; Cai et al., 2012; Fleitmann et al., 2007), pointing to a synchronous variability of the western (Arabian) and eastern (Bengal) Indian summer monsoon branches. Summer monsoon intensification during the B/A period was also coherent with other paleo-hydrological records across the Asian monsoon domain such as the Moomi, Timta and Dongge speleothem $\delta^{18}O$ records from Yemen, the western Himalaya and southeast China (Dykoski et al., 2005; Shakun et al., 2007; Sinha et al., 2005), and the Asian effective moisture index (Fig. 6.1f; Herzschuh, 2006). Minimum summer monsoon strength before 15 ka BP is also evident in speleothem records (Dykoski et al., 2005; Shakun et al., 2007) and reflected in the Asian effective moisture index. In turn, Holocene precipitation changes in Southeast China and Taiwan (*Chapter 5*) inferred from the $\delta D_{alkanes}$ record suggested higher moisture contribution from the Indian Ocean

into the NSCS after 9 ka BP (Fig. 6.1d). Enhanced relative moisture contribution from the Indian Monsoon domain was attributed to the strengthening of summer monsoon circulation across South Asia in agreement with results from the NBoB record. Moisture exported from the Indian Ocean into South China by the summer monsoon was associated to heavier hydrogen isotopic values compared to that from the Pacific Ocean delivered by tropical cyclones. In fact, the positive-most values in the $\delta D_{alkanes}$ record form the NSCS actually correspond with negative-most $\delta D_{alkanes}$ values in the NBoB record. Heavier isotopic values in the Indian Ocean moisture after 9−8 ka BP were partly attributed to a reduction of the continental effect on precipitation around Indochina. Before 9 ka BP, higher frequency of tropical cyclones making landfall in South China was considered to have a significant relative contribution to the annual balance of precipitation in the region and a strong imprint on the alkane isotopic signature. The enhanced tropical cyclone activity in South China was proposed as the product of a warming background state of the Indo-Pacific Warm Pool (IPWP) during the first part of the Early Holocene. The gradual reduction of the SST gradient across the Pacific throughout the Holocene (Conroy et al., 2008; Moy et al., 2002) likely caused an overall decrease of tropical cyclone activity and its contribution to yearly precipitation in the region of South China and Taiwan between 8 and 5 ka BP, giving way to a strongly dominant relative contribution of summer monsoon precipitation in the annual moisture balance. During the Late Holocene, the $\delta D_{alkanes}$ record from the NBoB clearly showed an overall weakening trend of the summer monsoon. However a trend of this type was not so clearly observed in the $\delta D_{alkanes}$ record form the NSCS. Here, enhanced activity of tropical cyclone activity over Taiwan after 4 ka BP, due to the establishment of a cooling background state of the IPWP, is likely to mask summer monsoon weakening in the record. Altogether, a warming background state of the IPWP was related to stronger of the summer monsoon circulation, whereas a cooling background state of the IPWP was related to weaker of summer monsoon circulation.

Altogether, results from *Chapter 3* and *Chapter 5* are in general agreement with the common notion that maximum summer monsoon strength was attained during the Early Holocene in response to maximum summer insolation around 11.5 ka BP (Fig. 6.1g). The Asian effective moisture index (Herzschuh, 2006) clearly shows optimum moisture conditions during the Early Holocene between 11 and 5 ka BP (Fig. 6.1f). However, the precise timing of maximum moisture shows regional inconsistency with locations under the influence of the Indian Monsoon recording maximum moisture earlier than those affected by the East Asian Monsoon (Fig. 6.1f); whereas

records from locations in the transitional areas between the two monsoon domains seem to display a prolonged maximum moisture period (e.g. Dongge Cave Speleothem $\delta^{18}O$ record in Southeast China; Fig. 6.1e). A partial explanation for this inconsistency is that large areas within the East Asian Monsoon domain are under the influence of the Meiyu Front which, though intrinsically linked to the summer monsoon circulation, is also associated to other factors such as the position and intensity of pressure cells over land and overseas (Jiang and Ni, 2004). Thus the location, timing, duration and strength of the Meiyu Front may vary over longer time scales in fashions partially associated to the Asian summer monsoon strength but also to other atmospheric features, particularly the position and strength of the Western North Pacific High (WNPH) and the subtropical jet. Unfortunately, the evolution of the Meiyu Front over millennial time scales is not disentangled from that of the summer monsoon and efforts should be focused in this direction for future research. Regarding the summer monsoon circulation, previous studies show that atmospheric circulation patterns and moisture transport during the summer monsoon are closely connected throughout the Indian and Pacific Oceans (Ding et al., 2004; Ding and Chan, 2005; Shi et al., 2008), for which makes sense to study the Asian summer monsoon as a single large scale phenomenon with uniform strength evolution across South and Southeast Asia, and regard the regional differences in precipitation patterns as the product of the interaction between summer monsoon circulation and local geographic, oceanographic and/or atmospheric features.

The hypothesis that summer monsoon reached maximum strength during the Early Holocene both in the Northern Bay of Bengal and the Northern South China Sea is considered valid in both regions. Mainly because we consider that the summer monsoon circulation system is one large phenomenon spanning across South and Southeast Asia and that other climatic features such as the Meiyu Front in China and tropical cyclones in the Pacific Ocean are strongly linked to the summer monsoon circulation but largely influenced by other partially independent atmospheric features.
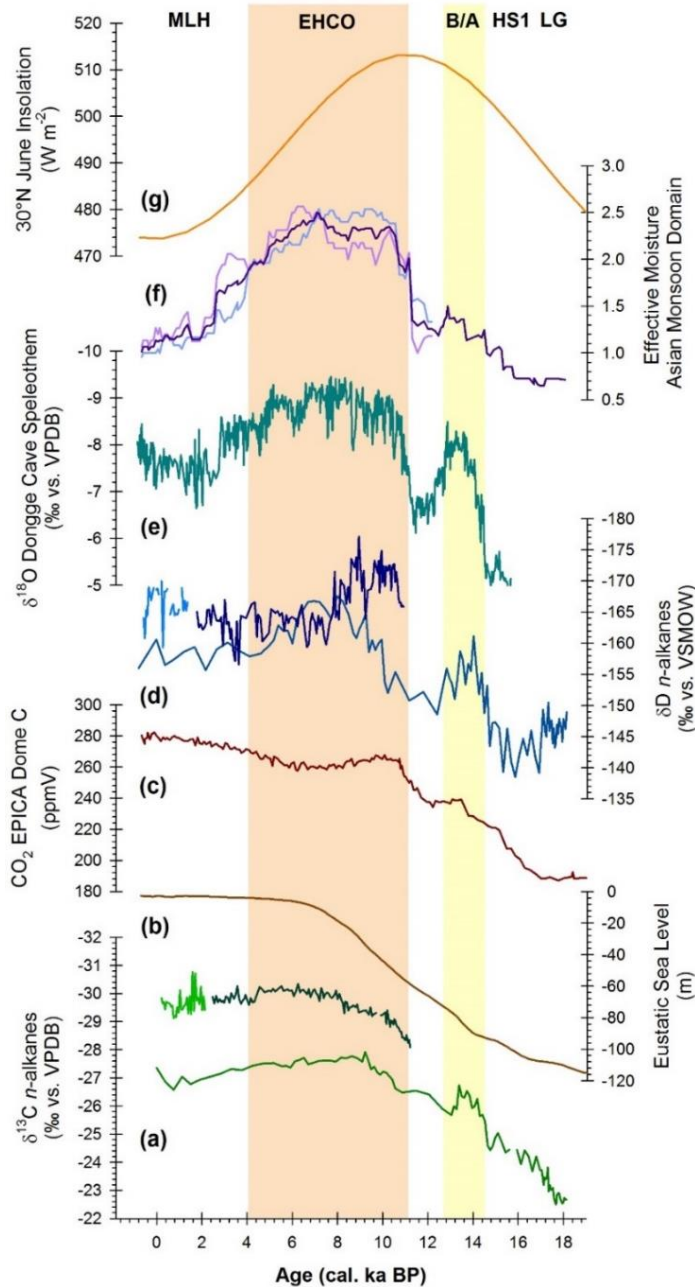
Fig. 6.1. Summary figure of vegetation and precipitation evolution around the Northern Bay of Bengal (NBoB) and the Northern South China Sea (NSCS) in relation to summer monsoon strength, eustatic sea level, atmospheric pCO_2 and Northern Hemisphere summer insolation. **(a)** Weighted-average of the n-C_{29} and n-C_{31} carbon isotopic records ($\delta^{13}C$ alkanes) from the NBoB (medium green line, *Chapter 3*); and the NSCS (dark and light green lines, *Chapter 5*); **(b)** relative eustatic sea level with respect to the present (Stanford et al., 2011); **(c)** EPICA Dome C ice-core Holocene and transition CO_2 record (Monnin et al., 2004); **(d)** Ice-volume-corrected weighted-average of the n-C_{29} and n-C_{31} hydrogen isotopic records (δD alkanes) from the NBoB (medium blue line, *Chapter 3*) and the NSCS (also corrected for temperature, dark and light blue lines, *Chapter 5*); **(e)** Chinese speleothem $\delta^{18}O$ record: Dongge

Cave, South China (Dykoski et al., 2005); **(f)** Asian Effective Moisture Index (light blue),effective moisture index in the Indian monsoon domain (light purple) and the East Asian monsoon domain (dark purple) (Herzschuh, 2006); **(g)** 30°N June insolation curve (Berger and Loutre, 1991). Axes are reversed in (a), (d) and (e) to show increase of C_3 vegetation and precipitation intensification towards the top of the graph. Abbreviations at the top are as follows: MLH: Mid-to-Late Holocene; EHCO: Early Holocene Climatic Optimum; B/A: Bölling/Alleröd; HS1: Heinrich Stadial 1; LG: Late Glacial.

6.1.3. Terrestrial vegetation composition over millennial time scales in relation to changes of summer monsoon strength in the Northern Bay of Bengal and the Northern South China Sea

Several long term vegetation records from monsoonal Asia (based either on sedimentary pollen composition and/or stable carbon isotopes) have pointed to monsoon precipitation as an important driver of vegetation composition (Demske et al., 2009; Dixit and Bera, 2013; Jiang and Ding, 2008; P. M. Liew et al., 2006; Sharma et al., 2006; Sun and Li, 1999; Wang et al., 2007; Xiao et al., 2014; Zhao et al., 2009). Hence, the hypothesis was established that terrestrial vegetation composition over millennial time scales is primarily driven by changes of summer monsoon strength in the Northern Bay of Bengal and the Northern South China Sea. This hypothesis is evaluated based on results from *Chapter 3* and *Chapter 5*.

Vegetation changes in the G-B-M basin deduced from the NBoB alkane $\delta^{13}C$ record (*Chapter 3*) indicated a shift from C_4-plant dominated ecosystems during the Late Glacial (LG) to mixed C_3/C_4-plant mixed vegetation during the Holocene. The highly significant correlation of δD and $\delta^{13}C$ records gave evidence of the strong link between vegetation composition and precipitation variability. However summer monsoon strength was not the sole driver of vegetation composition variability throughout the study period. It was also established that C_4 plants abundance was largely linked to $p CO_2$ variability during the LG and Heinrich Stadial 1 (HS1) periods and only became independent from atmospheric CO_2 concentration after about 15 ka BP. The balance between moisture availability, ambient temperature and atmospheric $p CO_2$ is critical to determine which one of these variables will exert the main role as stressor for vegetation (e.g. Pearcy and Ehleringer, 1984). In the NBoB, the switch from atmospheric $p CO_2$ to local moisture availability as main driver of vegetation composition seem to have taken place when $p CO_2$ became higher than 220 ppmV. This balance is expected to change in function of particular environmental conditions and plant biodiversity between locations and further research should be directed to

analyse the response of vegetal communities to regional environmental parameters in the geological past.

On the other hand, vegetation changes in Southeast China and Taiwan (*Chapter 5*) inferred from the NSCS $\delta^{13}C_{alkanes}$ record in combination with results from previous pollen records from the region suggested an overall predominance of C_3 vegetation under (semi) moist conditions throughout the Holocene. However, the $\delta^{13}C_{alkanes}$ record during the Early Holocene did not reflect vegetation changes as a function of moisture/precipitation variability in the Northern South China Sea (NSCS) region, but rather was interpreted as representing vegetation variability in response to eustatic sea level change. Larger expansion of the coastal plains over the exposed NSCS continental shelf due to lower eustatic sea level favoured the expansion of herbs and grasses before 8 ka BP contributing to higher $\delta^{13}C_{alkanes}$ values. The drowning of the shelf after 8 ka BP caused a migration of the shoreline closer to the foothills of mountain ranges, drastically reducing the extension of grasslands and allowing a better representation of tree vegetation in marine sedimentary archives, which cause a decrease of $\delta^{13}C_{alkanes}$ values after 8 ka BP. The role of sea level change as a driver of vegetation composition was as regulator of the habitat extension and its effect were much larger in the NSCS than in the NBoB mainly because in the latter case the full drowning of the coastal plain was prevented by continuous aggradation due to massive fluvial sediment delivery (Goodbred Jr. and Kuehl, 2000a).

Altogether, the role of summer monsoon strength as driver of vegetation variability is more clearly appreciated in the NBoB region than in the NSCS, which may partially result from differences in seasonality. Seasonality is considered stronger in the NBoB surroundings due to the larger proportion of total annual precipitation (70−80 %) focused in the summer monsoon months (June to September) as compared to the NSCS surroundings (40−60 %) (IAEA/WMO; 2015. Global Network of Isotopes in Precipitation. The GNIP Database. Accessible at: http://www.iaea.org/water). This would translate into a shorter growing season around the NBoB than in the NSCS and an important forcing mechanism for vegetation adaptations. The effect of stronger seasonality in the NBoB is also evident in the higher proportion of C_4 vegetation in this region (Holocene $\delta^{13}C_{alkanes} \approx 26-28$ ‰) as compared to the NSCS (Holocene $\delta^{13}C_{alkanes} \approx 28-31$ ‰).

The imprint of human activities on regional vegetation in the two study areas is unclear but not altogether discarded. Traces of human activity in the G-B-M delta region are possibly evident in the last 0.5 ka of the NBoB $\delta^{13}C_{alkanes}$ record, in which a sudden decrease in values is observed (Fig. 6.1a). This sharp negative excursion of $\delta^{13}C_{alkanes}$ values is nearly as large in magnitude and more abrupt (~1‰ over ~0.5 ka) than that observed at the beginning of the Holocene (~1.5 ‰ over ~1 ka; Fig. 6.1d). It is thus possible that such an abrupt change may be the result of advance irrigation techniques that allowed an increase in C_3 vegetation proportion through enhanced agriculture of rice and/or other C_3 crops in the G-B-M delta area even under monsoon weakening conditions during the Little Ice Age (LIA; Fig. 6.1d). In the region of South China and Taiwan, the NSCS $\delta^{13}C_{alkanes}$ record displays a subtle trend towards higher $\delta^{13}C_{alkanes}$ values through the last 2 ka, which could possibly be associated to the progressive clearance of natural forested areas to give way to croplands after the emergence of rice agriculture in Southeast China (ca. 5.0 ka BP) and Taiwan (ca. 4.8 ka BP) (Zhang and Hung, 2010). Enhanced agricultural activities during the last 2 ka have been inferred based on the analysis of terrestrial biomarkers in sediments from the Pearl River estuary (Strong et al., 2013).

The hypothesis that terrestrial vegetation composition over millennial time scales is primarily driven by changes of summer monsoon strength in the Northern Bay of Bengal and the Northern South China Sea is considered to be partially valid. The dependence is stronger in the NBoB region because of the clear dominance of the summer monsoon as provider of moisture on the annual balance. However the dependence is less clear in the NSCS region due to additional sources of moisture year around besides the summer monsoon. The bias introduced by changes in eustatic sea level partially masked the response of vegetation to precipitation variability in this region.

6.1.4. Export of terrigenous organic matter to the ocean by fluvial discharge in relation to summer monsoon strength

Evidence suggests that, after strong rainfall events, rivers display enhanced loads of terrestrial particulate organic carbon due to the wash-off of soils by intense precipitation (e.g. Herbeck et al., 2011). Therefore, the hypothesis was suggested that export of terrigenous organic matter to the

ocean is higher in periods of stronger summer monsoon due to enhanced fluvial discharge associated to higher precipitation amount. This hypothesis was explored in *Chapter 4*.

Terrestrial organic matter export to the NBoB continental slope over the last 18 ka was driven both by summer monsoon strength, which determined runoff intensity, and by relative eustatic sea level, which determined the morphology of the spatial connection between the Eastern Northern Bay of Bengal Shelf and the G-B-M river mouth. High terrestrial organic matter content (Fig. 6.2c) was observed during the Late Glacial (LG) and the Heinrich Stadial 1 (HS1) due to drastically lower eustatic sea level (between -120 m and -80 m respect to the present; Fig. 6.2d) which allowed a more direct connection between the Eastern Bengal Slope and the G-B-M river mouth. Previous evidence suggests that as much as two thirds of terrestrial particulate organic carbon are lost within river delta areas due to fast remineralization (Keil et al., 1997). Thus, smaller delta area, combined with shorter distance between the OM source and the depo-center, during low sea level stands may largely reduce organic matter remineralization and explain the higher content of terrestrial organic matter observed in glacial sedimentary records (Keil et al., 1997). Altogether, in the NBoB, a gradual shift in organic matter composition from terrestrial-dominated during the Late Glacial to marine-dominated during the Holocene was observed (Fig. 6.2b). A similar phenomenon has been previously reported for other shelf areas off-shore large river systems such as the Amazon (Schlünz et al., 1999), highlighting the major role that sea level plays worldwide as regulator of sedimentary organic matter sources in addition to terrestrial precipitation/runoff and marine productivity.

Terrestrial organic matter content was also high during the Bölling/Alleröd and the Early Holocene (Fig. 6.2c) under summer monsoon strengthening conditions in response to enhanced fluvial discharge (Fig. 6.2f). It has been previously reported that the export of terrestrial organic matter is largely facilitated by its sorption to mineral surfaces (Keil et al., 1997). Thus, the large availability of lithogenic particles washed-off jointly with organic matter from soils by strong rainfall provides an excellent vehicle to effectively transport terrestrial organic matter from land into the ocean by fluvial runoff. During these periods, old terrestrial degraded organic matter trapped in relict shelf deposits was also remobilized and flushed due to the occurrence of the melt water pulses 1A and 1B (Fig. 6.2e) in conjunction to the B/A and the EHCO, which caused fast flooding of the continental shelf due to enhanced sea level change rates (Stanford et al., 2011).

The hypothesis that export of terrigenous organic matter to the ocean is higher in periods of stronger summer monsoon due to enhanced fluvial discharge associated to higher precipitation amount is thus valid. However increased precipitation and runoff were not the main drivers of terrigenous organic matter export to the ocean. The role played by eustatic sea level in facilitating the export of terrestrial organic matter to the deep-sea, by shortening the distance between the basin and the depo-center and/or by remobilizing old OM deposits in the shelf, was of considerable magnitude even under minimum monsoon strength.
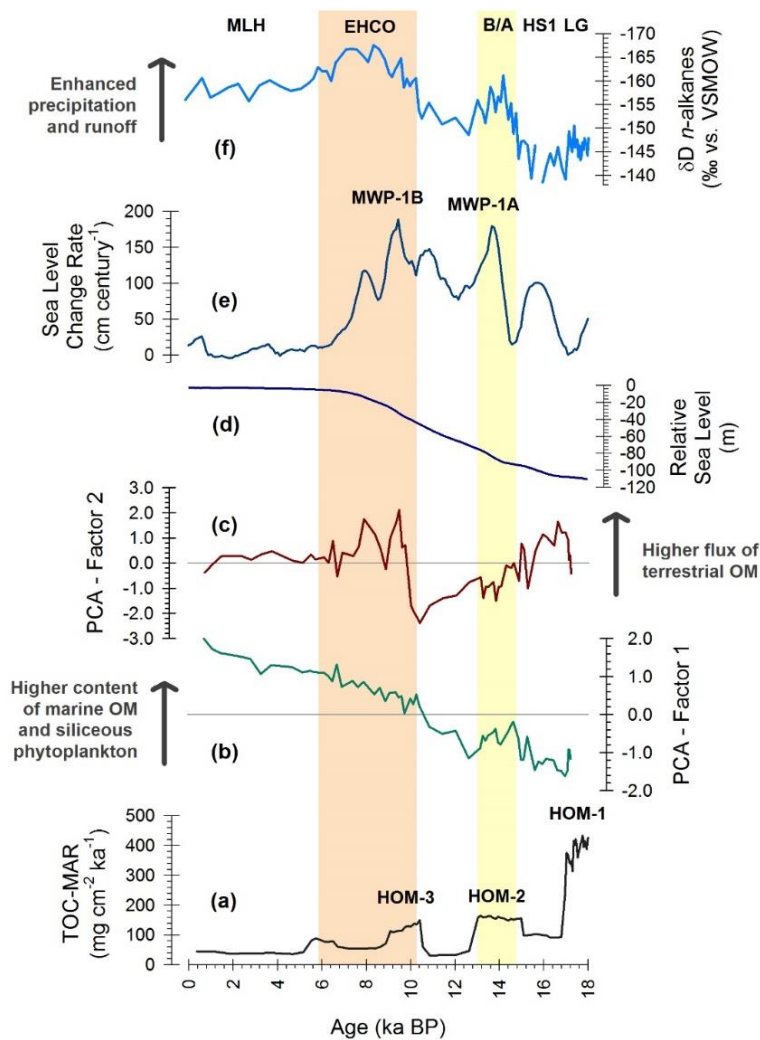
Fig. 6.2. Summary figure of organic matter accumulation and terrestrial organic matter export to the ocean in the Northern Bay of Bengal (NBoB) in relation to summer monsoon strength, eustatic sea level, and sea level change rate. **(a)** Total organic carbon mass accumulation rate (TOC-MAR) with periods of high organic matter accumulation

(HOM-1 to 3) indicated; **(b)** PCA-Factor 1 (49 % of the total variance of total hydrolysable amino acids composition) is interpreted as indicator for OM origin and degradation driven by sea level change; higher values indicate higher marine-versus-terrestrial OM contribution and higher proportion of siliceous-over-calcareous plankton; **(c)** PCA-Factor 2 (19% of the total variance of total hydrolysable amino acids composition) is interpreted as indicator for high flux of degraded terrestrial OM to the Eastern Bengal Slope. For comparison: **(d)** relative sea level with respect to the present (Stanford et al., 2011); **(e)** relative sea level change rate (Stanford et al., 2011), showing the Melt Water Pulses 1A and 1B (MWP-1A and -1B); **(f)** weighted-average of the n-C_{29} and n-C_{31} ice-volume-corrected hydrogen isotopic records from core SO188-342KL ($\delta D_{alkanes}$), as indicator of precipitation intensity over the lower G-B-M basin. Axis is reversed in (d) to show precipitation intensification towards the top of the graph. Color bars highlight periods of summer monsoon intensification. Abbreviations at the top are as follows: MLH: Mid-to-Late Holocene; EHCO: Early Holocene Climatic Optimum; B/A: Bölling/Alleröd; LG: Late Glacial.

6.1.5. Sedimentary organic matter accumulation and preservation in relation to summer monsoon strength

High flux of particulate organic carbon from the surface to the deep ocean has been previously been observed in combination with enhanced fluvial lithogenic flux during the summer monsoon season (Unger et al., 2003). Likewise, it has been observed that enhanced organic matter accumulation often results in enhanced preservation due to oxygen exposure reduction (Hartnett et al., 1998). Based on this observations, the hypothesis was proposed that sedimentary organic matter accumulation and preservation were higher in periods of stronger summer monsoon. This hypothesis was analyzed in *Chapter 4*.

In total, three periods of high organic matter accumulation (HOM-1 to -3) were identified (Fig. 6.2a): the Late Glacial (LG; HOM-1; 18−17 ka BP) the Bölling/Alleröd (B/A; HOM-2; 15−13 ka BP) and the first part of the Early Holocene Climatic Optimum (EHCO; HOM-3; 10.5−9.0 ka BP), whereas the Mid-to-Late Holocene (MLH; last 6 ka) was identified as a period of low organic matter accumulation. The organic carbon (OC) accumulation rate in the NBoB was maximum towards the LG (HOM-1) period (387 ± 47 mg OC cm^{-2} ka^{-1}; Fig. 6.2a) despite the minimum summer monsoon strength and the considerable reduction of precipitation and runoff (Fig. 6.2f). During this period organic matter was primarily of terrestrial origin characterized by high degree of degradation (Fig. 6.2b, c), but the large supply of lithogenic particles favored the export and burial of fresher marine organic matter as well. On the other hand, the B/A (HOM-2) and the first part of the EHCO (HOM-3) were both characterized by summer monsoon

intensification and high organic carbon accumulation in the sediments (157 ± 5 mg OC cm^{-2} ka^{-1} and 124 ± 13 mg OC cm^{-2} ka^{-1}, respectively; Fig. 6.2a) due both to enhanced fluvial discharge of terrestrial organic matter and lithogenic particles and to the increase of marine productivity driven by cyclonic-eddies powered by summer monsoon winds. Lower eustatic sea level as compared to the present during the B/A (-90 to -70 m) and the first part of the Early Holocene (-40 to -20 m) still facilitated transport of terrigenous material into the Eastern Bengal Slope in combination with summer monsoon strengthening (Fig. 6.2d, f). During the EHCO, however, the maximum freshening of the ocean surface, the high turbidity of the G-B-M river plume and the strong cloud cover in the NBoB during the EHCO prevented marine productivity to be as high as in other areas of the Bay of Bengal during this period, reflected in lower organic carbon accumulation rates (maximum 150 mg OC cm^{-2} ka^{-1} in the Eastern NBoB Slope versus $300-400$ mg OC cm^{-2} ka^{-1} offshore the Mahanadi River) (Phillips et al., 2014). The disconnection of the Eastern NBoB Slope from the G-B-M river mouth after 7 ka BP, when maximum sea level was reached (Fig. 6.2d), and the weakening of the summer monsoon after 6 ka BP (Fig. 6.2f) caused a final drop of organic carbon accumulation rates to minimum values during the MLH (> 80 mg OC cm^{-2} ka^{-1}; Fig. 6.2a).

Altogether, the export from the photic zone and preservation through the water column of organic matter, both terrestrial and marine, was largely promoted during periods of high coastal proximity and/or enhanced fluvial discharge by the ballasting effect of terrigenous lithogenic particles (e.g. Armstrong et al., 2002) which considerably reduced exposure time of organic matter to oxygen and to the action of biodegrading microorganisms. For instance, during the summer monsoon season, the large availability of lithogenic particles makes the export of particulate organic matter higher in the Bay of Bengal than in the Arabian Sea, an area likewise affected by the Indian summer monsoon but characterized by considerably higher productivity (Ramaswamy and Nair, 1994).

When compared to high productivity areas of the world with large organic carbon export flux towards the sediments, the organic carbon (OC) accumulation rate in the NBoB towards the end of the last glacial maximum (387 ± 47 mg OC cm^{-2} ka^{-1}) is of the same order of magnitude than that of the Arabian Sea (555 ± 441 mg OC cm^{-2} ka^{-1}), an area of high upwelling activity (Sirocko and Ittekkot, 1992). The situation, however, becomes considerably dissimilar during the Late Holocene, when organic carbon accumulation rates in the NBoB drop dramatically (about

300 mg OC cm^{-2} ka^{-1} less than during the Late Glacial period), due to the disconnection of the Eastern Bengal Slope from the G-B-M river mouth. These results are all the more important considering that Site 342KL is located at the margin of the Bay of Bengal submarine fan and not in the region of highest sediment accumulation (Weber et al., 2003). For comparison, OC accumulation rates in the upper Amazon Fan (ODP Site 938) were up to two orders of magnitude higher than those of Site 342KL during the late glacial period (10 400 mg OC cm^{-2} ka^{-1}), and are almost one order of magnitude lower than at Site 342KL in the present (14 mg OC cm^{-2} ka^{-1}) (Schlünz et al., 1999). In this light, the role played by river-connected continental margins on carbon sequestration during low sea level stands had likely major impacts on the global carbon budget and requires further investigation in the future.

The hypothesis that sedimentary organic matter accumulation and preservation were higher in periods of stronger summer monsoon is thus valid. In particular, both organic matter export and preservation were largely promoted by the increased availability of lithogenic ballast particles provided by fluvial runoff. However the role played by eustatic sea level as regulator of terrestrial versus marine organic matter input and active versus passive sedimentation in the continental margin is larger than that of precipitation and runoff during low sea level stands.

6.2. Conclusions

The first objective of this thesis was to reconstruct the natural variability of the Asian Summer Monsoon and its effects during the Late Quaternary through the analysis of changes in terrestrial vegetation composition, on-land precipitation patterns and the quality and quantity of organic matter exported to the deep ocean. Throughout this thesis, the information provided by terrestrial biomarkers and bulk organic matter composition from the Northern Bay of Bengal and the Northern South China Sea sediment cores, via the reconstruction of terrestrial vegetation composition, precipitation patterns, and organic matter sources and preservation state, allowed the reconstruction not only of summer monsoon variability but also of other climatic and oceanographic aspects linked to the summer monsoon in the study regions. These additional aspects include for instance fluvial export of organic and inorganic matter to the ocean, phytoplankton composition variability, and features of marine and atmospheric circulation (Fig. 6.3). Therefore, the first objective is considered successfully accomplished.
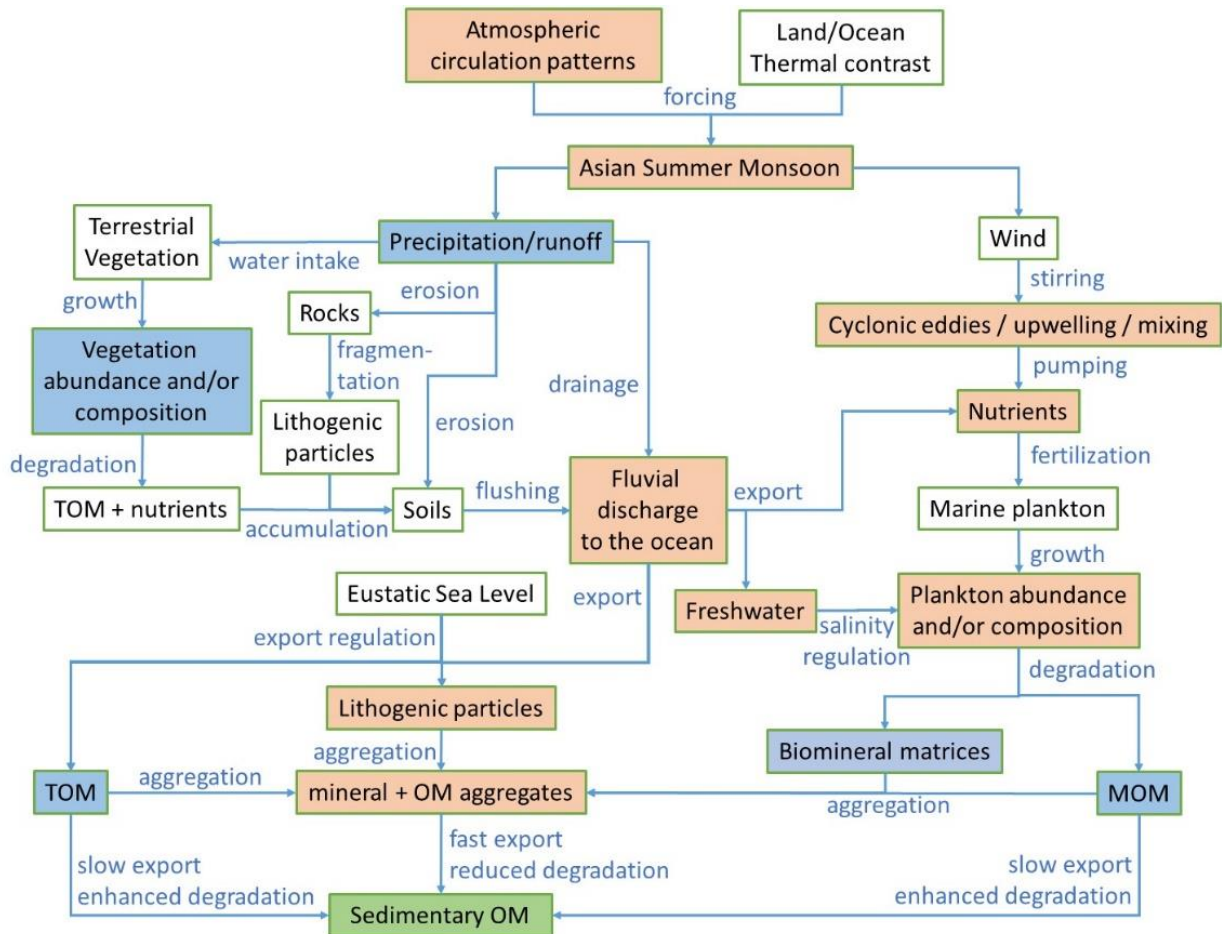
Fig. 6.3. Schematic diagram showing the relationships between the actors and processes connecting summer monsoon variability with sedimentary organic matter composition. Colored boxes indicate aspects reconstructed in this thesis: blue fillings indicate aspects reconstructed based on proxy evidence; red fillings indicate aspects reconstructed indirectly after proxy interpretation. Abbreviations are as follows: OM: organic matter; TOM: terrestrial organic matter; MOM: marine organic matter.

The second objective of this thesis was to identify the common and the specific patterns of summer monsoon variability between the South Asian and East Asian monsoon domains during the Late Quaternary. Through the analysis of on-land precipitation patters reconstructed in this study, and based on the circulation and moisture transport pathways studied in other works within monsoonal Asia, it is here considered that the summer monsoon should be studied as a single atmospheric phenomenon with span across South and Southeast Asia instead of the traditional

division between Indian and East Asian subsystems. In the case of the East Asian sector the complex interaction between the summer monsoon circulation and other atmospheric features such as tropical cyclones and the Meiyu Front make precipitation patterns much more complex than in the Indian sector. However, though intrinsically linked to the summer monsoon circulation, these patterns are partially independent and it is important to disentangle their imprint when interpreting paleo-environmental records aimed for the reconstruction of summer monsoon variability. With this vision in mind, we consider that the second objective of this thesis is also accomplished.

Altogether, the main conclusions of this thesis are:

(1) The summer monsoon is the most important driver of paleo-hydrologic records in both study regions though its imprint is larger in the NBoB than in the NSCS due to additional important sources of precipitation in the second case.

(2) The roles of additional precipitation sources besides the summer monsoon (such as tropical cyclones, both in the Indian and East Asian sectors, and the Meiyu Front, in China) may have important imprints on paleo-hydrologic records and should be properly assessed and quantified.

(3) The summer monsoon circulation reached maximum strength during the Early Holocene both in the NBoB and the NSCS regions, though the peak of maximum precipitation was not uniform across South and Southeast Asia due to the intervention of additional regional atmospheric, oceanographic and geographic factors in addition to summer monsoon circulation.

(4) Terrestrial vegetation composition over millennial time scales was primarily driven by changes of summer monsoon precipitation intensity, though the dependence was stronger in the NBoB than in the NSCS due to the larger role of summer monsoon as regulator of precipitation seasonality in the first case and the availability of additional precipitation sources in the second case.

(5) The export of terrigenous organic matter to the ocean was higher in periods of stronger summer monsoon precipitation due to enhanced fluvial discharge derived from increased runoff.

(6) The export of terrestrial organic matter to the ocean during periods of lower eustatic sea level was considerably large, even under minimum summer monsoon strength conditions, due to smaller delta area and significantly shorter distance between the river mouth and the continental shelf break.

(7) The export of organic matter to the deep ocean, its preservation through the water column and sediments, as well as its accumulation and burial were largely promoted by the increased availability of fluvial lithogenic ballasting particles.

(8) A warming IPWP background state was related to stronger Asian summer monsoon circulation and enhanced tropical cyclone activity in South China, whereas a cooling IPWP background state was related to weaker Asian summer monsoon circulation and enhanced tropical cyclone activity in Taiwan.

(9) The summer monsoon circulation system is a single phenomenon than spans across South and Southeast Asia whereas other climatic features such as the Meiyu Front in China and tropical cyclones both in the Pacific and Indian Oceans are strongly linked to the summer monsoon circulation but also largely regulated by other partially independent regional features.

6.3. Outlook

Based on the results and conclusions from this thesis we consider that future research should take into account some aspects identified in this thesis as missing or incomplete in the current state of the art of monsoon knowledge or proxy use. In the particular case of the NBoB and the NSCS tropical cyclones constitute an important source of precipitation in addition to summer monsoon and their contribution to the annual moisture balance should be properly assessed and disentangled in the geological past. Furthermore, in the specific case of the East Asian monsoon domain the evolution of the Meiyu Front should be carefully studied in relation to summer monsoon

circulation strength but also in relation to the strength of subtropical atmospheric features. All these topics can be further explored with the use of isotope enabled models and future studies focused on proxy/model comparisons are necessary to disentangle specific causes and effects through different regions across the Asian monsoon domain.

Vegetation/moisture relationships over the geological past should be studied preferably by in combination between isotopic and pollen records, as plants are highly adaptable organisms and their responses to moisture variability are non-linear. In this line, more studies focused towards plant ecophysiological responses to specific environmental gradients that affect plant wax production and/or isotopic composition in vegetation from tropical regions are highly required, as most of the current efforts are focused in vegetation from temperate regions. More studies focused on changes in modern regional vegetation composition in response to moisture variability across the Asian monsoon domain are necessary to determine the importance of the different sources of moisture to the vegetal communities in each region to further apply the results into the geological past. Furthermore, numerical models can be used to investigate the effects of other important drivers of vegetation such as pCO$_2$ and temperature in combination with moisture to determine regional ecological threshold points.

More comprehensive studies focused on organic matter recycling and transport by river systems are required to improve our understanding of the specific processes involved in different types/sizes of fluvial basins. Organic matter inventories and budgets should be carried out across the different courses of rivers to identify patterns of where and how organic matter is remineralized, recycled and/or exchanged in different river basins. Further efforts in this regard are also required for river estuaries and continental shelfs of river connected margins, to better understand the processes of export and exchange between terrestrial and marine organic matter.

Eustatic sea level should be considered and accounted for, when relevant, while interpreting paleo-records recovered from continental margins as it is a key regulator of the sediment sources to the sea floor and may strongly affect the representability of the records. Besides, the role played by river-connected continental margins on carbon sequestration during low sea level stands requires further investigation and should be accounted for the improvement of global carbon budgets in the geological past. Furthermore, it is considered that the architecture of deep-sea fans and canyon systems that serve as organic carbon funnels and deposits should be

carefully mapped and studied before the venturing of carbon budgets as sedimentation is no homogeneous throughout them and this could lead to considerable over/under- estimations.

The ocean/atmosphere interactions are just as important as land/ocean interactions in the regulation of summer monsoon circulation and ought to be taken into account when reconstructing the evolution of summer monsoon strength. More sensitivity studies should be performed with the use of numerical models to explore variability in teleconnections under different boundary conditions both in the present and in the geological past. Given the large amount of proxy evidence suggesting maximum summer monsoon strength between 11−8 ka BP, the implementation of a standard Early Holocene scenario is highly recommended for future model reconstructions across the Asian monsoon domain.

List of References

Aggarwal, P.K., Fröhlich, K., Kulkarni, K.M., Gourcy, L.L., 2004. Stable isotope evidence for moisture sources in the asian summer monsoon under present and past climate regimes. Geophys. Res. Lett. 31, 2–5. doi:10.1029/2004GL019911

Altabet, M., 1988. Variations in nitrogen isotopic composition between sinking and suspended particles: implications for nitrogen cycling and particle transformation in the open ocean. Deep. Res. 35, 535–554.

Altabet, M., Murray, D., Prell, W.L., 1999. Climatically linked oscillations in Arabian Sea denitrification over the past 1 m.y.: Implications for the marine N cycle. Paleoceanography 14, 732–743.

An, Z., Porter, S.C., Kutzbach, J.E., Xihao, W., Suming, W., Xiaodong, L., Xiaoqiang, L., Weijian, Z., 2000. Asynchronous Holocene optimum of the East Asian monsoon. Quat. Sci. Rev. 19, 743–762.

Ao, H., Dekkers, M.J., Qin, L., Xiao, G., 2011. An updated astronomical timescale for the Plio-Pleistocene deposits from South China Sea and new insights into Asian monsoon evolution. Quat. Sci. Rev. 30, 1560–1575.

Araguás-Araguás, L., Froehlich, K., Rozanski, K., 1998. Stable isotope composition of precipitation over southeast Asia. J. Geophys. Res. 103, 28721–28742. doi:10.1029/98JD02582

Armstrong, R. a., Lee, C., Hedges, J.I., Honjo, S., Wakeham, S.G., 2002. A new, mechanistic model for organic carbon fluxes in the ocean based on the quantitative association of POC with ballast minerals. Deep. Res. Part II Top. Stud. Oceanogr. 49, 219–236. doi:10.1016/S0967-0645(01)00101-1

Baker, A.J., Sodemann, H., Baldini, J.U.L., Breitenbach, S.F.M., Johnson, K.R., Hunen, J. Van, Pingzhong, Z., 2015. Seasonality of westerly moisture transport in the East Asian summer monsoon and its implications for interpreting precipitation δ18O. J. Geophys. Res. Atmos.

120, 5850–5862. doi:10.1002/2014JD022919.Received

Basumatary, S.K., Bera, S.K., Sangma, S.N., Marak, G., 2014. Modern pollen deposition in relation to vegetation and climate of Balpakram valley. Meghalaya, northeast India: Implications for Indo-Burma palaeoecological contexts. Quat. Int. 325, 30–40. doi:10.1016/j.quaint.2013.08.013

Bender, M.M., 1971. Variations in the 13C/12C ratios of plants in relation to the pathway of photosynthetic carbon dioxide fixation. Phytochemistry 10, 1239–1244.

Bera, S.K., 2003. Early Holocene pollen data from Mikir Hills, Assam, India. Paleobotanist 52, 121–126.

Berger, A., Loutre, M.F., 1991. Insolation values for the climate of the last 10 million years. Quat. Sci. Rev. 10, 297–317.

Berkelhammer, M., Sinha, A., Mudelsee, M., Cheng, H., Edwards, R.L., Cannariato, K.G., 2010. Persistent multidecadal power of the Indian Summer Monsoon. Earth Planet. Sci. Lett. 290, 166–172.

Berkelhammer, M., Sinha, A., Stott, L., Cheng, H., Pausata, F.S.R., Yoshimura, K., 2012. An abrupt shift in the Indian monsoon 4000 years ago. Geophys. Monogr. Ser. 198, 75–87.

Bhattacharya, K., Chanda, S., 1988. Late Quaternary vegetational history, palaeoecology and biostratigraphy of some deposits of Brahmaputra Basin, Upper Assam, India. J. Palynol. 23–24, 225–237.

Blasco, F., Bellan, M.F., Aizpuru, M., 1996. A vegetation map of tropical continental Asia at scale 1.5 million . J. Veg. Sci. 7, 623–634.

Bond, G.C., Showers, W., Elliot, M., Evans, M., Lotti, R., Hajdas, I., Bonani, G., Johnson, S., 1999. The North Atlantic's 1-2 kyr climate rhythm: relation to Heinrich events, Dansgaard/Oeschger cycles and the Little Ice Age. Geophys. Monogr. Ser. 112, 35–58.

Boos, W.R., Kuang, Z., 2010. Dominant control of the South Asian monsoon by orographic insulation versus plateau heating. Nature 463, 218–222.

Boulay, S., Colin, C., Trentesaux, a., Frank, N., Liu, Z., 2005. Sediment sources and East Asian

monsoon intensity over the last 450 ky. Mineralogical and geochemical investigations on South China Sea sediments. Palaeogeogr. Palaeoclimatol. Palaeoecol. 228, 260–277. doi:10.1016/j.palaeo.2005.06.005

Boulay, S., Colin, C., Trentesaux, A., Clain, S., Liu, Z., Lauer-Leredde, C., 2007. Sedimentary responses to the Pleistocene climatic variations recorded in the South China Sea. Quat. Res. 68, 162–172. doi:10.1016/j.yqres.2007.03.004

Braconnot, P., Loutre, M.F., Dong, B., Joussaume, S., Valdes, P., 2002. How the simulated change in monsoon at 6 Ka BP is related to the simulation of the modern climate: Results from the Paleoclimate Modeling Intercomparison Project. Clim. Dyn. 19, 107–121.

Braconnot, P., Otto-Bliesner, B., Harrison, S., Joussaume, S., Peterchmitt, J.-Y., Abe-Ouchi, A., Crucifix, M., Driesschaert, E., Fichefet, T., Hewitt, C.D., Kageyama, M., Kitoh, A., Laîne, A., Loutre, M.F., Marti, O., Merkel, U., Ramstein, G., Valdes, P., Weber, S.L., Yu, Y., Zhao, Y., 2007a. Results of PMIP2 coupled simulations of the Mid-Holocene and last Glacial Maximum - Part 1: experiments and large-scale features. Clim. Past 3, 261–277.

Braconnot, P., Otto-Bliesner, B., Harrison, S., Joussaume, S., Peterchmitt, J.-Y., Abe-Ouchi, A., Crucifix, M., Driesschaert, E., Fichefet, T., Hewitt, C.D., Kageyama, M., Kitoh, A., Loutre, M.F., Marti, O., Merkel, U., Ramstein, G., Valdes, P., Weber, L., Yu, Y., Zhao, Y., 2007b. Results of PMIP2 coupled simulations of the Mid-Holocene and Last Glacial Maximum - Part 2: feedbacks with emphasis on the location of the ITCZ and mid- and high latitudes heat budget. Clim. Past 3, 279–296.

Bray, E.E., Evans, E.D., 1961. Distribution of n-paraffins as a clue to recognition of source beds. Geochim. Cosmochim. Acta 22, 2–15. doi:10.1016/0016-7037(61)90069-2

Breitenbach, S., 2010. Changes in monsoonal precipitation and atmospheric circulation during the Holocene reconstructed from stalagmites from Northeastern India (Web Page). Sci. Tech. Rep. 10/06. Deutsche GeoForschungsZentrum, Potsdam, Germany.

Breitenbach, S.F.M., Adkins, J.F., Meyer, H., Marwan, N., Kumar, K.K., Haug, G.H., 2010. Strong influence of water vapor source dynamics on stable isotopes in precipitation observed in Southern Meghalaya, NE India. Earth Planet. Sci. Lett. 292, 212–220.

doi:10.1016/j.epsl.2010.01.038

Brusova, O., 2011. Compaction of deep sea siliciclastic sediments based on log data. University of Utah.

Bush, R.T., McInerney, F.A., 2013. Leaf wax n-alkane distributions in and across modern plants: Implications for paleoecology and chemotaxonomy. Geichimica Cosmochim. Acta 117, 161–179. doi:10.1016/j.gca.2013.04.016

Cai, Y., Zhang, H., Cheng, H., An, Z., Edwards, R.L., Wang, X., Tan, L., Liang, F., Wang, J., Kelly, M., 2012. The Holocene Indian monsoon variability over the southern Tibetan Plateau and its teleconnections. Earth Planet. Sci. Lett. 335–336, 135–144.

Camargo, S.J., Sobel, A.H., 2005. Western North Pacific tropical cyclone intensity and ENSO. J. Clim. 18, 2996–3006. doi:10.1175/JCLI3457.1

Chauhan, O.S., Rajawat Y., A.S.P., Sunneethi, J., Nayak, S.R., 2005. Weekly observations on dispersal and sink pathways of the terrigenous flux of the Ganga-Brahmaputra in teh Bay of Bengal during NE monsoon. Deep. Res. II 52, 2018–2030.

Chen, G., Huang, R., 2008. Influence of Monsoon over the Warm Pool on Interannual Variation on Tropical Cyclone Activity over the Western North Pacific. Adv. Atmos. Sci. 25, 319–328. doi:10.1007/s00376-008-0319-7

Chen, J., Li, Y., Yin, K., Jin, H., 2004. Amino acids in the Pearl River Estuary and adjacent waters: origins, transformation and degradation. Cont. Shelf Res. 24, 1877–1894.

Cheng, H., Edwards, R.L., Broecker, W.S., Denton, G.H., Kong, X., Wang, Y., Zhang, R., Wang, X., 2009. Ice Age Terminations. Science (80-.). 326, 248–252. doi:10.1126/science.1177840

Cheng, H., Lawrence Edwards, R., Wang, Y., 2006. A penultimate glacial monsoon record from Hulu Cave and two phase glacial terminations. Geology 34, 217–220.

Chiang, T.L., Wu, C.R., Chao, S.Y., 2008. Physical and geographical origins of the South China Sea Warm Current. J. Geophys. Res. Ocean. 113, 1–13. doi:10.1029/2007JC004794

Chikaraishi, Y., Naraoka, H., 2005. d13C and dD identification of sources of lipid biomarkers in

sediments of Lake Haruna (Japan). Geochim. Cosmochim. Acta 69, 3285–3297.

Chikaraishi, Y., Naraoka, H., Poulson, S.R., 2004. Hydrogen and carbon isotopic fractionations of lipid biosynthesis among terrestrial (C3, C4 and CAM) and aquatic plants. Phytochemistry 65, 1369–1381.

Clemens, S.C., Prell, W.L., Sun, Y., 2010. Orbital-scale timing and mechanisms driving Late Pleistocene Indo-Asian summer monsoons: Reinterpreting cave speleothem d18O. Paleoceanography 25, 10.1029/2010PA001926.

Colin, C., Kissel, C., Blamart, D., Turpin, L., 1998. Magnetic properties of sediments in the Bay of Bengal and the Andaman Sea: Impact of rapid North Atlantic Ocean climatic events on the strength of the Indian monsoon. Earth Planet. Sci. Lett. 160, 623–635. doi:10.1016/S0012-821X(98)00116-2

Colin, C., Turpin, L., Bertaux, J., Desprairies, A., Kissel, C., 1999. Erosional history of the Himalayan and Burman ranges during the last two glacial-interglacial cycles. Earth Planet. Sci. Lett. 171, 647–660.

Collins, J.A., Schefuß, E., Mulitza, S., Prange, M., Werner, M., Tharammal, T., Paul, A., Wefer, G., 2013. Estimating the hydrogen isotopic composition of past precipitation using leaf-waxes from western Africa. Quat. Sci. Rev. 65, 88–101.

Collins, J. a., Schefuß, E., Heslop, D., Mulitza, S., Prange, M., Zabel, M., Tjallingii, R., Dokken, T.M., Huang, E., Mackensen, A., Schulz, M., Tian, J., Zarriess, M., Wefer, G., 2011. Interhemispheric symmetry of the tropical African rainbelt over the past 23,000 years. Nat. Geosci. 4, 42–45. doi:10.1038/ngeo1039

Collins, W.D., Bitz, C.M., Blackmon, M.L., Bonan, G.B., Bretherton, C.S., Carton, J.A., Chang, P., Doney, S.C., Hack, J.J., Henderson, T.B., Kiehl, J.T., Large, W.G., McKenna, D.S., Santer, B.D., Smith, R.D., 2006a. The Community Climate System Model Version 3 (CCSM3). J. Clim. 19, 2122–2143.

Collins, W.D., Rasch, P.J., Hack, J.J., McCaa, J.R., Williamson, D.L., Briegleb, B.P., Bitz, C.M., Lin, S.J., Zhang, M., 2006b. The formulation and atmospheric simulation of the Community Atmosphere Model Version 3 (CAM3). Jounral Clim. 19, 2144–2161.

Collister, J.W., Rieley, G., Stern, B., Eglinton, G., Fry, B., 1994. Compound-specific d13C analyses of leaf lipids from plants with differing carbon dioxide metabolisms. Org. Geochem. 21, 619–627. doi:10.1016/0146-6380(94)90008-6

Conroy, J.L., Overpeck, J.T., Cole, J.E., Shanahan, T.M., Steinitz-Kannan, M., 2008. Holocene changes in eastern tropical Pacific climate inferred from a Galápagos lake sediment record. Quat. Sci. Rev. 27, 1166–1180. doi:10.1016/j.quascirev.2008.02.015

Contreras-Rosales, L.A., Jennerjahn, T., Tharammal, T., Meyer, V., Lückge, A., Paul, A., Schefuß, E., 2014. Evolution of the Indian Summer Monsoon and terrestrial vegetation in the Bengal region during the past 18 ka. Quat. Sci. Rev. 102, 133–148. doi:10.1016/j.quascirev.2014.08.010

Cowan, I.R., Farquhar, G.D., 1977. Stomatal function in relation to leaf metabolism and environment, in: Jennings, D.H. (Ed.), Integration of Activity in the Higher Plant. Cambridge University Press, pp. 471–505.

Craig, H., Gordon, L.I., 1965. Deuterium and oxygen 18 variations in the ocean and the marine atmosphere, in: Tongiorgi, E. (Ed.), Stable Isotopes in Oceanographic Studies and Paleotemperatures. Consiglio Nazionale Delle Ricerche, Pisa, pp. 9–130.

Curray, J.R., Emmel, F.J., Moore, D.G., 2003. The Bengal Fan: morphology, geometry, stratigraphy, history and processes. Mar. Pet. Geol. 19, 1191–1223.

Dai, L., Weng, C., 2015. Marine palynological record for tropical climate variations since the late last glacial maximum in the northern South China Sea. Deep Sea Res. Part II Top. Stud. Oceanogr. 122, 153–162. doi:10.1016/j.dsr2.2015.06.011

Dai, L., Weng, C., Mao, L., 2015. Patterns of vegetation and climate change in the northern South China Sea during the last glaciation inferred from marine palynological records. Palaeogeogr. Palaeoclimatol. Palaeoecol. 440, 249–258. doi:10.1016/j.palaeo.2015.08.041

Dansgaard, W., 1964. Stable isotopes in precipitation. Tellus 16, 436–468. doi:10.3402/tellusa.v16i4.8993

Dansgaard, W., Johnsen, S.J., Clausen, H.B., Dahl-Jensen, D., Gundestrup, N.S., Hammer, C.U., Hvidberg, C.S., Steffensen, J.P., Sveinbjörnsdottir, A.E., Jouzel, J., Bond, G., 1993.

Evidence for general instability of past climate from a 250-kyr ice-core record. Nature 364, 218–220.

Dauwe, B., Middelburg, J.J., 1998. Amino acids and hexosamines as indicators of organic matter degradation state in North Sea sediments. Limnol. Oceanogr. 43, 782–798.

Dauwe, B., Middelburg, J.J., Herman, M.J., Heip, C.H.R., 1999. Linking diagenetic alteration of amino acids and bulk organic matter reactivity. Limnol. Oceanogr. 44, 1809–1814.

Dayem, K.E., Molnar, P., Battisti, D.S., Roe, G.H., 2010. Lessons learned from oxygen isotopes in modern precipitation applied to interpretation of speleothem records of paleoclimate from eastern Asia. Earth Planet. Sci. Lett. 295, 219–230. doi:10.1016/j.epsl.2010.04.003

De La Rocha, C.L., Passow, U., 2007. Factors influencing the sinking of POC and the efficiency of the biological carbon pump. Deep. Res. Part II Top. Stud. Oceanogr. 54, 639–658. doi:10.1016/j.dsr2.2007.01.004

Dean, W.E., 2007. Sediment geochemical records of productivity and oxygen depletion along the margin of western North America during the past 60,000 years: teleconnections with Greenland Ice and the Cariaco Basin. Quat. Sci. Rev. 26, 98–114. doi:10.1016/j.quascirev.2006.08.006

Demske, D., Tarasov, P.E., Wünnemann, B., Riedel, F., 2009. Late glacial and Holocene vegetation, Indian monsoon and westerly circulation in the Trans-Himalaya recorded in the lacustrine pollen sequence from Tso Kar, Ladakh, NW India. Palaeogeogr. Palaeoclimatol. Palaeoecol. 279, 172–185.

Diefendorf, A.F., Freeman, K.H., Wing, S.L., Graham, H. V, 2011. Production of n-alkyl lipids in living plants and implications for the geologic past. Geochim. Cosmochim. Acta 75, 7472–7485.

Diefendorf, A.F., Mueller, K.E., Wing, S.L., Koch, P.L., Freeman, K.H., 2010. Global patterns in leaf 13C discrimination and implications for studies of past and future climate. Proc. Natl. Acad. Sci. 107, 5738–5743.

Ding, Y., Chan, J.C.L., 2005. The East Asian summer monsoon: an overview. Meteorol. Atmos. Phys. 89, 117–142.

Ding, Y., Li, C., Liu, Y., 2004. Overview of the South China Sea monsoon experiment. Adv. Atmos. Sci. 21, 343–360. doi:10.1007/BF02915563

Dixit, S., Bera, S.K., 2013. Pollen-inferred vegetation vis-á-vis climate dynamics since Late Quaternary from western Assam, Northeast India: Signal of global climatic events. Quat. Int. 286, 56–68. doi:10.1016/j.quaint.2012.06.010

Dixit, S., Bera, S.K., 2012. Holocene climatic fluctuations from Lower Brahmaputra flood plain of Assam, northeast India. J. Earth Syst. Sci. 121, 135–147.

Dong, L., Li, L., Li, Q., Liu, J., Chen, Y., He, J., Wang, H., 2015. Basin-wide distribution of phytoplankton lipids in the South China Sea during intermonsoon seasons: Influence by nutrient and physical dynamics. Deep Sea Res. Part II Top. Stud. Oceanogr. doi:10.1016/j.dsr2.2015.07.005

Dong, L., Su, J., Ah Wong, L., Cao, Z., Chen, J.-C., 2004. Seasonal variation and dynamics of the Pearl River plume. Cont. Shelf Res. 24, 1761–1777.

Douglas, P.M.J., Pagani, M., Brenner, M., Hodell, D.A., Curtis, J.H., 2012. Aridity and vegetation composition are important determinants of leaf-wax dD values in southeastern Mexico and Central America. Geochim. Cosmochim. Acta 97, 24–25. doi:10.1016/j.gca.2012.09.005

Dowling, C.B., Poreda, R.J., Basu, A.R., 2003. The groundwater geochemistry of the Bengal Basin: Weathering, chemsorption, and trace metal flux to the oceans. Geochim. Cosmochim. Acta 67, 2117–2136. doi:10.1016/S0016-7037(02)01306-6

Duan, Y., Wu, B., 2008. Hydrogen isotopic compositions and their environmental significance for individual n-alkanes in typical plants from land in China. Chinese Sci. Bull. 54, 461–467. doi:10.1007/s11434-008-0443-x

Duplessy, J.C., 1982. Glacial to interglacial contrasts in the northern Indian Ocean. Nature 295, 494–498.

Dupont, L., Schlütz, F., Teboh-Ewah, C., Jennerjahn, T.C., Paul, A., Behling, H., 2010. Two-step vegetation response to enhanced precipitation in Northeast Brazil during Heinrich event 1. Glob. Chang. Biol. 16, 1647–1660.

Durum, W.H., Haffty, J., 1963. Implications of the minor element content of some major streams of the world. Geochim. Cosmochim. Acta 27, 1–11.

Dykoski, C.A., Edwards, R.L., Cheng, H., Yuan, D., Cai, Y., Zhang, M., Lin, Y., Qing, J., An, Z., Revenaugh, J., 2005. A high-resolution, absolute-dated Holocene and deglacial Asian monsoon record from Dongge Cave, China. Earth Planet. Sci. Lett. 233, 71–86.

Eglinton, G., Hamilton, R.J., 1967. Leaf epicuticular waxes. Science (80-.). 156, 1322–1335.

Ehleringer, J.R., Cerling, T.E., 2002. C3 and C4 Photosynthesis. Encycl. Glob. Enviornmental Chang.

Ehleringer, J.R., Cerling, T.E., Helliker, B.R., 1997. C4 photosynthesis, atmospheric CO2 and climate. Oecologia 112, 285–299.

Erdosy, G., 1985. The origin of cities in the Ganges Valley. J. Econ. Soc. Hist. Orient 28, 81–109.

Farquhar, G.D., Ehleringer, J.R., Hubick, K.T., 1989. Carbon isotope discrimination and photosynthesis. Annu. Rev. Plant Physiol. Plant Mol. Biol. 40, 503–537.

Farquhar, G.D., O'Leary, M.H., Berry, J.A., 1982. On the relationship between carbon isotope discrimination and the intercellular carbon dioxide concentration in leaves. Aust. J. Plant Physiol. 9, 121–137.

Field, R.D., Jones, D.B.A., Brown, D.P., 2010. Effects of post-condensation exchange on the isotopic composition of water in the atmosphere. J. Geophys. Res. 115, D24305.

Fischer, H., Wahlen, M., Smith, J., Mastroianni, D., Deck, B., 1999. Ice core records of atmospheric CO2 around the last three glacial terminations. Science (80-.). 283, 1712–1714.

Fleitmann, D., Burns, S.J., Mangini, A., Mudelsee, M., Kramers, J., Villa, I., Neff, U., Al-Subbary, A.A., Buettner, A., Hippler, D., Matter, A., 2007. Holocene ITCZ and Indian monsoon dynamics recorded in stalagmites from Oman and Yemen (Socotra). Quat. Sci. Rev. 26, 170–188.

Gagosian, R.B., Peltzer, E.T., 1986. The importance of atmospheric input of terrestrial organic

material to deep sea sediments. Org. Geochem. 10, 661–669.

Galy, V., Eglinton, T., 2011. Protracted storage of biospheric carbon in the Ganges-Brahmaputra basin. Nat. Geosci. 4, 843–847.

Galy, V., Eglinton, T., France-Lanord, C., Sylva, S., 2011. The provenance of vegetation and environmental signatures encoded in vascular plant biomarkers carried by the Ganges-Brahmaputra rivers. Earth Planet. Sci. Lett. 304, 1–12.

Galy, V., France-Lanord, C., Lartiges, B., 2008a. Loading and fate of particulate organic carbon from the Himalaya to the Ganga-Brahmaputra delta. Geochim. Cosmochim. Acta 72, 1767–1787.

Galy, V., François, L., France-Lanord, C., Faure, P., Kudrass, H., Palhol, F., Singh, S.K., 2008b. C4 plants decline in the Himalayan basin since the Last Glacial Maximum. Quat. Sci. Rev. 27, 1396–1409.

Ganguli, B., 1938. Trends of agriculture and population in the Ganges Valley: A study in Agricultural economics. Methuen & Co., London.

Gao, X., Chen, S., Xie, X., Long, A., Ma, F., 2007. Non-aromatic hydrocarbons in surface sediments near the Pearl River estuary in the South China Sea. Environ. Pollut. 148, 40–47. doi:10.1016/j.envpol.2006.11.001

Gaye-Haake, B., Lahajnar, N., Emeis, K.-C., Unger, D., Rixen, T., Suthhof, A., Ramaswamy, V., Schulz, H., Paropkari, A.L., Guptha, M.V.S., Ittekkot, V., 2005. Stable nitrogen isotopic ratios of sinking particles and sedimetns from the northern Indian Ocean. Mar. Chem. 96.

Gent, P.R., Yeager, S.G., Neale, R.B., Levis, S., Bailey, D.A., 2010. Improvements in a half degree atmosphere/land version of the CCSM. Clim. Dyn. 34, 819–833.

Goodbred Jr., S.L., 2003. Response of the Ganges dispersal system to climate change: a source-to-sink view since the last interstade. Sediment. Geol. 162, 83–104.

Goodbred Jr., S.L., Kuehl, S.A., 2000a. The significance of large sediment supply , active tectonism , and eustasy on margin sequence development : Late Quaternary stratigraphy and evolution of the Ganges – Brahmaputra delta. Sediment. Geol. 133, 227–248.

Goodbred Jr., S.L., Kuehl, S.A., 2000b. Enormous Ganges-Brahmaputra sediment discharge during strengthened early Holocene monsoon. Geology 28, 1083–1086.

Hack, J.J., Caron, J.M., Yeager, S.G., Oleson, K.W., Holland, M.M., Truesdale, J.E., Rasch, P.J., 2006. Simulation of the global hydrological cycle in the CCSM Community Atmosphere Model Version 3 (CAM3): Mean Features. J. Clim. 19, 2199–2221.

Hartnett, H.E., Devol, A.H., 2003. Role of a strong oxygen-deficient zone in the preservation and degradation of organic matter: a carbon budget for the continental margins of northwest Mexico and Washington State. Geochim. Cosmochim. Acta 67, 247–264.

Hartnett, H.E., Keil, R.G., Hedges, J.I., Devol, A.H., 1998. Influence of oxygen exposure time on organic carbon preservation in continental margin sediments. Nature 391, 2–4.

He, J., Ju, J., Wen, Z., Lü, J., Jin, Q., 2007. A review of recent research on the East Asian summer monsoon. In: China, Monsoon meteorology. Adv. Atmos. Sci. 24, 972–992.

He, J., Zhao, M., Li, L., Wang, P., Ge, H., 2008. Sea surface temperature and terrestrial biomarker records of the last 260 ka of core MD05-2904 from the northern South China Sea. Chinese Sci. Bull. 53, 2376–2384. doi:10.1007/s11434-008-0289-2

He, Y.H., Guan, C.H., Gan, Z.J., 1992. Heat oscillation in the upper ocean of the southern South China Sea. Acta Oceanol. Sin. 11, 375–387.

Hecky, R.E., Mopper, K., Kilham, P., Degents, E.T., 1973. The amino acid and sugar composition of diatom cell-walls. Mar. Biol. 19, 323–331.

Hedges, J.I., Hare, P.E., 1987. Amino acid adsorption by clay minerals in distilled water. Geochim. Cosmochim. Acta 51, 255–259.

Hedges, J.I., Keil, R.G., 1995. Sedimentary organic matter preservation: an assessment and speculative synthesis. Mar. Chem. 49, 81–115. doi:10.1016/0304-4203(95)00013-H

Hedges, J.I., Keil, R.G., Benner, R., 1997. What happens to terrestrial organic matter in the ocean? Org. Geochem. 27, 195–212.

Hedges, J.I., Oades, J.M., 1997. Comparative organic geochemistries of soils and marine sediments. Org. Geochem. 27, 319–361.

Hemming, S.R., 2004. Heinrich events: massive Late Pleistocene detritus layers of the North atlantic and their global climate imprint. Rev. Geophys. 42, RG1005.

Hendy, C.H., 1971. The isotopic geochemistry of speleothems: I. The calculation of the effects of different modes of formation on the isotopic composition of speleothems and their applicability as palaeoclimatic indicators. Geochim. Cosmochim. Acta 35, 801–824.

Herbeck, L.S., Unger, D., Krumme, U., Liu, S.M., Jennerjahn, T.C., 2011. Typhoon-induced precipitation impact on nutrient and suspended matter dynamics of a tropical estuary affected by human activities in Hainan, China. Estuar. Coast. Shelf Sci. 93, 375–388.

Herzschuh, U., 2006. Palaeo-moisture evolution in monsoonal Central Asia during the last 50,000 years. Quat. Sci. Rev. 25, 163–178.

Higginson, M.J., Maxwell, J.R., Altabet, M. a, 2003. Nitrogen isotope and chlorin paleoproductivity records from the Northern South China Sea: remote vs. local forcing of millennial- and orbital-scale variability. Mar. Geol. 201, 223–250. doi:10.1016/S0025-3227(03)00218-4

Hoffmann, B., Kahmen, A., Cernusak, L.A., Arndt, S.K., Sachse, D., 2013. Abundance and distribution of leaf wax n-alkanes in leaves of Acacia and Eucalyptus trees along a strong humidity gradient in northern Australia. Org. Geochem. 62, 62–67.

Hopmans, E.C., Weijers, J.W.H., Schefuß, E., Herfort, L., Sinninghe-Damsté, J.S., Schouten, S., 2004. A novel proxy for terrestrial organic matter in sediments based on branched and isoprenoid tetraether lipids. Earth Planet. Sci. Lett. 224, 107–116.

Hou, J., D'Andrea, W.J., Huang, Y., 2008. Can sedimentary leaf waxes record D/H ratios of continental precipitation? Field, model, and experimental assessments. Geochim. Cosmochim. Acta 72, 3503–3517.

Hu, D., Böning, P., Köhler, C.M., Hillier, S., Pressling, N., Wan, S., Brumsack, H.J., Clift, P.D., 2012. Deep sea records of the continental weathering and erosion response to East Asian monsoon intensification since 14 ka in the South China Sea. Chem. Geol. 326–327, 1–18. doi:10.1016/j.chemgeo.2012.07.024

Hu, J., Peng, P., Chivas, A.R., 2009. Molecular biomarker evidence of origins and transport of

organic matter in sediments of the Pearl River estuary adjacent South china Sea. Appl. Geochemistry 24, 1666–1676.

Hu, J., Peng, P., G., J., Mai, B., Zhang, G., 2006. Distribution and sources of organic carbon, nitrogen and their isotopes in sediments of the subtropical Pearl River estuary and adjacent shelf, southern China. Mar. Chem. 98, 274–285.

Hu, J., Peng, P., Jia, G., Fang, D., Zhang, G., Fu, J., Wang, P., 2002. Biological markers and their carbon isotopes as an approach to the paleoenvironmental reconstruction of Nansha area, South china Sea, during the last 30 ka. Org. Geochem. 33, 1197–1204.

Huang, E., Tian, J., Qiao, P., Wan, S., Xie, X., Yang, W., 2015. Early interglacial carbonate-dilution events in the South China Sea: Implications for strengthened typhoon activities over subtropical East Asia. Quat. Sci. Rev. 125, 61–77. doi:10.1016/j.quascirev.2015.08.007

Huang, E., Tian, J., Steinke, S., 2011. Millennial-scale dynamics of the winter cold tongue in the southern South China Sea over the past 26 ka and the East Asian winter monsoon. Quat. Res. 75, 196–204.

Huang, J., Li, A., Wan, S., 2011. Sensitive grain-size records of Holocene East Asian summer monsoon in sediments of northern South China Sea slope. Quat. Res. 75, 734–744.

Hung, R., Gu, L., Zhou, L., Wu, S., 2006. Impact of the Thermal State of the Tropical Western Pacific on Onset Date and Process of the South China Sea Summer Monsoon. Adv. Atmos. Sci. 23, 909–924.

Ingalls, A.E., Lee, C., Wakeham, S.G., Hedges, J.I., 2003. The role of biominerals in the sinking flux and preservation of amino acids in the Southern Ocean along 170 W. Deep. Res. Part II Top. Stud. Oceanogr. 50, 713–738. doi:10.1016/S0967-0645(02)00592-1

Jennerjahn, T.C., Ittekkot, V., 1999. Changes in organic matter from surface waters to continental slope sediments off the São Francisco River, eastern Brazil. Mar. Geol. 161, 129–140.

Jennerjahn, T.C., Ittekkot, V., Arz, H.W., Behling, H., Pätzold, J., Wefer, G., 2004. Asynchronous terrestrial and marine signals of climate change during Heinrich events.

Science (80-.). 306, 2236–2239.

Jennerjahn, T.C., Ittekot, V., 1997. Organic matter in seidments in the mangrove areas and adjacent continental margins of Brazil: I. Amino acids and hexosamines. Oceanol. Acta 20, 359–369.

Jennerjahn, T.C., Soman, K., Ittekkot, V., Nordhaus, I., Sooraj, S., Priya, R.S., Lahajnar, N., 2008. Effect of land use on the biogeochemistry of dissolved nutrients and suspended and sedimentary organic matter in the tropical Kallada River and Ashtamudi estuary, Kerala, India. Biogeochemistry 90, 29–47.

Jiang, H., Ding, Z., 2008. A 20 Ma pollen record of East-Asian summer monsoon evolution from Guyuan, Ningxia, China. Palaeogeogr. Palaeoclimatol. Palaeoecol. 265, 30–38.

Jiang, J., Ni, Y., 2004. Diagnostic study on the structural characteristics of a typical mei-yu front system and its maintenance mechanism. Adv. Atmos. Sci. 21, 802–813.

Johnson, K.R., Ingram, B.L., 2004. Spatial and temporal variability in the stable isotope systematics of modern precipitation in China: implications for paleoclimate reconstructions. Earth Planet. Sci. Lett. 220, 365–377. doi:10.1016/S0012-821X(04)00036-6

Joussaume, S., Taylor, K.E., Braconnot, P., Mitchell, J.F.B., Kutzbach, J.E., Harrison, S.P., Prentice, I.C., Broccoli, A.J., Abe-Ouchi, A., Bartlein, P.J., Bonfils, C., Dong, B., Guiot, J., Herterich, K., Hewitt, C.D., Jolly, D., Kim, J.W., Kislov, A., Kitoh, A., Loutre, M.F., Masson, V., McAvaney, B., McFarlane, N., de Noblet, N., Peltier, W.R., Peterschmitt, J.Y., Pollard, D., Rind, D., Royer, J.F., Schlesinger, M.E., Syktus, J., Thompson, L., Valdes, P., Vettoretti, G., Webb, R.S., Wyputta, U., 1999. Monsoon changes for 6000 years ago: Results of 18 simulations from the Paleoclimate Modeling Intercomparison Project (PMIP). Geophys. Res. Lett. 26, 859–862.

Jouzel, J., Hoffmann, G., Koster, R.D., Masson, V., 2000. Water isotopes in precipitation: data/model comparison for present-day and past climates. Quat. Sci. Rev. 19, 363–379.

Jouzel, J., Vimeux, F., Caillon, N., Hoffmann, G., Masson-Delmotte, V., Parrenin, F., 2003. Magnitude of isotope/temperature scaling for interpretation of central Antarctic ice cores. J. Geophys. Res. 108, ACL 6.

Keil, R.G., Mayer, L.M., Quay, P.D., Richey, J.E., Hedges, J.I., 1997. Loss of organic matter from riverine particles in deltas. Geochim. Cosmochim. Acta 61, 1507–1511. doi:10.1016/S0016-7037(97)00044-6

Keil, R.G., Tsamakis, E., Hedges, J.I., 2000. Early diagenesis of particulate amino acids in marine systems, in: Goodfriend, G.A., Collins, M.J., Fogel, M.L., Macko, S.A., Wehmiller, J.F. (Eds.), Perspectives in Amino Acid and Protein Geochemistry. Oxford University Press, pp. 69–82.

Kienast, M., 2000. Unchanged nitrogen isotopic composition of organic matter in the South China Sea during the last climatic cycle: Global implications. Paleoceanography 15, 244–253.

Kienast, M., Calvert, S.E., Pelejero, C., Grimalt, J.O., 2001. A critical review of marine sedimentary delta C-13(org)-pCO(2) estimates: New palaeorecords from the South China Sea and a revisit of other low-latitude delta C-13(org)-pCO(2) records. Global Biogeochem. Cycles 15, 113–127. doi:Doi 10.1029/2000gb001285

Killops, S., Killops, V., 2005. Introduction to Organic Geochemistry, 2e. ed. Blackwell Publishing.

King, K.J., 1977. Amino acid survey of recent calcareous and siliceous deep-sea microfossils. Micropaleontology 23, 180–193. doi:10.2307/1485331

Kohn, M.J., 2010. Carbon isotope compositions of terrestrial C3 plants as indicators of (paleo)ecology and (paleo)climate. Proc. Natl. Acad. Sci. 107, 19691–19695.

Kolattukudy, P., Croteau, R., Buckner, J., 1976. Biochemistry of plant waxes, in: Kolattukudy, P. (Ed.), Chemistry and Biochemistry of Natural Waxes. Elsevier, Amsterdam, pp. 289–347.

Kripalani, R.H., Oh, J.H., Kulkarni, A., Sabade, S.S., Chaudhari, H.S., 2007. South Asian summer monsoon precipitation variability: Coupled climate model simulations and projections under IPCC AR4. Theor. Appl. Climatol. 90, 133–159.

Krishnan, R., Sugi, M., 2003. Pacific decadal oscillation and variability of the Indian summer monsoon rainfall. Clim. Dyn. 21, 233–242. doi:10.1007/s00382-003-0330-8

Kroon, D., Steens, T., Troelstra, S.R., 1991. Onset of monsoonal related upwelling in the western Arabian Sea as revealed by planktonic foraminifers, in: Prell, W.L., Niitsuma, N., Al., E. (Eds.), Proceedings of the Ocean Drilling Program, Scientific Results 117. pp. 257–263.

Krull, E., Sachse, D., Mügler, I., Thiele, A., Gleixner, G., 2006. Compound-specific d13C and d2H analyses of plant and soil organic matter: A preliminary assessment of the effects of vegetation change on ecosystem hydrology. Soil Biol. Biochem. 38, 3211–3221.

Kudrass, H.-R., Hofmann, A., Doose, H., Emeis, K.-C., Erlenkeuser, H., 2001. Modulation and amplification of climatic changes in the Northern Hemisphere by the Indian summer monsoon during the past 80 k.y. Geology 29, 63–66.

Kumar, S., Ramesh, R., 2005. Productivity measurements in the Bay of Bengal using the 15 N tracer : Implications to the global carbon cycle. Indian J. Mar. Sci. 34, 153–162.

Kumar, S., Ramesh, R., Bhosle, N.B., Sardesai, S., Sheshshayee, M.S., 2004a. Natural isotopic composition of nitrogen in suspended particulate matter in the Bay of Bengal. Biogeosciences 1, 63–70. doi:10.5194/bg-1-63-2004

Kumar, S., Ramesh, R., Sardesai, S., Sheshshayee, M.., 2004b. High new production in the Bay of Bengal: Possible causes and implications. Geophys. Res. Lett. 31, L18304. doi:10.1029/2004GL021005

Kumar, V., Krishnan, R., 2005. On the association between the Indian summer monsoon and the tropical cyclone activity over northwest Pacific. Curr. Sci. 88, 602–612.

Lachniet, M.S., 2009. Climatic and environmental controls on speleothem oxygen-isotope values. Quat. Sci. Rev. 28, 412–432.

Lamb, A.L., Wilson, G.P., Leng, M.J., 2006. A review of coastal palaeoclimate and relative sea-level reconstructions using δ13C and C/N ratios in organic material. Earth-Science Rev. 75, 29–57. doi:10.1016/j.earscirev.2005.10.003

Lambeck, K., Esat, T.M., Potter, E.-K., 2002. Link between climate and sea levels for the past three million years. Nature 419, 199–206.

Lau, K.M., Yang, S., 1997. Climatology and interannual variability of the Southeast Asian

monsoon. Adv. Atmos. Sci. 14, 141–162.

Lee, C., Cronin, C., 1984. Particulate amino acids in the sea: Effects of primary productivity and biological decomposition. J. Mar. Res. 42, 1075–1097. doi:10.1357/002224084788520710

Lee, C., Wakeham, S.G., Hedges, J.I., 2000. Composition and flux of particulate amino acids and chloropigments in equatorial Pacific seawater and sediments. Deep. Res. I 47, 1535–1568.

Lee, C.-Y., Liew, P.-M., 2010. Late Quaternary vegetation and climate changes inferred from a pollen record of Dongyuan Lake in southern Taiwan. Palaeogeogr. Palaeoclimatol. Palaeoecol. 287, 58–66. doi:10.1016/j.palaeo.2010.01.015

Lee, J.E., Fung, I., 2007. "Amount effect" of water isotopes and quantitative analysis of post-condensation processes. Hydrol. Process. doi:DOI: 10.1002/hyp.6637

LeGrande, A.N., Schmidt, G.A., 2009. Sources of Holocene variability of oxygen isotopes in paleoclimate archives. Clim. Past 5, 441–455.

Leuschner, D.C., Sirocko, F., 2000. The low-latitude monsoon climate during Dansgaard-Oeschger cacles and Heinrich Events. Quat. Sci. Rev. 19, 243–254.

Levitus, S., Boyer, T., 1994. World Ocean Atlas 1994. US Department of Commerce, Washington DC.

Lewis, S.C., LeGrande, A.N., Kelley, M., Schmidt, G.A., 2010. Water vapour source impacts on oxygen isotope variability in tropical precipitation during Heinrich events. Clim. Past 6, 325–343.

Li, C., Yanai, M., 1996. The Onset and Interannual Variability of the Asian Summer Monsoon in Relation to Land-Sea Thermal Contrast.

Li, G., Yan, W., Zhong, L., 2016. Element geochemistry of offshore sediments in the northwestern South China Sea and the dispersal of Pearl River sediments. Prog. Oceanogr. 141, 17–29. doi:10.1016/j.pocean.2015.11.005

Li, H.-C., Liew, P.-M., Seki, O., Kuo, T.-S., Kawamura, K., Wang, L.-C., Lee, T.-Q., 2013. Paleoclimate variability in central Taiwan during the past 30 Kyrs reflected by pollen, d13CTOC , and n-alkane- dD records in a peat sequence from Toushe Basin. J. Asian Earth

Sci. 69, 166–176. doi:10.1016/j.jseaes.2012.12.005

Li, M.C., Zhu, J.J., Li, L.X., 2009. Occurrence and altitudinal pattern of C4 plants on Qinghai Plateau, Qinghai province, China. Photosynthetica 47, 298–303.

Li, P., Qiao, P., Zheng, H., Fang, G., Huang, G., 1991. Environmental evolution of Zhujiang Delta in the past 10 000 years. China Ocean Press, Beijing.

Li, X.-H., Wei, G., Shao, L., Liu, L., Liang, X., Jian, Z., Sun, M., Wang, P., 2003. Geochemical and Nd isotopic variations in sediments of the South China Sea: a response to Cenozoic tectonism in SE Asia. Earth Planet. Sci. Lett. 211, 207–220.

Li, Y.-H., 1976. Denudation of Taiwan Island since the Pliocene Epoch. Geoogy 4, 105–107.

Liang, X.Z., Wang, W.C., 1998. Associations between China monsoon rainfall and tropospheric jets. Quat. J. R. Meteorol. Soc. 124, 2597–2623.

Liew, P.M., Huang, S.Y., Kuo, C.M., 2006. Pollen stratigraphy, vegetation and environment of the last glacial and Holocene - A record from Toushe Basin, central Taiwan. Quat. Int. 147, 16–33. doi:10.1016/j.quaint.2005.09.003

Liew, P.M., Lee, C.Y., Kuo, C.M., 2006. Holocene thermal optimal and climate variability of East Asian monsoon inferred from forest reconstruction of a subalpine pollen sequence, Taiwan. Earth Planet. Sci. Lett. 250, 596–605. doi:10.1016/j.epsl.2006.08.002

Linsley, B.K., Rosenthal, Y., Oppo, D.W., 2010. Holocene evolution of the Indonesian throughflow and the western Pacific warm pool. Nat. Geosci. 3, 578–583. doi:10.1038/ngeo920

Liu, H., Song, X., Huang, L., Tan, Y., Zhang, J., 2011. Phytoplankton biomass and production in northern South China Sea during summer: Influenced by Pearl River discharge and coastal upwelling. Acta Ecol. Sin. 31, 133–136. doi:10.1016/j.chnaes.2011.02.001

Liu, J., Chen, M., Chen, Z., Yan, W., 2010a. Clay mineral distribution in surface sediments of the South China Sea and its significance for in sediment sources and transport. Chinese J. Oceanol. Limnol. 28, 407–415. doi:10.1007/s00343-010-9057-7

Liu, J., Chen, Z., Chen, M., Yan, W., Xiang, R., Tang, X., 2010b. Magnetic susceptibility

variations and provenance of surface sediments in the South China Sea. Sediment. Geol. 230, 77–85. doi:10.1016/j.sedgeo.2010.07.001

Liu, J., Xiang, R., Chen, M., Chen, Z., Yan, W., Liu, F., 2011. Influence of the Kuroshio current intrusion on depositional environment in the Northern South China Sea: Evidence from surface sediment records. Mar. Geol. 285, 59–68. doi:10.1016/j.margeo.2011.05.010

Liu, J.T., Lin, H.L., Hung, J.J., 2006. A submarine canyon conduit under typhoon conditions off Southern Taiwan. Deep. Res. Part I Oceanogr. Res. Pap. 53, 223–240. doi:10.1016/j.dsr.2005.09.012

Liu, Q., Kaneko, A., Su, J., 2008. Recent Progress in Studies of the South China Sea Circulation. J. Oceanogr. 64, 753–762.

Liu, X., Dong, H., Yang, X., Herzschuh, U., Zhang, E., Stuut, J.-B.W., Wang, Y., 2009. Late Holocene forcing of the asian winter and summer monsoon as evidenced by proxy records from the northern Qinghai-Tibetan Plateau. Earth Planet. Sci. Lett. 280, 276–284.

Liu, Z., Colin, C., Li, X., Zhao, Y., Tuo, S., Chen, Z., Siringan, F.P., Liu, J., Huang, C.-Y., You, C.-F., Huang, K.-F., 2010. Clay mineral distribution in surface seidments of the northeastern South China Sea and surrounding fluvial drainage basins: Source and transport. Mar. Geol. 277, 48–60.

Liu, Z., Henderson, A.C.G., Huang, Y., 2008. Regional Moisture source changes Inferred from Late Holocene Stable Isotope Records. Adv. Atmos. Sci. 25, 1021–1028.

Liu, Z., Tuo, S., Colin, C., Liu, J.T., Huang, C.Y., Selvaraj, K., Chen, C.T.A., Zhao, Y., Siringan, F.P., Boulay, S., Chen, Z., 2008. Detrital fine-grained sediment contribution from Taiwan to the northern South China Sea and its relation to regional ocean circulation. Mar. Geol. 255, 149–155. doi:10.1016/j.margeo.2008.08.003

Liu, Z., Zhao, Y., Colin, C., Stattegger, K., Wiesner, M.G., Huh, C.-A., Zhang, Y., Li, X., Sompongchaiyakul, P., You, C.-F., Huang, C.-Y., Liu, J.T., Siringan, F.P., Le, K.P., Sathiamurthy, E., Hantoro, W.S., Liu, J., Tuo, S., Zhao, S., Zhou, S., He, Z., Wang, Y., Bunsomboonsakul, S., Li, Y., 2016. Source-to-Sink transport processes of fluvial sediments in the South China Sea. Earth-Science Rev. in press. doi:10.1016/j.earscirev.2015.08.005

Liu, Z.F., Li, X.J., Colin, C., Ge, H.M., 2010. A high-resolution clay mineralogical record in the northern South China Sea since the Last Glacial Maximum, and its time series provenance analysis. Chinese Sci. Bull. 55, 4058–4068. doi:10.1007/s11434-010-4149-5

Lückge, A., Deplazes, G., Schulz, H., Scheeder, G., Suckow, A., Kasten, S., Haug, G.H., 2012. Impact of Indus River discharge on productivity and preservation of organic carbon in the Arabian Sea over the twentieth century. Geol. 40, 399–402. doi:10.1130/G32608.1

Lüdmann, T., Wong, H.K., Berglar, K., 2005. Upward flow of North Pacific Deep Water in the northern South China Sea as deduced from the occurrence of drift sediments. Geophys. Res. Lett. 32, 1–4. doi:10.1029/2004GL021967

Lupker, M., Blard, P.-H., Lavé, J., France-Lanord, C., Leanni, L., Puchol, N., Charreau, J., Bourlès, D., 2012a. 10Be-derived Himalayan denudation rates and sediment budgets in the Ganga basin. Earth Planet. Sci. Lett. 333–334, 146–156.

Lupker, M., France-Lanord, C., Galy, V., Lavé, J., Gaillardet, J., Gajurel, A.P., Guilmette, C., Rahman, M., Singh, S.K., Sinha, R., 2012b. Predominant floodplain over mountain weathering of Himalayan sediments (Ganga basin). Geochim. Cosmochim. Acta 84, 410–432.

Lupker, M., France-Lanord, C., Galy, V., Lavé, J., Kudrass, H., 2013. Increasing chemical weathering in the Himalayan system since the Last Glacial Maximum. Earth Planet. Sci. Lett. 365, 243–252. doi:10.1016/j.epsl.2013.01.038

Lüttge, U., 2004. Ecophysiology of Crassulacean Acid Metabolism (CAM). Ann. Bot. 93, 629–652. doi:10.1093/aob/mch087

Madhu, N. V, Jyothibabu, R., Maheswaran, P.A., John Gerson, V., Gopalakrishnan, T.C., Nair, K.K.C., 2006. Lack of seasonality in phytoplankton standing stock (chlorophyll a) and production in the western Bay of Bengal. Cont. Shelf Res. 26, 1868–1883. doi:10.1016/j.csr.2006.06.004

Madhupratap, M., Gauns, M., Ramaiah, N., Prasanna Kumar, S., Muraleedharan, P.., de Sousa, S.., Sardessai, S., Muraleedharan, U., 2003. Biogeochemistry of the Bay of Bengal: physical, chemical and primary productivity characteristics of the central and western Bay

of Bengal during summer monsoon 2001. Deep Sea Res. Part II Top. Stud. Oceanogr. 50, 881–896. doi:10.1016/S0967-0645(02)00611-2

Meehl, G.A., Arblaster, J.M., Lawrence, D.M., Seth, A., Schneider, E.K., Kirtman, B.P., Min, D., 2006. Monsoon Regimes in the CCSM3. J. Clim. 19, 2482–2495.

Mehrotra, N., Shah, S.K., Bhattacharyya, A., 2014. Review of palaeoclimate records from Northeast India based on pollen proxy data of Late Pleistocene-Holocene. Quat. Int. 325, 41–54. doi:10.1016/j.quaint.2013.10.061

Merkel, U., Prange, M., Schulz, M., 2010. ENSO variability and teleconnections during glacial climates. Quat. Sci. Rev. 29, 86–100.

Meyer, V., 2012. Master Thesis: Geosciences. Faculty of Geosciences. University of Bremen.

Meyers, P.A., Ishiwatari, R., 1993. Lacustrine organic geochemistry - An overview of indicators of organic matter sources and diagenesis in lake sediments. Org. Geochem. 20, 867–900.

Milliman, J.D., Farnsworth, K.L., 2011. Rivers discharge to the Coastal Ocean: A global synthesis. Cambridge University Press.

Milliman, J.D., Kao, S., 2005. Hyperpycnal Discharge of Fluvial Sediment to the Ocean: Impact of super-typhoon Herb (1996) on Taiwanese rivers. J. Geoogy 113, 503–516.

Milliman, J.D., Syvitski, J.P.M., 1992. Geomorphic/Tectonic Control of Sediment Discharge to the Ocean: The Importance of Small Mountainous Rivers. J. Geol. 100, 525–544.

Möbius, J., Gaye, B., Lahajnar, N., Bahlmann, E., Emeis, K.-C., 2011. Influence of diagenesis on sedimentary d15N in the Arabian Sea over the last 130 kyr. Mar. Geol. 284, 127–138.

Mohtadi, M., Prange, M., Oppo, D.W., De Pol-Holz, R., Merkel, U., Zhang, X., Steinke, S., Lückge, A., 2014. North Atlantic forcing of tropical Indian Ocean climate. Nature 509, 76–80. doi:10.1038/nature13196

Mollenhauer, G., Schneider, R.R., Müller, P.J., Spiess, V., Wefer, G., 2002. Glacial/interglacial variablity in the Benguela upwelling system: Spatial distribution and budgets of organic carbon accumulation. Global Biogeochem. Cycles 16, 1–15. doi:10.1029/2001GB001488

Monnin, E., Indermühle, A., Dällenbach, A., Flückiger, J., Stauffer, B., Stocker, T.F., Raynaud,

D., Barnola, J.M., 2001. Atmospheric CO2 concentrations over the Last Glacial Termination. Science (80-.). 291, 112–114. doi:10.1126/science.291.5501.112

Monnin, E., Steig, E.J., Siegenthaler, U., Kawamura, K., Schwander, J., Stauffer, B., Stocker, T.F., Morse, D.L., Barnola, J.-M., Bellier, B., Raynaud, D., Fischer, H., 2004. Evidence for substantial accumulation rate variability in Antarctica during the Holocene, through synchronization of CO2 in the Taylor Dome, Dome C and DML ice cores. Earth Planet. Sci. Lett. 224, 45–54.

Mortyn, P.G., Thunell, R.C., 1997. Biogenic sedimentation and surface productivity changes in the Southern California Borderlands during the last glacial-interglacial cycle. Mar. Geol. 138, 171–192. doi:10.1016/S0025-3227(96)00105-3

Moy, C.M., Seltzer, G.O., Rodbell, D.T., Anderson, D.M., 2002. Variability of El Niño/Southern Oscillation activity at millenial timescales during the Holocene epoch. Nature 420, 162–165. doi:10.1038/nature01163.1.

Muraleedharan, K.R., Jasmine, P., Achuthankutty, C.T., Revichandran, C., Dinesh Kumar, P.K., Anand, P., Rejomon, G., 2007. Influence of basin-scale and mesoscale physical processes on biological productivity in the Bay of Bengal during the summer monsoon. Prog. Oceanogr. 72, 364–383.

Naqvi, S.W.A., 2010. Indian Ocean Margins, in: Liu, K.-K., Atkinson, L., Quiñones, R., Talaue-McManus, L. (Eds.), Carbon and Nutrient Fluxes in Continental Margins: A Global Synthesis. Springer Berlin Heidelberg, pp. 171–210.

Naqvi, S.W. a., Shailaja, M.S., Dileep Kumar, M., Sen Gupta, R., 1996. Respiration rates in subsurface waters of the northern Indian Ocean: evidence for low decomposition rates of organic matter within the water column in the Bay of Bengal. Deep Sea Res. Part II Top. Stud. Oceanogr. 43, 73–81. doi:10.1016/0967-0645(95)00080-1

Niedermeyer, E.M., Schefuß, E., Sessions, A.L., Mulitza, S., Mollenhauer, G., Schulz, M., Wefer, G., 2010. Orbital- and millennial-scale changes in the hydrologic cycle and vegetation in the western African Sahel: insights from individual plant wax dD and d13C. Quat. Sci. Rev. 29, 2996–3005.

O'Leary, M.H., 1988. Carbon Isotopes in Photosynthesis. Bioscience 38, 328–336.

O'Leary, M.H., 1981. Carbon isotope fractionation in plants. Phytochemistry 20, 553–567.

Ohsawa, S., Yusa, Y., 2000. Isotopic characteristics of typhonic rainwater: typhoons no. 13 (1993) and no. 6 (1996). Limnology 1, 143–149.

Osborne, C.P., Freckleton, R.P., 2009. Ecological selection pressures for C4 photosynthesis in the grasses. Proc. R. Soc. B 276, 1753–1760.

Palamenghi, L., 2012. Tectonic and Sea Level Control on the Transport and Depositional Processes in a Siliciclastic Sedimentary Basin. Insights from the Ganges-Brahmaputra Delta, Bengal Basin, Bangladesh. (Thesis). University of Bremen.

Palamenghi, L., Schwenk, T., Spiess, V., Kudrass, H.R., 2011. Seismostratigraphic analysis with centennial to decadal time resolution of the sediment sink in the Ganges-Brahmaputra subaqueous delta. Cont. Shelf Res. 31, 712–730. doi:10.1016/j.csr.2011.01.008

Pañuelas, J., Estiarte, M., 1997. Trends in plant carbon concentration and plant demand for N throughout this century. Oecologia 109, 69–73.

Pattan, J.N., Mir, I.A., Parthiban, G., Karapurkar, S.G., Matta, V.M., Naidu, P.D., Naqvi, S.W.A., 2013. Coupling between suboxic condition in sediments of the western Bay of Bengal and southwest monsoon intensification: A geochemical study. Chem. Geol. 343, 55–66.

Pausata, F.S.R., Battisti, D.S., Nisancioglu, K.H., Bitz, C.M., 2011. Chinese stalagmite d18O controlled by changes in the Indian monsoon during a simulated Heinrich event. Nat. Geosci. 4, 474–480.

Pearcy, R.W., Ehleringer, J.R., 1984. Comparative ecophysiology of C3 and C4 plants. Plant, Cell Environ. 7, 1–13.

Pedentchouk, N., Sumner, W., Tipple, B., Pagani, M., 2008. d13C and dD compositions of n-alkanes from modern angiosperms and conifers: An experimental set up in central Washington State, USA. Org. Geochem. 39, 1066–1071. doi:10.1016/j.orggeochem.2008.02.005

Pelejero, C., 2003. Terrigenous n-alkane input in the South china Sea: high-resolution records and surface sediments. Chem. Geol. 200, 89–103.

Pelejero, C., Grimalt, J.O., Heilig, S., Kienast, M., Wang, L., 1999. High-resolution Uk37 temperature reconstructions in the South China Sea over the past 220 kyr. Paleoceanography 14, 224–231.

Peltier, W.R., 2004. Global glacial isostasy and the surface of the Ice-Age Earth: the ICE-5G (VM2) model and GRACE. Annu. Rev. Earth Planet. Sci. 32, 111–149. doi:10.1146/annurev.earth.32.082503.144359

Peng, T.R., Wang, C.H., Huang, C.C., Fei, L.Y., Chen, C.T.A., Hwong, J.L., 2010. Stable isotopic characteristic of Taiwan's precipitation: A case study of western Pacific monsoon region. Earth Planet. Sci. Lett. 289, 357–366. doi:10.1016/j.epsl.2009.11.024

Peters, K.E., Sweeney, R.E., Kaplan, I.R., 1978. Correlation of Carbon and Nitrogen Stable Isotope Ratios in Sedimentary Organic Matter. Limnol. Oceanogr. 23, 598–604.

Phillips, S.C., Johnson, J.E., Giosan, L., Rose, K., 2014. Monsoon-influenced variation in productivity and lithogenic sediment flux since 110 ka in the offshore Mahanadi Basin, northern Bay of Bengal. Mar. Pet. Geol. 58, 502–525.

Pierson-Wickmann, A.-C., Reisberg, L., France-Lanord, C., Kudrass, H.R., 2001. Os-Sr-Nd results from sediments in the Bay of Bengal: Implications for sediment transport and the marine Os record. Paleoceanography 16, 435–444.

Ponton, C., Giosan, L., Eglinton, T.I., Fuller, D.Q., Johnson, J.E., Kumar, P., Collett, T.S., 2012. Holocene aridification of India. Geophys. Res. Lett. 39, L03704.

Prasanna Kumar, S., Nuncio, M., Narvekar, J., Kumar, A., Sardesai, S., de Souza, S.N., Gauns, M., Ramaiah, N., Madhupratap, M., 2004. Are eddies nature's trigger to enhance biological productivity in the Bay of Bengal? Geophys. Res. Lett. 31, L07309. doi:10.1029/2003GL019274

Prasanna Kumar, S., Nuncio, M., Ramaiah, N., Sardesai, S., Narvekar, J., Fernandes, V., Paul, J.T., 2007. Eddy-mediated biological productivity in the Bay of Bengal during fall and spring intermonsoons. Deep. Res. I 54, 1619–1640. doi:10.1016/j.dsr.2007.06.002

Prell, W.L., Murray, W.D., Clemens, S.C., Anderson, D.M., 1992. Evolution and variability of the Indian Ocean Summer Monsoon: evidence from the Western Arabian Sea drilling program. , in: Duncan, R.A., Rea, D.K., Kidd, R.B., von Rad, U., Weissel, J.K. (Eds.), Synthesis of Results from Scientific Drilling in Indian Ocean. Geophysical Monograph, American Geophysical Union, Washington D.C., pp. 375–378.

Prentice, I.C., Meng, T., Wang, H., Harrison, S.P., Ni, J., Wang, G., 2011. Evidence of a universal scaling relationship for leaf CO_2 drawdown along an aridity gradient. New Phytol. 190, 169–180.

Ramaswamy, V., Nair, R.R., 1994. Fluxes of material in the Arabian Sea and Bay of Bengal-Sediment trap studies. Proc. Indian Acad. Sci. (Earth Planet. Sci.) 103, 189–210.

Rao, C.K., Naqvi, S.W. a., Kumar, M.D., Varaprasad, S.J.D., Jayakumar, D. a., George, M.D., Singbal, S.Y.S., 1994. Hydrochemistry of the Bay of Bengal: possible reasons for a different water-column cycling of carbon and nitrogen from the Arabian Sea. Mar. Chem. 47, 279–290. doi:10.1016/0304-4203(94)90026-4

Rao, T.V.N., 2002. Spatial distribution of upwelling off the central east coast of India. Estuar. Coast. Shelf Sci. 54, 141–156.

Rao, V.P., Reddy, N.P., Rao, C.M., 1988. Clay mineral distribution in the shelf sediments off the northern part of the east coast of India. Cont. Shelf Res. 8, 145–151. doi:10.1016/0278-4343(88)90049-0

Rao, Z., Jia, G., Zhu, Z., Wu, Y., Zhang, J., 2008. Comparison of the carbon isotope composition of total organic carbon and long-chain n-alkanes from surface soils in eastern China and their significance. Chinese Sci. Bull. 53, 3921–3927. doi:10.1007/s11434-008-0296-3

Rao, Z., Zhu, Z., Jia, G., Henderson, A.C.G., Xue, Q., Wang, S., 2009. Compound specific dD values of long chain n-alkanes derived from terrestrial higher plants are indicative of the dD of meteoric waters: Evidence form surface soils in eastern China. Org. Geochem. 40, 922–930.

Rashid, H., England, E., Thompson, L., Polyak, L., 2011. Late glacial to Holocene Indian summer monsoon variability based upon sediment records taken from the Bay of Bengal.

Terr. Atmos. Ocean. Sci. 22, 215–228.

Reimer, P.J., Baillie, M.G.L., Bard, E., Bayliss, A., Beck, J.W., Bertrand, C.J.H., Blackwell, P.G., Buck, C.E., Burr, G.S., Cutler, K.B., Damon, P.E., Edwards, R.L., Fairbanks, R.G., Friedrich, M., Guilderson, T.P., Hogg, A.G., Hughen, K.A., Kromer, B., 2004. INTCAL04 terrestrial radiocarbon age calibration, 0-26 cal kyr BP. Radiocarbon 46, 1029–1058.

Rieley, G., Collister, J.W., Stern, B., Eglinton, G., 1993. Gas Chromatography/Isotope Ratio Mass Spectrometry of leaf wax n-alkanes from plants of differing carbon dioxide matabolisms. Rapid Commun. Mass Spectrom. 7, 488–491.

Risi, C., Bony, S., Vimeux, F., 2008. Influence of convective processes on the isotopic composition (d18O and dD) of precipitation and water vapor in the tropics: 2. Physical interpretation of the amount effect. J. Geophys. Res. Atmos. 113.

Risi, C., Noone, D., Frankenberg, C., Worden, J., 2013. Role of continental recycling in interseasonal variations of continental moisture as deduced from model simulations and water vapor isotopic measurements. Water Resour. Res. 49, 4136–4156.

Risi, C., Noone, D., Worden, J., Frankenberg, C., Stiller, G., Kiefer, M., Funke, B., Walker, K., Bernath, P., Schneider, M., Wunch, D., Sherlock, V., Deutscher, N., Griffith, D., Wennberg, P.O., Strong, K., Smale, D., Mahieu, E., Barthlott, S., Hase, F., García, O., Notholt, J., Warneke, T., Toon, G., Sayres, D., Bony, S., Lee, J., Brown, D., Uemura, R., Sturm, C., 2012. Process-evaluation of tropospheric humidity simulated by general circulation models using water vapor isotopologues: 1. Comparison between models and observations. J. Geophys. Res. Atmos. 117, D05303. doi:10.1029/2011JD016621

Robinson, D., 2001. δ15N as an integrator of the nitrogen. Trends Ecol. Evol. 16, 153–162. doi:10.1016/s0169-5347(00)02098-x

Robinson, R.S., Kienast, M., Albuquerque, A.L., Altabet, M., Contreras, S., De-Pol-Holz, R., Dubois, N., Francois, R., Galbraith, E., Hsu, T.-C., Ivanochko, T., Jaccard, S., Kao, S.-J., Kiefer, T., Kienast, S., Lehmann, M.F., Martinez, P., McCarthy, M., Möbius, J., Pedersen, T., Quan, T.M., Ryabenko, E., Schmittner, A., Schneider, R.R., Schneider-Mor, A., Shigemitsu, M., Sinclair, D., Somes, C., Studer, A., Thunell, R., Yang, J.-Y., 2012. A

review of nitrogen isotopic alteration in marine sediments. Paleoceanography 27, PA4203.

Romero, O.E., Kim, J.-H., Hebbeln, D., 2006. Paleoproductivity evolution off central Chile from the Last Glacial Maximum to the Early Holocene. Quat. Res. 65, 519–525. doi:10.1016/j.yqres.2005.07.003

Rommerskirchen, F., Plader, A., Eglinton, G., Chikaraishi, Y., Rullkötter, J., 2006. Chemotaxonomic significance of distribution and stable carbon isotopic composition of long-chain alkanes and alkan-1-ols in C4 grass waxes. Org. Geochem. 37, 1303–1332.

Rozanski, K., Araguás-Araguás, L., Gonfiantini, R., 1993. Isotopic patterns in modern global precipitation, in: Swart, P.K., Lohmann, K.C., McKenzie, J., Savin, S. (Eds.), Climate Change in Continental Isotopic Records. pp. 1–35.

Ruddiman, W.F., 2006. Orbital changes and climate. Quat. Sci. Rev. 25, 3092–3112.

Sachse, D., Billault, I., Bowen, G.J., Chikaraishi, Y., Dawson, T.E., Feakins, S.J., Freeman, K.H., Magill, C.R., McInerney, F. a., van der Meer, M.T.J.J., Polissar, P., Robins, R.J., Sachs, J.P., Schmidt, H.-L.L., Sessions, A.L., White, J.W.C.C., West, J.B., Kahmen, A., 2012. Molecular Paleohydrology: Interpreting the Hydrogen-isotopic composition of lipid biomarkers from photosynthesizing organisms. Annu. Rev. Earth Planet. Sci. 40, 221–249. doi:10.1146/annurev-earth-042711-105535

Sandweiss, D.H., Maasch, K.A., Anderson, D.G., 1999. Transitions in the Mid-Holocene. Science (80-.). 283, 499–500. doi:10.1126/science.283.5401.499

Sarkar, A., Sengupta, S., McArthur, J.M., Ravenscroft, P., Bera, M.K., Bhushan, R., Samanta, A., Agrawal, S., 2009. Evolution of Ganges-Brahmaputra western delta plain: clues from sedimentology and carbon isotopes. Quat. Sci. Rev. 28, 2564–2581.

Sarma, V.V.S.S., Krishna, M.S., Viswanadham, R., Rao, G.D., Rao, V.D., Sridevi, B., Kumar, B.S.K., Prasad, V.R., Subbaiah, C. V., Acharyya, T., Bandopadhyay, D., 2013. Intensified oxygen minimum zone on the western shelf of Bay of Bengal during summer monsoon: influence of river discharge. J. Oceanogr. 69, 45–55. doi:10.1007/s10872-012-0156-2

Sarma, Y.V.B., Rama Rao, E.P., Saji, P.K., Sarma, V.V.S.S., 1999. Hydrography and circulation of the Bay of Bengal during withdrawal phase of the southwest monsoon. Oceanol. Acta 22,

453–471.

Sauer, P.E., Eglinton, T.I., Hayes, J.M., Schimmelmann, A., Sessions, A.L., 2001. Compound-specific D/H ratios of lipid biomarkers from sediments as a proxy for environmental and climatic conditions. Geochim. Cosmochim. Acta 65, 213–222.

Schefuß, E., Kuhlmann, H., Mollenhauer, G., Prange, M., Pätzold, J., 2011. Forcing of wet phases in southeast Africa over past 17,000 years. Nature 480, 509–512. doi:10.1038/nature10685

Schefuß, E., Schouten, S., Jansen, J.H.F., Sinninghe-Damsté, J.S., 2003. African vegetation controlled by tropical sea surface temperatures in the mid-Pleistocene period. Nature 422, 418–421.

Schefuß, E., Schouten, S., Schneider, R.R., 2005. Climatic controls on central African hydrology during the past 20,000 years. Nature 437, 1003–1006. doi:10.1038/nature03945

Schimmelmann, A., Sessions, A.L., Mastalerz, M., 2006. Hydrogen Isotopic (D/H) composition of organic matter during diagenesis and thermal maturation. Annu. Rev. Earth Planet. Sci. 34, 501–533.

Schleifer, K.H., Kandler, O., 1972. Peptidoglycan types of bacterial cell walls and their taxonomic implications. Bacteriol. Rev. 36, 407–477.

Schlünz, B., Schneider, R.R., Müller, P.J., Showers, W.J., Wefer, G., 1999. Terrestrial organic carbon accumulation on the Amazon deep sea fan during the last glacial sea level low stand. Chem. Geol. 159, 263–281. doi:10.1016/S0009-2541(99)00041-8

Sessions, A.L., Burgoyne, T.W., Schimmelmann, A., Hayes, J.M., 1999. Fractionation of hydrogen isotopes in lipid biosynthesis. Org. Geochem. 30, 1193–1200.

Shakun, J.D., Burns, S.J., Fleitmann, D., Kramers, J., Matter, A., Al-Subary, A., 2007. A high-resolution, absolute-dated deglacial speleothem record of Indian Ocean climate from Socotra Island, Yemen. Earth Planet. Sci. Lett. 259, 442–456.

Shao, L., Li, X., Geng, J., Pang, X., Lei, Y., Qiao, P., Wang, L., Wang, H., 2007. Deep water bottom current deposition in the northern South China Sea. Sci. China Ser. D Earth Sci. 50,

1060–1066. doi:10.1007/s11430-007-0015-y

Sharma, C., Chauhan, M.S., 1994. Vegetation and climate since Last Glacial Maximum in Darjeeling (Mirik Lake), Eastern Himalaya. Proc. 29th Int. Geol. Congr. Part B 279–288.

Sharma, S., Joachimski, M.M., Tobschall, H.J., Singh, I.B., Sharma, C., Chauhan, M.S., 2006. Correlative evidences of monsoon variability, vegetation change and human inhabitation in Sanai lake deposit: Ganga Plain, India. Curr. Sci. 90, 973–978.

Shetye, S.R., 1993. The movement and implications of the Ganges-Brahmaputra runoff on entering the Bay of Bengal. Curr. Sci. 64, 32–38.

Shetye, S.R., Gouveia, A.D., Shenoi, S.S.C., Sundar, D., Michael, G.S., Nampoothiri, G., 1993. The western boundary current of the seasonal subtropical gyre in the Bay of Bengal. J. Geophys. Res. 98, 945–954.

Shetye, S.R., Shenoi, S.S.C., Gouveia, A.D., Michael, G.S., Sundar, D., Nampoothiri, G., 1991. Wind-driven coastal upwelling along the western boundary of the Bay of Bengal during the southwest monsoon. Cont. Shelf Res. 11, 1397–1408.

Shi, X., Chan, J.C.L., Chow, K.C., Ding, Y., 2008. Effects of upstream surface heat fluxes on the evolution of the South China Sea summer monsoon. Meteorol. Atmos. Phys. 100, 303–325. doi:10.1007/s00703-008-0311-x

Siezen, R.J., Mague, T.H., 1978. Amino acids in suspended particulate matter from oceanic and coastal waters of the Pacific. Mar. Chem. 6, 215–231.

Singh, S.P., Kumar Singh, S., Bhushan, R., 2011. Behavior of dissolved redox sensitive elements (U, Mo and Re) in the water column of the Bay of Bengal. Mar. Chem. 126, 76–88.

Sinha, A., Cannariato, K.G., Stott, L.D., Cheng, H., Edwards, R.L., Yadava, M.G., Ramesh, R., Singh, I.B., 2007. A 900-year (600 to 1500 A.D.) record of the Indian summer monsoon precipitation from the core monsoon zone of India. Geophys. Res. Lett. 34, L16707.

Sinha, A., Cannariato, K.G., Stott, L.D., Li, H.-C., You, C.-F., Cheng, H., Edwards, R.L., Singh, I.B., 2005. Variability of Southwest Indian summer monsoon precipitation during the Bølling-Ållerød. Geology 33, 813–816. doi:10.1130/G21498.1

Sirocko, F., Ittekkot, V., 1992. Organic carbon accumulation rates in the Holocene and glacial Arabian Sea: implications for O2-consumption in the deep-sea and atmospheric CO2 variations. Clim. Dyn. 7, 167–172.

Smith, B.N., Epstein, S., 1971. Two categories of 13C/12C ratios for higher plants. Plant Physiol. 47, 380–384.

Sonzogni, C., Bard, E., Rostek, F., 1998. Tropical sea-surface temperatures during the last glacial period: a view based on alkenones in Indian ocean sediments. Quat. Sci. Rev. 17, 1185–1201.

Southon, J., Kashgarian, M., Fontugne W.W.-S., M.Y., 2002. Marine Reservoir Correction for the Indian Ocean and Southeast Asia. Radiocarbon 44, 167–180.

Stanford, J.D., Hemingway, R., Rohling, E.J., Challenor, P.G., Medina-Elizalde, M., Lester, a. J., 2011. Sea-level probability for the last deglaciation: A statistical analysis of far-field records. Glob. Planet. Change 79, 193–203. doi:10.1016/j.gloplacha.2010.11.002

Staubwasser, M., Weiss, H., 2006. Holocene climate and cultural evolution in late prehistoric-early historic West Asia. Quat. Res. 66, 372–387.

Steinke, S., Glatz, C., Mohtadi, M., Groeneveld, J., Li, Q., Jian, Z., 2011. Past dynamics of the East Asian monsoon: No inverse behaviour between the summer and winter monsoon during the Holocene. Glob. Planet. Change 78, 170–177.

Stoll, H.M., Arevalos, A., Burke, A., Ziveri, P., Mortyn, G., Shimizu, N., Unger, D., 2007. Seasonal cycles in biogenic production and export in Northern Bay of Bengal sediment traps. Deep. Res. II 54, 558–580.

Strong, D., Flecker, R., Valdes, P.J., Wilkinson, I.P., Rees, J.G., Michaelides, K., Zong, Y.Q., Lloyd, J.M., Yu, F.L., Pancost, R.D., 2013. A new regional, mid-Holocene palaeoprecipitation signal of the Asian Summer Monsoon. Quat. Sci. Rev. 78, 65–76. doi:10.1016/j.quascirev.2013.07.034

Stuiver, M., Grootes, P.M., 2000. GISP2 Oxygen Isotope Ratios. Quat. Res. 53, 277–284. doi:10.1006/qres.2000.2127

Stuiver, M., Reimer, P.J., Reimer, R.W., 2005. CALIB 5.0 [WWW program and documentation].

Sturm, C., Zhang, Q., Noone, D., 2010. An introduction to stable water isotopes in climate models: benefits of forward proxy modelling for paleoclimatology. Clim. Past 6, 115–129.

Sun, X., Li, X., 1999. A pollen record of the last 37 ka in deep sea core 17940 from the northern slope of the South China Sea. Mar. Geol. 156, 227–244.

Sun, X., Li, X., Beug, H.-J., 1999. Pollen distribution in hemipelagic surface sediments of the South China Sea and its relation to modern vegetation distribution. Mar. Geol. 156, 211–226. doi:10.1016/S0025-3227(98)00180-7

Sun, X., Li, X., Luo, Y., Chen, X., 2000. The vegetation and climate at the last glaciation on the emerged continental shelf of the South China Sea. Palaeogeogr. Palaeoclimatol. Palaeoecol. 160, 301–316.

Suthhof, A., Ittekkot, V., Gaye-Hakke, B., 2001. Millennial-scale oscillation of denitrification intensity in the Arabian Sea during the late Quaternary and its potential influence on atmospheric N2O and global climate. Glob. Biogeochem. Cycles, 15, 637–649.

Suthhof, A., Jennerjahn, T.C., Schäfer, P., Ittekkot, V., 2000. Nature of organic matter in surface sediments from the Pakistan continental margin and the deep Arabian Sea: amino acids. Deep Sea Res. Part II Top. Stud. Oceanogr. 47, 329–351.

Terashima, M., 1991. Abundance of acidic amino acids and non-protein amino acids in carbonates and muddy sediments, and their relationship to diagenetic decomposition. Chem. Geol. 90, 123–131. doi:10.1016/0009-2541(91)90038-S

Tharammal, T., Paul, a., Merkel, U., Noone, D., 2013. Influence of last glacial maximum boundary conditions on the global water isotope distribution in an atmospheric general circulation model. Clim. Past 9, 789–809. doi:10.5194/cp-9-789-2013

Thomas, E.K., Clemens, S.C., Prell, W.L., Herbert, T.D., Huang, Y., Liu, Z., Sinninghe Damste, J.S., Sun, Y., Wen, X., 2014. Temperature and leaf wax 2H records demonstrate seasonal and regional controls on Asian monsoon proxies. Geology 42, 1075–1078. doi:10.1130/G36289.1

Unger, D., Herbeck, L.S., Li, M., Bao, H., Wu, Y., Zhang, J., Jennerjahn, T., 2013. Sources, transformation and fate of particulate amino acids and hexosamines under varying hydrological regimes in the tropical Wenchang/Wenjiao Rivers and Estuary, Hainan, China. Cont. Shelf Res. 57, 44–58. doi:10.1016/j.csr.2012.02.014

Unger, D., Ittekkot, V., Schäfer, P., Tiemann, J., 2005. Biogeochemistry of particulate organic matter from the Bay of Bengal as discernible from Hydrolysable neutral carbohydrates and amino acids. Mar. Chem. 96, 155–184.

Unger, D., Ittekkot, V., Schäfer, P., Tiemann, J., Reschke, S., 2003. Seasonality and interannual variability of particulate fluxes to the deep Bay of Bengal: influence of riverine input and oceanographic processes. Deep. Res. II 50, 897–923.

Unger, D., Schäfer, P., Ittekkot, V., Gaye, B., 2006. Nitrogen isotopic composition of sinking particles from the southern Bay of Bengal: Evidence for variable nitrogen sources. Deep. Res. I 53, 1658–1676.

Vandewiele, S., Cowie, G., Soetaert, K., Middelburg, J.J., 2009. Amino acid biogeochemistry and organic matter degradation state across the Pakistan margin oxygen minimum zone. Deep. Res. Part II Top. Stud. Oceanogr. 56, 318–334. doi:10.1016/j.dsr2.2008.05.035

Varkey, M.J., Murty, V.S.N., Suryanarayana, A., 1996. Physical oceanography of the Bay of Bengal and Andaman Sea. Oceanogr. Mar. Biol. an Annu. Rev. 34, 1–70.

Vinayachandran, P.N., Kurian, J., 2007. Hydrographic observations and model simulation of the Bay of Bengal freshwater plume. Deep. Res. I 54, 471–486.

Vinayachandran, P.N., Murty, V.S.N., Ramesh Babu, V., 2002. Observations of barrier layer formation in the Bay of Bengal during summer monsoon. J. Geophys. Res. 107, C128018.

Vogts, A., Schefuß, E., Badewien, T., Rullkötter, J., 2012. n-Alkane parameters from a deep sea sediment transect off southwest Africa reflect continental vegetation and climate conditions. Org. Geochem. 47, 109–119.

Vollmer, W., 2015. Peptidoglycan, in: Molecular Medical Microbiology. Elsevier Ltd, pp. 105–124. doi:10.1016/B978-0-12-397169-2.00006-8

Waelbroeck, C., Labeyrie, L., Michel, E., Duplessy, J.C., McManus, J.F., Lambeck, K., Balbon, E., Labracherie, M., 2002. Sea-level and deep water temperature changes derived from benthic foraminifera isotopic records. Quat. Sci. Rev. 21, 295–305.

Wan, S., Li, A., Clift, P.D., Jiang, H., 2006. Development of the East Asian summer monsoon: Evidence from the sediment record in the South China Sea since 8.5 Ma. Palaeogeogr. Palaeoclimatol. Palaeoecol. 241, 139–159.

Wang, Y. V, Larsen, T., Leduc, G., Andersen, N., Blanz, T., Schneider, R.R., 2013. What does leaf wax dD from a mixed C3/C4 vegetation region tell us? Geochim. Cosmochim. Acta 111, 128–139. doi:http://dx.doi.org/10.1016/j.gca.2012.10.016

Wang, B., Clemens, S.C., Liu, P., 2003. Contrasting the Indian and East Asian monsoons: Implications on geologic timescales. Mar. Geol. 201, 5–21.

Wang, P., Clemens, S.C., Beaufort, L., Braconnot, P., Ganssen, G., Jian, Z., Kershaw, P., Sarnthein, M., 2005. Evolution and variability of the Asian monsoon system: state of the art and outstanding issues. Quat. Sci. Rev. 24, 595–629.

Wang, S., Guan, Y., Guan, T., Huang, J., 2012. Oscillation in frequency of tropical cyclones passing Taiwan and Hainan Islands and the relationship with summer monsoon * 30, 966–973.

Wang, S., Lü, H., Liu, J., Negendank, J., 2007. The early Holocene optimum inferred from a high-resolution pollen record of Huguangyan Maar Lake in southern China. Chinese Sci. Bull. 52, 2829–2836. doi:DOI 10.1007/s11434-007-0419-2

Wang, Y., Cheng, H., Edwards, R.L., He, Y., Kong, X., An, Z., Wu, J., Kelly, M.J., Dykoski, C.A., Li, X., 2005. The Holocene Asian Monsoon: Links to Solar Changes and North Atlantic Climate. Science (80-.). 308, 854–857. doi:10.1126/science.1106296

Wang, Y., Cheng, H., Edwards, R.L., Kong, X., Shao, X., Chen, S., Wu, J., Jiang, X., Wang, X., An, Z., 2008. Millennial- and orbital-scale changes in the East Asian monsoon over the past 224,000 years. Nature 451, 1090–1093.

Wang, Y., Liu, X., Herzschuh, U., 2010. Asynchronous evolution of the Indian and East Asian Summer Monsoon indicated by Holocene moisture patterns in monsoonal central Asia.

Earth-Science Rev. 103, 135–153.

Wang, Y., Ren, M., Zhu, D., 1986. Sediment supply to the continental shelf by the major rivers of China. J. Geol. Soc. London. 143, 935–944. doi:10.1144/gsjgs.143.6.0935

Wang, Y.J., Cheng, H., Edwards, R.L., An, Z.S., Wu, J.Y., Shen, C.C., Dorale, J.A., 2001. A High-Resolution Absolute-Dated Late Pleistocene Monsoon Record from Hulu Cave, China. Science (80-.). 294, 2345–2348. doi:10.1126/science.1064618

Wang, Z., Qian, Y., 2009. The relationship of land-ocean thermal anomaly difference with mei-yu and South China Sea summer monsoon. Adv. Atmos. Sci. 26, 169–179. doi:10.1007/s00376-009-0169-y

Weber, M.E., Wiedicke, M.H., Kudrass, H.R., Hübscher, C., Erlenkeuser, H., 1997. Active growth of the Bengal Fan during sea-level rise and highstand. Geology 25, 315–318. doi:10.1130/0091-7613(1997)025<0315:AGOTBF>2.3.CO;2

Weber, M.E., Wiedicke-Hombach, M., Kudrass, H.R., Erlenkeuser, H., 2003. Bengal Fan sediment transport activity and response to climate forcing inferred from sediment physical properties. Sediment. Geol. 155, 361–381.

Webster, P.J., Magana, V.O., Palmer, T.N., Shukla, J., Tomas, R.A., Yanai, M., Yasunari, T., 1998. Monsoons: processes, predictability, and prospects for prediction, in the TOGA decade. J. Geophys. Res. 103, 14451–14510.

Wei, G., Liu, Y., Ma, J., Xie, L., Chen, J., Deng, W., Tang, S., 2012. Nd, Sr isotopes and elemental geochemistry of surface sediments from the South China Sea: Implications for Provenance Tracing. Mar. Geol. 319–322, 21–34. doi:10.1016/j.margeo.2012.05.007

Weijers, J.W.H., Schouten, S., van den Donker, J.C., Hopmans, E.C., Sinninghe-Damsté, J.S., 2007. Environmental controls on bacterial tetraether membrane lipid distribution in soils. Geochim. Cosmochim. Acta 71, 703–713.

Weiss, H., Bradley, R.S., 2001. What drives societal collapse? Science (80-.). 291, 609–610. doi:10.1126/science.1058775

Weng, Q., 2007. A historical perspective of river basin management in the Pearl River Delta of

China. J. Environ. Manage. 85, 1048–1062. doi:10.1016/j.jenvman.2006.11.008

Willmott, C., Feddema, J., 1992. A More Rational Climatic Moisture Index. Prof. Geogr. 44, 84–88. doi:10.1111/j.0033-0124.1992.00084.x

Wu, W., Liu, T., 2004. Possible role of the "Holocene Event 3" on the collapse of Neolithic Cultures around the Central Plain of China. Quat. Int. 117, 153–166. doi:10.1016/S1040-6182(03)00125-3

Wu, Z.Y., 1980. Vegetation in China. Science Press (in Chinese), Beijing.

Wyrtki, K., 1971. Oceanographic atlas of the International Indian Ocean Expedition. National Science Foundation, Washington DC.

Xiao, X., Haberle, S.G., Shen, J., Yang, X., Han, Y., Zhang, E., Wang, S., 2014. Latest Pleistocene and Holocene vegetation and climate history inferred from an alpine lacustrine record, northwestern Yunnan Province, southwestern China. Quat. Sci. Rev. 86, 35–48. doi:10.1016/j.quascirev.2013.12.023

Xu, W., Yan, W., Chen, Z., Chen, H., Huang, W., Lin, T., 2014. Organic matters and lipid biomarkers in surface sediments from the northern South China Sea: origins and transport. J. Earth Sci. 25, 189–196. doi:10.1007/s12583-014-0412-z

Yadava, M.G., Ramesh, R., 2005. Monsoon reconstruction from radiocarbon dated tropical Indian speleothems. The Holocene 15, 48–59.

Yang, S., Tang, M., Yim, W.W.-S., Zong, Y., Huang, G., 2011. Burial of organic carbon in Holocene sediments of the Zhujiang (Pearl River) and Changjiang (Yangtze River) estuaries. Mar. Chem. 123, 1–10.

Yang, T.N., Lee, T.Q., Meyers, P. a., Song, S.R., Kao, S.J., Löwemark, L., Chen, R.F., Chen, H.F., Wei, K.Y., Fan, C.W., Shiau, L.J., Chiang, H.W., Chen, Y.G., Chen, M. Te, 2011. Variations in monsoonal rainfall over the last 21 kyr inferred from sedimentary organic matter in Tung-Yuan Pond, southern Taiwan. Quat. Sci. Rev. 30, 3413–3422. doi:10.1016/j.quascirev.2011.08.017

Yang, W., Zheng, H., Wang, K., Xie, X., Chen, G., Mei, X., 2008. Sedimentary characteristics of

Yang, W., Zheng, H., Wang, K., Xie, X., Chen, G., Mei, X., 2008. Sedimentary characteristics of terrigenous debris at site MD05-2905 in the northeastern part of the South China Sea since 36 ka and evolution of East Asian monsoon. Front. Earth Sci. China 2, 170–176.

Yu, F., Zong, Y., Lloyd, J.M., Leng, M.J., Switzer, A.D., Yim, W.W.-S., Huang, G., 2012. Mid-Holocene variability of the East Asian monsoon based on bulk organic δ13C and C/N records from the Pearl River estuary, southern China. The Holocene 22, 705–715. doi:10.1177/0959683611417740

Yu, G., Liew, P., Xue, B., Li, Z., 2003. Surface pollen and vegetation reconstruction from central Taiwan and nothern mountains of Taiwan. Chinese Sci. Bull. 48, 291–295.

Yuan, D., Cheng, H., Edwards, R.L., Dykoski, C.A., Kelly, M.J., Zhang, M., Qing, J., Lin, Y., Wang, Y., Wu, J., Dorale, J.A., An, Z., Cai, Y., 2004. Timing, duration and Transitions of the Last Interglacial Asian Monsoon. Science (80-.). 304, 575–578.

Zhang, C., Hung, H., 2010. The emergence of agriculture in southern China. Antiquity 84, 15. doi:10.1017/S0003598X00099737

Zhang, P., Cheng, H., Edwards, R.L., Chen, F., Wang, Y., Yang, X., Liu, J., Tan, M., Wang, X., Liu, J., An, C., Dai, Z., Zhou, J., Zhang, D., Jia, J., Jin, L., Johnson, K.R., 2008. A Test of Climate, Sun, and Culture Relationships from an 1810-Year Chinese Cave Record. Science (80-.). 322, 940–942. doi:10.1126/science.1163965

Zhao, H.T., 1990. Evolution of the Pearl River Estuary. Ocean Press, Beijing, China.

Zhao, Y., Yu, Z., Chen, F., Zhang, J., Yang, B., 2009. Vegetation response to Holocene climate change in monsoon-influenced region of China. Earth-Science Rev. 97, 242–256. doi:10.1016/j.earscirev.2009.10.007

Zhisheng, a, Kutzbach, J.E., Prell, W.L., Porter, S.C., 2001. Evolution of Asian monsoons and phased uplift of the Himalaya-Tibetan plateau since Late Miocene times. Nature 411, 62–66. doi:10.1038/35075035

Zhou, B., Zheng, H., Yang, W., Taylor, D., Lu, Y., Wei, G., Li, L., Wang, H., 2012. Climate and vegetation variations since the LGM recorded by biomarkers from a sediment core in the northern South China Sea. J. Quat. Sci. 27, 948–955. doi:10.1002/jqs.2588

Zhou, B., Zheng, H., Yang, W., Wei, G., Li, L., Wang, H., 2011. Organic carbon records since the Last Glacial period in the northern South China sea sediments: implications for vegetation and environmental changes. Quat. Sci. 31, 8–16. doi:10.3969/j.issn.1001

Outline of Contributions

Peer-reviewed papers in international scientific journals

<u>Contreras-Rosales, L.A.</u>, Jennerjahn, T., Tharammal, T., Meyer, V., Lückge, A., Paul, A., Schefuß, E. Evolution of the Indian Summer Monsoon and terrestrial vegetation in the Bengal region during the past 18 ka. *Quaternary Science Reviews* 102 (2014): 133-148. **(Chapter 3)**.

> **Contributions:** Contreras-Rosales L.A. conducted the major part of the analysis and interpretation of the proxy data and wrote most of the manuscript (except for the modeling sections) with scientific and editorial advice from the co-authors.

<u>Contreras-Rosales, L.A.</u>, Schefuß, E.2, Meyer V., Palamenghi, L., Lückge, A., Jennerjahn, T. Origin and fate of sedimentary organic matter in the northern Bay of Bengal during the last 18 ka. *Global and Planetary Change*, submitted. **(Chapter 4)**.

> **Contributions:** Contreras-Rosales L.A. conducted the largest part of the analysis and interpretation of the data and wrote the manuscript with scientific and editorial advice from the co-authors.

<u>Contreras-Rosales, L.A.</u>, Jennerjahn, T., Schefuß, E. Precipitation and vegetation history in Southeast China and Taiwan throughout the Holocene: links between Asian Summer Monsoon strength and tropical cyclone activity. In preparation. **(Chapter 5)**.

> **Contributions:** Contreras-Rosales L.A. was involved in the collection, preparation and analysis of part of the samples, conducted the analysis and interpretation of the data and wrote the manuscript with scientific and editorial advice from the co-authors.

International scientific conferences

<u>Contreras-Rosales, L.A.</u>, Jennerjahn, T., Meyer, V., Lückge, A., Schefuß, E. Late Quaternary history of the East-Indian Monsoon evolution: evidence from sedimentary organic matter. *26th International Meeting on Organic Geochemistry (IMOG 2013)*. Tenerife, Spain, September 16-20, 2013. Poster presentation.

> **Contributions:** Contreras-Rosales L.A. prepared the poster with scientific and editorial advice from the co-authors and presented it at the conference.

<u>Contreras-Rosales, L.A.</u>, Jennerjahn, T., Tharammal, T., Meyer, V., Lückge, A., Paul, A., Schefuß, E. Evolution of the Indian Summer Monsoon and terrestrial vegetation in the Bengal region during the last 18 ka. *European Geosciences Union General Assembly 2014 (EGU-2014)*. Vienna, Austria, April 27 to May 02, 2014. Poster presentation.

> **Contributions:** Contreras-Rosales L.A. prepared the poster with scientific and editorial advice from the co-authors and presented it at the conference.

Acknowledgements

I would like to thank deeply my direct supervisors Dr. Tim Jennerjahn and Dr. Enno Schefuß for giving me the opportunity of doing a PhD and for their encouragement, support and guidance throughout the course of my research. Also, I would like to thank the members of my PhD co-supervision committee Prof. Dr. Dierk Hebbeln, Dr. Andreas Lückge and Dr. Hauke Reuter for the fruitful discussions during the committee meetings.

With deep gratitude I want to acknowledge the support of the German Federal Ministry of Education and Research (BMBF) for providing the funds that made this PhD project possible in the framework of the project CARIMA.

Likewise, I want to thank the Bremen International Graduate School for Marine Sciences (GLOMAR) and its staff members who made possible all the scientific activities that highly enriched my academic PhD life. Especially, I would like to acknowledge GLOMAR economic support that made possible my attendance to the course "Molecular Organic Biogeochemistry" (NIOZ, The Netherlands, 2012), and the scientific conferences "IMOG-2013" (Tenerife, Spain) and "EGU-2014" (Vienna, Austria).

Many thanks as well to the crew and scientific staff of the oceanographic campaigns SO188, SO221, and MD147 on board the research vessels RV *Sonne* and RV *Marion Dufresne* for the recovery of the marine sediment cores used in this research project.

Many and deep thanks to the lab technicians Christina Stashock, Dorothee Dasbach and Dieter Peterke at ZMT, and Ralph Kreutz at MARUM for their valuable work during the analysis of sediment samples. Likewise, many, many thanks to Dr. Britta Beckmann, Vera Meyer, Franziska Heeling, Andreas Eich, Olaf Winckler, Sina Schüler, Christopher Vogel, Oliver Helten and Jessica Volz for their valuable assistance during the preparation of sediment samples for analysis. Moreover, I would like to thank the ZMT staff members who assisted my PhD research in terms of logistical, administrative and technical support, particularly Petra Käpnick and Gabriele Böhme who went far beyond their duties with their kindness and willingness to help in all sorts of matters and for their sincere friendship.

Likewise, I want to thank other members of the CARIMA project who collaborated with me throughout my PhD research, particularly Dr. Mahyar Mohtadi, Dr. Stephan Steinke, Dr. Luisa Palamenghi, Dr. Thejna Tharammal and Dr. André Paul.

Besides, I would like to give special thanks to Dr. Lucia Herbeck and Dr. Anita Flohr for the translation of this thesis abstract to German.

I want to give many, many, thanks to all my colleagues and friends at the ZMT for making my PhD days so wonderful: especial thanks to my officemates Shilly Elizabeth David, Swati Sappal, Sven Forke, Karin Gesierich, and Marc Einsporn for the chats and jokes, and for the joyful and difficult moments we shared alike; to my colleague/friend/housemate Francisca Wit for receiving me so warmly in her home and for the so many wonderful chats over tea we shared; to Marianna Audfroid and Fritz Meyer for all the fantastic weekends at the farm and for sharing with us their delicious wines and jellies, and to Maryam Shahraki, Alejandra Sepúlveda, Celeste Sánchez, Anita Flohr, Debora Pestana, Kim Vane and Dieuwke Hoeijmakers, for all the fun and unforgettable moments we shared.

I would also like to thank my friends in Bremen outside the scientific world, particularly Elena Saez, Cristina Arias and Petra Zeiler for pulling me out of the PhD bubble, and for adding so much spice and fun to my wonderful time in Bremen.

Finally, I want to give my biggest and deepest thanks to my family, both in Mexico and in The Netherlands who supported me without limits through the best and the most difficult moments of my PhD. With deepest gratitude and love, I want to thank my husband Jasper for his infinite support and patience with my PhD project from beginning to end, for encouraging me on the decision of moving to Bremen, and for his greatest care, love, support and understanding through the last, and most difficult, months while I was writing this thesis. Also with deepest gratitude and love, I want to thank my mother Lourdes and my sister Diana for their great hope and trust in me, for their understanding, support and encouragement in my life-changing decision of studying in Europe, and for their inexhaustible love that never lets me feel alone despite the great distance from home. With deepest love, I want to thank my grandfather Gastón and my grandmother Enriqueta, for their unfailing love and support, and for showing me the meaning of strength and perseverance. To my aunt Beatriz for inspire in me the love for science and for her love and support. To my father Cuauhtémoc for securing my best possible academic formation as well as

for his love and support. To my dearest friends Karla and Cecilia, for their love, support and friendship over so many years and for sharing all my fortunes and misfortunes with equal interest. And to my family in The Netherlands Robert, Annemarie, Robin and Jason, for receiving me so warmly into the family and giving me a new place to call home, and for their love and support ever since I arrived to Europe.

Erklärung

Name: Lorena Astrid Contreras Rosales

Anschrift: Provence 37, 3524 RP, Utrecht, The Netherlands

Hiermit versichere ich, dass ich

1. die Arbeit ohne unerlaubte fremde Hilfe angefertigt habe,

2. keine anderen als die von mir angegebenen Quellen und Hilfsmittel benutzt habe und

3. die den benutzten Werken wörtlich oder inhaltlich entnommenen Stellen als solche kenntlich gemacht habe.

Bremen, den ....

(Unterschrift)